Quasi-Free Scattering off Neutron-Rich Oxygen and Fluorine Isotopes at Relativistic Beam Energies at R^{3}B

Tahani Hamad Almusidi

Doctor of Philosophy

University of York

Physics

January 2022

Abstract

The structure of the neutron-rich oxygen and fluorine isotopes with 11 neutrons up to 14 neutrons has been investigated by utilizing the quasi-free scattering (QFS) in inverse kinematics with a proton-rich target at the $\mathrm{R^3B}$ setup at GSI-Helmholtz Centre for Heavy Ion Research in Darmstadt, Germany.

To analyse the reaction channels of interest $^{19}\mathrm{O(p,2p)}^{18}\mathrm{N}$, $^{20}\mathrm{O(p,2p)}^{19}\mathrm{N}$, $^{21}\mathrm{F(p,2p)}^{20}\mathrm{O}$, $^{22}\mathrm{F(p,2p)}^{21}\mathrm{O}$, and $^{23}\mathrm{F(p,2p)}^{22}\mathrm{O}$, the delivered relativistic incoming beam from the FRagment Separator (FRS) was identified using a variety of detectors in front of the reaction area. In addition, the outgoing particles are identified around and after the reaction area. Therefore, the ALADIN dipole magnet was used after the reaction area to separate the reaction products.

The gathered data were used to deduce the inclusive reduction factor for the simple cases by comparing the inclusive experimental cross section to the total theoretical one of the related orbit based on the eikonal reaction theory. Furthermore, the study presents a comparison between the experimental and theoretical momentum distributions for the residuals of interest.

This study has shown a good agreement between the measured and calculated momentum distributions. Furthermore, the obtained inclusive reduction factors support the claim of the weak or no dependence on isospin asymmetry. Moreover, the value of the obtained inclusive reduction factor of the reaction channel $^{22}\mathrm{F(p,2p)}^{21}\mathrm{O}$ is within the range of the reduction factors of the oxygen isotopic chain.

Furthermore, the obtained result from testing the future $\mathrm{R^3B}$ Si-tracker in STFC Daresbury is presented. This tracker aims to increase the sensitivity of hadron-induced quasi-free scattering at the $\mathrm{R^3B}$ setup.

Contents

List of Tables

List of Figures

Acknowledgment

I would like to take this opportunity to express my gratitude to the supportive people who have helped me at some point over the past years.

I am grateful to my supervisor, Dr. Stefanos Paschalis, for giving me the opportunity to work on this research and participate in other experiments. I am thankful for his supervision, constant guidance, encouragement, valuable discussion, and corrections. This thesis could not have been done without his incredible help.

Special thanks to King Saud University and the Royal Embassy of Saudi Arabia Cultural Bureau for their financial support.

A massive thanks to Dr. Matthias Holl and Dr. Ina Syndikus for their support during the analysis. Thanks to Dr. Marc Labiche, Dr. Michael Heil, and Julien TAIEB. I appreciate the training and their kindness. I also thank Matthew Pickin, Dr. Ryo Taniuchi, and Warren Langthorne. Thank you to all my friends. I appreciate your love and support.

Finally, I am grateful to my family for their unconditional love, care, support, and prayers. I am grateful to have all of you in my life; you mean everything to me. You are my inspiration to reach my dreams and my comfort when I falter. My heartfelt appreciation goes to my mother and father for their eternal love and care. They are the ones who set the path for me to follow my dreams. Also, I am thankful to my brothers, Abdulrahman and Abdulhakim, who devoted their time and traveled abroad to join me during my Ph.D. journey. I am deeply sorry for the time I spent away from my beloved family. Each day away from them feels like years.

Declaration

I declare that this thesis is a presentation of original work and I am the sole author. This work has not previously been presented for an award at this, or any other, University. All sources are acknowledged as References.

Chapter 1: Introduction

Between 1911 and 1932, the picture of the nucleus and its component of proton and neutron had been identified. Ernest Rutherford (1871-1937), the father of Nuclear Physics, discovered the existence of the nucleus in 1911 and pictured it as a central positive charge [1]. Then, a particle of a mass equal to one and a charge of zero, called a neutron, was introduced in 1932 by James Chadwick (1891-1974) [2]. Since their discovery, theoretical models and experimental investigations have been carried out to understand nuclear structure. One of the theoretical models that describes the nuclei structure is the nuclear shell model developed by Maria Goeppert-Mayer (1906-1972) and Johannes Hans Daniel Jensen in 1949 [3, 4]. Up to now, the experimental techniques have been improved to explore and explain the nuclear structure and properties. Thus, nuclei far from stability have been accessible. New nuclear phenomena appear, and as a consequence, modifications to the nuclear shell model have been applied. By way of illustration, all discovered nuclei are shown in the nuclei chart in Figure 1, where the nuclei are ordered according to their proton and neutron numbers. The black-colored area in the chart indicates the stable nuclei. This area includes 293 isotopes stable or with a lifetime longer than four billion years. Overall, more than 3000 isotopes were discovered, while the theoretical models predict more [5, 6].

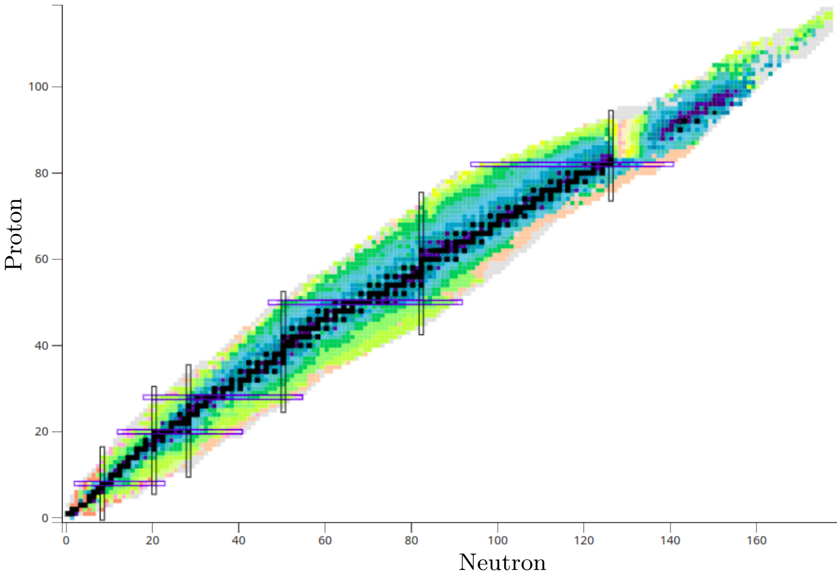

Figure 1: The nuclei chart. The stable nuclei are exhibited in black. Other colors indicate the radioactive nuclei [6].

Despite the nuclear shell model modification, there is still a mismatch between the theoretical predictions and experimental measurements of the shell occupancies, which is outlined by various studies investigating the occupation probability of a single particle (spectroscopic factors SF). This mismatch is described in terms of the reduction factor R_s, and it goes from zero to one.

Gathered data from extensive research based on electron-induced proton knockout reactions $(e, e^{'}p)$ and nucleon-knockout reactions reveals that the reduction factor has shown a strong dependence on the difference in separation energies $\Delta \mathrm{S} = \mathrm{S_p} - \mathrm{S_n}$ for proton removal and $\Delta \mathrm{S} = \mathrm{S_n} - \mathrm{S_p}$ for neutron removal as illustrated in Figure 2 [7]. The difference in separation energies is used to measure the asymmetry of the proton and neutron binding energy. A closer inspection of oxygen and fluorine isotopes from left to right in the presented data in Figure 2 can allow a deeper insight into the reduction factor. The data point $^{24}\mathrm{O}(-\mathrm{n})$ of the one-neutron removal reaction with a significant negative value of the difference in separation energies $\Delta \mathrm{S} = -21.3\,\mathrm{MeV}$ shows a reduction factor $\mathrm{R_s} = 1.06(15)$. This reaction was performed at the National Superconducting Cyclotron Laboratory (NSCL) at Michigan State University using beam energies of 92.3 MeV/nucleon on a ^{9}Be target. This result indicates that the measured cross section agrees with the calculated one that utilizes the eikonal reaction model and the shell-model nuclear structure [8]. The $^{14}\mathrm{O}(-\mathrm{p})$ data point of one-proton knockout reaction with ΔS equal to -18.5 MeV has a reduction factor of 0.76(11), where a large error bar can be seen in Figure 2. The reaction was performed at the Heavy Ion Research Facility in Lanzhou (HIRFL) on a carbon target at a high energy beam of 305 MeV/nucleon [9, 10]. The data point $^{16}\mathrm{O}(-\mathrm{p})$ of the single-proton knockout reaction in the center of Figure 2 shows a reduction factor of 0.68(4) in the experimental cross sections relative to the calculated one based on the shell model and eikonal reaction theory. This finding agrees with the deduced reduction factor 0.67(5) from a high-energy electron-induced proton knockout reaction $(\mathrm{e}, \mathrm{e}^{\prime}\mathrm{p})$, indicated by the black data point. Moreover, the data point $^{16}\mathrm{O}(-\mathrm{n})$ of the single-neutron removal reaction in the center of Figure 2 reveals a reduction in the experimental cross sections relative to the calculated cross section based on the shell model and eikonal reaction theory by a factor of 0.56(3). Both reactions, $^{16}\mathrm{O}(-\mathrm{p})$ and $^{16}\mathrm{O}(-\mathrm{n})$, were made using a 2100 MeV/nucleon beam on a carbon target at Berkeley [9, 11]. The data point $^{25}\mathrm{F}(-\mathrm{p})$ of the proton removal reaction with ΔS equal to 10.17 MeV shows a significant reduction factor of 0.48(5). This reaction was performed by using a carbon target and beam energy of 218 MeV/nucleon [7]. Overall, these results indicate that the reduction factor of removing weakly-bound nucleons, where ΔS takes a substantial negative value, are close to unity while deeply-bound ones, where ΔS takes a significant positive value, are much smaller than unity.

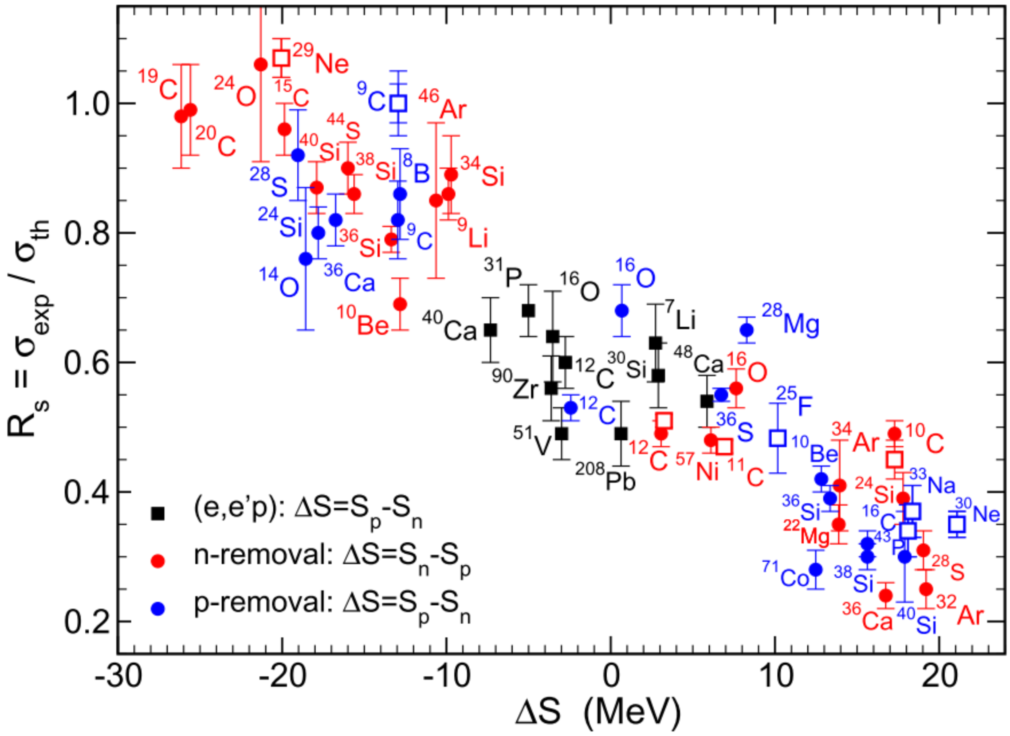

Figure 2: The calculated reduction factor R_s of the experimental and theoretical inclusive cross sections of single-nucleon removal as a function of the difference in separation energies ΔS, where $\Delta S = S_p - S_n$ for proton removal in blue, and $\Delta S = S_n - S_p$ for neutron removal in red. ΔS is used to quantify the asymmetry of the proton and neutron Fermi surfaces. Furthermore, the data of new higher-energy are indicated by open squares. While the gathered data from electron-induced proton knockout reactions are indicated by solid black squares [7].

This finding contradicts other studies that have established a weak or no depends on neutron-proton asymmetries [12–14]. This weak or no depends has been seen in the results from transfer reactions (p,d) of $^{34}_{18}\mathrm{Ar}_{16}$, $^{36}_{18}\mathrm{Ar}_{18}$, and $^{46}_{18}\mathrm{Ar}_{28}$, as exhibited in Figure 3. Also, what is interesting about the data in this figure is that the observed range of the reduction factor for the proton-rich nucleus of $^{34}_{18}\mathrm{Ar}_{16}$ goes from 0.65 to 0.75. This range differ from the neutron-knockout reaction study, whereas it goes from 0.35 to 0.45 as illustrated in Figure 2. Furthermore, the weaker or no dependence finding was also reported by data from a quasi-free scattering (p,2p) in inverse kinematics of oxygen isotopic chain, ^{14,16,17}O and $^{21-23}$O, as presented in Figure 4 [13].

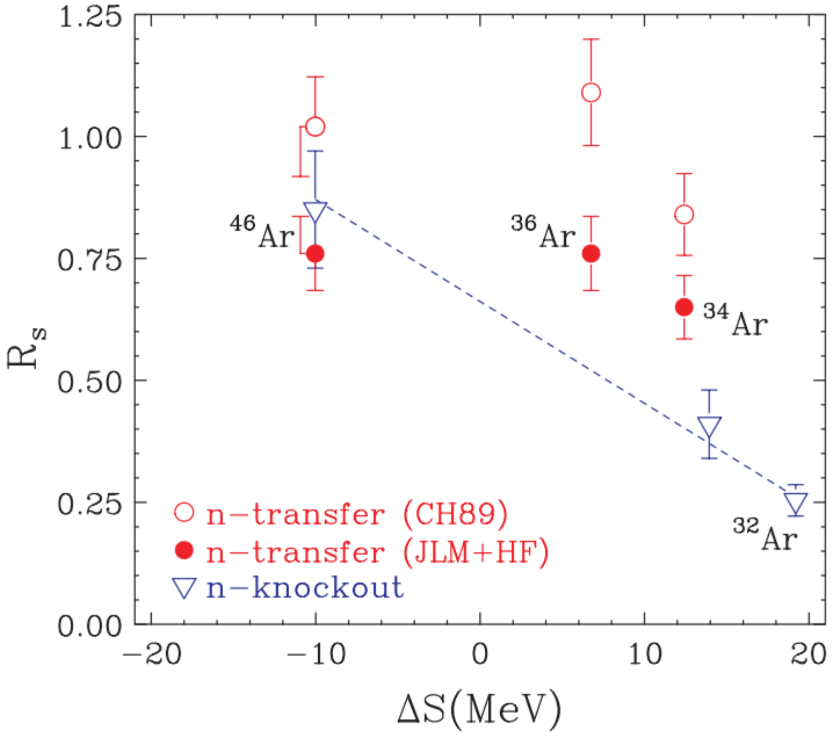

Figure 3: The reduction factor R_s as a function of the ΔS parameter for $^{34}_{18}Ar_{16}$, $^{36}_{18}Ar_{18}$, and $^{46}_{18}Ar_{28}$. The transfer reaction (red) shows a weaker dependence than the knockout reaction (blue) [12].

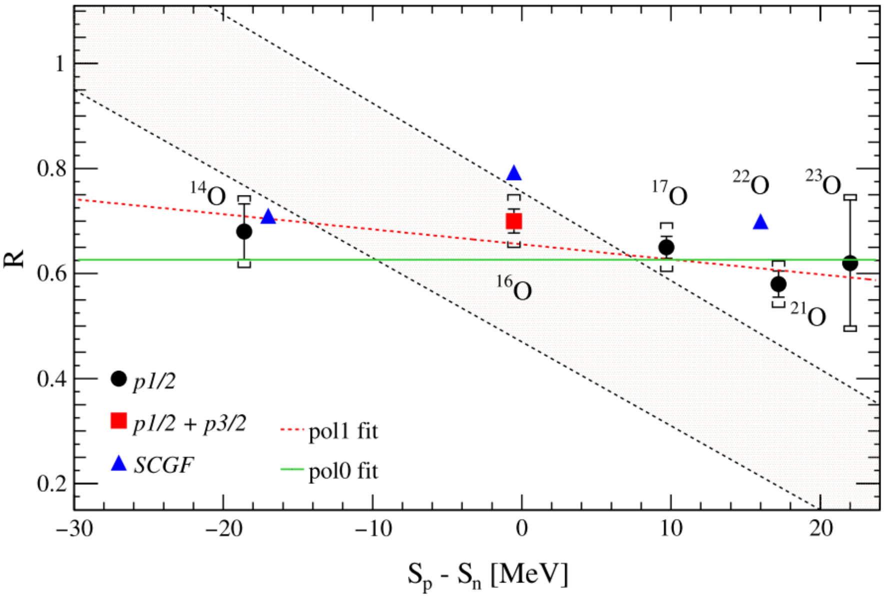

Figure 4: The reduction factor R_s as a function of the $\Delta S = S_p - S_n$ parameter for data deduced from a quasi-free scattering (p,2p) of $^{14,16,17}O$, and $^{21-23}O$. It shows a week dependence than the shaded area that represents the data of knockout reaction [13].

Another study supports the weaker or no dependence of the reduction factors on the isospin asymmetry deduced from the quasi-free scattering (p,2p) of the oxygen isotopic chain ^{14,16,18,22,24}O is shown in Figure 5 [14].

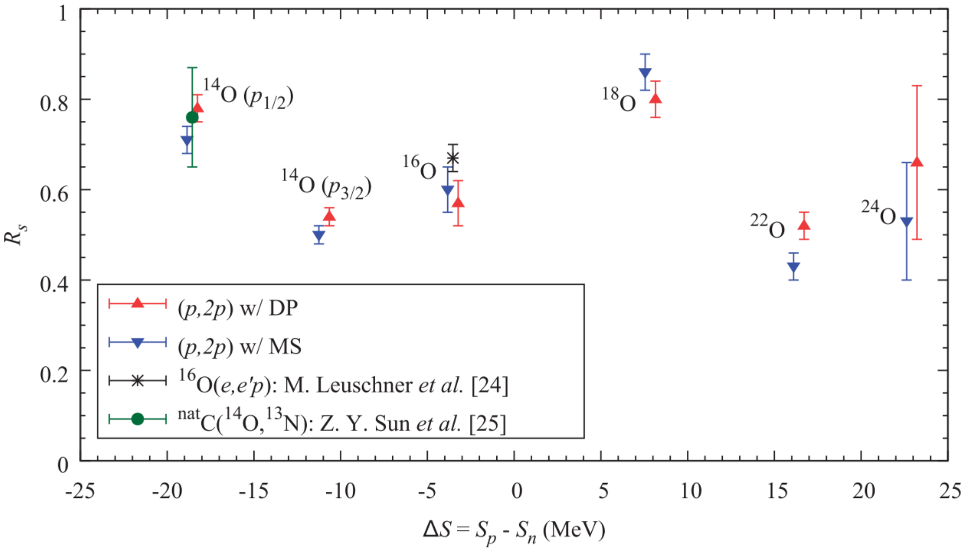

Figure 5: The reduction factor R_s, deduced using two different optical potentials, as a function of the $\Delta S = S_p - S_n$ parameter for the ^{14,16,18,22,24}O isotopes. The quasi-free scattering (p,2p) was utilized to obtain the data. It shows no dependence on the difference in separation energies [14].

The dependence of the reduction on the isospin is a debatable area. A possible explanation for this reduction may be the nucleon-nucleon correlations (NN), which have not been dealt with appropriately in the nuclear shell model, or deficiencies in the utilized reaction model. Questions on the individual contributions of nucleon-nucleon correlations and the neutron-proton asymmetry to depletion of the single-particle have been raised in need of further investigation.

This study aims to contribute to this growing area of research by completing the systematic analysis of the neutron-rich side of the oxygen isotopic chain and investigating the neutron-rich side of the fluorine isotopic chain, especially ^{19,20}O and $^{21-23}$F. All nuclei of interest with 11 neutrons up to 14 neutrons are selected based on their nucleon separation energies, as illustrated in Table 1. This variety is appropriate for investigating the dependence of the reduction factor R_s on the isospin asymmetry ΔS. Furthermore, this dissertation aims to assist in unraveling the mysteries surrounding the fluorine nuclei and its oxygen core. The simple shell model predict ^{28}O to be the last bound oxygen. Contrary to expectations, ^{24}O is the last bound oxygen isotope in the nuclei chart. Though adding one additional proton and six neutrons gives the last bound fluorine ^{31}F. The most recent investigation on ^{25}F nuclei ($^{24}O_{core} + 1$ proton) performed at RIKEN Nishina Center and Center of Nuclear Study establishes a remarkable difference between its oxygen core $^{24}O_{core}$ and free ^{24}O nucleus [15]. This reaction was made by utilizing a quasi-free knockout reaction at 270 MeV/nucleon in inverse kinematics. In the current study, the single-particle structure of these short-lived nuclei ^{19,20}O and $^{21-23}$F was accessed by using the quasi-free scattering (QFS) reaction in inverse kinematics with a proton-rich target. This reaction is viewed as a scattering that only evolves the nucleus of interest nucleon and target proton without any disruption to the nucleus component. Furthermore, the reaction was made in complete kinematics measurements using the R^{3}B setup at GSI-Helmholtz Centre for Heavy Ion Research in Darmstadt, Germany.

Table 1: Proton and neutron separation energy of the oxygen and fluorine isotopes according to [16].

	^{19}O	^{20}O	^{21}O	^{22}O	^{23}O	^{24}O
S_p (MeV)	17.1	19.3	21.0	23.2	24.4	25.5
S_n (MeV)	4.0	7.6	3.8	6.6	2.7	4.2
	^{20}F	^{21}F	^{22}F	^{23}F	^{24}F	^{25}F
S_p (MeV)	10.4	11.1	12.6	13.3	14.4	14.5
S_n (MeV)	6.6	8.1	5.2	7.6	3.8	4.3

The overall structure of this thesis takes the form of nine chapters, including this introduction, first chapter, and the development and testing of the R^{3}B Si-tracker, eighth chapter. The remaining chapters proceed as follows: Chapter Two gives a brief overview of the theoretical concepts of this research. Chapter Three shows the experimental setup that is used for this study. Chapter Four analyses the gathered data during the S393 experiment. Chapter Five outlines the performed simulation. Chapter Six presents the analysis findings in detail, focusing on the experimental observables and the obtained reduction factor for all the reactions of interest. Chapter Seven discusses the obtained results. Finally, chapter Nine presents the conclusion and the outlook.

Chapter 2: Theory

The theory chapter begins with the independent particle model and the shell model. The second section in this chapter illustrates the usage of the spectroscopic factor and the reduction factor. The chapter ends with a description of the quasi-free scattering reaction in inverse kinematics employed in this work to study the structure of neutron-rich nuclei.

2.1 The Independent Particle Model (IPM) and Shell Model

The independent particle model describes nucleons inside the nucleus matter; it assumes that nucleons move smoothly in an average potential V(r) created by interactions with other nucleons without colliding. A realistic form for the shell-model potential is sketched in Figure 6 and written as [17]:

$$\mathrm{V(r)} = \frac{-\mathrm{V_0}}{1 + \exp[\frac{\mathrm{r-R}}{\mathrm{a}}]} \tag{1}$$

Here, $\mathrm{V_0}$ is the potential depth. R is the mean radius, and it is equal to $1.25\mathrm{A}^{\frac{1}{3}}$ where the depth of the potential is equal to $0.5\mathrm{V_0}$. a is the surface diffusion parameter that gives the skin thickness $4\mathrm{a}\ln 3$ where the depth of the potential changes from $0.9\mathrm{V_0}$ to $0.1\mathrm{V_0}$. The sketched shell-model potential indicates that the potential has a negative value, and its curve is flat at the center of the nucleus, where $\mathrm{r} = 0$, since the single nucleon feels the interaction from all surrounding nucleons. Thus, the potential gets weaker as the nucleon gets closer to the surface, where $\mathrm{r = R}$, till it ends at zero value outside the nucleus surface [5, 17].

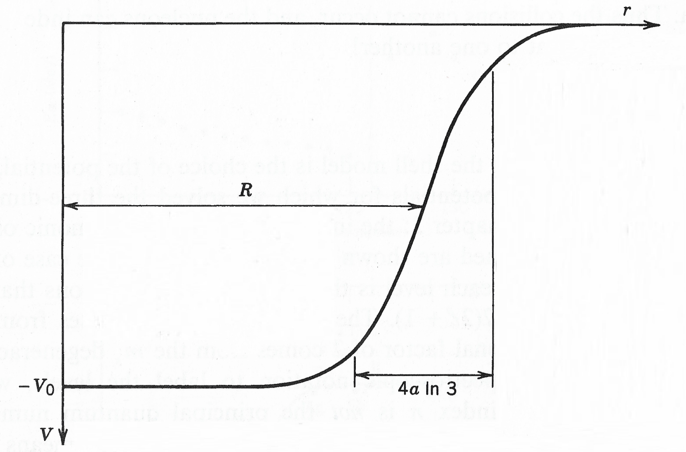

Figure 6: A sketch of the shell-model potential V(r). It can be clearly seen that the potential has a negative value $-\mathrm{V_0}$ at the nucleus center and get weaker as the nucleon gets closer to the surface at radius R, which it is equal to $1.25\mathrm{A}^{\frac{1}{3}}$ [17].

Solving the Schrödinger equation using the realistic form for the shell model potential in equation 1 gives the shell structure, where the nucleons move in, as shown on the left side of Figure 7 [17].

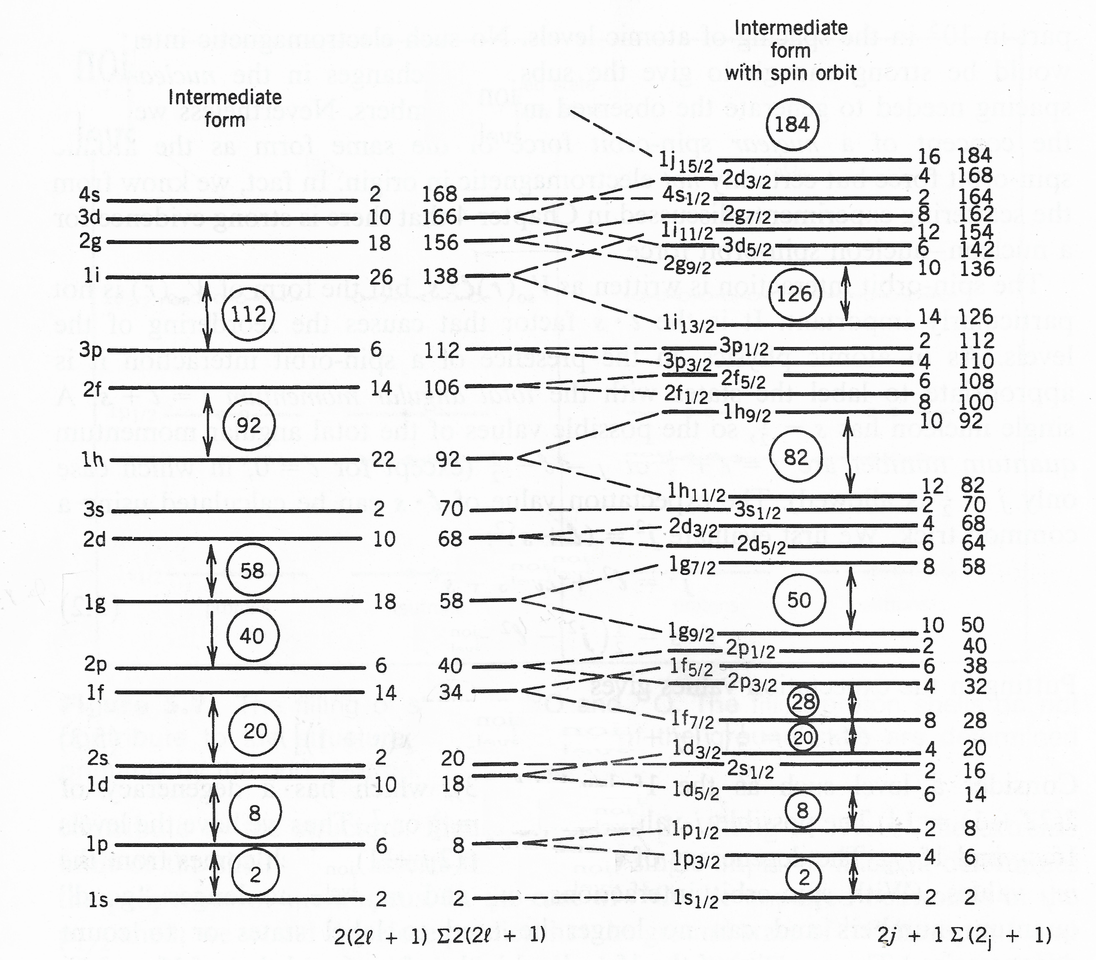

Figure 7: The left side of the figure shows the energy levels calculated with the realistic form for the shell model potential of figure 6. The right side shows the modified energy levels obtained by including the spin-orbit interaction. The splits in the energy levels with l > 0 into two new levels resulting from the spin-orbit interaction [17].

Each orbit is labeled by the number of nodes of its wave function (n = 1, 2, ...), and notation (s, p, d, f, g) for (l = 0, 1, 2, 3, 4) in sequence and it is shown in the left side of each orbit. Furthermore, the occupancy of each orbit is given by $2(2l + 1)$ nucleons as illustrated in the right side of the intermediate form's orbits. It is necessary here to clarify that protons and neutrons are reviewed individually to fill the shell structure. By way of illustration, the first level can be filled with two protons as well as two neutrons. Furthermore, both neutron and proton orbits are subjected to Pauli's exclusion principle. In other words, two identical nucleons within the same orbit cannot have similar quantum numbers; the configurations of two identical nucleons only exist in the total spin state S = 0, where the similar nucleons have different spins.

These defined orbits are grouped to form shells and the shell gap refers to the space between the two following shells. A fully occupied shell with nucleons forms a closed shell, and the sum of nucleons within the closed shell is called a magic number, which is represented by the circled number at the top of each closed shell, i.e., 2, 8, 20, 40, 58, etc. What is interesting in the magic numbers is the indication of the stable nuclei that characterized with a spherical potential and a total angular momentum and parity of $J^\pi = 0^+$. Furthermore, the closed shell is called a core, and the shell structure refers to the pattern of the upper orbits of the core.

In terms of enhancing the shell-model potential and to form an appropriate magic number, the term of spin-orbit interaction $V_{ls}(r)$ is added:

$$V_{ls}(r) = V_{so}(r)\,(\overrightarrow{l}\,.\,\overrightarrow{s}) \tag{2}$$

where $V_{so}(r)$ is the spin-orbit potential, a function of the distance r and obtained by the derivative of the density over r with appropriate strength and s is a nucleon spin. The effect of the spin-orbit interaction is illustrated on the right side of Figure 7. It breaks the orbits with $l > 0$ into two new orbits and tags them by the total angular momentum $j = l \pm \frac{1}{2}$ besides the number of nodes of its wave function and notation. The orbits with the larger j are shifted downward because of the negative value of $V_{so}(r)$, and the splitting increases as the l value increases. Further, each newly generated orbit can be occupied by $2j + 1$ nucleons. Thus, the magic number are reproduced, i.e., 2, 8, 20, 28, 50, etc. [5, 17–19].

An evidence of the magic numbers can be clearly seen in the case of the nucleon separation energy as illustrated in Figure 8. What stands out in the figure is removing nucleons that occupy fully filled orbit just below the shell gap requires more energy than extracting nucleons filling an orbit above the shell gap [17].

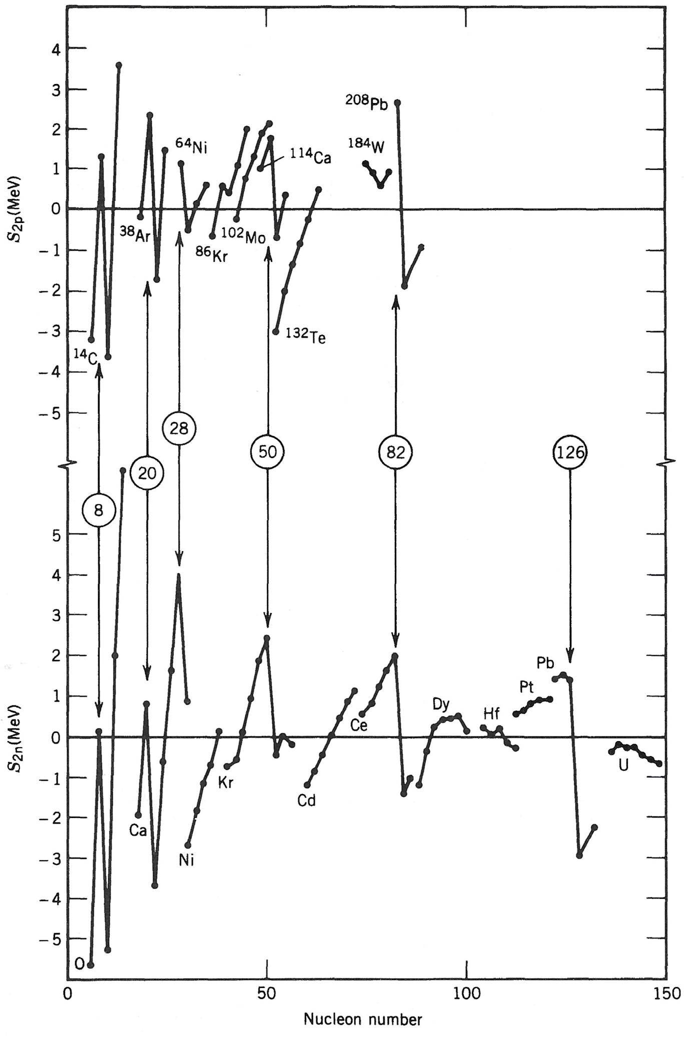

Figure 8: The two-nucleon separation energy as a function of nucleons number for a sequences of isotones; it shows an abrupt decrease at the circled magic numbers 8, 20, 28, 50, 82, 126 [17].

Furthermore, it is interesting to note that the closed shells are often treated as a vacuum inert core because whole orbits are occupied, and the nucleons cannot modify their single-particle states. In contrast, the following shell above the closed-shell can be partially occupied with nucleons, where degrees of freedom and nucleon-nucleon interaction cause nucleons to move within the orbits. This partially occupied shell is named the valence shell, and its nucleons are called valence nucleons. Thus, a configuration can be defined as the occupancy pattern of the valence nucleons over various orbits within the valence shell. All probable configurations (occupancy patterns) are mixed many times until reaching an equilibrium.

As discussed above, the total angular momentum and parity of the nuclear ground state of nuclei with an even number of protons and neutrons, which are known as even-even nuclei, are $J^\pi = 0^+$. On the other hand, the odd-even and even-odd nuclei are different from even-even nuclei in their total angular momentum and parity, which are the half-integral angular momentum J and $(-1)^{\mathrm{l}}$ parity of the unpaired nucleon. In contrast to the previous nuclei, the odd-odd nuclei have angular momentum equal to an integer between the limits $|\mathrm{j_n} - \mathrm{j_p}| \leq \mathrm{J} \leq \mathrm{j_n} + \mathrm{j_p}$ and their parity are given by $(-1)^{\mathrm{l_n}+\mathrm{l_p}}$ of unpaired nucleons [19].

The application of the shell model can be illustrated briefly by considering the filling of the shell model levels to produce ${}^{19}_{8}\mathrm{O}_{11}$ and ${}^{20}_{8}\mathrm{O}_{12}$, as shown in Figure 9. The ground state of the even-odd nuclei ${}^{19}_{8}\mathrm{O}_{11}$ has a spin and parity of $\frac{5}{2}^+$ [6]; it is characterized by the odd neutron in the $\nu 1\mathrm{d}_{5/2}$ with a spin of $\frac{5}{2}$ and parity of $(-1)^{l=2}$. In comparison, the ground state of the even-even nuclei ${}^{20}_{8}\mathrm{O}_{12}$ is 0^+ since all the nucleons are paired.

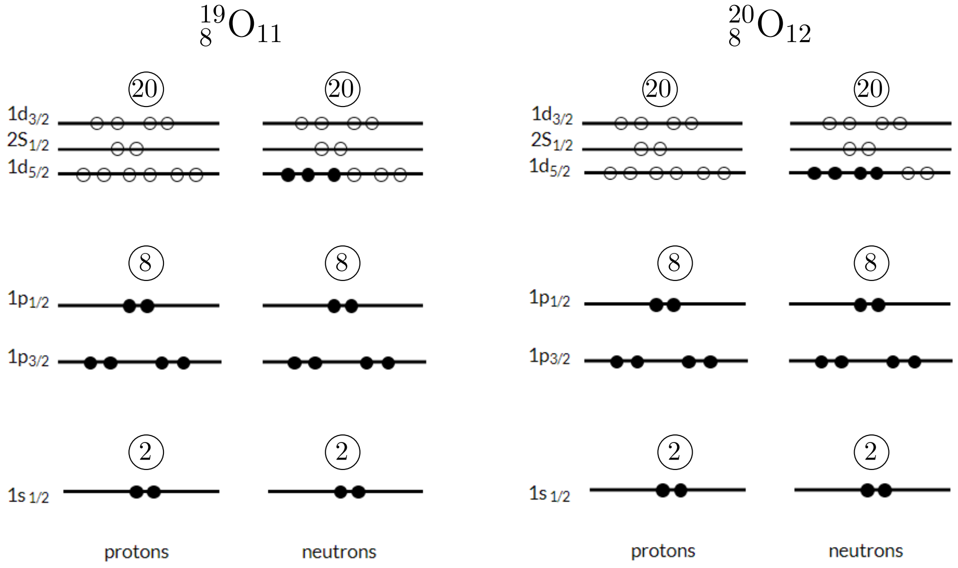

Figure 9: The filling of protons and neutrons shells in ${}^{19}_{8}\mathrm{O}$ and ${}^{20}_{8}\mathrm{O}$. The circled numbers denote the magic numbers.

2.2 The Spectroscopic Factor (SF) and Reduction Factor ($\mathrm{R_s}$)

The modification on the occupancy of the single-particle orbits is associated with the nucleon-nucleon correlations. For the purpose of examination, the experimental measurements are linked to the microscopic theories by a significant quantity called spectroscopic factor (SF). It reflects the information of the single-particle occupancy of a parent state and the overlap of its wave function with the daughter system after the reaction. It can be obtained experimentally by measuring the exclusive cross sections of a certain state. For more clarification, consider removing a nucleon from an initial state of the parent nucleus A with a spin ($\mathrm{I_A}$) and the initial state many-body wave functions of $\Psi_\mathrm{i}^\mathrm{A}$. As a consequence, a final state of daughter nucleus $\mathrm{A}-1$ is formed with a spin of ($\mathrm{I_{A-1}}$) and a final state many-body wave functions of $\Psi_\mathrm{f}^\mathrm{A-1}$. Thus, the overlap function has an angular momentum $|\,\mathrm{I_A}-\mathrm{I_{A-1}}\,| \le \mathrm{j} \le \mathrm{I_A}+\mathrm{I_{A-1}}$ and given by:

$$\langle \overrightarrow{\mathrm{r}}, \Psi_\mathrm{f}^\mathrm{A-1} | \Psi_\mathrm{i}^\mathrm{A} \rangle = \sum_\mathrm{j} \mathrm{c_j^{if}}\, \Psi_\mathrm{j}(\overrightarrow{\mathrm{r}}) \tag{3}$$

The Ψ_j is normalized to unity and the theoretical spectroscopic factor is written as $\mathrm{S_j^{if}} = |\mathrm{c_j^{if}}|^2$. The predicted value of theoretical spectroscopic factor $\mathrm{S_j}$ is equal to one for removing a nucleon from a pure single-particle state, and it is equal to $2\mathrm{j}+1$ for removing a nucleon from a filled orbit of a total angular momentum j. In the isospin representation, the spectroscopic factor is written in the form $\mathrm{C^2S_j}$, where $\mathrm{C^2}$ is the square of the isospin coupling coefficient [20].

The spectroscopic factor is used to obtain the theoretical cross section for a single nucleon-removal to a given final state of the residue (a specific core state) nI^π and is given as:

$$\sigma_\mathrm{theo}(\mathrm{nI}^\pi) = \sum_\mathrm{j} \mathrm{C^2S_{c.m.}}(\mathrm{nI}^\pi, \mathrm{lj})\, \sigma_\mathrm{sp}(\mathrm{S_N}, \mathrm{lj}) \tag{4}$$

where $\sigma_\mathrm{sp}(\mathrm{S_N}, \mathrm{lj})$ is the single-particle removal cross section that shows strong dependence on both the orbital angular momentum l and nucleon separation energy S_N. It is given by the sum of the inelastic $\sigma_\mathrm{sp}^\mathrm{inel}$ and elastic $\sigma_\mathrm{sp}^\mathrm{elas}$ cross section. $\mathrm{C^2S_{c.m.}}(\mathrm{nI}^\pi, \mathrm{lj})$ is the shell-model spectroscopic factors with a center-of-mass motion correction since it is calculated in a harmonic-oscillator basis and it is equal to $[\mathrm{A}/(\mathrm{A}-1)]^\mathrm{N}\mathrm{C^2S}(\mathrm{nI}^\pi, \mathrm{lj})$, where N is the oscillator quanta number that is related to the major shell of the removed nucleon [7, 11, 20].

With regard to the reduction factor $\mathrm{R_s}$, it can be defined as the ratio between the experimental and theoretical spectroscopic factor:

$$\mathrm{R_s} = \frac{\mathrm{S_{exp}}}{\mathrm{S_{theo}}} \tag{5}$$

However, the experimental partial (exclusive) cross section $\sigma_\mathrm{exp,\,exclusive}$ for a specific nucleon at the state of interest is reduced from the single-particle removal cross section $\sigma_\mathrm{sp}(\mathrm{S_N}, \mathrm{lj})$ by the experimental spectroscopic factor:

$$\mathrm{S_{exp}} = \frac{\sigma_\mathrm{exp,\,exclusive}}{\sigma_\mathrm{sp}(\mathrm{S_N}, \mathrm{lj})} \tag{6}$$

Predominantly, the shell model wave function is distributed over multiple states as shown in Figure 10, the experimental spectroscopic factors for $^{91}_{40}\mathrm{Zr}$ from $^{90}\mathrm{Zr(d,p)}^{91}\mathrm{Zr}$ reaction, where the spectroscopic factor strength is denoted by length of the thick line [17].

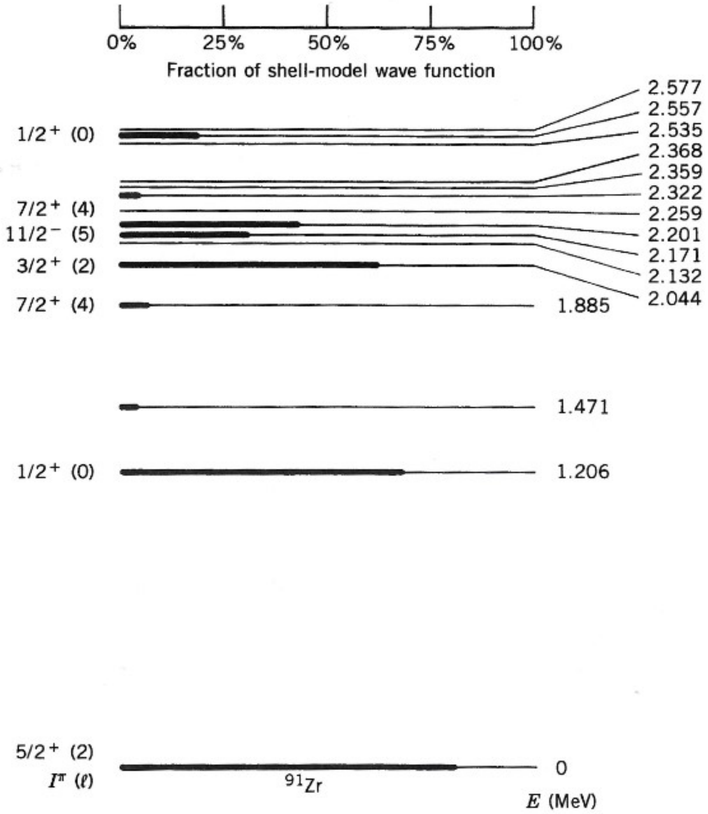

Figure 10: The level scheme for $^{90}\mathrm{Zr(d,p)}^{91}\mathrm{Zr}$; the shading length of each level represents the single-particle strengths. Thus, the ground state is an almost pure $d_{5/2}$ shell model state [17].

2.3 Quasi-Free Scattering (QFS) Reaction in Inverse Kinematics

The electron-induced proton-knockout reaction $(\mathrm{e,e^{'}p})$ provides a proper tool to investigate the dependence of the reduction factor. Still, one major drawback of this approach is that it is limited to the proton-removal channel of stable nuclei. In contrast, the hadronic knockout reaction is a powerful tool for studying the structure of exotic nuclei. The quasi-free scattering reaction (QFS) is a direct way to investigate the structure of nuclei and provides an alternative approach to deduce the spectroscopic factors. This reaction is known as (p,2p) for proton removal or (p,pn) for neutron removal [21]. In this reaction, a projectile proton (p) at high energy of a few hundred MeV with a kinetic energy k_p and momentum $\overrightarrow{\mathrm{P}}_{\mathrm{p}}$ incidents a stationary target of the nucleus of interest (A) and hits a single nucleon (N) at its internal motion with a kinetic energy $\mathrm{k_N}$ and momentum $\overrightarrow{\mathrm{P}}_{N}$. As a result, the bound nucleon (N) is knocked out from a particular shell, causing a hole in the final nucleus (A-1), as shown in Figure 11. The two scattered nucleons with a kinetic energy $\mathrm{k_{p'}}$,$\mathrm{k_{N'}}$ and momentum $\overrightarrow{\mathrm{P}}_{\mathrm{p'}}$,$\overrightarrow{\mathrm{P}}_{\mathrm{N'}}$ emerge at an opening angle θ_0 of 80° in the Lab system without further reactions, and the opening angle is written as [22]:

$$\cos\theta_0 = \sin\theta_1\,\sin\theta_2\,\cos(\phi_2-\phi_1)+\cos\theta_1\,\cos\theta_2 \tag{7}$$

Where θ is the polar angle of the scattered proton and ϕ is the azimuth angle of the scattered proton. This scattering process occurs only at sufficient energy that reduces the de-Broglie wavelength $\lambda = \mathrm{h/P_p}$ of the incident proton, where h is Planck's constant. This condition is required for a localized reaction since the de-Broglie wavelength is decreased to be less than the average distance between two neighboring nucleons in the nucleus, which is about 2 fm.

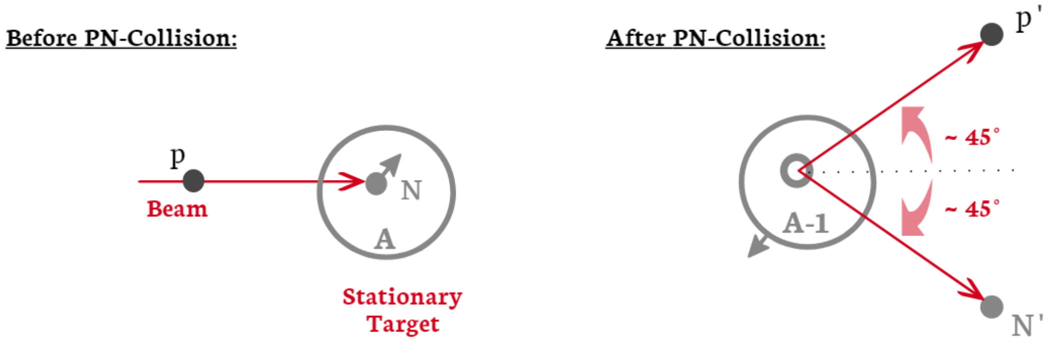

Figure 11: Schematic of a quasi-free scattering (QFS) reaction in normal kinematics.

Because of momentum conversation, the momentum of the removed nucleon before the reaction equals the momentum of the recoil nucleus:

$$\overrightarrow{P}_{\mathrm{N}} = -\overrightarrow{P}_{\mathrm{A-1}} \tag{8}$$

leads to:

$$\overrightarrow{P}_{\mathrm{p}} = \overrightarrow{P}_{\mathrm{N'}} + \overrightarrow{P}_{\mathrm{p'}} + \overrightarrow{P}_{\mathrm{A-1}} \tag{9}$$

and the energy conservation gives:

$$\mathrm{E_p} + \mathrm{m_A c^2} = \mathrm{E_{p'}} + \mathrm{E_{N'}} + \mathrm{E_{A-1}} \tag{10}$$

The created hole in the corresponding state with a given nlj can overlap with the ground state of the residual nucleus. On the other hand, if the hole is created in a deeper state, an additional excitation energy $\mathrm{E^*_{A-1}}$ will be added to the residual nucleus. Thus, the outcome of the reaction is determined by the excitation energy since the separation energy $\mathrm{S_N}$ of the removed nucleon equals the sum of the separation threshold of the least bound nucleon $\mathrm{Q_N}$ and the excitation energy as the following:

$$\mathrm{S_N} = \mathrm{Q_N} + \mathrm{E^*_{A-1}} = \mathrm{K_p} - [\mathrm{K_{p'}} + \mathrm{K_{N'}} + \mathrm{K_{A-1}}] \tag{11}$$

The excitation energy plays a significant influence on the reaction. If the excitation energy $\mathrm{E^*_{A-1}} > \mathrm{Q_N}$, the residual nucleus will breakup via particle emission. While lower excitation energy $\mathrm{E^*_{A-1}} < \mathrm{Q_N}$ causes the residual nucleus to decay via γ-ray [20, 23].

Another significant aspect of quasi-free scattering is the target. Since the nuclei of interest in this work are short-lived radioactive nuclei, the reaction is employed in inverse kinematics where a relativistic beam of the nuclei of interest hits a thin proton rich target as shown in Figure 12. Furthermore, the quasi-free scattering in inverse kinematics is more surface localised compared to electron scattering.

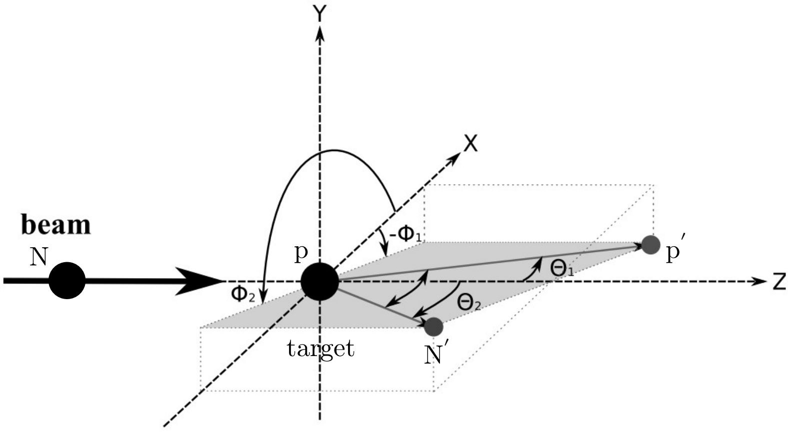

Figure 12: Schematic of a quasi-free scattering (QFS) reaction in inverse kinematics, where a nucleon (N) of a nucleus of interest hits a proton (p) of a proton rich stationary target. As a result, the scattered proton $p^{'}$ and nucleon $N^{'}$ are emerge with an opening angle θ_0 that equals the sum of θ_1 and θ_2 of the scattered proton and nucleon, respectively. The difference between their azimuthal angles $|\phi_1 - \phi_2|$ is approximately 180° indicates that the scattered particles are emitted back-to-back. The schematic is taken from [24] and modified for more clarification.

Furthermore, the eikonal theory is the basis for describing the total cross sections and momentum distributions of the recoiled residual nucleus of the quasi-free scattering. The eikonal scattering waves approximation assumes that the projectile's path through the field of the target nucleus is a straight line.
The eikonal wave function is written as [25]:

$$\psi_{\mathrm{k}}^{+/-}(\mathrm{r}) = \mathrm{e}^{\mathrm{ik.r}}\,\mathrm{S}^{+/-}(\mathrm{b}) \tag{12}$$

where $\psi_{\mathrm{k}}^{+/-}(\mathrm{r})$ is the quantum mechanical state of the particles. $(+)$ indicates the incoming particles and $(-)$ indicates the outgoing particles. $\mathrm{S}^{+/-}(\mathrm{b})$ is the scattering matrix for the scattering description of the incoming and outgoing wave function, and the impact parameter b defined as the absolute value of the transverse component of $\mathrm{r}(\mathrm{z},\mathrm{b})$ as illustrated in Figure 13.

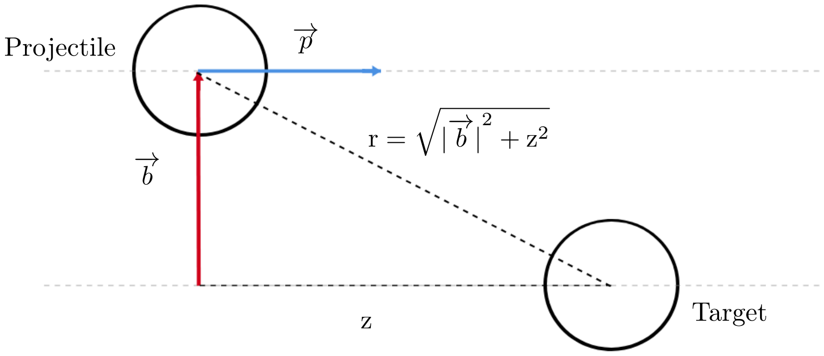

Figure 13: A schematic of the impact parameter b. It is represented by the vertical distance between the projectile trajectory and the target nucleus.

The scattering matrix is defined as the distortion and absorption measurement of the incoming and outgoing particles. Thus, it can also be called survival amplitude. In the term of the eikonal approximation, the scattering matrix is given as [26]:

$$\mathrm{S}^{+/-}(\mathrm{b}) = \exp\left[\mathrm{i}\,\chi^{+/-}(\mathrm{b})\right] \tag{13}$$

The eikonal phase $\chi^{+/-}(\mathrm{b})$ is given by [26]:

$$\chi^{+/-}(\mathrm{b}) = -\frac{1}{\hbar\,\nu}\int_{\mathrm{a}(+/-)}^{\mathrm{c}(+/-)} \mathrm{dz}\,\mathrm{U}^{+/-}_{\mathrm{opt}}(\mathrm{r}) \tag{14}$$

where ν is the relative velocity. The integration limits $\mathrm{a}(+/-)$ and $\mathrm{c}(+/-)$ depend on the reaction mechanism and described particle, i.e. $\mathrm{a} = -\infty$ and $\mathrm{c} = \mathrm{b}$ for the incoming particle (+) and $\mathrm{a} = \mathrm{b}$ and $\mathrm{c} = \infty$ for the outgoing particle ($-$). $\mathrm{U}^{+/-}_{\mathrm{opt}}(\mathrm{r})$ is the optical potential of the core+target or nucleon+target scattering [23, 25].

The survival amplitude for the incoming and outgoing waves is written as:

$$\mathrm{S}^{+/-}(\mathrm{b}) = \exp\left[-\frac{\mathrm{i}}{\hbar\,\nu}\int_{\mathrm{a}(+/-)}^{\mathrm{c}(+/-)} \mathrm{dz}\,\mathrm{U}^{+/-}_{\mathrm{opt}}(\mathrm{r})\right] \tag{15}$$

The framework of the Distorted Wave Impulse Approximation (DWIA) is used to estimate the differential cross section. The distorted waves are calculated from the real part of the complex mean nuclear potential, while the absorption effects are presented by the imaginary part.

The standard expression for the DWIA cross section is written as [27]:

$$\frac{\mathrm{d}^3\sigma}{\mathrm{dT_N}\,\mathrm{d}\Omega'_{\mathrm{p}}\,\mathrm{d}\Omega_{\mathrm{N}}} = \mathrm{K}'\,\frac{\mathrm{d}\sigma_{\mathrm{pN}}}{\mathrm{d}\Omega}|\mathrm{F(Q)}|^2 \tag{16}$$

where K' is a kinematic factor and it depends on the momenta and angles of the nucleons, $|\mathrm{F(Q)}|^2$ is the momentum distribution of the knocked-out nucleon N, and $\mathrm{d}\sigma_{\mathrm{pN}}/\mathrm{d}\Omega$ is the differential QFS cross section and it is proportional to the square of the scattering matrix element $|\tau_{\mathrm{pN}}|^2$, thus it is related to the transition amplitude [27]:

$$\mathrm{T_{p,pN}} = \sqrt{\mathrm{S(lj)}}\langle\chi^{(-)}_{\mathrm{k'_p}}\,\chi^{(-)}_{\mathrm{k_N}}|\tau_{\mathrm{pN}}|\chi^{(+)}_{\mathrm{k_p}}\Psi_{\mathrm{jlm}}\rangle \tag{17}$$

where S(lj) is the spectroscopic amplitude of the bound nucleon with quantum numbers (lj), $\chi^{(-)}_{\mathrm{k_p}}\,\chi^{(-)}_{\mathrm{k_N}}$ the distorted wave functions of the scattered proton in presence of the residual nucleus $(A-1)$, $\chi^{(+)}_{\mathrm{k_p}}$ the distorted wave function of the incoming proton in the presence of the target nucleus A, and Ψ_{jlm} the bound-state wavefunction of the removed nucleon.

The transition amplitude can be written as [27]:

$$\begin{aligned}\mathrm{T_{p,pN}} = \sqrt{\mathrm{S(lj)}}\int \mathrm{d}^3\mathrm{r}'_{\mathrm{pA-1}}\,\mathrm{d}^3\mathrm{r}'_{\mathrm{NA-1}}\,\mathrm{d}^3\mathrm{r}_{\mathrm{pA}}\,\mathrm{d}^3\mathrm{r}_{\mathrm{NA-1}} \times \tau(\mathrm{r}'_{\mathrm{pA-1}},\mathrm{r}'_{\mathrm{NA-1}};\mathrm{r}_{\mathrm{pA}},\mathrm{r}_{\mathrm{NA-1}}) \times \chi^{(-)*}_{k'_p}(r'_{pA-1})\\ \chi^{(-)*}_{k_N}(r'_{NA-1})\chi^{(+)}_{k_p}(r_{pA})\,\psi_{jlm}(r_{NA-1})\end{aligned} \tag{18}$$

Some of the integrals are eliminated. Furthermore, the coordinates of the proton have been associated with the nucleon's coordinates N by $\mathrm{r_{pA}} = \mathrm{r_{pN}} + \mathrm{r_{NA}}$. As a result of the small range of the pN interaction comparable to the nuclear size, the integral in equation 18 will take a considerable small value of $\mathrm{r_{pN}}$, $\mathrm{r_{pN}} \ll \mathrm{r_{NA}}$. Therefore, the T matrix is reduced over $\mathrm{r_{NA-1}}$ coordinate and written as [27]:

$$\mathrm{T_{p,pN}} = \sqrt{\mathrm{S(lj)}}\,\tau(\mathrm{k}^{'}_{\mathrm{pN}},\mathrm{k_{pN}};\mathrm{E}) \int \mathrm{d}^3\mathrm{r_{NA-1}} \times \chi^{(-)*}_{\mathrm{k}^{'}_{\mathrm{p}}}(\mathrm{r_{NA-1}})\,\chi^{(-)*}_{\mathrm{k_N}}(\mathrm{r_{NA-1}})\,\chi^{(+)}_{\mathrm{k_p}}(\alpha\mathrm{r_{NA-1}})\,\psi_{\mathrm{jlm}}(\mathrm{r_{NA-1}}) \tag{19}$$

where $\tau(\mathrm{k}^{'}_{\mathrm{pN}},\mathrm{k_{pN}};\mathrm{E})$ is the Fourier transform of the pN τ-matrix in equation 18, and $\alpha = (\mathrm{A}-1)/\mathrm{A}$.
The transition matrix is then given as [27]:

$$\mathrm{T_{p,pN}} = \sqrt{\mathrm{S(lj)}}\,\tau(\mathrm{k}^{'}_{\mathrm{pN}},\mathrm{k_{pN}};\mathrm{E})\langle\Psi_{\mathrm{f}}|\Psi_{\mathrm{i}}\rangle \tag{20}$$

Also it can be rewritten as [27]:

$$\mathrm{T_{p,pN}} = \sqrt{\mathrm{S(lj)}}\,\tau(\mathrm{k}^{'}_{\mathrm{pN}},\mathrm{k_{pN}};\mathrm{E}) \int \mathrm{d}^3\mathrm{r}\exp\left[-\mathrm{i}\mathrm{Q.r}\right]\mathrm{S}(\mathrm{b},\theta)\,\psi_{\mathrm{jlm}}(\mathrm{r}) \tag{21}$$

where Q is the missing momentum defined as $\mathrm{Q} = \mathrm{k}^{'}_{\mathrm{p}} + \mathrm{k_N} - \alpha\mathrm{k_p}$, θ is a function of the angles between the scattered nucleons $\theta^{'}_{\mathrm{p}}$ and θ_{N}, $\theta \equiv \theta(\theta^{'}_{\mathrm{p}},\theta_{\mathrm{N}})$, and $\mathrm{S}(\mathrm{b},\theta)$ is the product of scattering matrices (survival amplitude) given by [27]:

$$\mathrm{S}(\mathrm{b},\theta) = \mathrm{S_{pA}}(\mathrm{E_p},\mathrm{b})\ \mathrm{S_{p'A-1}}(\mathrm{E}^{'}_{\mathrm{p}},\theta^{'}_{\mathrm{p}},\mathrm{b})\ \mathrm{S_{NA-1}}(\mathrm{E_N},\theta_{\mathrm{N}},\mathrm{b}) \tag{22}$$

where $\mathrm{S_{pA}}$ is the scattering matrices of the initial proton-target, $\mathrm{S_{p'A-1}}$ is the scattering matrices of the final proton-residual nucleus, and $\mathrm{S_{NA-1}}$ is the scattering matrices of the nucleon-residual nucleus.
The bound-state wave function is the solution of the radial Schrödinger equation together with the spin-orbit potential, and it is written as [27]:

$$\psi_{\mathrm{ljm}} = \frac{\mathrm{u_{lj}(r)}}{\mathrm{r}} \sum_{\mathrm{m_l,m_s}} \langle \mathrm{lm_l s m_s}|\mathrm{jm}\rangle \mathrm{Y_{lm_l}}(\hat{\mathrm{r}})\chi_{\mathrm{m_s}} \tag{23}$$

where $\mathrm{u_{lj}}$ are the radial wave-functions, $\langle \mathrm{lm_l s m_s}|\mathrm{jm}\rangle$ are the Clebsch-Gordan coefficients, $\chi_{\mathrm{m_s}}$ are the spinors, and $\mathrm{Y_{lm_l}}$ are the spherical harmonics.
Finally, the total cross section for QFS is given by using the eikonal transition matrix in equation 21 and written as [27]:

$$\sigma_{\mathrm{QFS}} = \mathrm{S(lj)}\,\frac{2\pi}{2\mathrm{j}+1}\sum_{\mathrm{m}}\langle\frac{\mathrm{d}\sigma_{\mathrm{pN}}}{\mathrm{d}\Omega}\rangle\,|\mathrm{C_{lm}}|^2\int_0^{+\infty}\mathrm{db}\,\mathrm{b}\,|\langle\mathrm{S(b)}\rangle|^2\int_{-\infty}^{+\infty}\mathrm{dz}\,|\frac{\mathrm{u_{lj}(r)}}{\mathrm{r}}\mathrm{P_{lm}(b,z)}|^2 \tag{24}$$

where $\mathrm{P_{lm}}$ are Legendre polynomials and $\mathrm{C_{lm}}$ is a normalization factor.

Chapter 3: Experimental Setup

This study examines the quasi-free scattering (QFS) reaction in inverse kinematics of $^{19-20}$O and $^{21-23}$F by utilizing the R^{3}B setup. The overall structure of the experiment is presented in detail within this chapter. It starts with the description of producing the incoming beam at the GSI accelerator facility in Germany, followed by the R^{3}B setup where the detectors and their significant detection concepts are discussed. Subsequently, this chapter will then end with an overview of the data acquisition and trigger system.

3.1 Beam Production

The radioactive cocktail beam of light nuclei with an atomic number $z \leq 10$ was produced before the S393 experiment's outset, and its production was made by several stages, as shown in Figure 14. It started at an ion source to generate stable ions of ^{40}Ar at the west end of the GSI facility in Darmstadt, Germany. Then, the generated ions were injected into the UNIversal Linear Accelerator (UNILAC) [28], which accelerates the generated ions up to an energy of 11.5 AMeV. For further acceleration, the primary ^{40}Ar^{11+} ion beam was injected into the ring accelerator SIS-18, the Heavy-ion synchrotron 18 (German: SchwerIonenSynchrotron 18) [29].

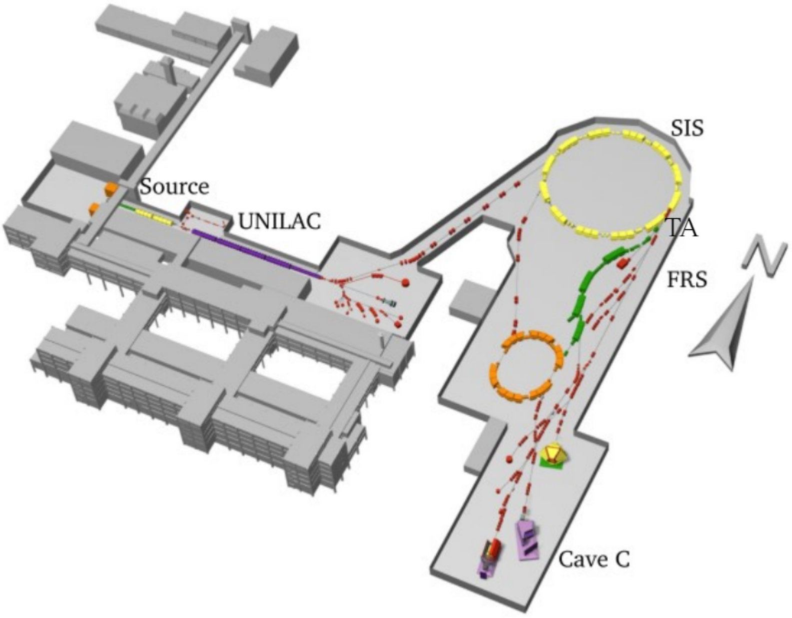

Figure 14: Sketch of the GSI accelerator facility. The ion source generates ions. Then UNILAC (universal linear accelerator) and SIS18 (Schwerionen Synchrotron, heavy-ion synchrotron) accelerate the stable primary beam before hitting the production target at the beginning of the FRS (fragment separator). Through the FRS, the secondary beam is guided to Cave C, where the R^{3}B setup is located [23].

The SIS-18 kept the ion beam in a circular path until achieving the desired energy. With its maximum magnetic bending power of $\mathrm{B}\rho_{\max} = 18\,\mathrm{Tm}$, the SIS-18 can deliver maximum energies of 1 - 4.5 GeV/nucleon based on the ion species. At the final accelerator stage for the S393 experiment, the desired primary ion beam with an energy of 490 AMeV was released for a certain period with a length of 2 s. Thus, the beam was injected in the shape of a spill with an intensity of 6×10^{10} ions/spill. Then, the beam was directed to the production target area (TA), where a beryllium target with an areal density of $4.011\mathrm{g/cm}^2$ was located at the entrance of the FRagment Separator (FRS) [30], to create the secondary beam. The wide range of the produced light nuclei via the fragmentation reaction were separated by the FRS. The FRS structure in Figure 15 shows several independent stages for transferring the beam to three branches serving various experimental areas, including cave C, where the experimental setup was located. Each step has a 30-degree dipole magnet for deflecting ions, five quadruple magnets divided before and after the dipole for ion focusing, and two correcting sextupole magnets for ion stabilizing.

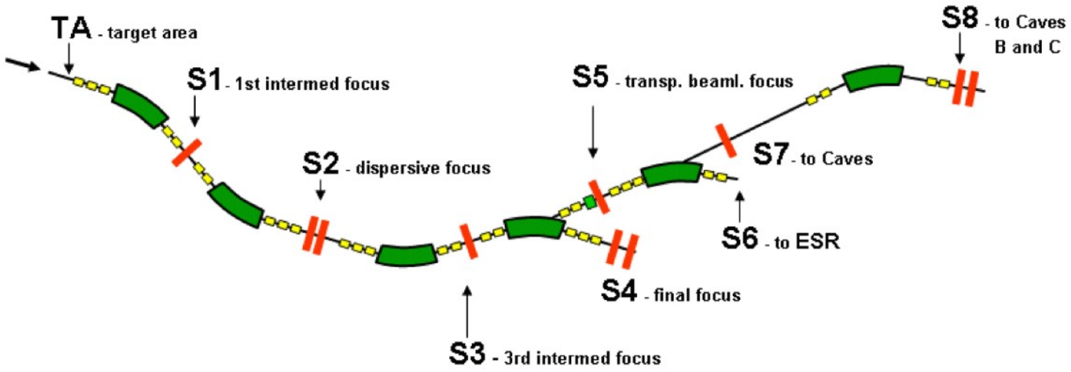

Figure 15: Schematic drawing of the FRagment Separator (FRS). The radioactive secondary beam was generated via the reaction with target area TA at the entrance of the FRS. The sequences of the dipole magnets (green) were employed to separate the fragments. While the quadrupole magnets (yellow) were used for focusing the beam. At the last stage, a scintillator (S8) was used for beam diagnostics, and the $\mathrm{R}^3\mathrm{B}$ setup at cave C was provided with a radioactive beam [25].

Figure 16 shows an example of $^{18}\mathrm{F}$ secondary beam produced by fragmentation of 500 MeV/nucleon $^{40}\mathrm{Ar}$ primary beam in a Be target with an areal density of $2\mathrm{g/cm}^2$ [31]. The secondary beam is analysed by the $\mathrm{B}\rho - \Delta\mathrm{E} - \mathrm{B}\rho$ technique; the combination of the magnetic rigidity analysis and the energy loss in Al degrader with an areal density of $11\,\mathrm{g/cm}^2$ at the second focal plane. The first $\mathrm{B}\rho$ separation stage is made by the usage of the first and second dipole magnet in the FRS. It separates the fragments of interest with mass-over-charge ratio $\mathrm{A/z} = 18/9$ and filters out the unreacted beam and other fragments with a different ratio by deflecting them onto different paths regarding their magnetic rigidity as:

$$\mathrm{B}\rho = \frac{\mathrm{A}}{\mathrm{z}}\,\beta\,\gamma \tag{25}$$

where:

B: The strength of the magnetic field, adjusted for the desired ion.

ρ: The curvature radius of the ion's trajectory, depends on the FRS's geometry.

β: The velocity of the ion in the unit of the speed of light and it equals to v/c.

γ: The Lorentz factor and it equals to $1/\sqrt{1-\beta^2}$.

However, the secondary ion beam still involves other species at the second focal plane because of the FRS momentum acceptance $\Delta p/p = 2\,\%$. Thus, a wedge-shaped degrader can be placed at second focal plane for additional selection if a pure beam is required. The ions are slowed down since the energy loss is proportional to z^2 as illustrated in the Beth-Bloch formula [32]:

$$-\frac{\mathrm{dE}}{\mathrm{dx}} = 4\pi \mathrm{N_A r_e^2 m_e c^2}\ \frac{\rho \mathrm{Z}}{\mathrm{A}}\ \frac{\mathrm{q}^2}{\beta^2}\ [\ln(\frac{\mathrm{W_{max}}}{\mathrm{I}}) - \beta^2]] \tag{26}$$

where:

$\mathrm{N_A}$: The Avogadro's number, $6.022 \times 10^{23}\,\mathrm{mole}^{-1}$

$\mathrm{r_e}$: The classical radius of the electron and it is equal to $2.818 \times 10^{-15}\,\mathrm{m}$

$\mathrm{m_e}$: The rest mass of the electron and it is equal to $9.109 \times 10^{-31}\mathrm{Kg}$

ρ: The density of the medium

Z: The atomic number of the medium

A: The mass number of the medium

q: The electrical charge of the incoming ion, equivalents to the charge number z because the ions are entirely stripped

I: The ionization potential of the medium and it depends on its Z value

$\mathrm{W_{max}}$: The maximum transferred energy and it is equal to $2\mathrm{m_e c^2}\beta^2\gamma^2$

Then, different charges will be separated in the second $\mathrm{B}\rho$ separation stage, where the third and fourth dipole magnets are located. The $\mathrm{B}\rho - \Delta\mathrm{E} - \mathrm{B}\rho$ technique significantly improves the purity of the beam.

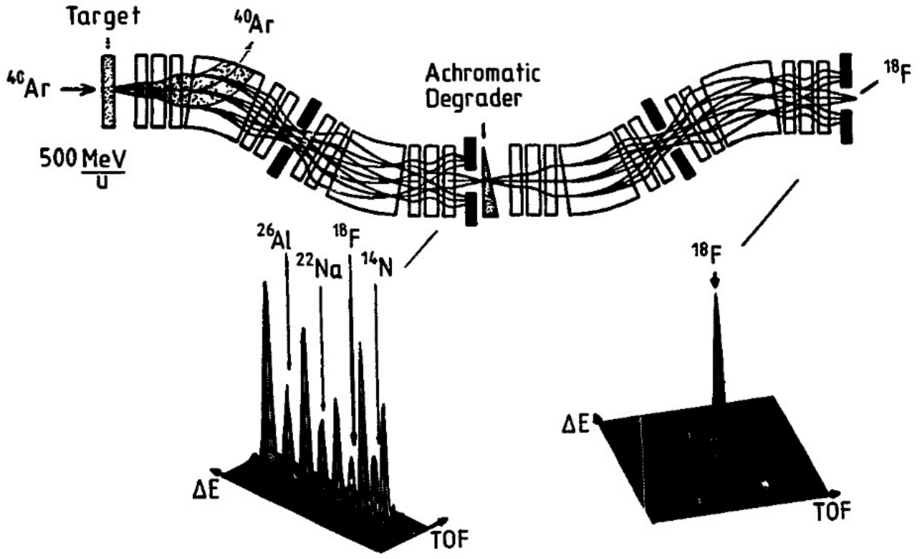

Figure 16: An illustration for the separation principle of the FRS. It is shown the complete stages of obtaining the ^{18}F secondary beam produced by fragmentation of 500 MeV/u ^{40}Ar primary beam in a $2\,\mathrm{g/cm^2}$ Be target. The secondary beam is provided by the $\mathrm{B}\rho - \Delta\mathrm{E} - \mathrm{B}\rho$ method [31].

Returning to the figure 15, setting a degrader at the second focal plane was avoided for the S393 experiment since it aims to cover a wide range of the cocktail beam. The data from S2 and S8 scintillators were the main interest for beam diagnostics. However, due to overload of S2 with the high particle rate, data from S8 without S2 has been used. Furthermore, six settings of the FRS were used as shown in Table 2 to provide cave C with a radioactive beam of variety isotopes A/z from 1.4 to 3.0 [23, 25, 33].

Table 2: The FRS settings for the S393 experiment; setting 3 is selected for this research.

Setting	Bρ (Tm)
1	5.6729
2	6.9105
3	8.1230
4	9.0440
5	9.4631
6	9.8814

3.2 R^{3}B Setup

The delivered secondary beam of the neutron-rich nuclei reacted with a fixed target in cave C. The R^{3}B setup [34] for the S393 experiment contained various detectors at the incoming particles identification area, the reaction area, and the outgoing particles-branches identification area to provide complete measurements, as shown in Figure 17. It allowed measuring the incoming and outgoing beam in addition to the produced nucleons and gamma rays as summarized in Table 4 at the end of this section, while more details about these detectors are introduced within the following subsection.

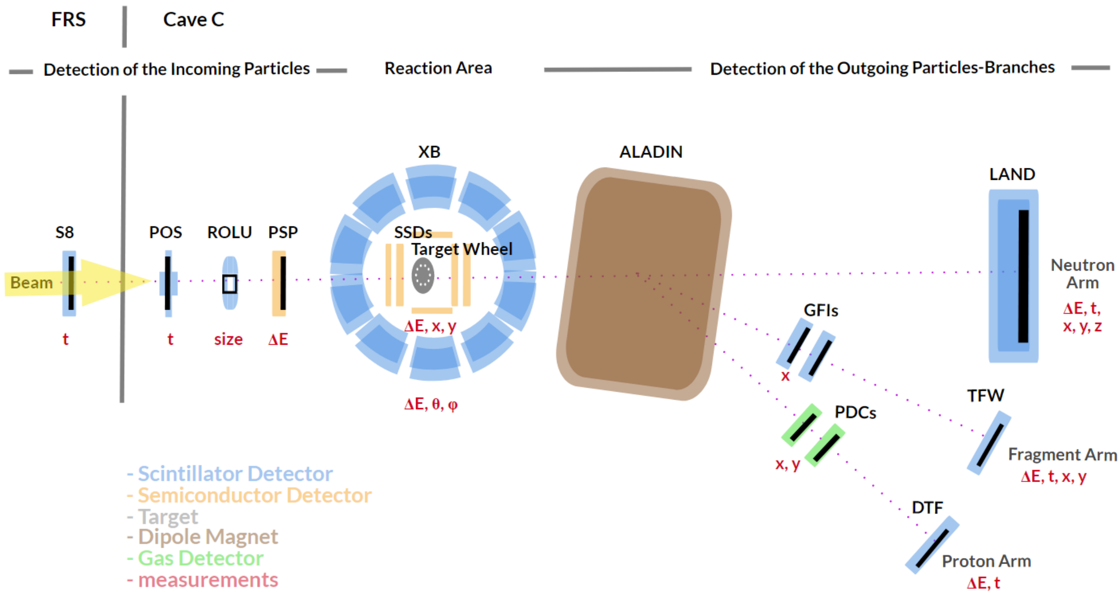

Figure 17: Sketch of the S393 Setup at cave C (not to scale). The FRS provided cave C with mixed radioactive beam. The delivered beam was identified in the incoming particles identification area by the usage of the POS detector together with the S8 and PSP detector. Then, the identified beam reacted with the target in the reaction area, surrounded by the Crystal ball XB and the tracker detectors DSSDs for gamma rays and protons detection. The produced charged outgoing particles via the reaction were bent by the effect of the dipole magnet ALADIN. Consequently, three paths were caused; the neutron arm to the LAND detector, the fragment arm passes through the GFIs to the TFW detector, and the proton arm goes through the PDCs to the DTF.

3.2.1 Detection of the Incoming Particles

The delivered mixed beam to the S393 experiment was identified by the first three main detectors at cave C, as shown in Figure 17. The POS and PSP detectors were used to determine the velocity and charge of the incoming beam, respectively, and the ROLU detector was utilized for the beam spot size adjustment by vetoing any ions that are outside its acceptance.

POS Detector:
A significant advantage of placing the POS detector at the entrance of cave C as illustrated in Figure 17 is the determination of the incoming particle velocity β. POS was used as a start-trigger for the data acquisition and time reference for R^{3}B setup, which will be introduced in more detail in section 3.3. The detector consists of a square plastic scintillator with a volume of $5 \times 5 \times 0.2\,\mathrm{cm}^3$ [25]. Once the incoming charged particle pass through scintillator, its energy is deposited in an atom's electron. As a result, this electron is elevated to a higher energy state. Then, the absorbed energy will be dissipated by falling the electron back to the ground state or a lower energy state in the form of visible light. The emitted light must be converted into a photoelectrons [35, 36]. Therefore, this square plastic scintillator is attached to four photomultiplier tubes via light guides, as shown in Figure 18. It was used for measuring the Time-of-Flight (TOF) between the S8 detector, at the end of FRS, and the POS detector, at the entrance of cave C, over a distance (d) in order to determine the velocity of the incoming beam, which is written as [25]:

$$\beta = \frac{\mathrm{v}}{\mathrm{c}} = \frac{\mathrm{d}\,/\,\mathrm{TOF}}{\mathrm{c}} \tag{27}$$

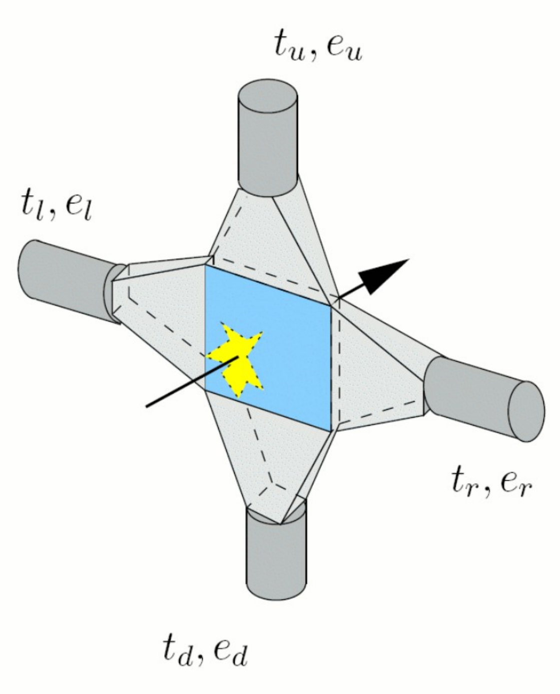

Figure 18: A sketch of the POS detector. It is made of a scintillator indicated in a blue square that produces light when an ion passes through it, denoted as a black arrow. For the time (t) and energy (e) measurements, the generated light is guided via light guides at each side of the scintillator to four PhotoMultiplier-Tubes (PMTs) [37].

ROLU Detector

The incoming beam size was constrained using the ROLU detector, the second detector from the left in the S393 experiment sketch. Its name stands for the German words; Rechts, Oben, Links, and Unten, which means Right, Top, Left, and Bottom. Therefore, it consists of four independent movable plastic scintillators with a volume of $9.5 \times 10 \times 0.5\,\text{cm}^3$ for each slab, as shown in Figure 19. These slabs are adjusted to make a rectangle window to determine the acceptance of the beam size [25].

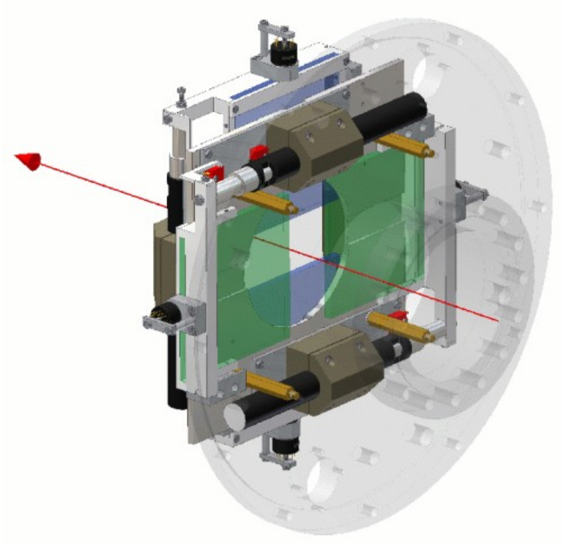

Figure 19: The ROLU detector is made of four movable scintillator plates; two in the x-axis indicated by green color and two paddles in y-axis indicated by blue color [24].

The Position Sensitive Pin Diode Detector (PSP):

The PSP detector is a square plate of high resistivity silicon of n-type with an active volume of $4.5 \times 4.5 \times 0.03$ cm^3, as shown in Figure 20a. One of its sides is the anode side, which is implemented with Boron ions to form a p-n junction, while the other is the cathode side [38]. Due to this configuration, the electron-hole pairs are produced within the depleted volume when a charged particle pass through. These pairs are fluttered away and transported to the respective electrodes under the effect of the applied electric field to form pulses [36]. Thus, the deposited incoming ion in the PSP provides five readouts. Four from the four corners of the anode side and one from the back side for the total energy deposition. Q1, Q2, Q3, and Q4, gives a two-dimensional positions reconstruction x and y, which can be measured by assuming the collected charge fraction is proportional to the distance between an incident position and the electrode:

$$\mathrm{x} = \frac{(\mathrm{Q}_2 + \mathrm{Q}_3) - (\mathrm{Q}_4 + \mathrm{Q}_1)}{\mathrm{Q}_1 + \mathrm{Q}_2 + \mathrm{Q}_3 + \mathrm{Q}_4} \tag{28}$$

$$\mathrm{y} = \frac{(\mathrm{Q}_1 + \mathrm{Q}_2) - (\mathrm{Q}_3 + \mathrm{Q}_4)}{\mathrm{Q}_1 + \mathrm{Q}_2 + \mathrm{Q}_3 + \mathrm{Q}_4} \tag{29}$$

For position calibration, a pixel mask was inserted next to the PSP detector. It is made of scintillating pixels, and has an active size of 21×21 square pixels. The pixels are arranged in a grid as shown in Figure 20b, where the distance between them is 0.2 cm. Each square pixel has a length of 0.05 cm and inlaid into a plastic plate that is used as a light guide to a PhotoMultiplier-Tube (PMT). The pixel mask can be moved remotely to be used during the pixel calibration runs. However, the pixel mask did not work during the

S393 experiment. So, it was not used for position measurements.

The other readout from the cathode side Q identifies the charge of incoming ion by providing the energy-loss measurement, as previously illustrated in the Beth-Bloch formula in equation 26. so it was only used for the incoming ion charge measurement, while the position information was deduced from the silicon-strip-detectors (SSDs) as a consequence of its superior resolution [23, 24].

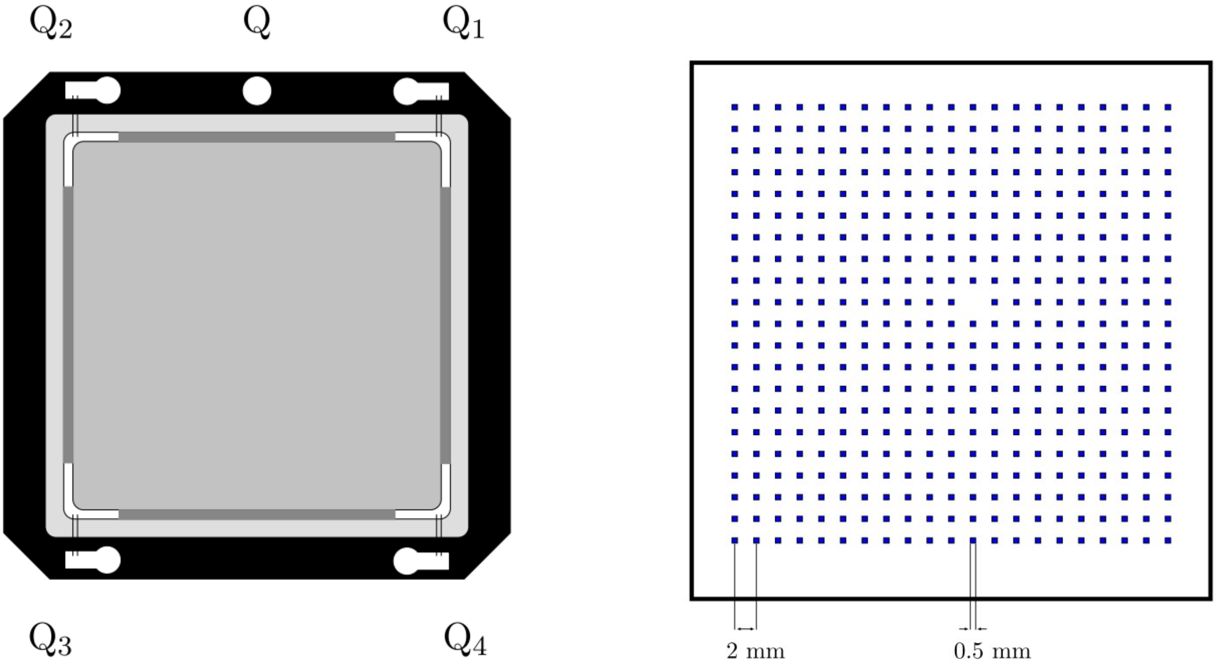

(a) PSP detector [38]

(b) Pixel mask [38].

Figure 20: (a) The anode side of the PSP detector. The deposited incoming ion in the PSP provides five readout channels; one from each of the corners of the anode side; Q1, Q2, Q3, and Q4, that gives a two-dimensional positions reconstruction x and y. The other readout from the cathode Q at the back side identifies the incoming ion charge by providing the energy-loss measurements. (b) A schematic drawing of the pixels mask with an active size of 21 × 21 square pixel. It was inserted next to the PSP detector for the position calibration.

3.2.2 Reaction Area

After the identification stage, the radioactive beam reached the reaction area, consisting of a vacuum reaction chamber surrounded by the crystal ball (XB). The vacuum reaction chamber enclosed the target wheel, where the position of the target of interest was fixed in front of the incoming beam. Furthermore, eight Silicon Strip Detector (SSDs) were used inside the vacuum chamber for complete measurements, as shown in Figure 17.

Target Wheel

The target wheel was connected to a motor in order to rotate the wheel. The targets were then shifted between runs during the experiment, and the chosen target was positioned in the beamline as shown in Figure 21. The wheel has eight settings with a size of 3 × 3 cm^2 for various thicknesses of different target materials; CH_2, C, and Pb, Table 3 shows the targets that were used for this research. However, the ninth position was left empty for the background measurements [23].

Figure 21: A picture of the vacuum reaction chamber surrounds the target wheel and the Silicon Strip Detectors (SSDs) [23].

Table 3: A list of the used targets in this work and their characteristics. Both of them were used to reconstruct the H target. The systematic uncertainty of the target thickness is assumed to be 2 %.

No.	Target	Thickness (mm)	Density (g/cm^3)	Areal Density (mg/cm^2)
1	CH_2	4.98	0.92	458.16
2	C	3.03	1.84	557.52

The Silicon Strip Detectors (SSDs)

Each Silicon Strip Detector (SSD) provides two-dimensional position measurements besides the charge identifications for the passed ions. Thus, four detectors surrounded the reaction target in the form of an open box shape to measure the scattered nucleons. Furthermore, two detectors were mounted before the target and two detectors after as shown in Figure 22; this arrangement was performed for tracking purposes. However, the box-shape detectors were not used because of several obstacles.

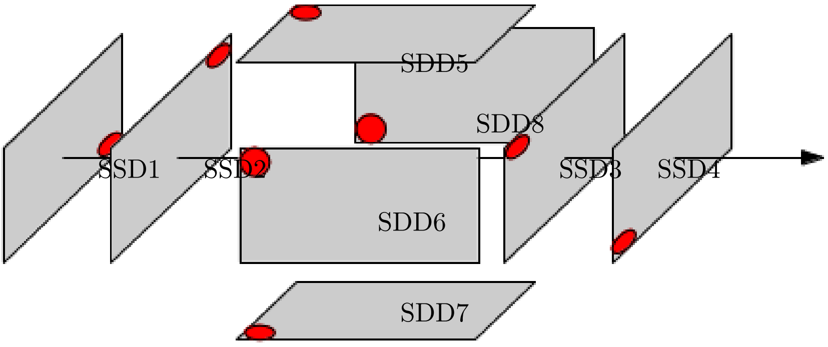

Figure 22: The Silicon-Strip-Detectors (SSDs) orientation for S393 experiment, the red dots mark the first strip on the detector [24].

Each detector has an active volume of $7.2 \times 4.0 \times 0.03$ cm^3, as shown in Figure 23, with a total readout channels of 1024. Its ohmic side corresponds to the y-axis, known as k-side, and it has 384 strips. Every strip is read out since the implant pitch is 104 μm. In contrast, the junction side corresponds to the x-axis, known as the s-side, with 2560 strips. However, the strips of the s-side were reduced to 640 strips since the implant pitch is 27.5 μm with the corresponding 110 μm readout pitch [23, 24].

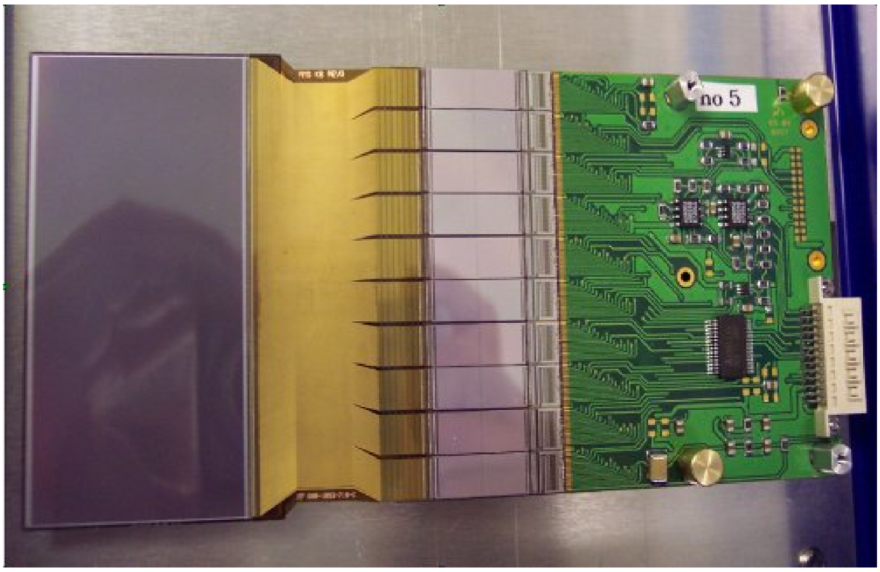

Figure 23: Picture of a silicon-strip detector (SSD). The rectangular active area with a size of $7.2 \times 4\,\mathrm{cm}^2$ is shown on the left. The sensor is made of two perpendicular sides; the largest dimension is k-side (n-side), and the other dimension is s-side (p-side). Both of them give 1024 strips that are attached to the front-end electronics board on the right by capton cables [24].

The Crystal Ball (XB)

The vacuum reaction chamber, which encapsulates the target wheel and the SSDs detectors, was surrounded by the Crystal Ball (XB). It is fundamental to detect the scattered nucleons and emitted gamma rays from the de-excited fragments. The XB has a spherical shell constructed in two vertically movable hemispheres to adjust the target and detectors in the reaction area, as shown in Figure 24. The spherical shell is made of

162 independent modules of NaI(Tl) crystal; 12 pentagonal, denoted by A, and 150 modules in three various forms of hexagonal crystals, represented by B, C, and D, as shown in Figure 25. This configuration allows each crystal to cover the same solid angle of 77 msr. Though, only 159 modules have been used in the R^{3}B setup to accommodate space for beam pipe and the holding structure of the reaction chamber inside shell. Each scintillating crystal has a thickness of 20 cm. Consequently, the spherical shell has an inner and outer radius of 25 and 45 cm.

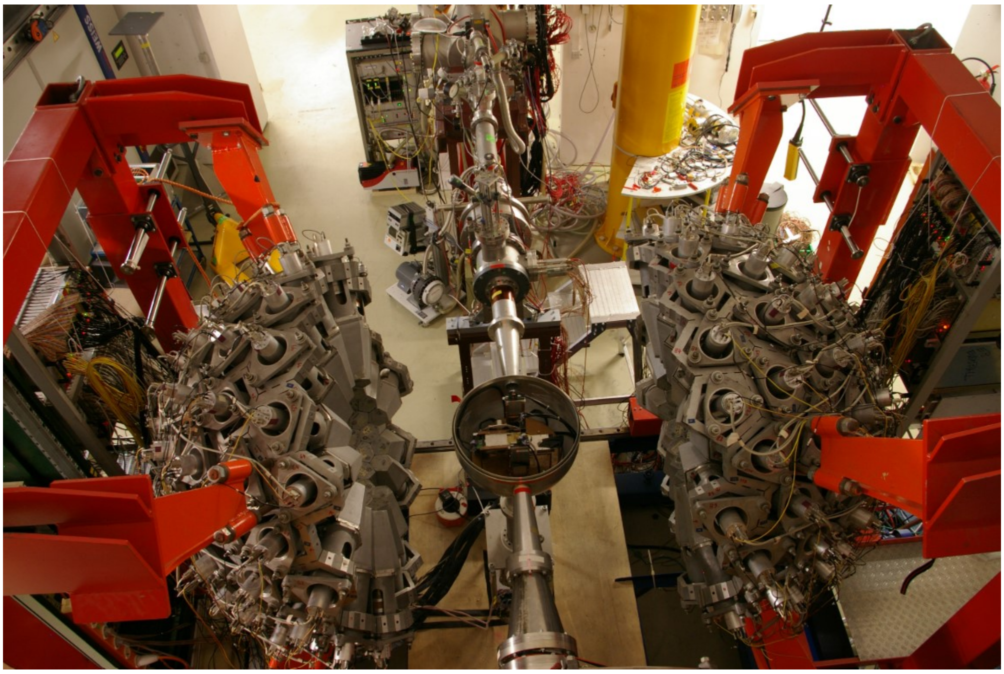

Figure 24: Photo of the opened Crystal Ball detector (XB) during the preparation of the S393 experiment [24].

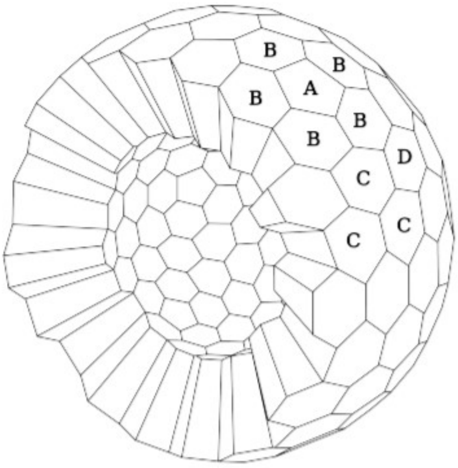

Figure 25: Schematic drawing for the configuration of Crystal Ball. shows the four geometrical crystals shapes; 12 crystals in the shape of pentagonal (A) and 150 crystals in three various forms of hexagonal crystals (B, C, and D) [39].

The emitted gamma-ray from the de-excited fragment interacts with the matter and deposits its energy in three main mechanisms depending on its energy. It might be entirely absorbed in one step by a bound electron in the crystal leading to expelling this electron as illustrated in Figure 26a, known as the photoelectric effect. The difference between the incident gamma-ray energy $h\,\upsilon$ and the binding energy B_e of the ejected electron from the atom is equal to the kinetic energy of the ejected electron T, and it is written as [18]:

$$T = h\upsilon - B_e \tag{30}$$

where h is Planck constant. Another possible mechanism is the energy of the incident gamma-ray might be partially deposited by an elastic collision with an electron as illustrated in Figure 26b, known as the Compton effect. The energy difference between the incident gamma-ray $h\upsilon_0$ and the scattered gamma-ray $h\,\upsilon$ at an angle θ is equal to the kinetic energy of the recoil electron T at an angle ϕ, and it is written as [18]:

$$T = h\upsilon_0 - h\upsilon \tag{31}$$

Another possible mechanism is the Pair production that occurs if its energy is higher than 1.02 MeV, where the energy of the incident gamma-ray is fully transferred into a positron-electron pair as illustrated in Figure 26c. This interaction can be written as [18]:

$$h\upsilon = (T_- + mc^2) + (T_+ + mc^2) \tag{32}$$

where where T_- is the kinetic energy of the electron, T_+ is the kinetic energy of the positron, and $mc^2 = 0.511\,\text{MeV}$ is the rest energy of the electron or positron.

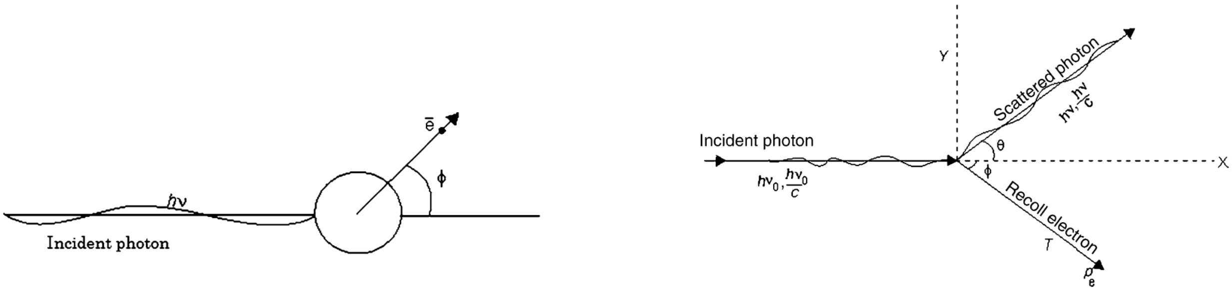

(a) Photoelectric effect [18]

(b) Compton effect [18]

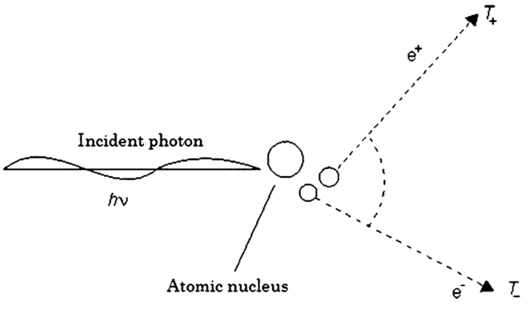

(c) Pair-Production [18]

Figure 26: A schematic of the three main possible interaction that accrued when gamma-ray hits a crystal. (a) Photoelectric effect (b) Compton effect (c) Pair-Production.

Within the Crystal Ball, the emitted gamma-ray might be fully absorbed in the first hit crystal or might be partially absorbed in the first hit crystal and pass to the neighbour crystal. All possible reactions can emit light from the scintillator crystals. Thus, the outer surface of each crystal is connected to a standard PhotoMultiplier-Tube (PMT) to convert the emitted light caused via the reacted gamma rays to an electric signal. Furthermore, readouts of the 64 crystals in the forward hemisphere have been modified to detect the scattered proton generated from the quasi-free scattering reaction, as shown in Figure 27. These modified readouts measure signals generated by both gamma rays and protons. Thus, the readouts are classified into gamma and proton branches. Gamma branch is different from the proton branch in several respects. Gamma branch is read out at the final pickup anode (P) of the PMT. The recorded signal is split after being preamplified to measure both its time, processed with a Constant Fraction Discriminator (CFD) and then recorded with a Time-to-Digital Converter (TDC), and energy using a Charge-to-Digital Converter (QDC). In contrast, the proton branch is read out at the last dynode (DY8) and only record the energy using QDC. Furthermore, the proton readout is not preamplified, and its gain is approximately 15 times smaller than the standard PMT's gain used for gamma readout. Also, pulses of proton readout have a positive polarity and decay length of around 1 μs compared to the gamma pulses with a negative polarity and a decay length of about 200 ns. The polarity is switched by using an inductive coupling before being sending into the QDC [40, 41].

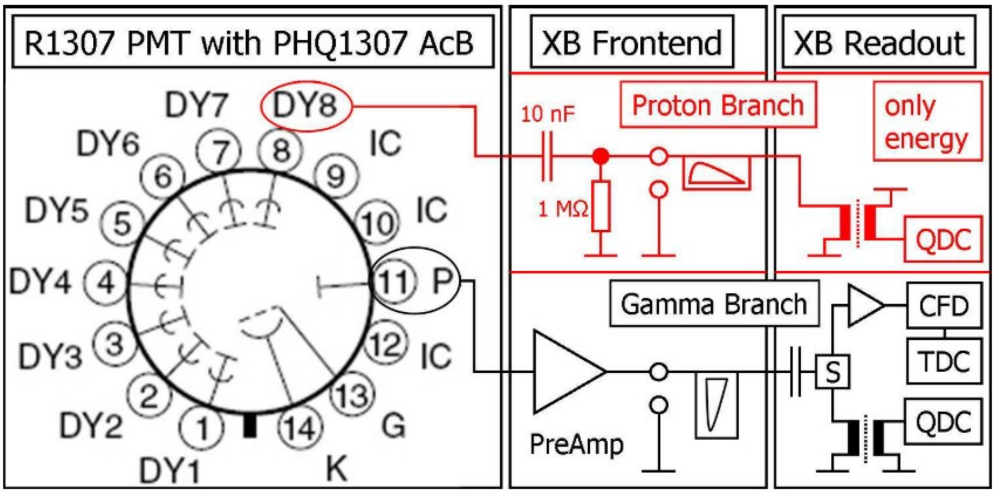

Figure 27: A plot of the readout circuitry for the crystal ball. The proton branch in the schematic is evident from the gamma branch by the red color [41].

3.2.3 A Large Acceptance Dipole Magnet (ALADIN)

The beam-like reaction particles leave the reaction area in the forward direction into A Large Acceptance DIpole magNet (ALADIN), made of two coils. The magnet gap has a size of $0.5\,\mathrm{m} \times 1.54\,\mathrm{m}$. Its angular acceptance is $\pm 60\,\mathrm{mrad}$ [42]. The magnet's current can be adjusted for full acceptance measurements for the TFW detector. Its maximum bending power equals $2.3\,\mathrm{Tm}$, and it corresponds to a current of 2500 A [21]. However, the saturation effects are not negligible above 1900 A, where the relation between the magnetic field $\vec{B}(\vec{r},\mathrm{I})$ and the applied current I is not linear [24]. The beam-like reaction particles, fragments and protons, are deflected into different directions according to their A/z ratio and velocity, as illustrated in equation 25. On the other hand, the uncharged particles, neutrons, are not affected by ALADIN. Therefore, the detection setup after ALADIN is split into three branches; the neutron branch, the fragment branch, and the proton branch, as shown in Figure 17.

3.2.4 Detection of the Outgoing Particles-Branches

As previously stated, charged particles bend according to their magnetic rigidity. Neutrons pass undisturbed through the magnetic field. Therefore, the neutron's path was equipped with the Large Area Neutron Detector (LAND), with a charged-particle veto detector in front of it. In contrast to neutrons, the fragments with $A/z > 1$ were deflected with an angle around $17\,^\circ$ and detected by two scintillating-fiber detectors (GFIs) and a Time-of-Flight Wall (TFW) [43]. In addition, the protons were bent with an angle of $30\,^\circ$, and its path was equipped with two Proton Drift Chambers (PDCs), and a time-of-flight wall (DTF) [24] as illustrated in Figure 17.

Neutron Arm

The Large Area Neutron Detector (LAND)

The LAND detector were located at $0\,^\circ$ and around 13 m behind the target on the neutron arm to provide the neutron's time of flight measurements. It forms an active volume of $2 \times 2 \times 1\,\mathrm{m}^3$ by compiling ten planes, illustrated in Figure 28. Each plane is made of 20 modules with an active volume of $2 \times 0.1 \times 0.1\,\mathrm{m}^3$ for each paddle. Subsequent planes are mounted to form an arrangement where the paddles are perpendicular to each other to provide a two-dimensional position. Closer inspection of the paddle in Figure 29 shows it consists of eleven iron sheets and ten plastic scintillator sheets. The two outer iron sheets have a thickness of 2.5 cm, while the other nine inner iron and ten plastic sheets have a thickness of 0.5 cm. Thus, when a neutron hits a paddle, it interacts with the iron and produces a charged particle, a proton. The generated proton hits the plastic scintillator and induces light. Therefore, each paddle is attached to two photomultipliers to obtain its time, energy, and position [44].

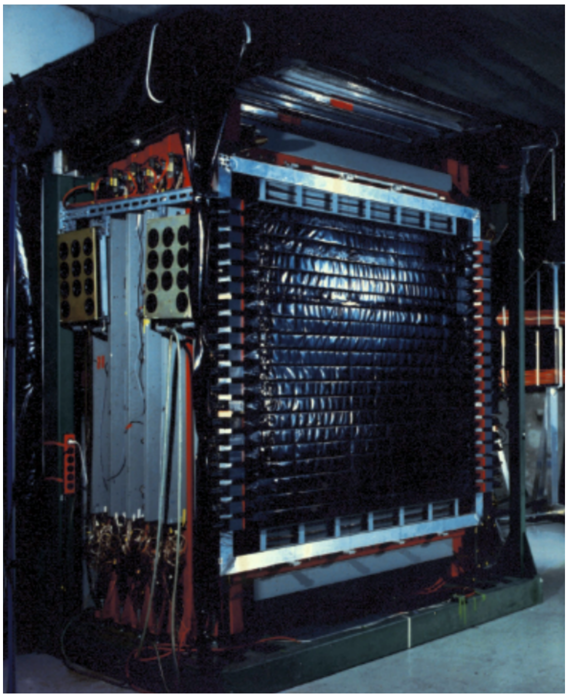

Figure 28: Photo of the Large Area Neutron Detector (LAND), whilst its cover is opened. It has an active volume of $2 \times 2 \times 1\,\mathrm{m}^3$ by compiling a total of ten planes. Each plane is made of 20 paddles with an active volume of $2 \times 0.1 \times 0.1\,\mathrm{m}^3$ [43].

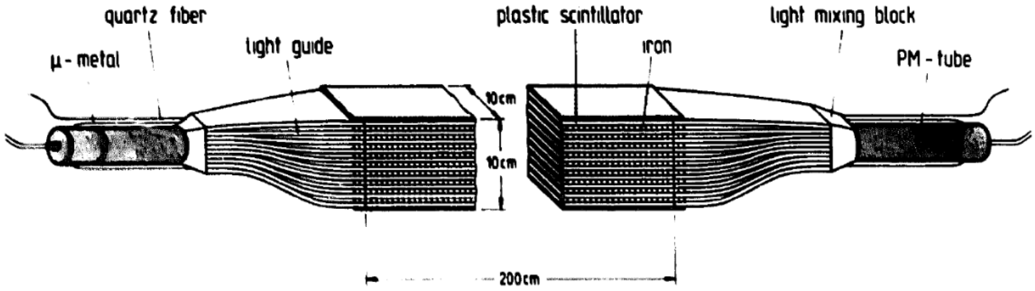

(a) A schematic of LAND paddle [44]

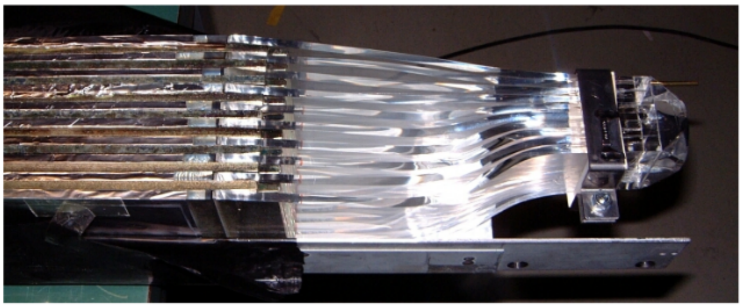

(b) A photo of LAND paddle [24]

Figure 29: (a) A schematic of a single paddle structure of the LAND detector. It is made of 11 sheets of iron; the two outer iron sheets have a thickness of 0.25 cm while the rest have a thickness of 0.5 cm and ten sheets of plastic scintillator with a thickness of 0.5 cm. (b) A photo of the LAND single paddle structure.

Fragment Arm

Fiber Detectors (GFIs)

The term GFI refers to Grosser FIber detector, a German name that means the large fiber detector. It was utilized in the R^3B setup to reconstruct the fragments' trajectories. The detector has an overall area of $50 \times 50\,\text{cm}^2$ made of 480 scintillating fibers as illustrated in Figure 30a. Each fiber has an active volume of $50 \times 0.1 \times 0.1\,\text{cm}^3$, and it is coated with an optical cladding for guiding the light and avoiding cross-talk. Each fiber is readout in its two ends. One end is attached to a position-sensitive photomultiplier (PSPM) by using a grid mask as shown in Figure 30b. The PSPM consists of 16 mesh-type dynodes, known as a photocathode, and a grid of a multi-wire anode made of 34 wires in (u , v) coordinate; 18 in the u direction, and 16 in the v direction. Its usage is raised by the correlation between the number of the hit fibre and the PSPM grid. When a charged particle hits the fibre, it generates light. Then this generated light is guided on the mask, and it appears as a light spot on the photocathode plane. Then, the grid reconstructs the (u , v) spot coordinate and associates the plane's light position with the hit fibre. In contrast, the other end is connected to a usual photomultiplier (PMT) for triggering and timing purposes. However, the time measurements were not provided during the S393 experiment [25, 45].

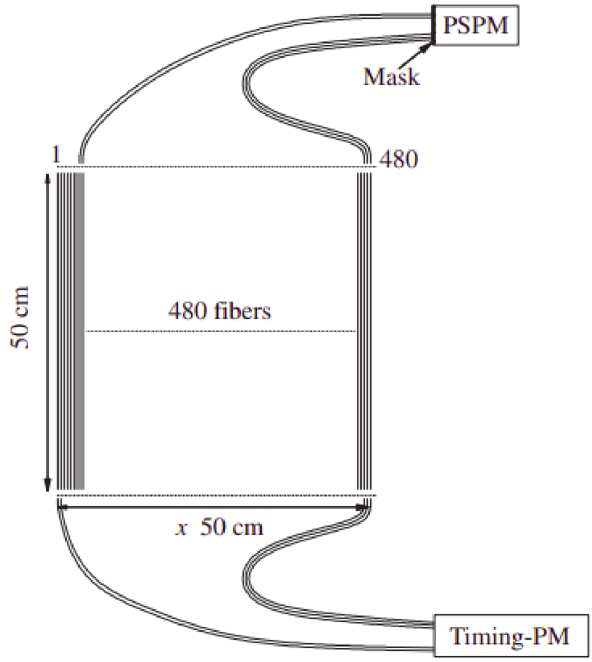

(a) A schematic view of GFI [45].

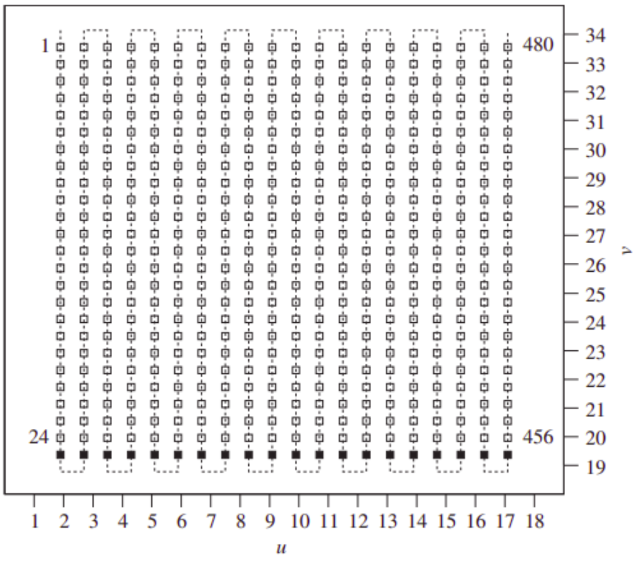

(b) A Grid Mask for the GFI [45].

Figure 30: (a) A schematic of the fibers identification detector (GFI). The detector consists of 480 scintillating fibers. Each fiber is readout in its two ends. One end is connected to a grid mask to connect the fiber to its Position-Sensitive PhotoMultipliers (PSPM), while the other end is connected to a conventional PMT. (b) A schematic of the grid mask for the fibers detector.

Time of Flight Wall Detector (TFW)

The TFW detector was included in the R^3B setup to provide the time-of-flight measurements, velocity, and identify the charge of the tracked fragments. It was the last detector on the fragment arm and located approximately 11 m from the target. It has an overall active volume of $189 \times 147 \times 0.5\,\mathrm{cm}^3$ made of 32 plastic scintillator paddles as shown in Figure 31. These paddles are divided into two orthogonal plans; 14 horizontal plastic scintillating paddles with an active volume of 147 × 10.4 × 0.5 cm^3 and 18 vertical plastic scintillating paddles with an active volume of 189 × 10.4 × 0.5 cm^3. Each side of the paddle is connected to a photomultiplier tube for time and energy loss measurements [24, 46].

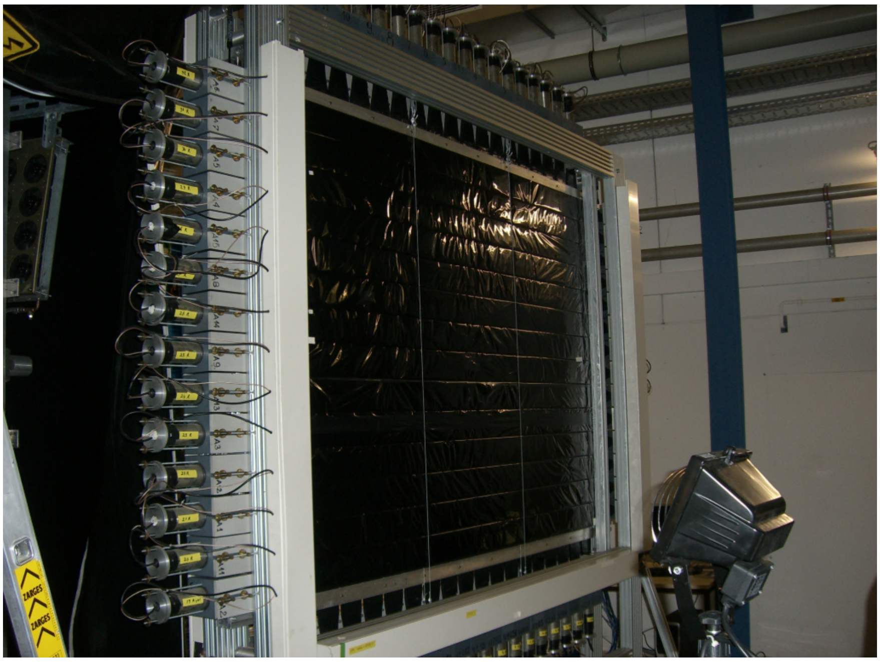

Figure 31: A picture of TFW identification detectors on the fragment arm at R^3B setup. It consists of 14 horizontal plastic scintillating paddles and 18 vertical plastic scintillating paddles that make an overall active volume of 189 × 147 × 0.5 cm^3. Each paddle is wrapped with black plastic to reduce the loss in the generated photons in the scintillator and the noise from external light [46].

Proton Arm

Proton Drift Champers Detectors (PDCs)

The PDC detector is a wire chamber detector with a total size of 120 × 100 × 15 cm including the frames, filled with a mixed gas of 80% Argon (Ar) and 20% Carbon Dioxide (CO_2). Two PDCs were used for protons trajectories determination. They were located at 2 and 3m behind the magnet on the proton arm. Its active area of 80 × 100 cm^2 has 256 read-out channels; 144 sense wires on the x-axis for one layer, and 112 wires on the y-axis for the other layer. Each layer has eight planes, and each is formed by eight hexagonal drift cells as shown in Figure 32. The hexagonal shape with a diameter of 1.6 cm is defined by six field wires surrounding two sense wires.

In the PDC detector, the passed proton ionizes the gas and generates an electron. This electron drifts to the closest sense wires, and causes a cascade of ionization collected on the sense wire. Thus, the current is proportional to the energy of the detected proton [24].

Time of Flight Detector (DTF)

The DTF refers to the German name "Dicke ToF wand," which means Thick ToF wall. The detector was located at the end of the proton branch to provide time-of-flight and energy measurements of the reacted protons. It is made of nine scintillator paddles as shown in Figure 33; six verticals paddles form an active volume of $120 \times 120 \times 1.5\,\mathrm{cm}^3$, and three separated horizontal paddles by a distance of 44 cm. Each horizontal paddle has an active volume of $10.4 \times 140 \times 1.5\,\mathrm{cm}^3$.

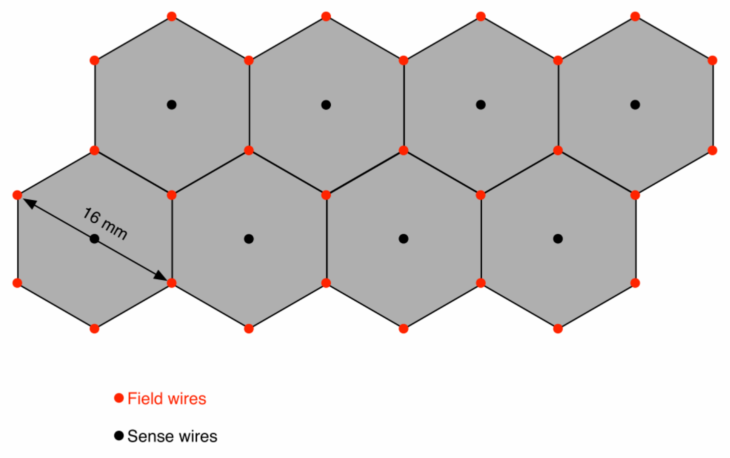

Figure 32: A schematic of the hexagonal drift cells of the PDC detector. The sense wires are indicated by the black circle, while the red circle shows the field wires [24].

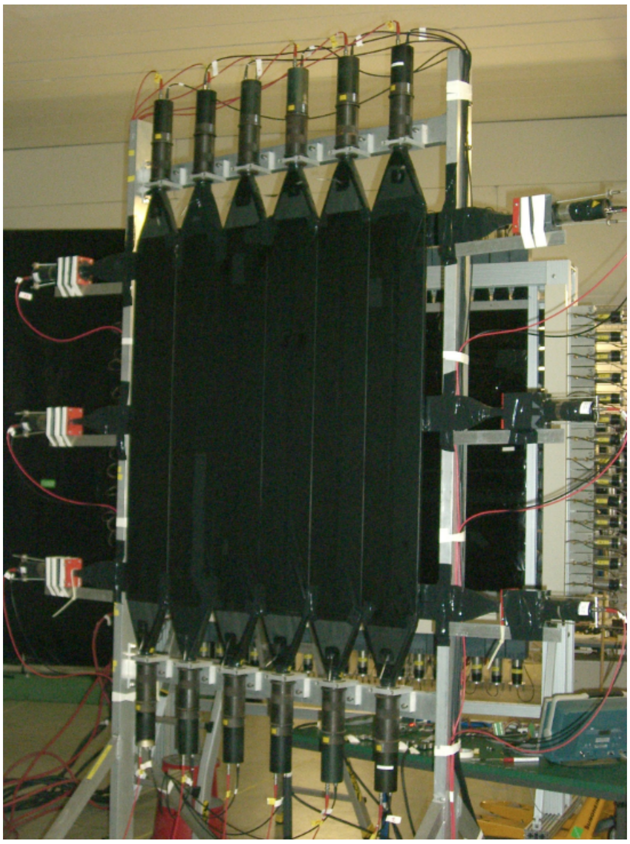

Figure 33: Photo of DTF detector for the protons identification. It is made of six scintillating vertical paddles and three separated horizontal scintillating paddles [24].

Table 4: Characterization of the used detectors in the S393 experiment. Their position and angle are given with respect to the target position in z-axis.

Detector	Utilization	Angle (°)	Position (cm)	Size (cm)	Measurement
POS	Determination of the incoming particle velocity and time reference for R^3B setup	0	-140.000	$5 \times 5 \times 0.2$	t
PSP	The incoming ion charge measurement	0	-88.900	$4.5 \times 4.5 \times 0.03$	∂E
SSD01	Identification of the incoming particle trajectories determination	0	-6.440	$7.2 \times 4.0 \times 0.03$	∂E , (x, y)
SSD02	Identification of the incoming particle trajectories	0	-3.680	$7.2 \times 4.0 \times 0.03$	∂E , (x, y)
XB	Detection of the scattered nucleons and emitted gamma rays from the deexcited fragments	0	0.000	$4.5 \times 4.5 \times 0.03$	∂E, (θ, ϕ)
SSD03	Identification of the outgoing particle trajectories	0	11.110	$7.2 \times 4.0 \times 0.03$	∂E , (x, y)
SSD04	Identification of the outgoing particle trajectories	0	13.880	$7.2 \times 4.0 \times 0.03$	∂E, (x, y)
LAND	Neutron time-of-flight determination	0	1337.000	$200 \times 200 \times 100$	t , ∂E, (x, y, z)
GFI01	Fragment trajectories determination	15	466.084	$50 \times 50 \times 0.1$	(x)
GFI02	Fragment trajectories determination	15	525.745	$50 \times 50 \times 0.1$	(x)
TFW	Fragments time-of-flight, energy, and charge identification	15	1120.381	$189 \times 147 \times 0.5$	t , ∂E, (x, y)
PDC01	The protons trajectories determination	30	439.980	$120 \times 100 \times 15$	(x, y)
PDC02	The protons trajectories determination	30	960.780	$120 \times 100 \times 15$	(x, y)
DTF	Proton time-of-flight and energy measurement	30	960.780	$120 \times 120 \times 1.5$	t , ∂E

3.3 Data Acquisition System (DAQ)

The Multi-Branch System (MBS) was used as data acquisition (DAQ) [37, 47] for the S393-experiment. The (DAQ) converts the analog electrical signals from different detectors into digital values stored in List-Mode Data files (LMDs). Events of interest are distinguished by the DAQ based on dead time of the system, the triggers generated by various detectors in the setup, and the downscale factor. The trigger is a logic signal delivered by an individual detector to declare that the measured voltage exceeds the adjusted threshold. Triggers signals are processed immediately, while the others are delayed. The delay is required to give the DAQ time to accept or disregard the events. Figure 34 illustrates the flow of the signal from a scintillating detector. The signal is split into two branches; energy and time branch. In the energy branch, the signal is delayed to a Charge-to-Digital Converter (QDC). While in the time branch, a Constant Fraction Discriminator (CFD) passes two signals: a delayed signal to a Time-to-Digital Converter (TDC) and an immediate signal to the trigger module. Consequently, the trigger module forwards it to the DAQ, where the readout decision is made. Then, a master trigger is sent from the main DAQ to read out both the timing and energy signal if the event is accepted [23, 48].

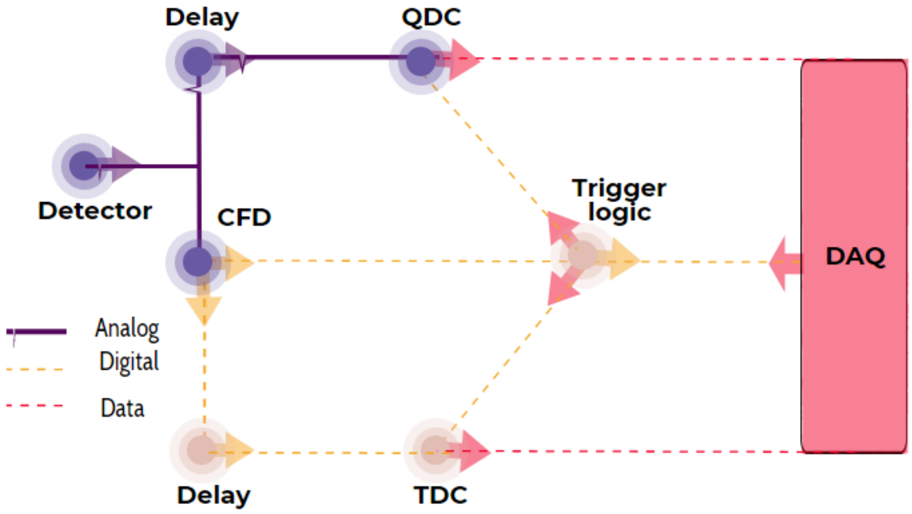

Figure 34: The flow of the signal from a scintillator along the electronics chain. The signal is divided into two branches; energy and time branch. In the energy branch, the signal is delayed to the QDC. While in the time branch, the CFD passes two signals: a delayed signal to a TDC and an immediate signal to the trigger module. The trigger module forwards it to the DAQ, where the readout decision is made. Then, a master trigger is sent from the main DAQ to read out both the time and energy signal if the event is accepted.

The VME Universal LOgic Module (VULOM) is used as a trigger logic module (TRLO) [49]. The TRLO combines triggers coming from different detectors to Trigger PATterns (Tpat), $\text{Tpat} = 2^{(\text{Tbit}-1)}$. Table 5 presents two main kinds of triggers used in S393 experiment; the first one is an on-spill trigger, which is in coincidence with the FRS trigger corresponding to the delivery of beam to the R^3B setup. The on-spill trigger indicates the events of interest for the reaction channels. While the off-spill trigger is in anti-coincidence with the FRS trigger, it denotes the required events for detectors calibrations. Furthermore, the early pile-up trigger is created by the POS detector and requires a time delay to both the previous and next event, and the late-trigger is a pending trigger that rejects triggers within a time period of 150 ns after generating the MINmum Bias trigger (Min.B) [25]. The positive sign (+) indicates that the detector is required for a specific trigger pattern. In contrast, the negative sign (−) denotes an anti-coincidence requirement. This can be illustrated by the MINimum Bias (MIN.B) trigger in Table 5. Its required trigger pattern is written as Spill-on + POS − ROLU, where the spill-on trigger from the FRS must be coincidental with a single from the POS detector and no signal from the ROLU.

A more detailed list of the used on-spill triggers during the S393 experiment is shown in Table 6. The first two columns present the trigger pattern (Tpat) and the trigger name. The following columns display the required detectors for the trigger pattern. The trigger rates are scaled-down with a downscale factor (DS) as shown in the last column. The downscale factor is used to record a high-intensity rate of the ion beam and reduce both dead-time and storage space. For illustration, every 64th event is accepted for the Fragment trigger.

Table 5: Used on-spill and off-spill triggers during the S393 experiment.

	On-Spill Trigger		
Tbit (n)	Tpat (2^{n-1})	Name	Description
1	1	MINimum Bias (MIN.B)	Spill-on + POS − ROLU
2	2	Fragments	MIN.B + TFW − Pile-up
3	4	FRS S8	Spill-on + S8
4	8	Crystal Ball Sum	Crystal Ball Sum + Fragment − late-trigger
5	16	DTF Proton	DTF + Fragment
6	32	Good Beam Pile-up	Min.B − Pile-up
7	64	Pixel	Pixel detector + Min.B
8	128	Neutron	LAND + Fragment
		Off-Spill Trigger	
Tbit (n)	Tpat (2^{n-1})	Name	Description
9	256	Crystal Ball Muon	Crystal Ball sum delayed − Min.B
10	512	Land Cosmic	LAND Cosmic − Min.B
11	1024	TFW Cosmic	Fragment delayed − Min.B
12	2048	Crystal Ball Gamma	Crystal Ball or delayed − Min.B
13	4096	DTF Cosmic	DTF delyaed − Min.B
14	8192	NTF Cosmic	NTF − Min.B
15	16384	Crystal Ball L/R Muon	Crystal Ball L/R − Min.B

Table 6: The required triggers of various detectors and the downscale factor of setting 3 for the triggers patterns (Tpat), on-spill. The used triggers for the present analysis are highlighted.

On-Spill trigger

Tpat	Trigger Name	Detectors								DS
		S8	POS	ROLU	Pixel	XB	DTF	TFW	LAND	
1	Good Beam		+	−						128.00
2	Fragments		+	−				+		64.00
4	FRS S8	+								2048
8	Crystal Ball Sum		+	−		+		+		1.00
16	Proton		+	−			+	+		1.00
32	Pile-up		+	−						128.00
64	Pixel		+	−	+					1.00
128	LAND		+	−				+	+	1.00

Chapter 4: Analysis

The obtained data from different detectors in the R^3B setup, as reviewed in chapter 3, will be treated in this chapter to deduce information about the internal structure of the nuclei of interest. Three experimental observables will be investigated; the cross section of the quasi-free scattering, gamma rays from the de-excited fragment, and the momentum distributions of the remaining fragment after the quasi-free scattering reaction.

The first section of this chapter introduces the required software for the analysis. The next two sections identify the incoming isotopes and outgoing fragments of interest. Then they are followed by three sections focusing on identifying the quasi-free scattering reaction, examining the geometrical acceptance and the produced gamma rays. The final sections introduce the inclusive and exclusive cross section of the quasi-free scattering and the momentum distributions.

4.1 Land02 Framework

The generated data by various detectors in the S393 experiment were sorted event-by-event in the List Mode Data (LMD) files, then extracted by land02 framework into an analysable format, root files. The software package land02 is developed by Håkan Johansson [50]. Additionally to the unpacking process, this approach performs the calibration and synchronization of the detectors. The calibration parameters were applied to the recorded data during the unpacking as well. The data are sorted into several levels as shown in Figure 35 and illustrated in Table 7 that summarize all detectors in the setup up to a specific calibration step to check the results and follow the calibration procedure.

The calibration of various detectors will not be presented in this work since they have been performed and discussed by other collaborators; Christoph Caesar [49], Marcel Heine [48] , Matthias Holl [23], Alina Movsesyan [51], Paloma Díaz Fernández [24], Ronja Thies [43], and Ina Syndikus [25].

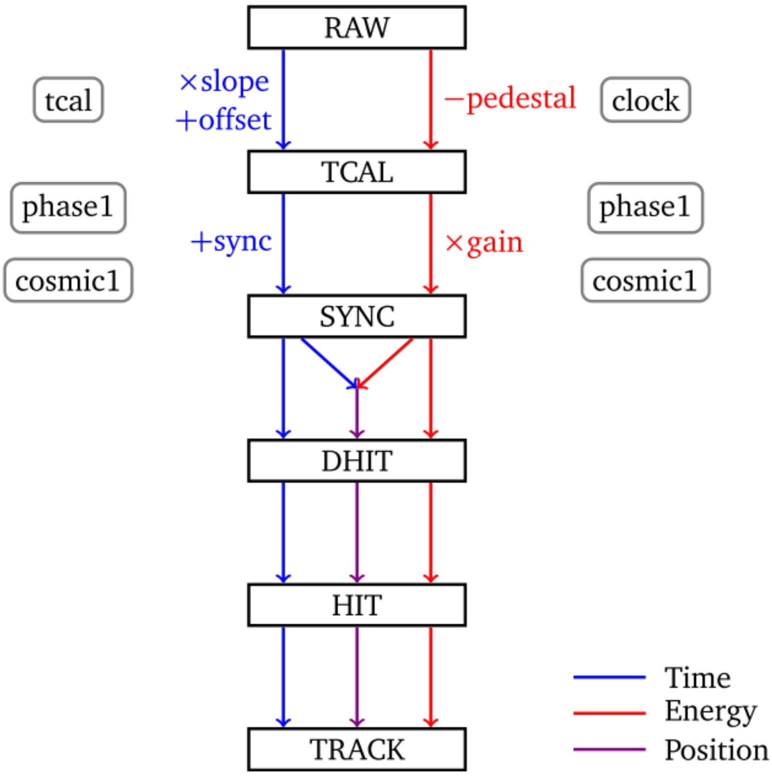

Figure 35: Schematic of data calibration levels in land02 and the related calibration routines [23].

Table 7: Data levels and unpacking in Land02 [50]

Data Level	Description
RAW	The unprocessed LMD binary data is presented without being calibrated and given in units of channels of the readout electronics. Thus, the energy measurements are given in ADC or QDC channels, while time measurements are given in TDC channels.
TCAL	The TCAL level converts the time measurements from channel numbers (TDC) to time units (ns) by the tcal calibration routine, where offset and slope parameters are used. Additionally, it subtracts the pedestal value from the measured energy values QDC by the clock calibration routine. However, at this level, each subunit of a detector is treated individually.
SYNC	The cosmic1 and phase1 calibration routines are used to compose all individual subunits of a detector as a unit, e.g., paddles in the TFW and LAND detector. The channels are synchronized with respect to each other by adding an offset parameter to time measurements. The calibration routines depend on the detector type, e.g., heavy ions are used for the TFW and cosmic rays for LAND. Moreover, energy values are converted from channel to energy unit of MeV by applying gain matching factors.
DHIT	The Detector-HIT (DHIT) level reconstructs the position, time, and energy of the particle hit in the detector internal (u, v) coordinates or paddle number (i, j) by combining the energy and time information from the SYNC level.
HIT	The position information of the hit from the DHIT level is transformed from the internal detector coordinates into the lab frame coordinates, external (x, y) coordinate, in cm.
TRACK	The particle hits from various detectors are combined to reconstruct its trajectory through the R^3B setup. The TRACK level inside land02 identifies the incoming beam and neutrons. However, the tracker software must be utilised to determine the beam-like charged fragments.

4.2 Incoming Particles Identification

As previously stated, the secondary beam was delivered to cave C by the FRagment Separator (FRS). Consequently, the selection of isotopes of interest is required for the analyses; ^{20}O, ^{19}O, ^{23}F, ^{22}F, and ^{21}F. For identification, two values were extracted from the detectors before the reaction area; the charge z of the incoming isotopes and their mass over charge ratio (A/z). The calibration procedure for the incoming particles identification was carried out by Marcel Heine [48], where the illustrated calibration steps in Figure 35 and Table 7 for the utilized detectors were described. The results of identifying the incoming beam for the third setting and CH_2 target is shown in Figure 36.

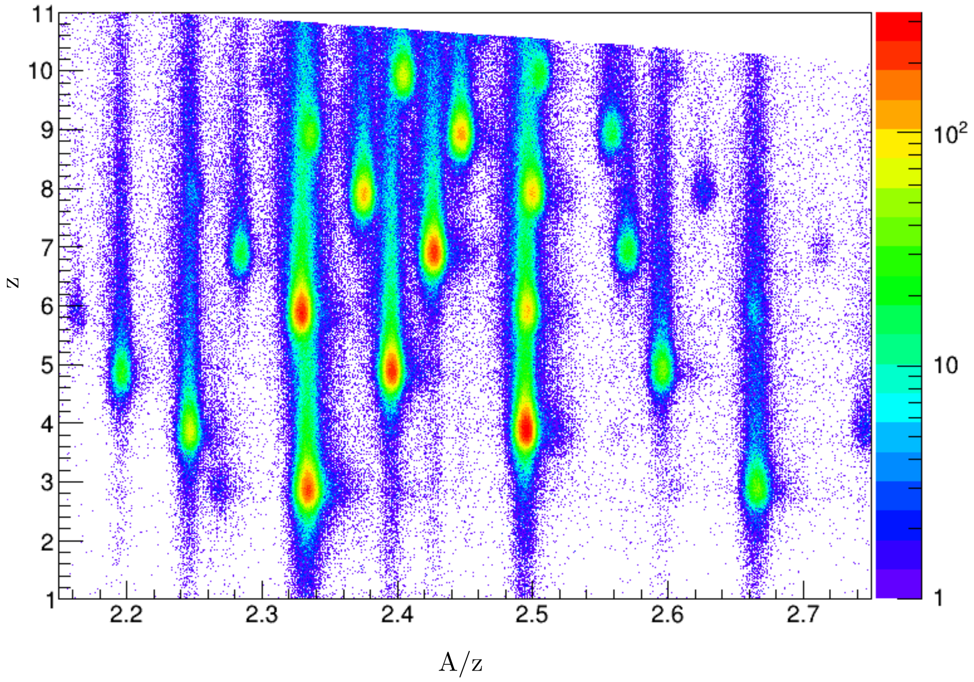

Figure 36: Incoming isotopes identification for setting 3 and CH_2 target. The trigger of the MINimum Bias Tpat&1 == 1 was selected. The isotopes of interest were analysed by applying a two-dimensional cut.

A two-dimensional cut that contains events within the selected ellipse of the incoming isotope of interest was then applied for the analysis. The two-dimensional cut is exemplified in the determination of ^{20}O, where $z = 8$ and $\frac{A}{z} = 2.5$. The main concern for the selection in this plot is the shared tail among the y-axis at A/z =2.5. This shared tail can be examined by the projection on the y-axis, as shown in Figure 37. The figure shows that the oxygen peak at z=8 is built above the carbon tail, though the carbon events won't affect the final result since an additional selection will be performed in section 4.3.

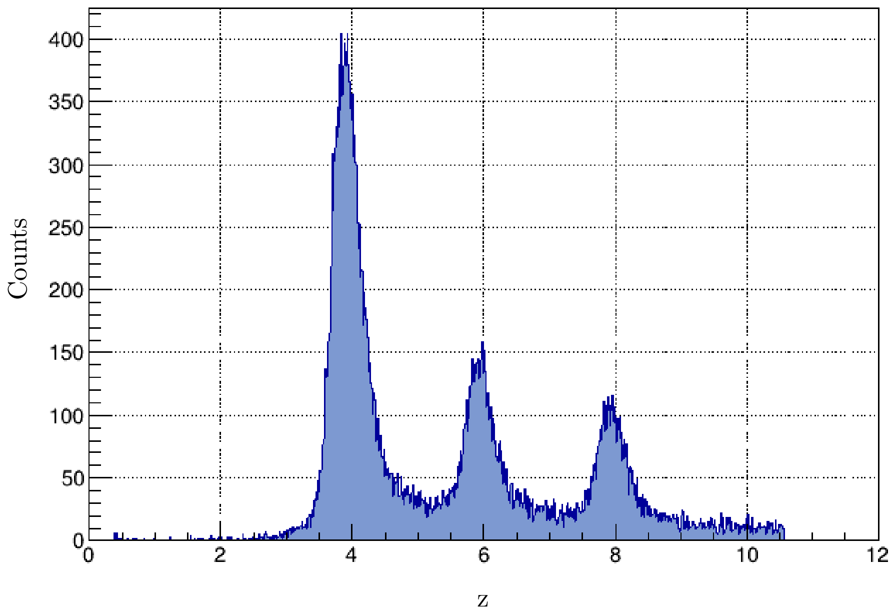

Figure 37: A projection on the y-axis of the obtained two-dimensional plot of the incoming isotopes identification, which is presented in Figure 36, for isotopes with a mass-over-charge ratio A/z equals to 2.5.

The ellipse cut for the isotope selection was obtained by fitting the normal distribution of the charge and mass-over-charge ratio. The obtained mean and the double standard deviations 2σ were used then to determine the center and extend the semi-axis of the cut. The applied two-dimensional cut is written as:

$$(\frac{\frac{\mathrm{A}}{\mathrm{z}} - (\mathrm{Mean})_{\frac{\mathrm{A}}{\mathrm{z}}}}{2(\sigma)_{\frac{\mathrm{A}}{\mathrm{z}}}})^2 + (\frac{\mathrm{z} - (\mathrm{Mean})_{\mathrm{z}}}{2(\sigma)_{\mathrm{z}}})^2 \leq 1 \tag{33}$$

The total number of the incoming particle of interest resulted from the applied two-dimensional cut on the incoming particles identification plot is listed in Table 8. However, these listed numbers are not used in the cross section since an additional selection will be applied for the incoming particle identification, as will be illustrated in section 4.3.

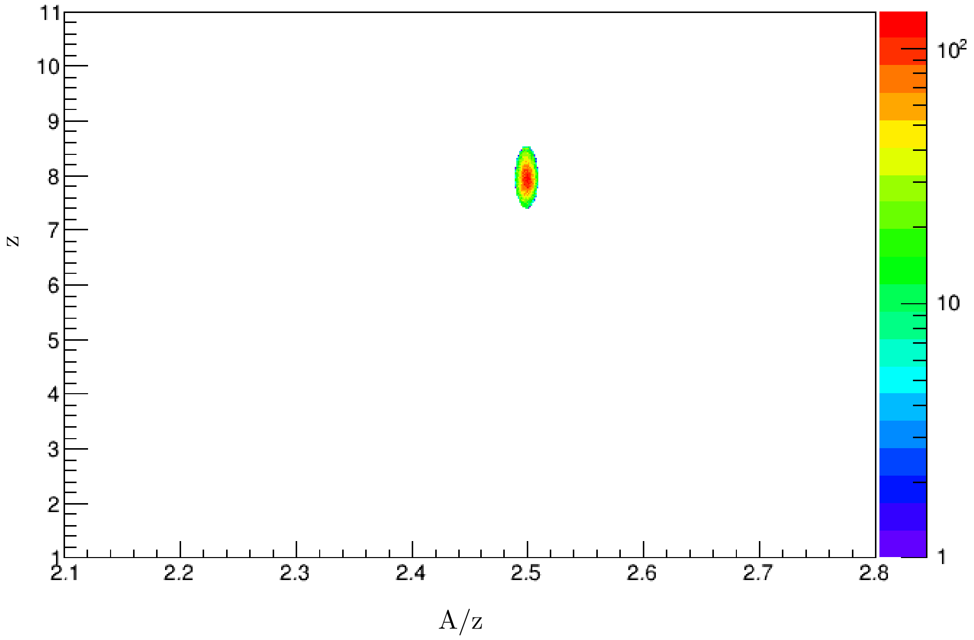

Figure 38: The outcome of the two-dimensional cut for the ^{20}O on the incoming isotopes identification plot for setting 3 and CH_2 target. The trigger of the MINimum Bias Tpat&1 == 1 was selected.

Table 8: The total number of incoming isotopes of interest for this work during a specific time duration for each used target.

Incoming Beam	The total number of particles					
	CH_2	Duration (h)	C	Duration (h)	Empty	Duration (h)
^{20}O	13×10^6	15.15	5.5×10^6	8.22	8.5×10^6	7.90
^{19}O	12×10^6		5.9×10^6		7.1×10^6	
^{23}F	2.2×10^6		1.1×10^6		1.3×10^6	
^{22}F	14×10^6		7.2×10^6		8.6×10^6	
^{21}F	6.5×10^6		3.1×10^6		3.9×10^6	

4.3 Outgoing Particles Identification

The incoming particles identification is followed by the outgoing particle identification to study the reaction channels of interest. Two values were extracted from the detectors after the reaction area; the charge z of the outgoing particles and their masses A. Thus, the approach begins with the charge determination based on the energy-loss measurements in the closest SSD detector after the target (SSD03) and the TFW detector at the end of the fragment arm, as shown in Figure 17.

For the TFW, time measurements are calculated by using various parameters, and it is written as [33]:

$$\mathrm{t_{cal} = t_{raw} \,.\, a_{ch\to ns}\, (+T_{cal}) + T_{diff} + T_{sync}} \tag{34}$$

where the TDC channel numbers are converted into time units in ns by the slope parameter $\mathrm{a_{ch\to ns}}$. Furthermore, cable lengths and processing times are taken into account by the offset $\mathrm{T_{cal}}$. The time of the two

PM tubes located at the ends of each paddle is synchronized by adjusting the offset of the time-difference $\mathrm{T_{diff}}$. Thus, the hit in the middle of a given paddle will give a time difference equal to zero. Then, all paddles in the TFW are synchronized versus each other by using the offset time-synchronization $\mathrm{T_{sync}}$. In the same way, energy measurements are calculated by using similar approach including the subtraction of the QDC pedestal using the calibration routine clock, where the pedestal can be defined as the QDC entry for a channel with no signal from the detector [33]:

$$\mathrm{e_{cal}} = (\mathrm{e_{raw}} - \mathrm{e_{pedestal}}) \cdot \mathrm{a_{ch \to MeV}} \frac{\mathrm{E_{sync}}}{\mathrm{E_{diff}}} \tag{35}$$

The utilized calibration parameters for the TFW detector in this analysis were carried out by Christoph Caesar [49]. For the SSDs, the calibration routine clock is utilized to subtract the pedestals for a given strip. Then, the deposited energies in neighboring strips are sorted into clusters to determine the energy loss and the position of the passing particle. More details are presented in the thesis of Matthias Holl [23].

Comparing charge values between the mentioned detector is required to ensure that no reactions occurred between the target and TFW detector. Then, the outgoing mass is reconstructed using the obtained charge information and the flight path through ALADIN, performed via utilizing the tracker. This procedure allows distinguishing reactions in the target from the material of the $\mathrm{R^3B}$ setup along the fragment's path.

4.3.1 Charge Identification

The charge identification of the outgoing particles was obtained via the correlation between the energy loss in the TFW and the k-side of the third SSD detector. The k-side of the third SSD detector was chosen since the s-side of the third and fourth SSDs have a worse energy resolution, and the k-side of the fourth SSD has a lot of broken strips. The result of the correlational analysis is presented in Figure 39 for setting 3 of the FRS and $\mathrm{CH_2}$ target. The diagonal fragments begin with fluorine (F) on the top and end with helium (He); thus, as described in section 4.2, a two-dimensional cut that contains events within the ellipse of the selected outgoing isotope was then applied for the analysis. The semi-axis and position of the asymmetric elliptic are obtained by the normal distribution fit of the energy loss in the TFW and third SSDs. The mean and the standard deviation are used to determine the ellipsis's center and semi-axis. In contrast to section 4.2, the 2σ would be used to extend the left side of the ellipse, while a higher value would be applied to extend the right side because of the asymmetric semi-axis as indicated in Figure 39 for the nitrogen isotopes.

For identifying the produced fragment of interest from the reacted beam, the two-dimensional cut containing the events of interest within the chosen asymmetric elliptic was applied under the Crystal Ball Sum trigger Tpat&8 == 8. On the other hand, a cut of the unreacted events within the selected ellipse was applied under the Fragments trigger Tpat&2 == 2. Interestingly, Figure 39 shows that the carbon spot is distant from the oxygen spot; thus, the oxygen events are not affected by the carbon tail introduced in Figure 37. This approach gives equivalent efficiencies in detecting particles in the fragment arm for unreacted and reacted particles, and both of them will be used in the cross section.

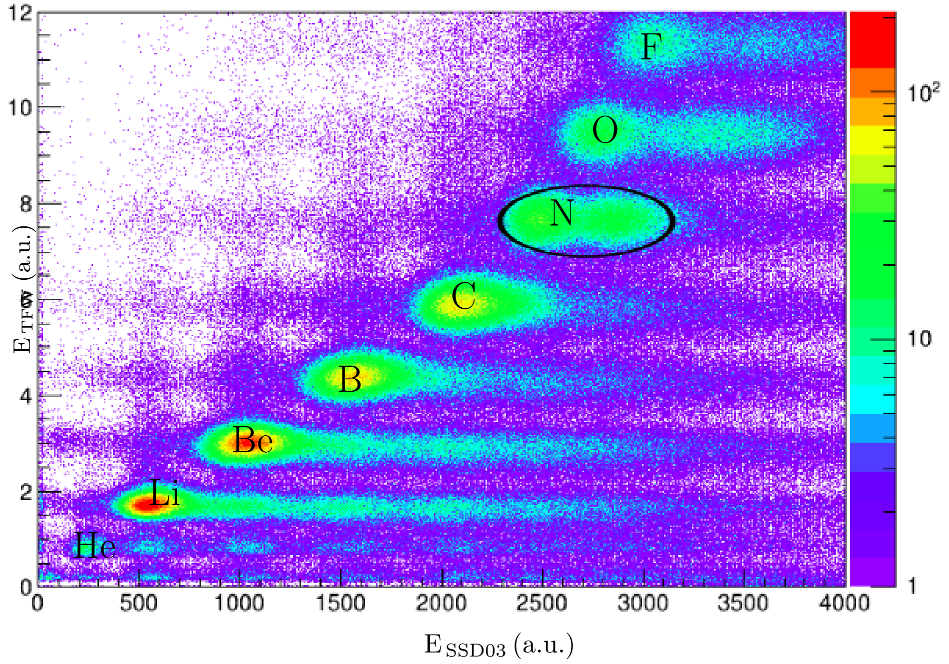

Figure 39: Charge identification of the outgoing particles for setting 3, and CH_2 target without applying a cut on the incoming beam. For clarification, the trigger of the MINimum Bias Tpat&1 == 1 was selected for the reacted and unreacted particles. The isotopes of interest for this research are fluorine, oxygen, and nitrogen.

4.3.2 Mass Identification

For the final identification of the outgoing isotopes, Ralf's tracker [52], a software package developed by Ralf Plag, was utilized to determine the fragment mass A of the identified charge z. Similar to what was explained earlier in equation 25 for the incoming particles, the trajectory of a outgoing charged particle in ALADIN depends on the strength of the magnetic field B, mass over charge ratio A/z of the charged particle, and its velocity β. The magnetic field $\overrightarrow{B}(\overrightarrow{r}, \mathrm{I})$ of ALADIN is measured and parameterized into a field map, and that leads to the Bρ value for a given trajectory and current I.

Ralf's tracker utilizes the information of the measured positions and time of the charged particle hits from various detectors to reconstruct the trajectory of the charged particle and determine its flight path and velocity β. Furthermore, three basic approaches can be used to obtain the trajectory of the charged particle; forward tracking to calculate the outgoing trajectory, backward tracking to calculate the incoming trajectory, and mixed tracking for a combination of the incoming and outgoing trajectory. The forward tracking requires at least two positions before ALADIN and one after it, and the backward tracking requires the opposite, while the mixed tracking requires at least two positions before ALADIN and two after it. In this research, the forward tracking approach was used since the incoming particles and their trajectories were identified via land02. The two positions before ALADIN in the x and y-axis are provided by the third and fourth SSDs detectors, located between the target and ALADIN. On the other hand, the one position after ALADIN in the x-axis only is provided by the two GFIs detectors located in the fragment arm, which leads to the usage of the TFW detector at the end of the fragment arm for providing y-position besides the time-of-flight. For the detector position calibration, the information of the detectors positions in the R^3B

setup, the charge of the outgoing particles, and the applied current of ALADIN are required as inputs for the tracker. The calibration is performed by using the unreacted beam. As a result, the difference between the calculated position by the tracker and the measured position in the $\mathrm{R^3B}$ setup is equal to an offset, called residual. Thus, the obtained residuals should be close to zero. Consequently, the detectors before and after ALADIN were aligned relative to a straight line to minimize the corresponding residuals.

For the time-of-light (ToF) calibration, the velocity at the target center β_0 obtained by the tracker is supposed to match the calculated velocity by Atima [53], which is listed in Table 9 for all reaction channels. Besides, the velocities of the incoming beam β_{in} and the outgoing unreacted beam β_{out} are expected to match in the center of the target, as illustrated in Figure 40 for the reaction channel of $^{20}\mathrm{O(p,2p)}^{19}\mathrm{N}$.

Table 9: The velocity of the incoming beam of different reaction channels at the center of target provided by Atima calculations $(\beta_0)_{\mathrm{Atima}}$ and the tracker $(\beta_0)_{\mathrm{tracker}}$. The empty target run of setting 3 is utilized, and the Fragments trigger Tpat&2 == 2 was applied. Moreover, the thickness of each detector before the target is considered for the Atima calculations.

Incoming Beam	$(\beta_0)_{\mathrm{Atima}}$	$(\beta_0)_{\mathrm{tracker}}$
$^{20}\mathrm{O}$	0.721	0.722
$^{19}\mathrm{O}$	0.739	0.739
$^{23}\mathrm{F}$	0.711	0.714
$^{22}\mathrm{F}$	0.728	0.729
$^{21}\mathrm{F}$	0.744	0.745

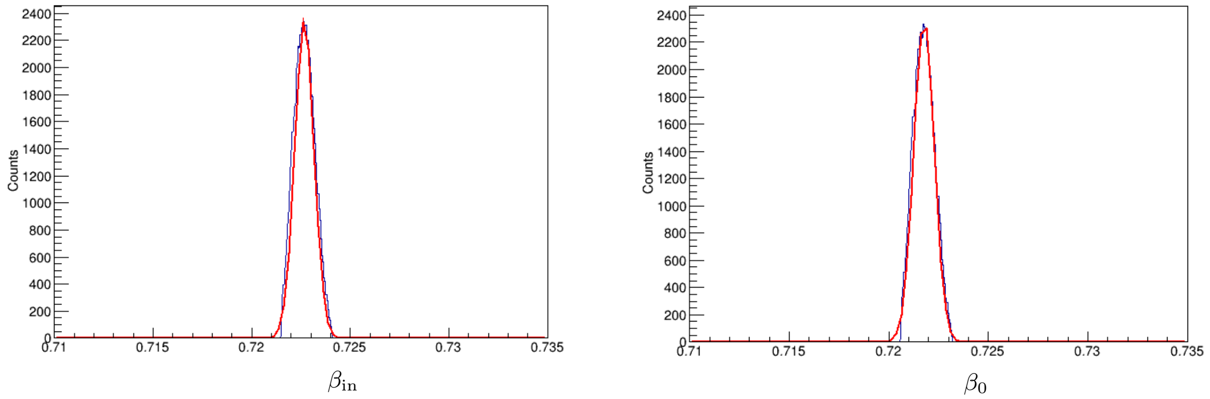

(a) The velocity of the incoming ^{20}O at the entrance of cave C.

(b) The velocity of the incoming ^{20}O at the center of the target.

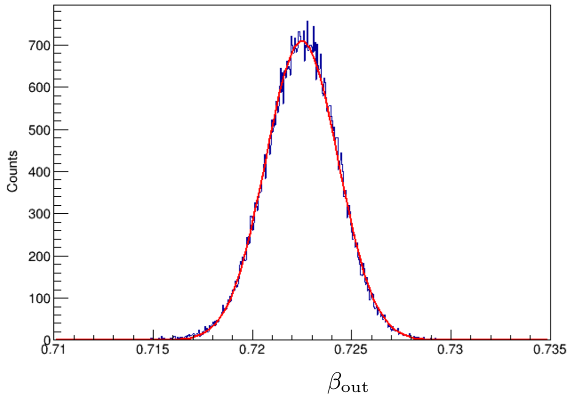

(c) The velocity of the outgoing unreacted ^{20}O at the end of the fragment arm.

Figure 40: The measured velocities of the unreacted beam of ^{20}O for setting 3 and empty target run with the trigger of Fragments Tpat&2 == 2. (a) The velocity of the incoming ^{20}O at the entrance of cave C, which was measured by the S8 and POS detector and done in land02, it is equal to around 0.723 ± 0.001. (b) The velocity of the incoming ^{20}O at the center of the target, which was done via the tracker, it is equal to approximately 0.722 ± 0.001. (c) The velocity of the outgoing unreacted ^{20}O, which was measured between the POS and TFW detector, and done via the tracker, it is equal to 0.722 ± 0.002. These values are close to the obtained velocity from Atima, as presented in Table 9.

The obtained mass distribution for the reacted ^{20}O beam with the CH_2 target is shown in Figure 41; both the Crystal Ball Sum trigger Tpat&8 == 8 and a cut on detecting two protons in the Crystal Ball were applied. The condition of detecting two protons will explained in more detail in the next section. The nitrogen fragment with the mass of interest A=19 caused by the QFS reaction is the first peak on the right. While losing additional neutrons during the reaction leads to other nitrogen isotopes with a mass of 18, 17, etc as shown in the figure from right to left.

The total number of the tracked events under the peak A=19 can be obtained by fitting a Gaussian function to the normal distribution of the mass spectrum. The obtained mean and the double standard deviations 2σ are then used to determine the required range for taking the integral under the peak A=19.

After taking the integral, the obtained total number is corrected by the corresponding downscale factor DS showed in Table 6. In this reaction, the carbon and hydrogen contribute to the final measurement; thus the carbon contribution in the CH_2 was subtracted. Furthermore, similar approach is used for the number of unreacted events for the ^{20}O at A=20 under the required Fragments trigger Tpat&2 == 2 as exhibited in Figure 42.

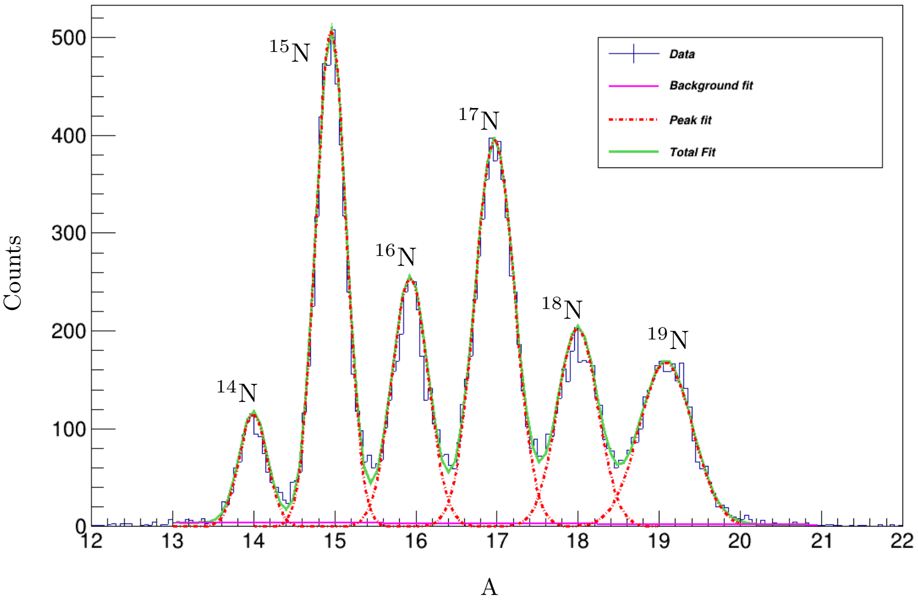

Figure 41: Mass identification of the outgoing nuclei produced by the reacted ^{20}O beam. The nitrogen fragments are detected in coincidence with two detected protons in the Crystal Ball detector. This plot is drawn for setting 3, CH_2 target, and the applied trigger of the Crystal Ball Sum Tpat&8 == 8. For the analysis, a cut on ^{19}N events is required for the ^{20}O(p, 2p)^{19}N reaction channel identification.

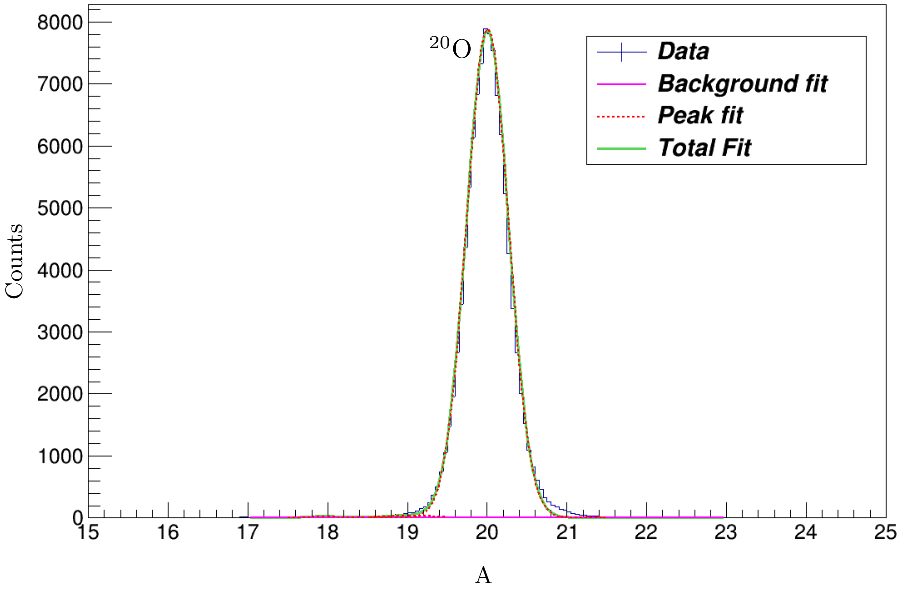

Figure 42: Mass identification of the unreacted nuclei ^{20}O. This plot is drawn for setting 3, CH_2 target, and the applied trigger of Fragments Tpat&2 == 2.

4.4 Quasi-Free Scattering Identification

The Crystal Ball identifies the quasi-free scattering reaction by examining the number of scattered protons and their angular correlation in coincidence with detecting fragments of interest. The number of the scattered protons was obtained by using the addback algorithm on an event-by-event basis. The algorithm treats other detected particles, gamma rays, and neutrons separately to avoid causing the background to their spectra. Moreover, the crystals' electronic readouts were adjusted to record events with deposited energy higher than a given threshold to eliminate the noise level. These thresholds were applied to the crystal ball simulation as well, which will be explained in more detail in Chapter 5. On the other hand, events with deposited energy higher than the a maximum limit of gamma rays were set to infinity (inf). The forward side of the crystal ball can record these energies in the proton branch, as shown in Figure 43. Consequently, every recorded event has a list of information; crystals number, time information in ns, deposited energy in MeV, etc. Some events are considered lost since they have invalid time or energy values (nan).

The reacted particle is likely to deposit its whole energy inside a cluster of neighboring crystals before it stops or leaves the detector. A secondary particle might be produced from the interaction between the incident particle and the detector material. Its energy might be deposited in the same crystal or first neighboring crystal. Therefore, the addback reconstructs deposited energies in the crystals by summing data from each deposited energy in neighbors' crystals. During the reconstruction of the deposited energies, care was taken to check their eligibility. It starts with the first crystal in the list and goes through the crystals until it finds the highest deposited energy as illustrated in Figure 44. Once the highest energy crystal is determined, it goes under examination to be sorted it in an appropriate branch. It is assigned as gamma if it has finite energy in the gamma branch. Otherwise, it is assigned as a proton if it has infinite energy in the gamma branch and finite energy in the proton branch. After the main crystal of the highest energy was determined, the algorithm will set its energy to zero and add the energies of the neighboring crystals before setting them to zero. Following the reconstruction of the first cluster, the eligibility checking will be repeated to create a new cluster. The total number of the created gamma or proton clusters is named multiplicity. The scattering angle of the reacted particles was obtained from measuring the angle at the center of the main crystal with respect to the center of the crystal ball. The scattering angle is essential for Doppler correction.

However, wrong identification and central crystal assumption limit the accuracy of the algorithm. It can occur by classifying neutrons as gamma-rays since the neutrons deposit sufficient energy in the crystals and create secondary particles. Also, the central crystal assumption might add direct neighbors that are related to different reacted particles.

Another significant aspect is the calibration of the Crystal Ball, which must be done before the addback approach. It is treated under three headings: the energy calibration for the gamma-ray branch and proton branch for each given crystal and the time synchronization of all crystals. Gamma-ray calibration was obtained by using three radioactive sources for the S393 experiment; ^{22}Na, ^{88}Y, and ^{60}Co. In contrast, the proton calibration was prepared by using the cosmic muons. For the time synchronization, calibration parameters were obtained by using a source emitting two gamma-rays coincidentally. Then, the resulting parameters were then applied to the readout of the gamma-ray and proton. For more details of the used calibration, an extensive clarification of the Crystal Ball calibration can be found in the thesis of Ronja Thies [43].

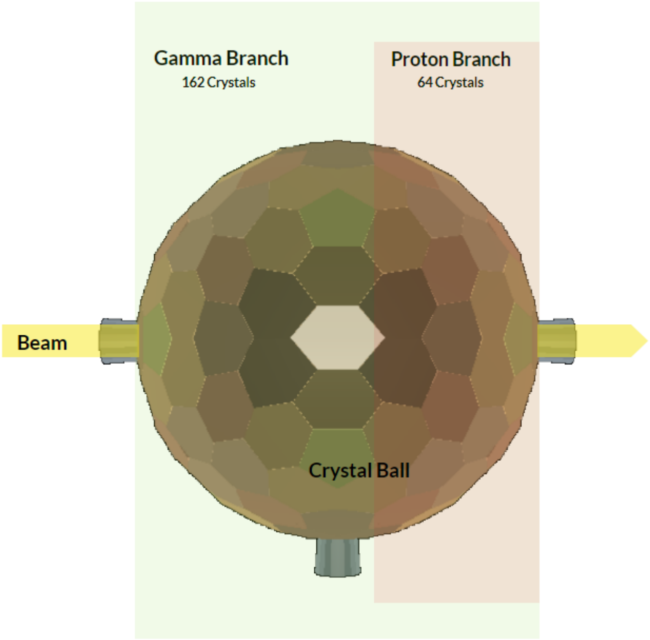

Figure 43: Schematic of readout branches of the crystal ball detector. The forward side of the crystal ball can detect both gamma-rays and protons.

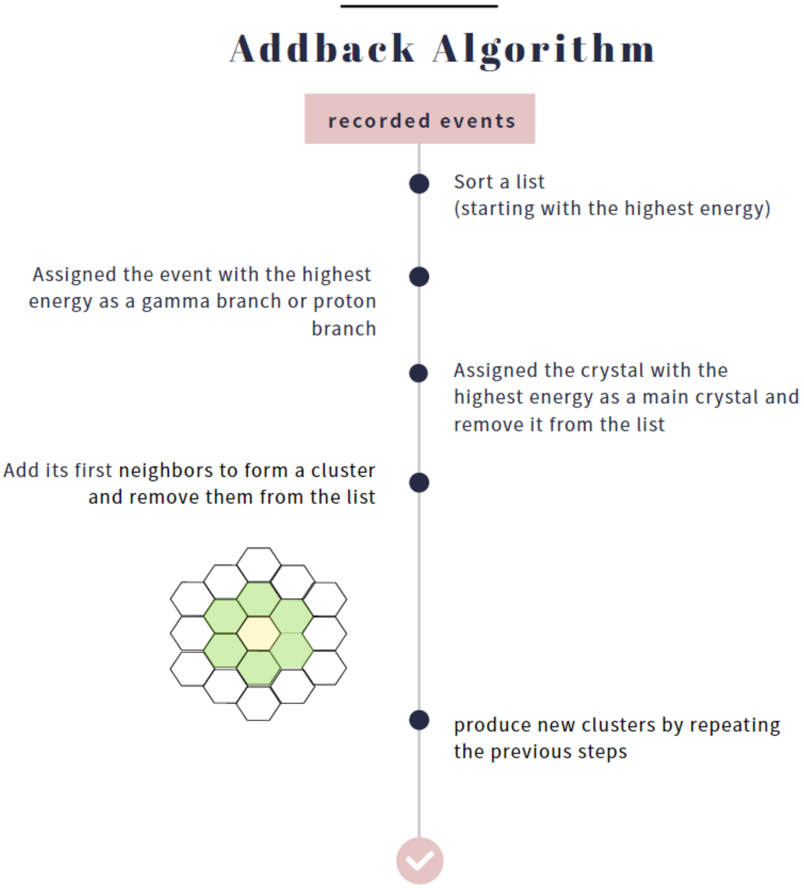

Sort a list (starting with the highest energy)

Assigned the event with the highest energy as a gamma branch or proton branch

Assigned the crystal with the highest energy as a main crystal and remove it from the list

Add its first neighbors to form a cluster and remove them from the list

produce new clusters by repeating the previous steps

Figure 44: Illustration of the addback algorithm for the detected events in the crystal ball.

4.4.1 Proton Multiplicity

The coincidence of detecting two protons in the Crystal Ball with the fragment of interest characterizes the quasi-free scattering reaction channel. The detected protons multiplicity by the Crystal Ball is exemplified by the $^{20}\mathrm{O}(\mathrm{p}, 2\mathrm{p})^{19}\mathrm{N}$ reaction channel in Figure 45. It is apparent from this figure that the dominated multiplicity for this reaction is equal to two, which indicates the quasi-free scattering. Thus, a cut on events with two detected protons is required to analyse the quasi-free scattering reaction. However, not all the two generated protons from the quasi-free scattering reactions are detected. Thus, all measured cross sections for (p,2p) reaction channel are corrected by the two-proton detection efficiency of the Crystal Ball from the simulation, as will be illustrated in more detail in section 4.7 and chapter 5.

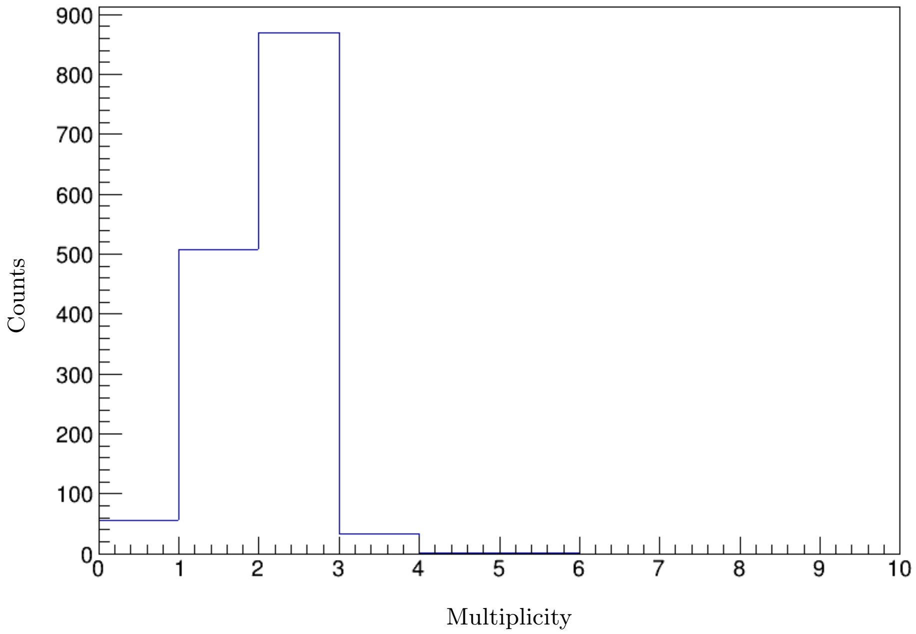

Figure 45: Proton multiplicity (proton clusters) in the Crystal Ball for the H target of setting 3. A cut of detecting $^{19}\mathrm{N}$ and the trigger of the Crystal Ball Sum Tpat&8 == 8 was applied.

4.4.2 Protons Angular Correlation

Besides the scattered proton multiplicity, the quasi-free scattering reaction was identified by the protons angular correlation with a coincidence of detecting the fragment of interest. Both polar angle θ, relative to the z-axis (beam axis in the lab system), and azimuth angle ϕ, relative to the x-axis, of the two scattered protons, in the laboratory frame show a strong correlation due to the momentum conservation of the reaction as shown in Figure 46 for $^{20}\mathrm{O}(\mathrm{p}, 2\mathrm{p})^{19}\mathrm{N}$ reaction. For a realistic angular distribution, the angles were randomized within the area of the corresponding crystal to obtain a smooth distribution. Strong evidence of the back-to-back scattering is shown in the azimuthal angular correlation in Figure 46a for the CH_2 target and Figure 46c for the carbon target. While the polar angular correlation in Figure 46b for the CH_2 target and Figure 46d for the carbon target exhibit a diagonal band indicates the protons scattered with an opening angle θ_0 of approximately 80° with respect to each other, which is given by equation 7 and presented in Figure 47a, the red curve indicates the distribution for CH_2 target, and the blue curve indicates the distribution for the C target. Furthermore, the distributions of the difference between the azimuthal angles ($\Delta\phi$) of the two scattered protons from $^{20}O(p, 2p)^{19}N$ reaction is around 180° as shown in Figure 47b. The red curve indicates the distribution for CH_2 target, and the blue curve indicates the distribution for the C target. Additionally, a cut of Crystal Ball Sum trigger $Tpat\&8 == 8$ and proton multiplicity of 2 was applied.

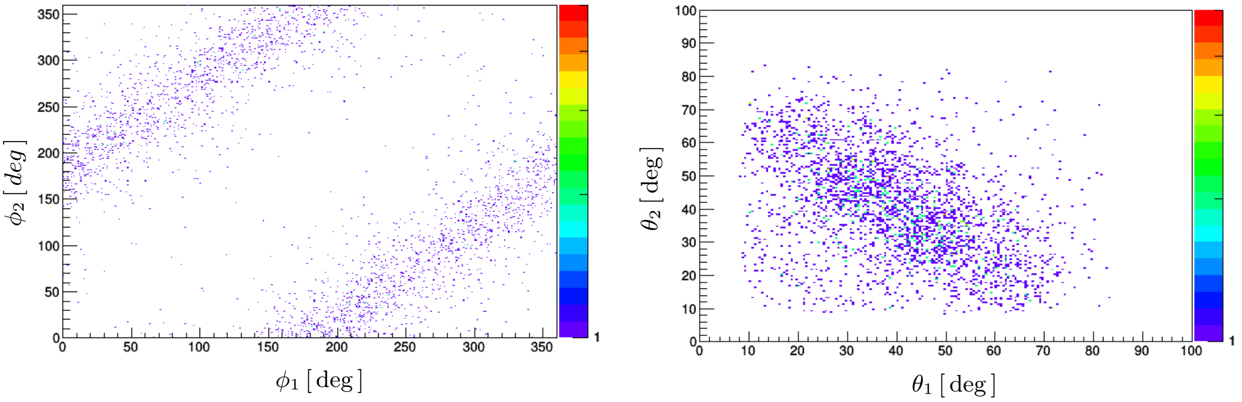

(a) The azimuthal angular correlation, CH_2 target

(b) The polar angular correlation, CH_2 target

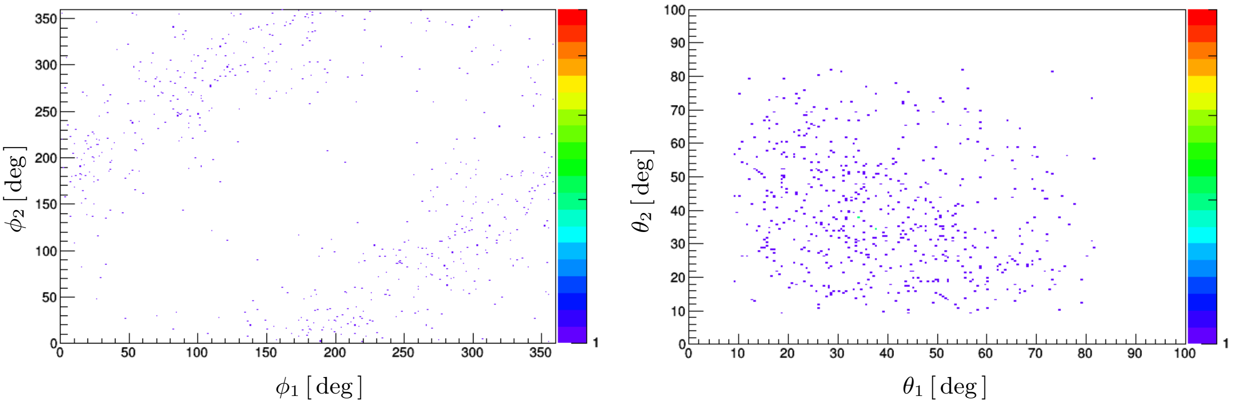

(c) The azimuthal angular correlation, C target

(d) The polar angular correlation, C target

Figure 46: The angular correlation of the scattered protons from the quasi-free scattering reaction in coincidence with ^{19}N for the CH_2 and C target of setting 3. A cut of Crystal Ball Sum trigger $Tpat\&8 == 8$ and proton multiplicity of 2 was applied.

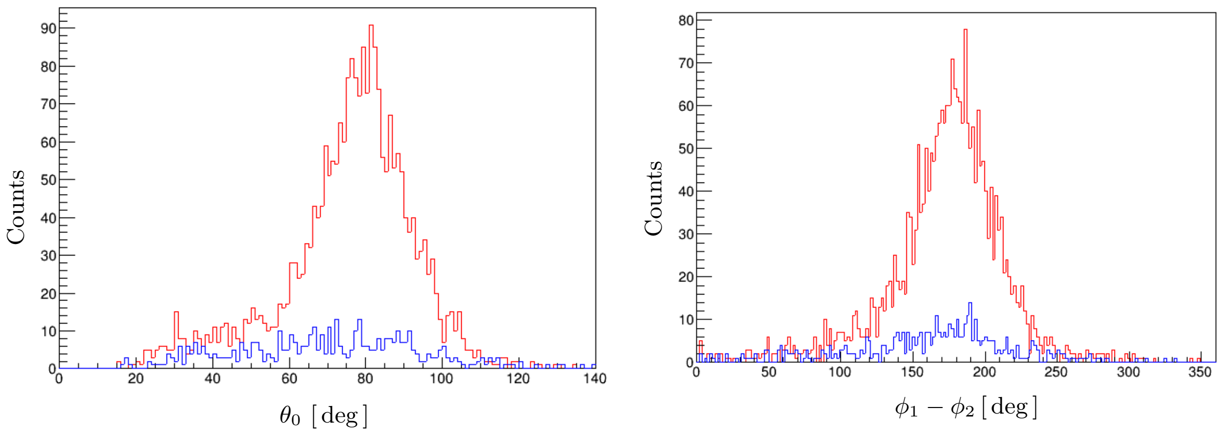

(a) Opening angle distribution.

(b) The distribution of ($\Delta\phi$).

Figure 47: (a) The distribution of the opening angle (θ_0) between the two protons from quasi-free scattering $^{20}\mathrm{O(p, 2p)}^{19}\mathrm{N}$ in coincidence with $^{19}\mathrm{N}$ for $\mathrm{CH_2}$, the red curve, and C target, the blue curve, of setting 3. A cut of Crystal Ball Sum trigger $Tpat\&8 == 8$ and proton multiplicity of 2 was applied. (b) The distributions of the difference between the azimuthal angles ($\Delta\phi$) of the two scattered protons from quasi-free scattering $^{20}\mathrm{O(p, 2p)}^{19}\mathrm{N}$ in coincidence with $^{19}\mathrm{N}$ for $\mathrm{CH_2}$, the red curve, and C target, the blue curve, of setting 3. A cut of Crystal Ball Sum trigger $Tpat\&8 == 8$ and proton multiplicity of 2 was applied.

4.5 Geometrical Acceptance

The acceptance of the residual nuclei after the QFS reaction was checked. The benefit of this approach is to ensure that the geometrical coverage of the used detectors covers the particles' spread. Thus, positions in a two-dimensional plot of the first detector before the reaction, target, and last detector after the reaction were examined. This can be exemplified by checking the acceptance of particles involved in the $^{20}\mathrm{O(p, 2p)}^{19}\mathrm{N}$ reaction channel for the $\mathrm{CH_2}$ target. The hits in the x-axis and y-axis of the incoming $^{20}\mathrm{O}$ at the SSD02 detector and the $\mathrm{CH_2}$ target are illustrated in Figures 48a and 48b, respectively. Furthermore, the positions of outgoing $^{19}\mathrm{N}$ nuclei in the TFW detector are shown in Figure 48c, where the Crystal Ball trigger Tpat&8 $==$ 8 has been applied in addition to a proton multiplicity of two.

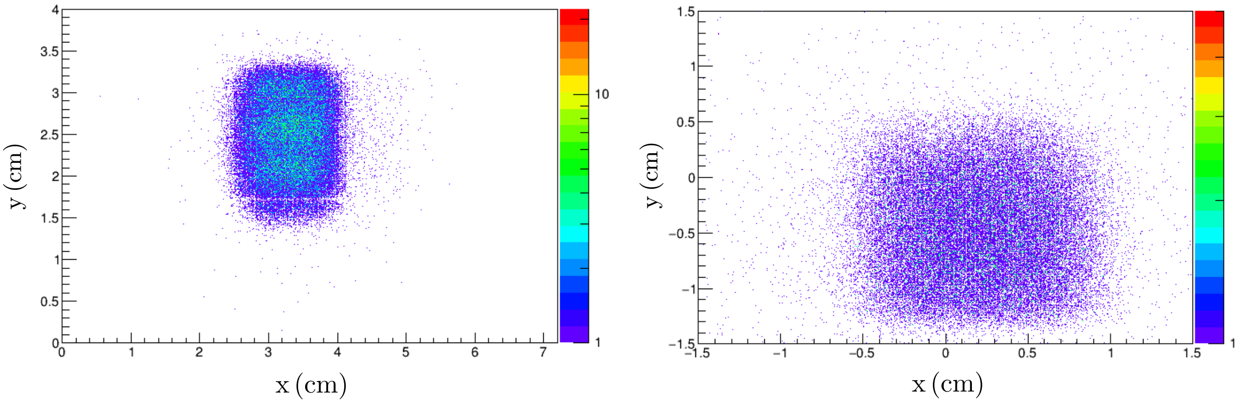

(a) ^{20}O hits at the SSD02 detector.

(b) ^{20}O hits at the CH$_2$ target.

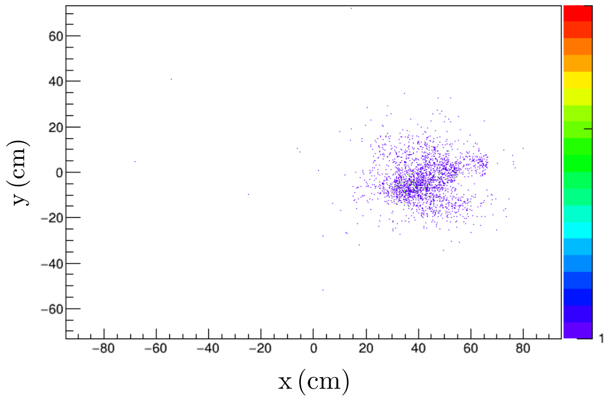

(c) ^{19}N hits at the TFW detector.

Figure 48: The geometrical acceptance of the SSD02 detector with an active area of $7.2 \times 4.0\,\mathrm{cm}^2$, target with an area of 3×3 cm^2, and TFW detector with an active area of 189×147 cm^2 for the $^{20}\mathrm{O(p,2p)}^{19}\mathrm{N}$ reaction.

4.6 Gamma-ray Spectrum

Gamma rays from the de-excitation process of the outgoing fragments were detected by the Crystal Ball, as mentioned in section 4.4. However, gamma-ray analyses went through three main steps; addback, doppler correction, and simulation. The addback approach was illustrated in section 4.4. Thus, after reconstruction of the gamma-ray clusters, the Doppler correction is required since the gamma rays are emitted from the outgoing fragments moving at relativistic speeds as illustrated in table 9. The Doppler corrected energy of the detected gamma-ray is written as:

$$\mathrm{E_{cm}} = \mathrm{E_{lab}}\,\gamma\,(1-\beta\cos\theta_{\mathrm{cr}}) \tag{36}$$

where:

$\mathrm{E_{cm}}$: Gamma-ray energy in the center of mass frame

$\mathrm{E_{lab}}$: Gamma-ray energy in the lab frame

γ: The Lorentz factor $\gamma = \frac{1}{\sqrt{1-\beta^2}}$

β: The velocity of the de-exciting fragment, in the unit of the speed of light $\beta = \frac{\mathrm{v}}{\mathrm{c}}$

θ_{cr}: The angle at the center of the central crystal of the cluster.

After applying Doppler correction, a comparison was made between the obtained gamma spectrum and level scheme from the literature for the daughter nucleus of interest. An example of this is the level scheme of the bound state of the daughter nucleus ^{19}N, as shown in Figure 49. Consequently, a simulation approach will be utilized to identify the contribution from different excited states by comparing the final experimental gamma-ray spectra to the simulated spectra. The simulation is written in more detail in the next chapter.

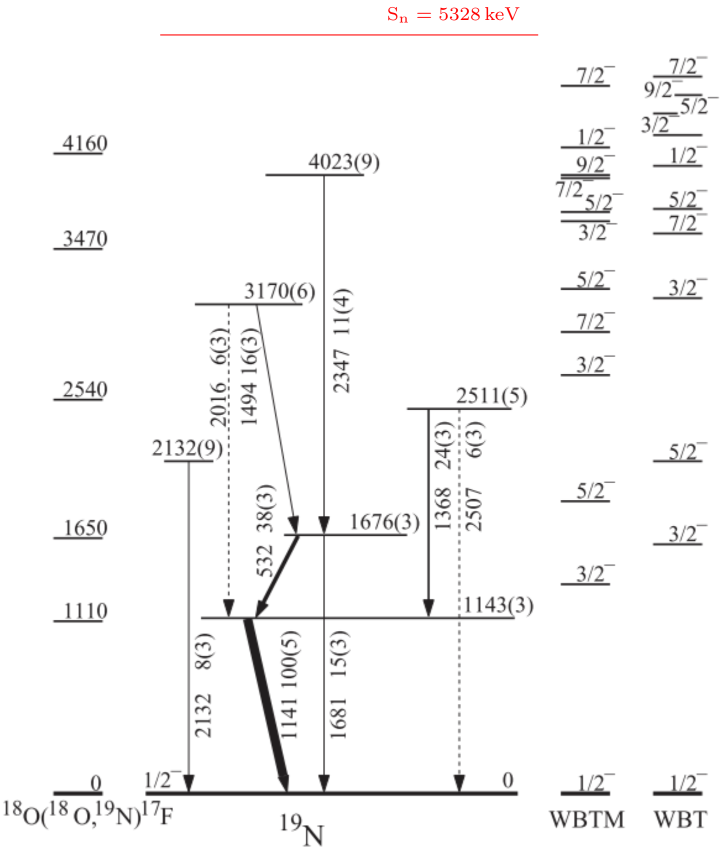

Figure 49: Level scheme of ^{19}N. Along with each transition arrow, the energy in keV, uncertainty in keV, and corresponding intensity are illustrated, where the width of each arrow is proportional to the gamma-ray intensity [54].

4.7 Cross Section

The cross section is a measure of the probability of the quasi-free scattering reaction $^{A}X(p,2p)^{A-1}Y$ to occur between the projectile of the nuclei of interest and the target. This probability depends on the number of the incoming isotopes, the number of the reaction products, and the target properties. Thus, the experimental inclusive cross section is written as:

$$\sigma_{\mathrm{incl}} = \frac{\mathrm{N_r}}{\mathrm{N_i} \cdot \epsilon_{\mathrm{XB,\,2p}} \cdot \tau_{\mathrm{t}}} \tag{37}$$

where:

$\mathrm{N_r}$: The total number of reaction products ^{A-1}Y.

$\mathrm{N_i}$: The total number of the incoming particles ^{A}X, and can be approximated by calculating the number of unreacted nuclei due to the low reaction probability.

$\epsilon_{\mathrm{XB,\,2p}}$: Crystal ball efficiency of detecting two scattered protons, produced by the quasi-free scattering, in coincidence with the generated fragment ^{A-1}Y. In this part, the simulation is employed to obtain the crystal ball efficiency because the total number of the quasi-free scattering events generated during the experiment is not known.

τ_t: The number of scattering centers in the target and it is calculated by knowing the target's density ρ_t, thickness d_t and atomic mass A_t and Avogadro's constant $N_A = 6.022 \times 10^{23} \mathrm{mol}^{-1}$. The properties of the chosen targets for this work are listed in Table 10, and the number of scattering centers is written as:

$$\tau_t = \frac{\rho_t \cdot d_t \cdot N_A}{A_t} \tag{38}$$

Table 10: Characteristics of the used targets in this work.

Target	Density ρ_t(g/cm^3)	Thickness d_t(mm)	Atomic Mass A_t(g/mol)
CH_2	0.92	4.98	12.011
C	1.84	3.03	14.027

The statistical uncertainty of the experimental inclusive cross section $\delta_{\sigma_{\mathrm{incl}}}$ can be calculated using its associated statistical variables, and it is written as:

$$\delta_{\sigma_{\mathrm{incl}}} = \sigma_{\mathrm{incl}} \sqrt{(\frac{\delta_{N_r}}{N_r})^2 + (\frac{\delta_{N_i}}{N_i})^2} \tag{39}$$

where (δ_{N_r}) and (δ_{N_i}) are the uncertainty of the reacted and incoming particles selection, respectively. The statistical uncertainty will be presented separately with the systematic uncertainty at the final result. The overall systematic uncertainties is around 6% [55].

Furthermore, it is apparent from Table 10 that two sets of data, the polyethylene CH_2 and the carbon target under suitable cuts, were selected to measure the cross section of the quasi-free scattering reaction on hydrogen. In other words, the carbon target is used as background measurement to estimate the carbon atoms contributions in the CH_2 target. Therefore, the hydrogen cross section can be calculated by taking half of the difference between the two cross sections:

$$\sigma_H = \frac{1}{2} [\, \sigma_{CH_2} - \sigma_C \,] \tag{40}$$

Accordingly, its statistical uncertainty is given by:

$$\delta_{\sigma_H} = \frac{1}{2} [\, \sqrt{(\delta_{\sigma_{CH_2}})^2 + (\delta_{\sigma_C})^2} \,] \tag{41}$$

As an alternative approach, the experimental inclusive cross section for the reconstructed hydrogen target can be calculated directly by equation 37. In this case, the number of reacted events with reconstructed hydrogen target N_r is given by:

$$N_r(H) = \frac{1}{2} [\, N_r(CH_2) - \frac{N_i(CH_2)}{N_i(C)} \frac{\tau_t(CH_2)}{\tau_t(C)} N_r(C) - (1 - \frac{\tau_t(CH_2)}{\tau_t(C)}) \frac{N_i(CH_2)}{N_i(MT)}) N_r(MT)] \tag{42}$$

This equation was used to obtain the histogram of interest of the reconstructed H target to obtain the required measurements for the analysis, such as gamma-ray spectrum and momentum distribution.

The experimental inclusive cross section are then used to calculate the experimental exclusive cross section $\sigma_{\mathrm{excl,\,i}}$ for each excited state i. It can be obtained by identifying the population of each state $\mathrm{p_i}$, which will be explained in more detail in section 5.3.2. The exclusive experimental cross section for a specifically excited state i is given by:

$$\sigma_{\mathrm{excl,\,i}} = \mathrm{p_i} \times \sigma_{\mathrm{incl}} \tag{43}$$

Consequently, the experimental exclusive cross section for the ground state $\sigma_{\mathrm{excl,\,G.S}}$ is given by:

$$\sigma_{\mathrm{excl,\,G.S}} = \sigma_{\mathrm{incl}} - \sum_{\mathrm{i}} \sigma_{\mathrm{excl,\,i}} \tag{44}$$

Accordingly, its statistical uncertainty is written as:

$$\delta_{\sigma_{\mathrm{excl,\,G.S}}} = \sqrt{(\delta_{\sigma_{\mathrm{incl}}})^2 + \sum_{\mathrm{i}} (\delta_{\sigma_{\mathrm{excl,\,i}}})^2} \tag{45}$$

4.8 Momentum Distributions

In the quasi-free scattering reactions, the shape and width of the momentum distribution of the remaining nuclei after the reaction reflect the internal momentum distribution of the removed proton in the projectile, as illustrated in equation 8. This examination allows estimating the orbital angular momentum of the removed proton from the projectile by comparing the experimental and theoretical data.
The tracker calculates the experimental momentum of the fragments in the laboratory frame $\mathrm{P_{lab}}$ and it is decomposed into the longitudinal component $\mathrm{P}_{||}$, that is parallel to the beam direction, which points to the z-axis, and the transverse component $\mathrm{P}_{\perp}$, that is perpendicular to the beam:

$$\mathrm{P_{lab}} = \beta\gamma\,\mathrm{m} \tag{46}$$

where β is the velocity of the beam, γ is the Lorentz factor, and m is the fragment mass.

$$\overrightarrow{\mathrm{P}_{lab}} = \overrightarrow{\mathrm{P}_{||}} + \overrightarrow{\mathrm{P}_{\perp}} \tag{47}$$

The transverse component $\mathrm{P}_{\perp}$ is Lorentz-invariant since it represents the momentum in a plane perpendicular to the fragment momentum. It can be calculated by measuring the angles of the incidence projectiles and outgoing fragments using the DSSDs detectors, as shown in Figure 50.

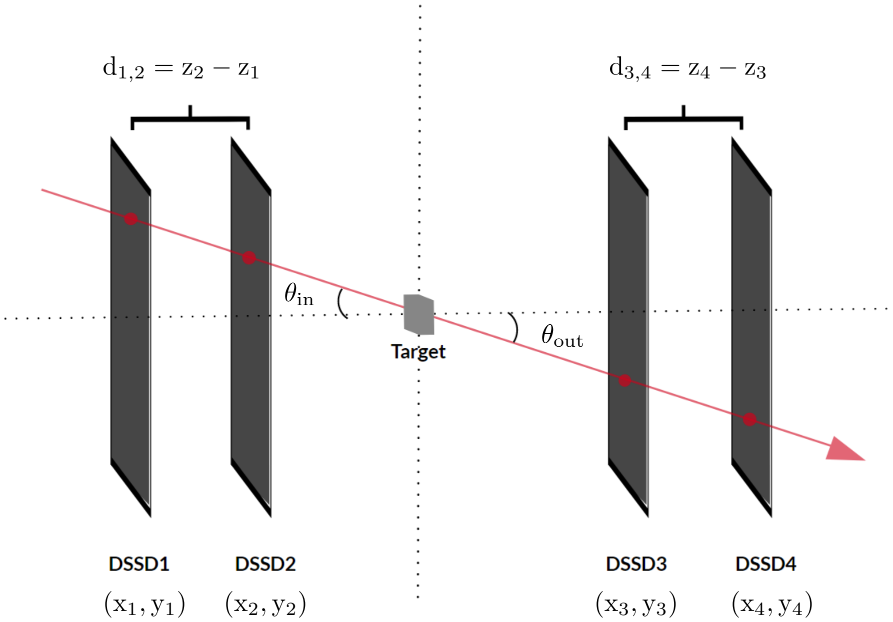

Figure 50: A sketch for the determination of the incoming and outgoing angles by the DSSDs detectors. For simplicity, the distances between the DSSDs do not resemble the actual distances in the experiment.

$$\theta_{x,in} = \tan^{-1}\left(\frac{x_2 - x_1}{d_{1,2}}\right) \quad , \quad \theta_{y,in} = \tan^{-1}\left(\frac{y_2 - y_1}{d_{1,2}}\right) \tag{48}$$

$$\theta_{x,out} = \tan^{-1}\left(\frac{x_4 - x_3}{d_{3,4}}\right) \quad , \quad \theta_{y,out} = \tan^{-1}\left(\frac{y_4 - y_3}{d_{3,4}}\right) \tag{49}$$

$$\theta_x = \theta_{x,out} - \theta_{x,in} \quad , \quad \theta_y = \theta_{y,out} - \theta_{y,in} \tag{50}$$

$$P_x = P_{lab} \cos\theta_x \quad , \quad P_y = P_{lab} \cos\theta_y \tag{51}$$

$$P_\perp = \sqrt{P_x^2 + P_y^2} \tag{52}$$

In contrast to the transverse component $P_\perp$, the longitudinal component $P_{||}$ is not Lorentz-invariant since it is parallel to the beam axis, and it is written as:

$$P_{||,lab} = \sqrt{P_{lab}^2 - P_\perp^2} \tag{53}$$

$$P_{||,cm} = \beta_{fra}\,(P_{||,lab} - \beta_0\,\gamma\,m) \tag{54}$$

where $\mathrm{P}_{||\,,\,\mathrm{lab}}$ and $\mathrm{P}_{||\,,\,\mathrm{cm}}$ are the longitudinal component in the laboratory and center-of-mass frame. β_{fra} is the velocity of the fragments after the reaction and β_0 is the velocity of the incoming beam.
Therefore, the total momentum in the center-of-mass frame is written as:

$$\mathrm{P}_{\mathrm{cm}} = \sqrt{\mathrm{P}_{\perp}^2 + \mathrm{P}_{||,\,\mathrm{cm}}^2} \tag{55}$$

In addition, the scattering angle and momentum distribution of the unreacted beam were used to determine the straggling of the target σ_{str} and its effects on the momentum distribution of the R^{3}B setup. The straggling in the target is given by:

$$\sigma_{\mathrm{str}} = \sqrt{(\sigma_{\mathrm{target}})^2 - (\sigma_{\mathrm{MT}})^2} \tag{56}$$

where σ_{target} is the standard deviation from the Gaussian fit of the momentum distribution of the unreacted incoming beam for a specific target. While the empty target run was utilized to obtain σ_{MT}.

Figure 51 and 52, and Table 11 and 12 illustrate this effect for the unreacted beam of ^{20}O for different targets.

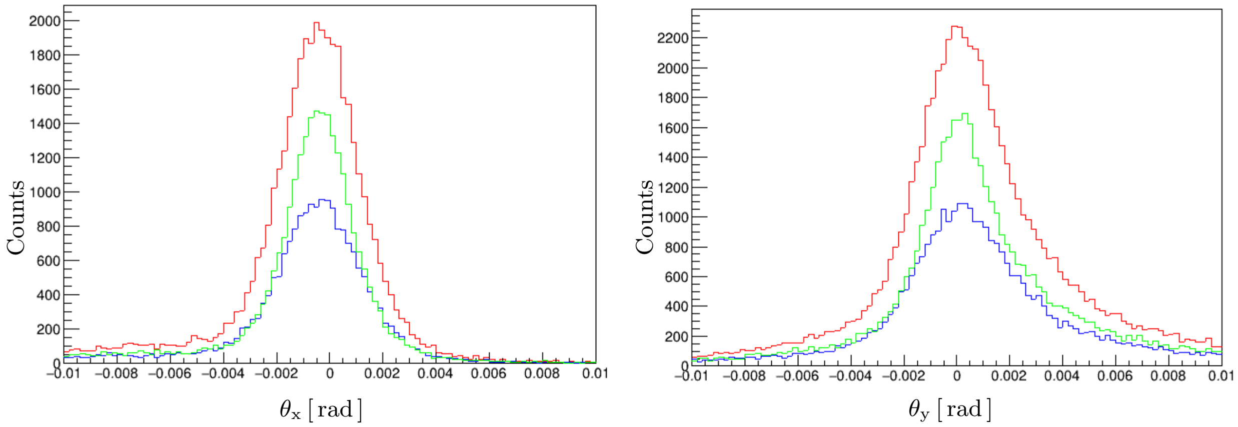

(a) The x-component of the scattering angle

(b) The y-component of the scattering angle

Figure 51: The scattering angle of the unreacted ^{20}O beam for the CH$_2$ target indicated by the red curve, the C target indicated by the blue curve, and the empty target indicated by the green curve. A cut of Fragment trigger Tpat&2 == 2 was applied.

Table 11: The measured angular straggling of the unreacted ^{20}O beam for CH_2, and C target of setting 3. It is obtained from the Gaussian fit of the angular distribution in figure 51 in addition to the calculated one by Atima. The uncertainties for the Atima calculation values are obtained from the 2% uncertainty of the target thickness.

Target	σ_θ (mrad)	$\sigma_{\mathrm{str},\,\theta}$ (mrad)	
	Measured	Measured	Atima
CH_2	$\sigma_{\theta_x} = 1.42 \pm 0.02$	$\sigma_{\mathrm{str},\,\theta_x} = 0.87 \pm 0.03$	0.83±0.01
	$\sigma_{\theta_y} = 1.63 \pm 0.03$	$\sigma_{\mathrm{str},\,\theta_y} = 0.83 \pm 0.04$	
C	$\sigma_{\theta_x} = 1.47 \pm 0.03$	$\sigma_{\mathrm{str},\,\theta_x} = 0.95 \pm 0.04$	0.97±0.01
	$\sigma_{\theta_y} = 1.70 \pm 0.07$	$\sigma_{\mathrm{str},\,\theta_y} = 0.96 \pm 0.07$	
MT	$\sigma_{\theta_x} = 1.12 \pm 0.02$		
	$\sigma_{\theta_y} = 1.40 \pm 0.02$		

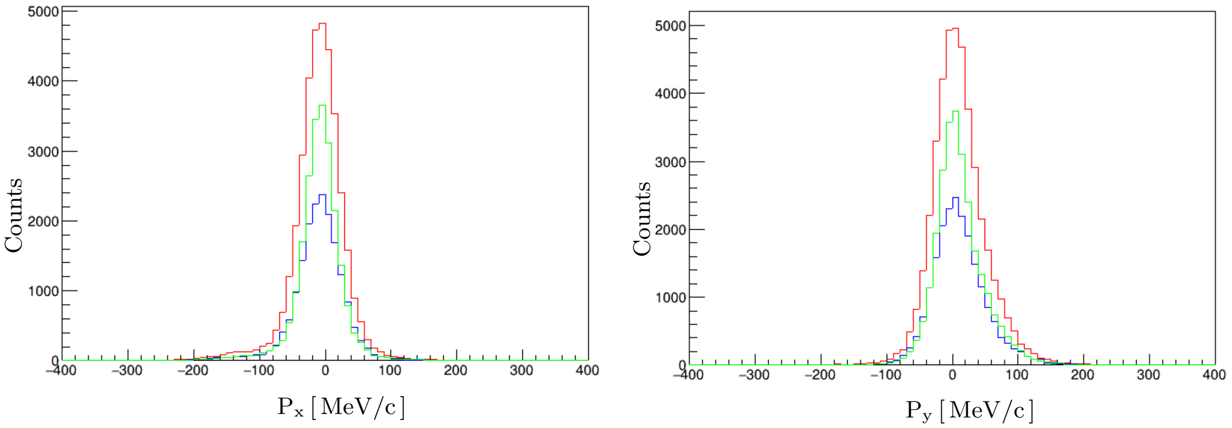

(a) The x-component of the transverse momentum

(b) The y-component of the transverse momentum

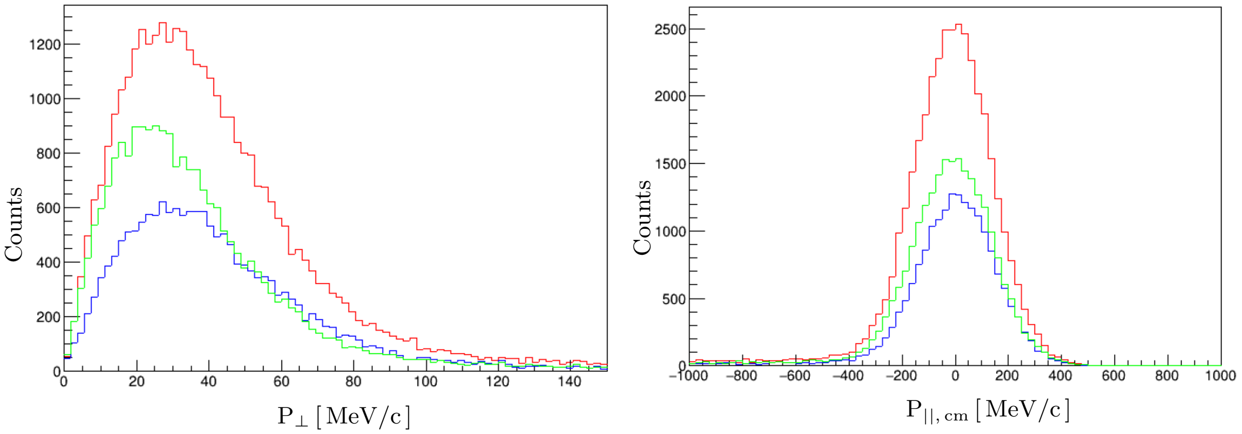

(c) The transverse momentum

(d) The longitudinal momentum

Figure 52: The momentum distributions of the unreacted ^{20}O beam for the CH_2 target indicated by the red curve, the C target indicated by the blue curve, and the empty target indicated by the green curve. A cut of Fragment trigger Tpat&2 == 2 was applied.

Table 12: The momentum resolution of the unreacted ^{20}O beam for CH_2 and C target of setting 3. It is obtained from the Gaussian fit of the momentum distribution in figure 52.

Target	σ_{p} (MeV/c)	$\sigma_{\mathrm{str,\,p}}$ (MeV/c)
CH_2	$\sigma_{\mathrm{p_x}} = 30.0 \pm 0.1$	$\sigma_{\mathrm{str,\,p_x}} = 15.6 \pm 0.2$
	$\sigma_{\mathrm{p_y}} = 35.8 \pm 0.7$	$\sigma_{\mathrm{str,\,p_y}} = 15.5 \pm 0.7$
C	$\sigma_{\mathrm{p_x}} = 30.8 \pm 0.2$	$\sigma_{str,\,p_x} = 17.1 \pm 0.3$
	$\sigma_{\mathrm{p_y}} = 36.6 \pm 0.2$	$\sigma_{str,\,p_y} = 17.1 \pm 0.3$
MT	$\sigma_{\mathrm{p_x}} = 25.6 \pm 0.2$	
	$\sigma_{\mathrm{p_y}} = 32.3 \pm 0.2$	

It is apparent from Table 12 that the width of the x and y component of the transverse momentum distribution of the empty target has the smallest value compared to the carbon and CH_2 target, which both have approximately similar widths.

As was pointed out at the beginning of this section, by measuring the remaining fragment's momentum distribution, we can infer the momentum and, consequently, the removed nucleon's orbit while in the nucleus. Figure 53 shows the momentum distributions of the reacted ^{20}O beam for the CH_2 target indicated by the red curve, the C target indicated by the blue curve, and the empty target indicated by the green curve. A cut of Crystal Ball trigger Tpat&8 == 8, and a multiplicity of two proton in coincidence with the fragment of interest ^{19}N was applied.

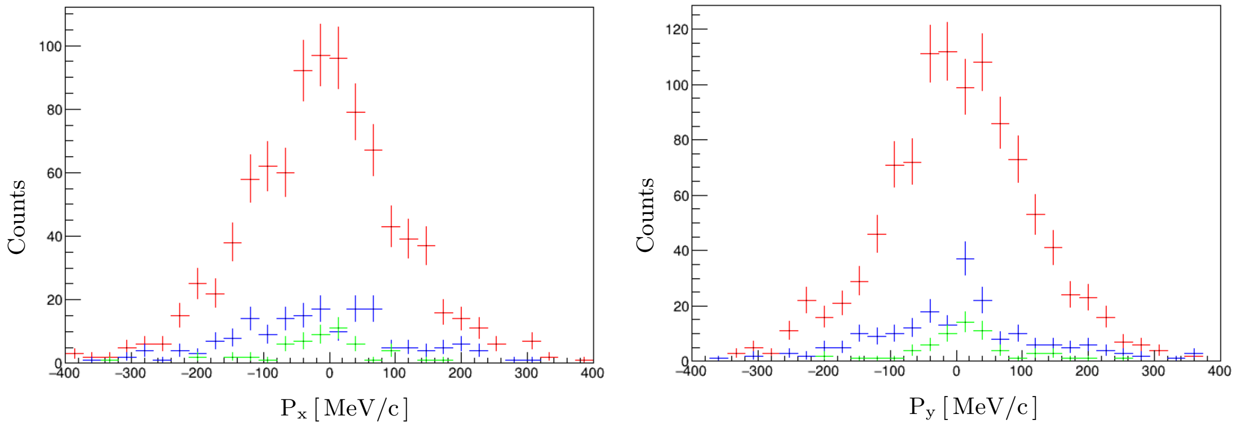

(a) The x-component of the transverse momentum

(b) The y-component of the transverse momentum

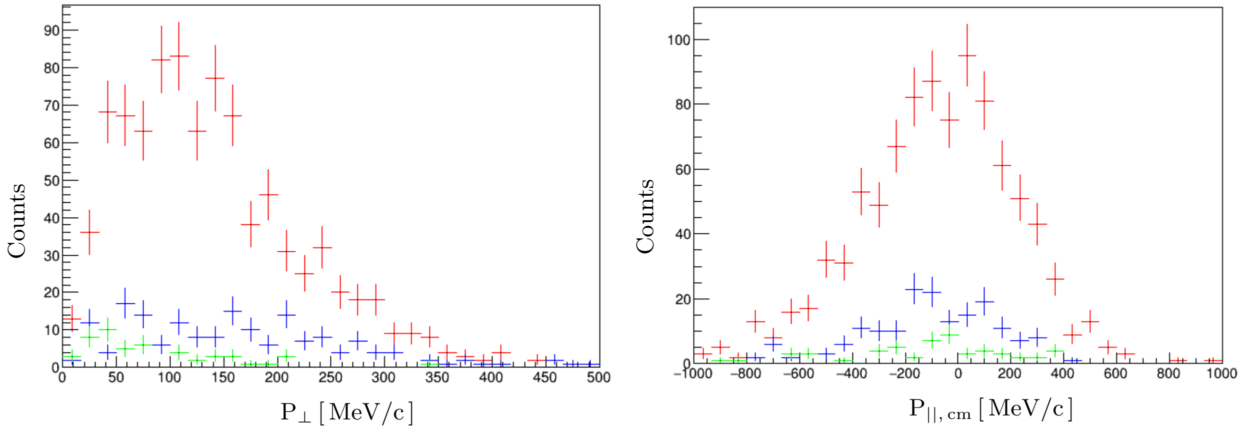

(c) The transverse momentum

(d) The longitudinal momentum

Figure 53: The momentum distributions of the reacted ^{20}O beam for the CH_2 target indicated by the red curve, the C target indicated by the blue curve, and the empty target indicated by the green curve. A cut of XB trigger Tpat&8 == 8, and a multiplicity of two proton in coincidence with the fragment of interest ^{19}N were applied.

The experimental momentum distribution of the reconstructed H target was obtained by using equation 42 to subtract the illustrated histograms in Figure 53. The outcome of the subtraction is shown in Figure 54.

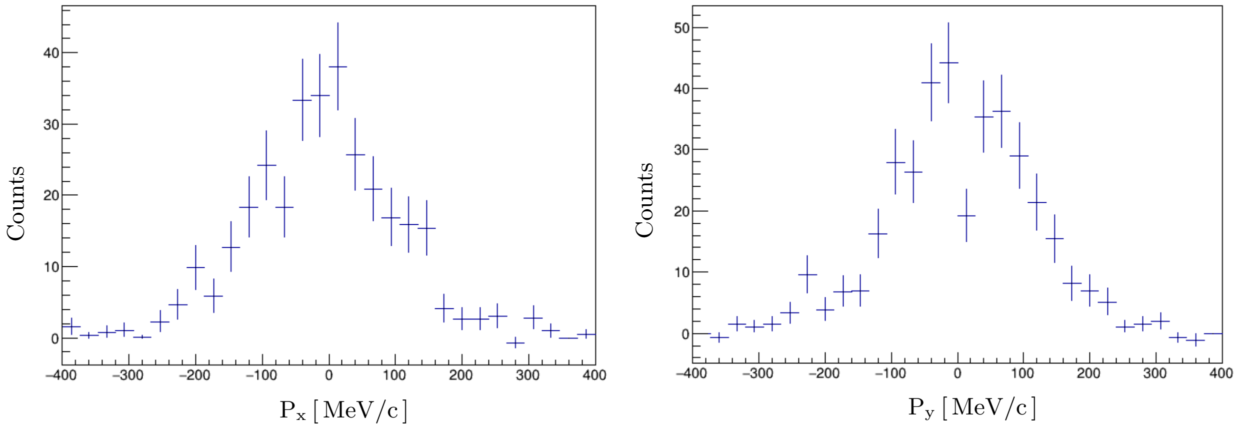

(a) The x-component of the transverse momentum

(b) The y-component of the transverse momentum

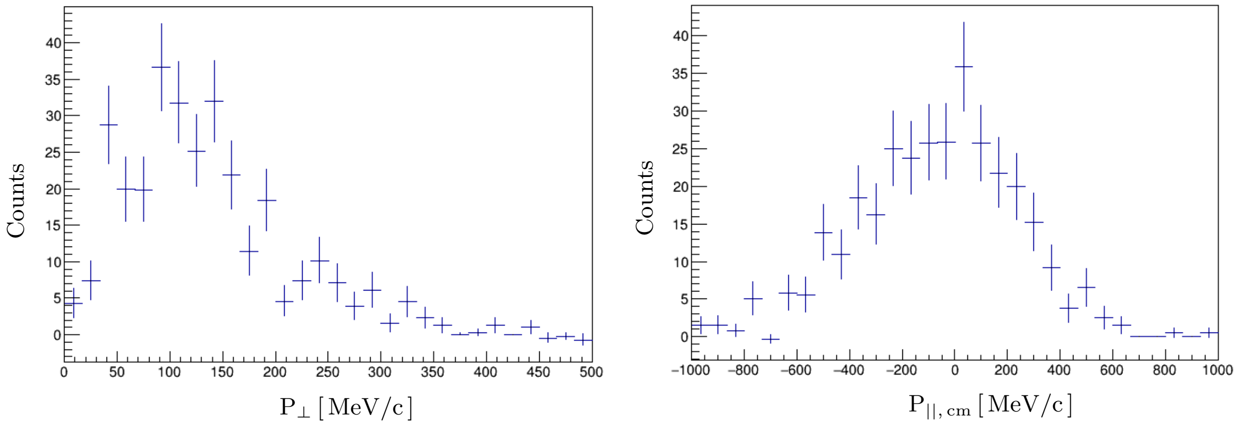

(c) The transverse momentum

(d) The longitudinal momentum

Figure 54: The momentum distributions of the reacted ^{20}O beam for the reconstructed H target. A cut of XB trigger Tpat&8 == 8, and a multiplicity of two proton in coincidence with the fragment of interest ^{19}N was applied.

What stands out in Figures 52 and 54 is the nucleon's internal momentum causes broadening of the width of the distribution. The orbit of the removed proton for the reaction channel can be determined by comparing the inclusive experimental momentum distribution of the residual to the theoretical momentum distribution for the reconstructed H target after taking into account the broadening due to the finite experimental resolution, which is listed in Table 12. Furthermore, the theoretical momentum distribution is scaled by the inclusive reduction factor R_s, that can be obtained by taking the ratio between the experimental inclusive cross section to the sum of the theoretical single-particle cross sections of the related orbits, and it is written as:

$$R_{\mathrm{incl}} = \frac{\sigma_{(\mathrm{incl,\,exp})}}{\sum \sigma_{(\mathrm{s.p.,\,theo})}} \tag{57}$$

Chapter 5: Simulation

The simulation of the Crystal Ball detector and the interaction of both scattered protons and emitted gamma-rays are essential to analyse the quasi-free scattering reactions $^{20}O(p,2p)^{19}N$. Examining the response of the XB detector is required in order to extract the physical quantities of interest, i.e., the inclusive and exclusive cross section and the spectroscopic factor. The simulation is performed by using R3BRoot and is presented in the first section of this chapter. The following section deals with generating events of interest, i.e., the two outgoing protons and emitted gamma rays. The last section presents the Crystal Ball detector response to the generated events.

5.1 R3BRoot Framework

The interaction of the removed nucleons and gamma-rays with the Crystal Ball detector was simulated by utilizing the R3BRoot software package developed at GSI and based on ROOT, FAIRSoft, and FAIRROOT [56]. The framework performs simulations and analysis of the experimental data by generating events and implementing them in the detectors besides including required functionality such as track and visualization [24, 57]. In this work, the generator of the quasi-free scattering, target, Crystal Ball detector, and SSDs detectors of the R^3B setup are included in the R3BRoot simulation.

5.2 Event Generator

5.2.1 Quasi-Free Scattering Reaction Generator

The generator of the quasi-free scattering events is a modified version based on the Goldhaber model first implemented by L. Chulkov and rewritten in C++ by Valerii Panin [24, 25]. The quasi-free scattering reaction between a projectile-like nucleus with the four-momentum $\mathrm{P} = (\overrightarrow{P}, \omega_\mathrm{p})$ and a target proton $\mathrm{p}_0 = (\overrightarrow{p_0}, \omega_0)$ is described by using the Feynman diagram formalism that is illustrated in Figure 55. The four-momentum conservation is written as:

$$\mathrm{P} + \mathrm{p}_0 = \mathrm{Q} + \mathrm{q}_0 + \mathrm{q}_1 \tag{58}$$

where $\mathrm{Q} = (\overrightarrow{Q}, \mathrm{E}_\mathrm{Q})$ for the daughter nucleus, $\mathrm{q}_0 = (\overrightarrow{q_0}, \mathrm{E}_0)$ for the scattered proton, and $\mathrm{q}_1 = (\overrightarrow{q_1}, \mathrm{E}_1)$ for the knocked-out nucleon [58]. The reaction is broken into two vertices; one describes the separation reaction of the division of the nucleus P into the residual Q, and a virtual intermediate proton with the four-momentum p_e, it is written as $\mathrm{P} \rightarrow \mathrm{Q} + \mathrm{p}_\mathrm{e}$, where $\mathrm{p}_\mathrm{e} = \mathrm{P} - \mathrm{Q} = \mathrm{q}_0 + \mathrm{q}_1 - \mathrm{p}_0$ [25, 58]. The other describes the elastic scattering process and it is written as $\mathrm{p}_0 + \mathrm{p}_\mathrm{e} \rightarrow \mathrm{q}_0 + \mathrm{q}_1$. Furthermore, for the inverse kinematics case in the laboratory frame, the target-like proton is at rest $|\mathrm{p}_0| = 0$ [58].

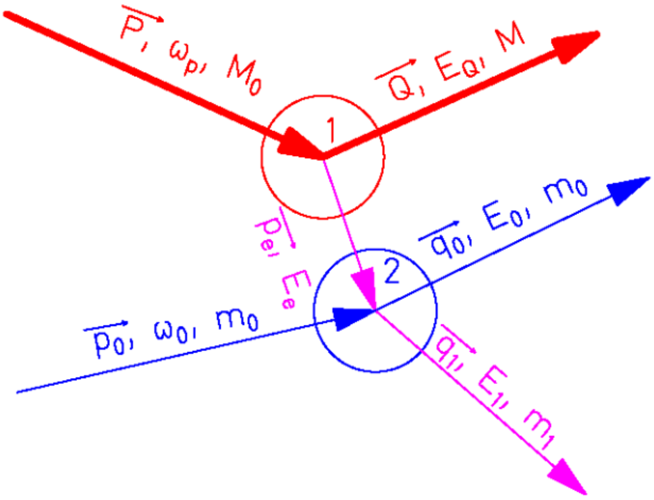

Figure 55: Feynman diagram for the quasi-free scattering in the impulse approximation. It represents the reaction by two vertices; vertex 1 represents the dissociation reaction, while vertex 2 corresponds to the elastic scattering process [59].

To simulate the quasi-free scattering of a specific reaction channel, the experimental beam energy at the center of the target E_0 and the momentum distribution of the outgoing fragment σ_P are required inputs as well as the mass of the incoming isotope, outgoing fragment, and scattered protons. Table 13 shows the experimental inputs for the simulation of the quasi-free scattering.

Table 13: The experimental input to simulate the quasi-free scattering generator for different reaction channels.

Incoming Beam	E_0 (MeV/nucleon)	σ_P (MeV/c)
^{20}O	412.03	109.29
^{19}O	449.31	110.97
^{23}F	395.46	60.47
^{22}F	426.73	114.06
^{21}F	461.77	97.50

Then, the quasi-free scattering output, ASCII file, is written in an appropriate structure for the following step. It provides information about the reaction products such as particle ID, momentum, the start position (vertex), angles, etc. The output of the simulated generator for the quasi-free scattering can be illustrated by Figure 56 that shows the angular correlation of the polar and azimuthal angles of the scattered protons via the quasi-free scattering reaction $^{20}\mathrm{O}(\mathrm{p}, 2\mathrm{p})^{19}\mathrm{N}$. Moreover, Figure 60 shows the opening angle (θ_0) between the scattered proton is around 80° and the difference between the azimuthal angles ($\phi_1 - \phi_2$) of the scattered proton is about 180°, as expected.

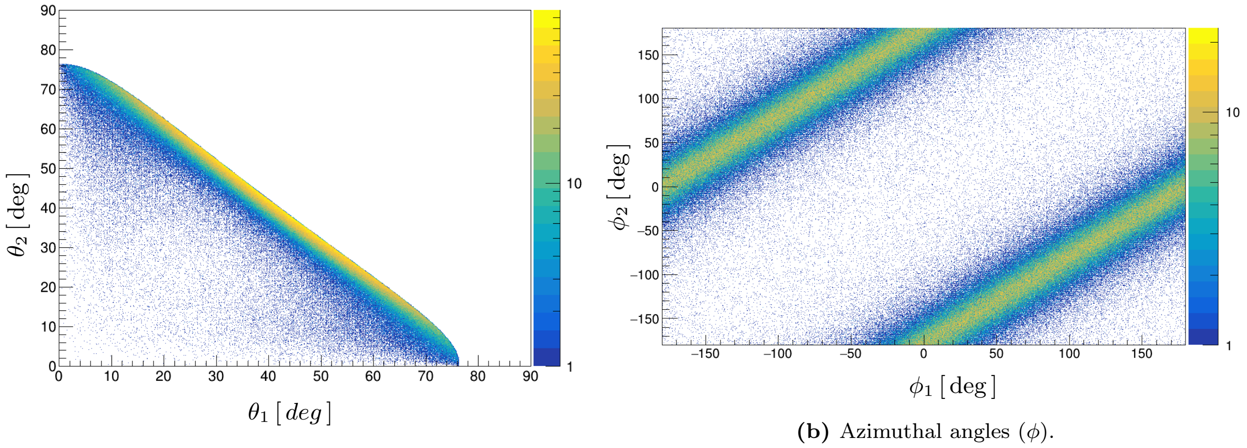

(a) Polar angles (θ).

(b) Azimuthal angles (ϕ).

Figure 56: The simulated correlations of polar (θ) and azimuthal (ϕ) angles of two generated protons from quasi-free scattering $^{20}\mathrm{O(p,2p)}^{19}\mathrm{N}$ in inverse kinematics.

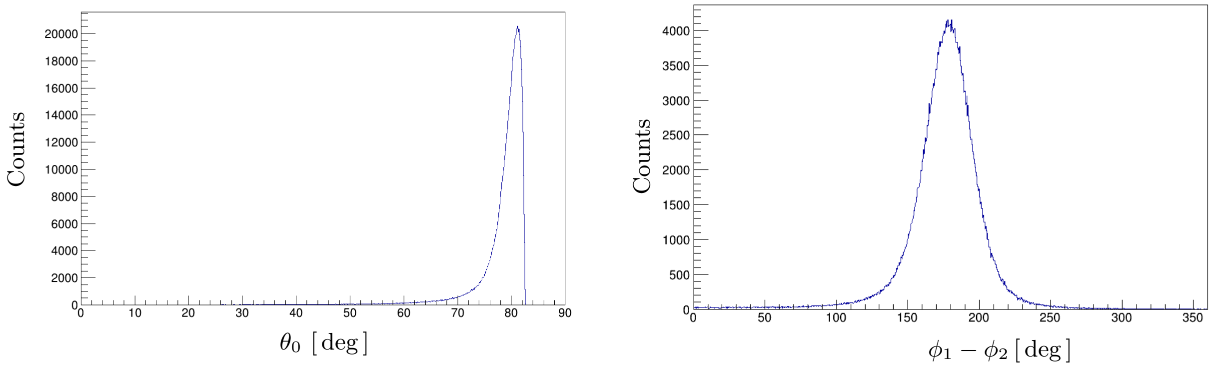

(a) Opening angle distribution.

(b) The distribution of ($\Delta\phi$).

Figure 57: (a) The simulated distribution of the opening angle θ_0 between the two generated protons from quasi-free scattering $^{20}\mathrm{O(p,2p)}^{19}\mathrm{N}$ in inverse kinematics. (b) The simulated distribution of the difference between the azimuthal angles ($\Delta\phi$) of the two scattered protons from quasi-free scattering $^{20}\mathrm{O(p,2p)}^{19}\mathrm{N}$ in inverse kinematics.

For the analysis, the generated events of the output have the Cartesian components of the fragments and scattered protons momentum written to an ASCII file, which is used for the following step to add gamma-rays cascade by using a routine.

5.2.2 Gamma-ray

The generated Lorentz-boosted gamma-rays from the fragments de-excitations were added to the output of the quasi-free scattering. The generated gamma-rays were considered to emit isotropically in the fragment rest frame. However, the analysis of a specific reaction only includes gamma-rays if the transitions correspond to the observed transitions in the experimental gamma-ray spectrum. For the reaction channel of $^{20}\mathrm{O(p,2p)}^{19}\mathrm{N}$, the observed transition from the $3/2^-$ state is a known transition in the literature as illustrated in Figure 49 and Table 14. Only its transition will be added to the output of the quasi-free scattering.

Table 14: The state parties and energies of different excited states for ^{19}N gamma-rays according to [6, 54].

J^{π}	E_{state} [MeV]	E_{γ} [MeV]	
		Direct decay	Cascade
$3/2^-$	1.143 (3)	1.141	-
$5/2^-$	1.676 (3)	1.681	0.532 + 1.141
$3/2^-$, $5/2^+$	2.132 (9)	2.132	-
$1/2^+$	2.511 (5)	2.507	1.3688 + 1.141
$7/2^-$	3.170 (6)	-	2.016 + 1.141
			1.494 + 0.532 + 1.141
$7/2^-$	4.023 (9)	-	2.347 + 1.681

Consequently, Cartesian components of the generated gamma-rays were added in the output ASCII file besides the characteristics of the emitted particles. The generated ASCII file was then used as an input for simulating the quasi-free scattering reaction of $^{20}\mathrm{O(p, 2p)}^{19}\mathrm{N}$ with Lorentz-boosted gamma-rays in the Crystal Ball.

5.3 Crystal Ball Response

The crystal ball detector responses to protons from the QFS reactions and gamma rays from the fragments de-excitations were simulated via the R3Broot. The performed simulation contains the target, the SSDs detectors, and their holding structures beside the Crystal Ball detector. The output file went through several steps to be analysed.
The first step in the analysis is to digitise the output root file of the R3BRoot simulations. The second approach is to broaden the simulated gamma peaks according to the obtained experimental energy resolutions to apply the same experimental conditions for a realistic detector response. The output file is then converted to a root file that matches the experimental files. The final approach of analyzing the output file of the simulation is applying the same addback algorithm and Doppler correction to the simulated data as it is done for the experimental data.

5.3.1 Efficiency of Detecting two Protons in the Crystal Ball

The Crystal Ball efficiency of detecting two scattered protons from the generated events of the QFS over a specific energy threshold for individual crystals is essential to correct the experimental inclusive cross-section as illustrated previously in equation 37. The efficiency is given by the ratio between the number of the simulated events of the two detected protons by the crystal ball $\mathrm{N_{mul=2}}$ and the total number of generated events of the quasi-free scattering $\mathrm{N_{tot}}$, which is 100,000 for this work:

$$\epsilon_{\mathrm{XB,\,2p}} = \frac{\mathrm{N_{mul=2}}}{\mathrm{N_{tot}}} \tag{59}$$

Figure 58 shows the obtained multiplicity of the detected protons by the XB for the simulated $^{20}\mathrm{O(p,2p)}^{19}\mathrm{N}$ reaction. The dominated multiplicity in this figure is equal to two.

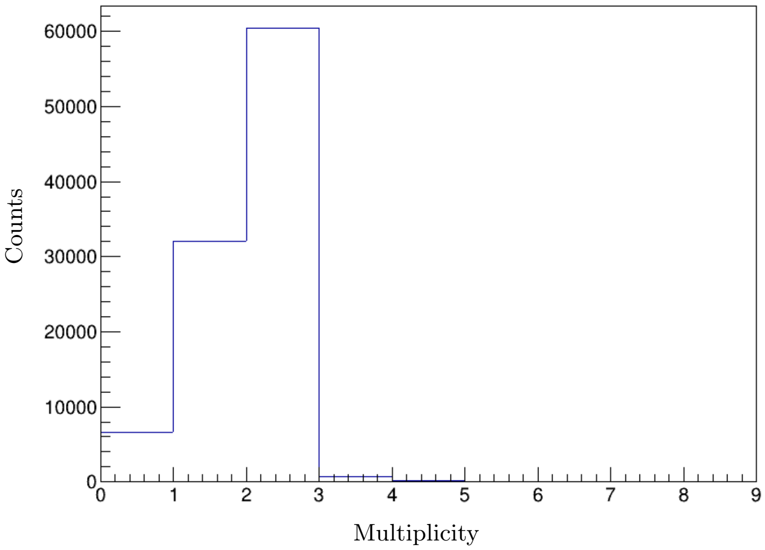

Figure 58: The multiplicity of the detected proton by the Crystal Ball for the simulated $^{20}\mathrm{O(p,2p)}^{19}\mathrm{N}$ reaction.

The results of the Crystal Ball efficiency of detecting the two scattered protons from the generated quasi-free scattering for different reaction channels are shown in Table 15.

Table 15: The efficiency of detecting two protons from the quasi-free scattering $\mathrm{(p,2p)}$ for different reaction channels.

Reaction Channel	Energy (MeV)	$\mathrm{S_p}$ (MeV)	Efficiency (%)
$^{20}\mathrm{O(p,2p)}^{19}\mathrm{N}$	412.03	19.349	60.4
$^{19}\mathrm{O(p,2p)}^{18}\mathrm{N}$	449.31	17.069	62.9
$^{23}\mathrm{F(p,2p)}^{22}\mathrm{O}$	395.46	13.290	58.6
$^{22}\mathrm{F(p,2p)}^{21}\mathrm{O}$	426.73	12.558	61.7
$^{21}\mathrm{F(p,2p)}^{20}\mathrm{O}$	461.77	11.133	63.5

Two factors can explain the increase in the efficiency of detecting two protons by the Crystal Ball. These are the beam energy of the projectile $\mathrm{E_{in}}$ and the binding energy of the removed proton from the projectile $\mathrm{S_p}$. To illustrate the effect of the beam energy on the Crystal Ball efficiency, a simulation of the $^{20}\mathrm{O(p,2p)}^{19}\mathrm{N}$ reaction was performed for various beam energies, as illustrated in Figure 59. It is apparent from this figure that the efficiency increases as the beam energy increase, and this evolution referee to the dependence of the opening angle $\boldsymbol{\theta_0}$ between the scattered protons on the beam energy $\mathrm{E_{in}}$, which can be seen in Figure 60a. The second factor is the proton separation energy in the incoming nucleus that characterizes the internal momentum distributions of the proton , which can be calculated by using [60]:

$$\sigma = \sigma_0 \sqrt{\frac{\mathrm{A_f}\,.\,\mathrm{A_r}}{\mathrm{A_p}}} \tag{60}$$

where $\mathrm{A_p}$ is the projectile mass, $\mathrm{A_f}$ is the fragment mass, $\mathrm{A_r}$ is the residual mass, and σ_0 is a constant related to the binding energy of the proton in the nucleus. This effect is linked to the dependence of the opening angle distribution θ_0 on the separation energy, which can be seen in Figure 60b.

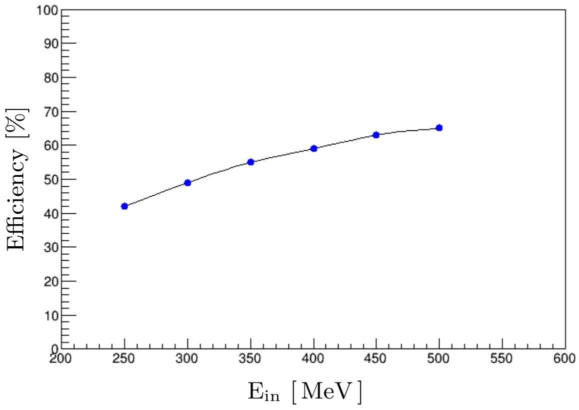

Figure 59: Crystal Ball efficiency of detecting two protons as a function of the beam energy for $^{20}\mathrm{O(p,2p)}^{19}\mathrm{N}$ reaction.

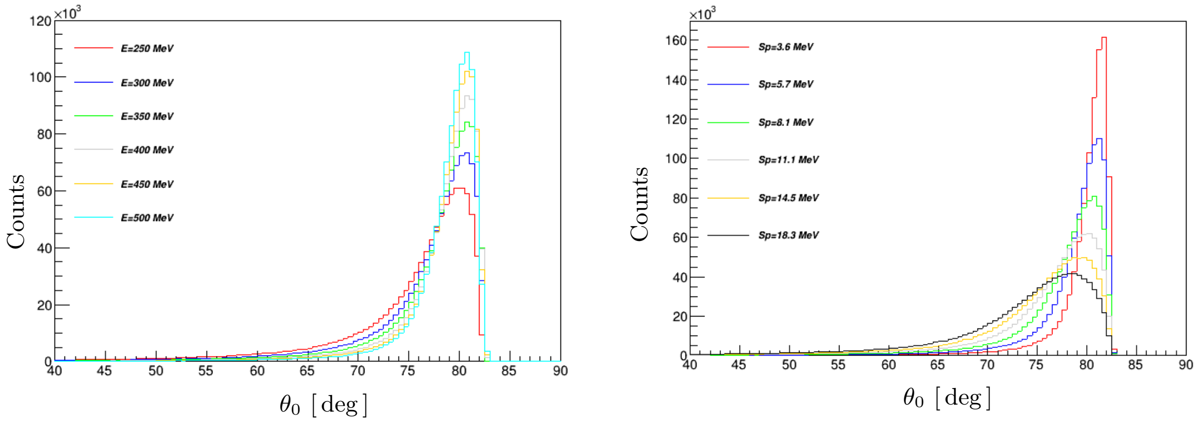

(a) Opening angle distribution.

(b) Opening angle distribution.

Figure 60: (a) The simulated distribution of the opening angle θ_0 between the two generated protons from quasi-free scattering $^{20}\mathrm{O(p,2p)}^{19}\mathrm{N}$ in inverse kinematics for various beam energies. (b) The simulated distribution of the opening angle θ_0 between the two generated protons from quasi-free scattering $^{20}\mathrm{O(p,2p)}^{19}\mathrm{N}$ in inverse kinematics at 400 MeV for various separation energies.

5.3.2 Gamma-Ray of the Fragment Bound States

The Crystal Ball response to the simulated gamma-rays and background from the quasi-free scattering in coincidence with detecting two protons are used to fit the experimental gamma spectrum. This can be illustrated by the fitting results obtained from the Crystal Ball response to the simulated gamma-ray of the considered excited state and the background from the quasi-free scattering for the reaction channel $^{20}\mathrm{O(p,2p)}^{19}\mathrm{N}$ as shown in Figure 61. The fit was done simultaneously for both single spectrum, which is shown in the left side of Figure 61, and sum spectrum, that is shown in the right side of Figure 61. The reduced χ^2 of the total fit function is equal to 1.17. Both spectra display one peak around 1.143 MeV that is produced by the decay of the $3/2^-$ state to the ground state $1/2^-$ as indicated in the level scheme of gamma-rays of the bound state of the daughter nucleus ^{19}N in Figure 49.

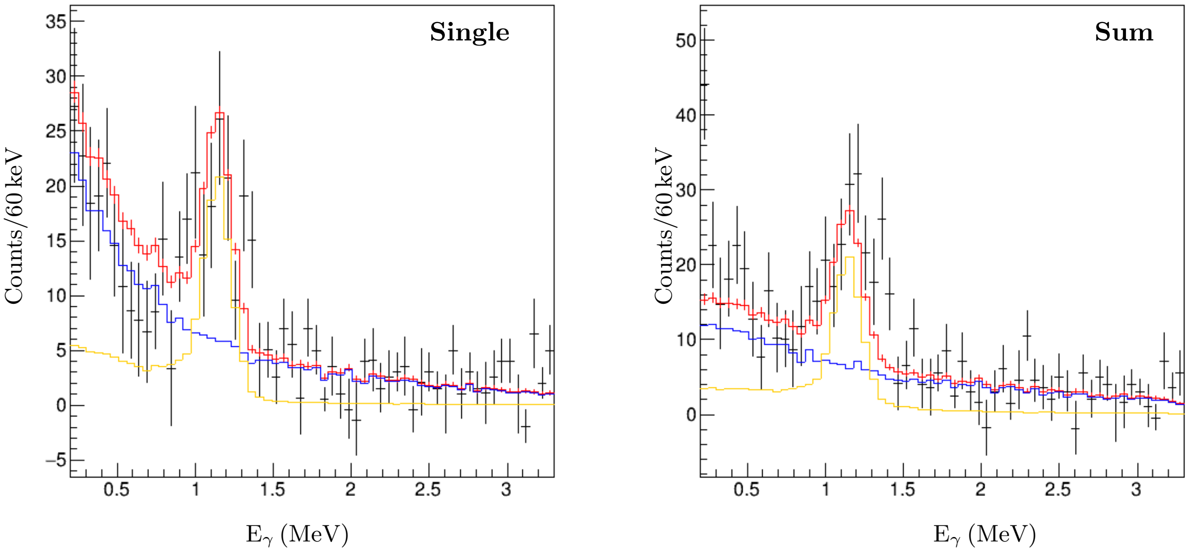

Figure 61: The single and sum of the fitted simulated gamma-ray spectra of the de-excited ^{19}N to the experimental data for the H_2 target. The measurement was done in coincidence with the detection of two protons for both data. The reduced χ^2 of the total fit function is equal to 1.17. The experimental data are indicated by black crosses, total fit in red, simulated first excited state in orange, background in blue.

As explained earlier in section 4.7, the population p_i of the quasi-free scattering reactions for a specific excited state i of the residual $(A-1)$ is essential to calculate the exclusive cross section. It can be given by the ratio between the events of the experimental gamma-ray spectrum $N_{i,exp}$ and the total number of the the measured quasi-free scattering $N_{tot,exp}$:

$$p_i = \frac{N_{i,exp}}{N_{tot,exp}} \tag{61}$$

where:

$$N_{i,exp} = N_{\gamma,fit}\frac{N_{tot,\,sim}}{N_{\gamma,\,sim}} \tag{62}$$

$N_{\gamma,fit}$ is the integral of the excited state i of the fitted gamma-rays spectrum, $N_{tot,\,sim}$ is the total number of simulated quasi-free scattering events for the excited state i, and $N_{\gamma,\,sim}$ the integral of the simulated gamma-rays spectrum. Consequently, the exclusive cross section for each excited state i can be obtained by using equation 43.

The Crystal Ball efficiency of detecting gamma-ray for the considered excited state $3/2^-$ of the de-excited ^{19}N is shown in Table 16.

Table 16: The efficiency of detecting the simulated gamma-ray for the considered excited state of ^{19}N.

J^π	Energy (MeV)	Efficiency (%)
$3/2^-$	1.143	38.38

Chapter 6: Results

This chapter reports the results of analysing the reaction channels of ^{20}O(p, 2p)^{19}N, ^{19}O(p, 2p)^{18}N, ^{23}F(p, 2p)^{22}O, ^{22}F(p, 2p)^{21}O, and ^{21}F(p, 2p)^{20}O.
The obtained information will be presented for each reaction channel, including the mass identification, QFS identification, geometrical acceptance, gamma rays, cross sections, reduction factor, and momentum distributions.

6.1 The Reaction Channel ^{20}O(p, 2p)^{19}N

The even-even $^{20}_{8}O_{12}$ projectile hits the stationary CH$_2$, C, and empty targets with an approximate velocity of 0.72 at the center of the target and its equivalent energy around 412 MeV/nucleon. The filling of the shell model levels is produced as shown in Figure 62. The ground state spin and parity of ^{20}O is 0^+ since all the nucleons are paired. The binding energy of a proton and neutron in the projectile is $S_p = 19.349$ MeV and $S_n = 7.608$ MeV, respectively. The outcome of the QFS reaction is the odd-even $^{19}_{7}N_{12}$ fragment. The binding energy of a proton and neutron in the fragment is $S_p = 16.350$ MeV and $S_n = 5.328$ MeV, respectively. The spin and parity of the residual fragment depends on the orbit of the removed proton. If the proton is removed from the $\pi 1p_{1/2}$ orbit as illustrated in the left side of Figure 62, the ^{19}N residual is expected to be in the

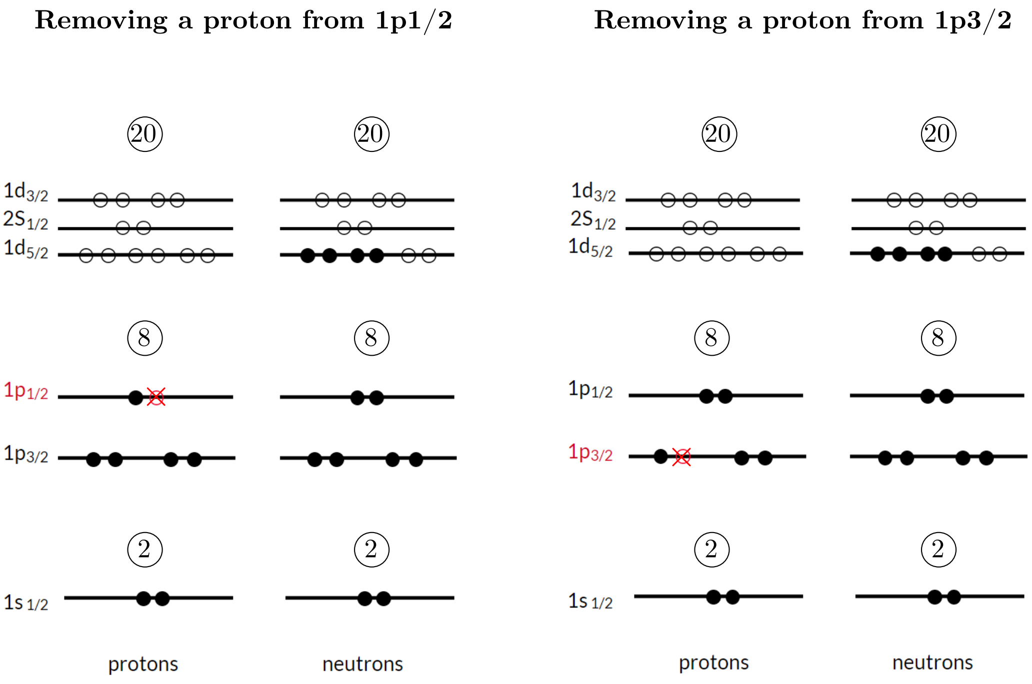

Figure 62: The shell structure of the even-even nucleus $^{20}_{8}O_{12}$ in the Independent Particle Model (IPM). The red circle indicates the removed proton in $^{20}_{8}O_{12}$. The outcome of this reaction is $^{19}_{7}N_{12}$ in its ground state if the proton was removed from $\pi 1p_{1/2}$ orbit in the left side, or a low-lying excited state if the proton was removed from $\pi 1p_{3/2}$ orbit in the right side.

ground state with a spin and parity of $1/2^-$. Another considered possibility is removing a proton from the $\pi 1p_{3/2}$ orbit as illustrated in the right side of Figure 62 and the fragment will be excited with a spin and parity of $3/2^-$. However, in the current study, the possibility of removing a proton from the $\pi 1s_{1/2}$ level is not considered since it leads to unbound ^{19}N fragment.

6.1.1 Mass Identification

The mass distribution of the reacted ^{20}O beam with the CH_2, C, and empty target after gating on the $z - 1 = 7$ are shown in Figure 63; the Crystal Ball Sum trigger Tpat&8 $==$ 8 was applied in addition to detecting two protons in the Crystal Ball For the selection of reacted beam. The nitrogen fragment with the mass of interest A=19 is the first peak on the right. The other nitrogen isotopes with a mass of 18, 17, etc. are caused by losing additional neutrons during the reaction. The number of tracked events A=19 is obtained by taking the integral under its fitted peak. Therefore, another cut will be applied on the mass of the outgoing fragment for further analysis. The neutron separation energy has a significant impact on the statistics of ^{19}N. The neutron separation energy is higher than the energies of the excited states of ^{19}N, as shown in Figure 49, leading to ^{19}N peak with high statistics.

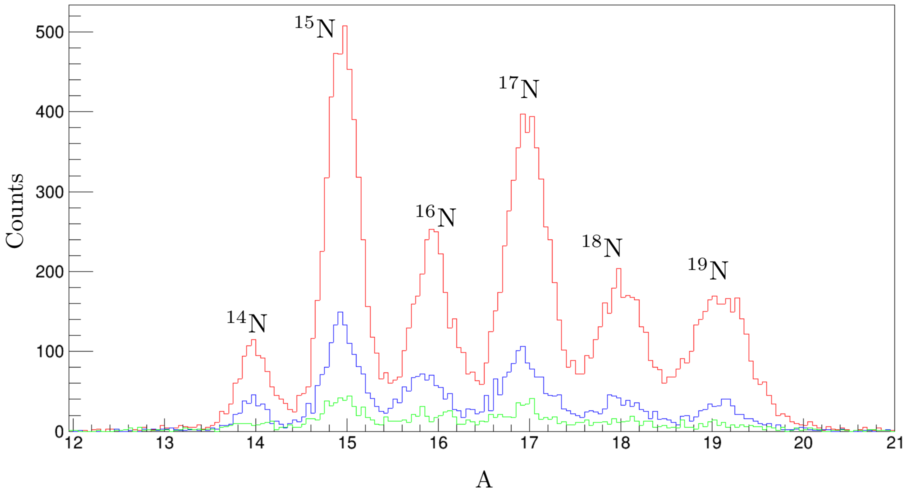

Figure 63: Mass identification of the outgoing nuclei produced by the reacted beam ^{20}O. ^{19}N is the outgoing particle of interest since it is caused by the quasi-free scattering off ^{20}O. This plot is drawn for setting 3, for all targets with the trigger of the Crystal Ball Sum Tpat&8 $==$ 8. The reaction with the CH_2 target is indicated in red, C in blue, empty target in green.

6.1.2 Angular Correlations

The measured polar and azimuthal angles of the two scattered protons in the $^{20}\mathrm{O(p, 2p)}^{19}\mathrm{N}$ reaction in coincidence with ^{19}N show a strong correlation as illustrated in Figure 46a and Figure 46b for CH_2 target and Figure 46c and Figure 46d for C target. A cut of Crystal Ball Sum trigger Tpat&8 $==$ 8 and proton multiplicity of 2 was applied. For a realistic angular distribution, the angles are randomized within the area of the corresponding crystal. The distribution of the opening angle θ_0 between the scattered protons in coincidence with ^{19}N is approximately 80° as shown in Figure 47a. Furthermore, the distributions of the difference between the azimuthal angles ($\Delta\phi$) of the two scattered protons from the $^{20}\mathrm{O(p,2p)}^{19}\mathrm{N}$ in coincidence with ^{19}N is around 180° as shown in Figure 47b . For both distributions, the red curve indicates the distribution for CH_2 target, and the blue curve indicates the distribution for the C target. Also, a cut of Crystal Ball Sum trigger Tpat&8 == 8 and proton multiplicity of 2 was applied.

6.1.3 Gamma-Rays

The observed single peak at 1.143 MeV in the single and sum of the fitted simulated gamma-ray spectra of the de-excited ^{19}N residual fragment to the experimental data for the H_2 target in Figure 61 show a direct decay from the $3/2^-$ state to the ground state $1/2^-$ as illustrated in level scheme of ^{19}N in Figure 49. The ground state and the first excited state in the daughter nuclei ^{19}N ($1/2^-$ g.s., $3/2^-$) are caused by the coupling between the proton hole in $\pi 1\mathrm{p}_{1/2}$ orbit as shown in the left side of Figure 62 to the (0^+ g.s., 2^+) states of the ^{20}O core, respectively [54].

The population $\mathrm{p_i}$ of the observed excited state $3/2^-$ in Figure 61 is shown in Table 17. It can be calculated by using equation 61.

Table 17: The population of the considered excited state of the de-excited ^{19}N residual fragment.

J^π	E_{state} (MeV)	$\mathrm{p_i}$ (%)
$3/2^-$	1.143 (3)	44 ± 4

6.1.4 Cross Sections

As previously stated, the experimental inclusive cross section of the reconstructed H target can be obtained by using equation 37 and its statistical uncertainty by equation 39. Consequently, the exclusive experimental cross section for the excited state $3/2^-$ can be obtained by using equation 43, and that leads to the exclusive experimental cross section of the ground state $1/2^-$, which can be calculated by utilizing equation 44 while its statistical uncertainty can be calculated by equation 45. The measured cross sections of the quasi-free scattering for all considered states of ^{19}N with the statistical uncertainty are shown in Table 18.

Table 18: The experimental inclusive and exclusive cross sections for the quasi-free scattering of the $^{20}\mathrm{O(p,2p)}^{19}\mathrm{N}$ reaction channel for the reconstructed H target.

Inclusive cross section	Exclusive cross section		
σ_H (mb)	J^π	E_{state} (MeV)	σ_H (mb)
12.6 (4)	$3/2^-$	1.143 (3)	5.5 (5)
	$1/2^-$	0	12.6 (4) − 5.5 (5) = 7.1 (6)

6.1.5 Spectroscopic and Reduction Factor

The inclusive reduction factor can be obtained by taking the ratio between the experimental inclusive cross section to the DWIA calculations based on eikonal theory [27]. The calculations were performed by C. Bertulani. The $\pi 1\mathrm{p}_{1/2}$ orbit is considered by the theory to be fully occupied by $2\mathrm{j}+1=2$ protons and its full cross section is supposed to equal $2 \times \sigma_{\mathrm{s.p}}$. In the same manner, the $\pi 1\mathrm{p}_{3/2}$ orbit is considered to be fully occupied by $2\mathrm{j}+1=4$ protons and its full cross section is equal to $4 \times \sigma_{\mathrm{s.p}}$ as shown in Table 19. However, the reaction channel $^{20}\mathrm{O(p,2p)}^{19}\mathrm{N}$ is a complicated case because there is some $\pi 1\mathrm{p}_{3/2}$ strength surviving in the bound daughter nucleus but not all of it. Therefore, the inclusive cross section can not divide by the sum of the theoretical full cross sections of the related orbits $\pi 1\mathrm{p}_{1/2}$ and $\pi 1\mathrm{p}_{3/2}$. As a result, the inclusive reduction factor is not presented for this reaction channel.

Table 19: The theoretical cross section and SF of the reaction channel $^{20}\mathrm{O(p,2p)}^{19}\mathrm{N}$.

Orbit	$\sigma_{s.p}$ (mb)	$\mathrm{C}^2\mathrm{S}$	$\sigma_{\mathrm{full\,state}}$ (mb)
$\pi 1\mathrm{p}_{1/2}$	4.649	2	9.298
$\pi 1\mathrm{p}_{3/2}$	4.792	4	19.17

6.2 The Reaction Channel $^{19}\mathrm{O(p,2p)}^{18}\mathrm{N}$

The even-odd $^{19}_{8}\mathrm{O}_{11}$ projectile hits the stationary CH_2, C, and empty targets with an approximate velocity of 0.74 at the center of the target and its equivalent energy around 449 MeV/nucleon. The filling of the shell model levels is produced as shown in Figure 64. Its ground state spin and parity is $5/2^+$ since it is determined by the unpaired neutron in the orbit $\pi 1\mathrm{d}_{5/2}$. The binding energy of a proton and neutron in the projectile is $\mathrm{S_p} = 17.069$ MeV and $\mathrm{S_n} = 3.956$ MeV, respectively.

The outcome of the QFS reaction is the odd-odd $^{18}_{7}\mathrm{N}_{11}$ fragment. The binding energy of a proton and neutron in the fragment is $\mathrm{S_p} = 15.208$ MeV and $\mathrm{S_n} = 2.828$ MeV, respectively. The $^{18}\mathrm{N}$ remains in its ground state after removing a proton from the $\pi 1\mathrm{p}_{1/2}$ orbit as illustrated in the left side of Figure 64. The ground state has been measured as 1^- and it is determined by the the coupling between the proton hole in the $\pi 1\mathrm{p}_{1/2}$ and the unpaired neutron in the sd shell. However, the sd neutron configurations produce six states with negative parities; 0^- (one state), 1^- (two states), 2^- (two states), 3^- (one state). For illustration, the configuration of $(\pi 1\mathrm{p}_{1/2})^{-1}\,(\nu 1\mathrm{d}_{5/2})^3$ produces spin and parity of (2^-, 3^-), $(\pi 1\mathrm{p}_{1/2})^{-1}\,(\nu 1\mathrm{d}_{5/2})^2\,(\nu 2s_{1/2})^1$ configuration produces (0^-, 1^-), and $(\pi 1\mathrm{p}_{1/2})^{-1}\,(\nu 1\mathrm{d}_{5/2})^2\,(\nu 1d_{3/2})^1$ configuration produces (1^-, 2^-). Also, it is possible to remove a proton from the $\pi 1\mathrm{p}_{3/2}$ orbit as illustrated in the right side of Figure 64 and the fragment is considered to be excited with negative parities.

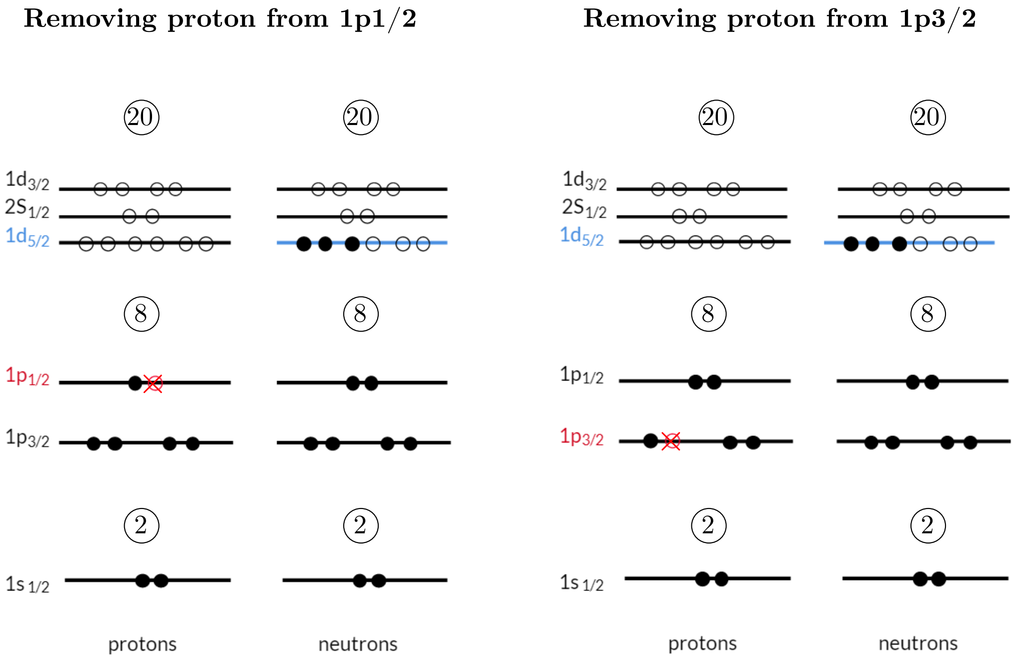

Figure 64: The shell structure of the even-odd $^{19}_{8}O_{11}$ nucleus in the Independent Particle Model (IPM). The red circle indicates the removed proton in $^{19}_{8}O_{11}$. The outcome of this reaction is $^{18}_{7}N_{11}$ in its ground state if the proton was removed from $\pi 1p_{1/2}$ orbit in the left, or a low-lying excited state if the proton was removed from $\pi 1p_{3/2}$ orbit in the right.

6.2.1 Mass Identification

The mass distribution of the reacted ^{19}O beam with the CH$_2$, C, and empty target after gating on the $z - 1 = 7$ is shown in Figure 65; the Crystal Ball Sum trigger Tpat&8 == 8 was applied. The nitrogen fragment with the mass of interest A=18 is the first peak on the right. The other nitrogen isotopes with a mass of 17, 16, etc. are caused by losing additional neutrons during the reaction. The events of interest A = 18 is obtained by taking the integral under its fitted peak. The neutron separation energy affects the ^{18}N peak because the neutron separation energy is close to the energies of the excited states of the de-excited ^{18}N residual fragment, as shown in Figure 71.

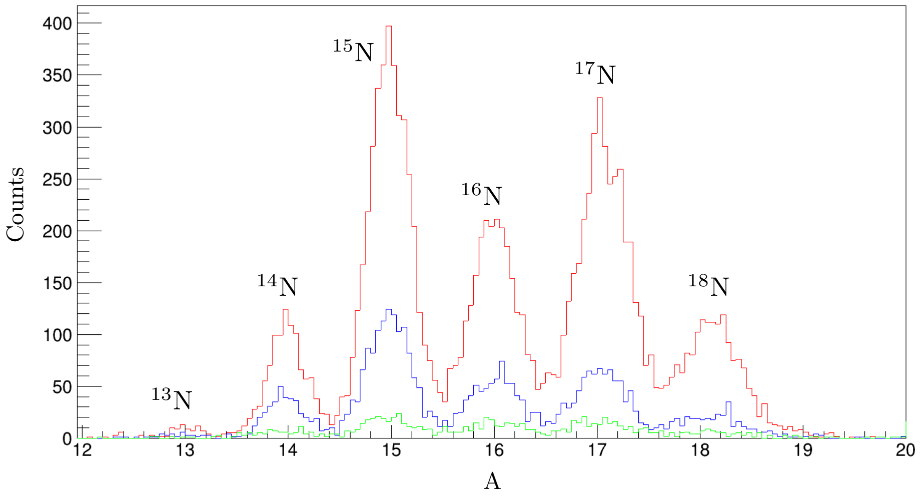

Figure 65: Mass identification of the outgoing nuclei produced by the reacted beam ^{19}O. ^{18}N is the outgoing particle of interest since it is caused by the quasi-free scattering off ^{19}O. This plot is drawn for setting 3, for all targets with the trigger of the Crystal Ball Sum Tpat&8 == 8. The reaction with the CH_2 target is indicated in red, C in blue, empty target in green.

6.2.2 Proton multiplicity

The dominated multiplicity of detecting the scattered protons by the Crystal Ball is equal to two, which characterizes the quasi-free scattering off ^{19}O as shown in Figure 66 for the reconstructed H target. The protons were detected in coincidence with the fragment of interest ^{18}N.

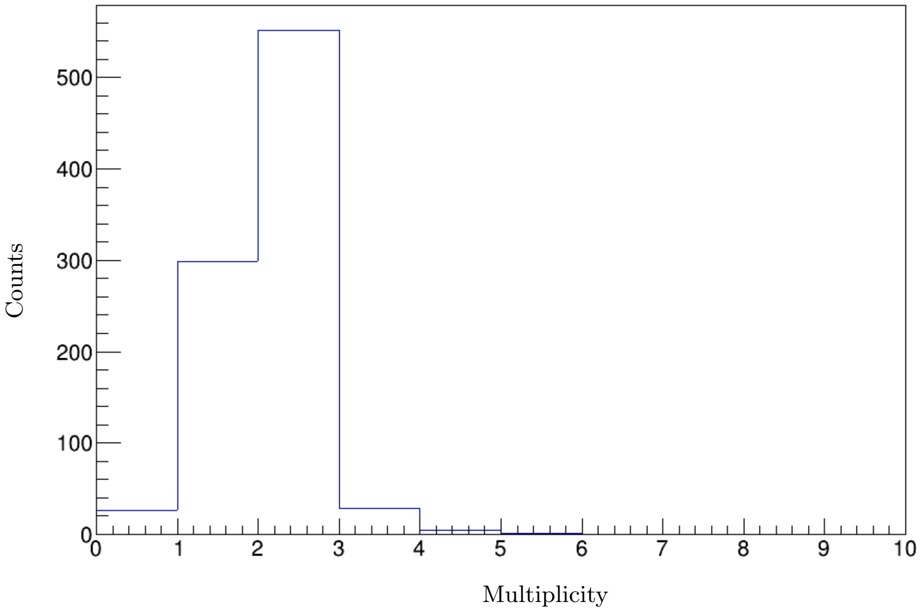

Figure 66: Proton multiplicity (proton clusters) in the Crystal Ball for the reconstructed H target of setting 3. The protons were detected in coincidence with detecting ^{18}N and the trigger of the Crystal Ball Sum Tpat&8 == 8 was applied.

6.2.3 Angular Correlations

As expected the measured polar and azimuthal angles of the two scattered protons in the quasi-free scattering reaction $^{19}\mathrm{O}(\mathrm{p},2\mathrm{p})^{18}\mathrm{N}$ in coincidence with $^{18}\mathrm{N}$ exhibits a correlation between them as illustrated in Figure 67a and Figure 67b for CH_2 target and Figure 67c and Figure 67d for C target. The angles are randomized and a cut of Crystal Ball Sum trigger Tpat&8 == 8 and proton multiplicity of 2 was applied.

Moreover, the distribution of the opening angle θ_0 between the two produced protons from quasi-free scattering $^{19}\mathrm{O}(\mathrm{p},2\mathrm{p})^{18}\mathrm{N}$ in coincidence with $^{18}\mathrm{N}$ is about 80° as presented in Figure 68a. The distributions of the difference between the azimuthal angles ($\Delta\phi$) of the two scattered protons in coincidence with $^{18}\mathrm{N}$ is approximately 180°, as shown in Figure 68b . For both figures, a cut of Crystal Ball Sum trigger Tpat&8 == 8 and proton multiplicity of 2 was applied. Also, the red curve shows the distribution for CH_2 target, and the blue curve shows the distribution for the C target.

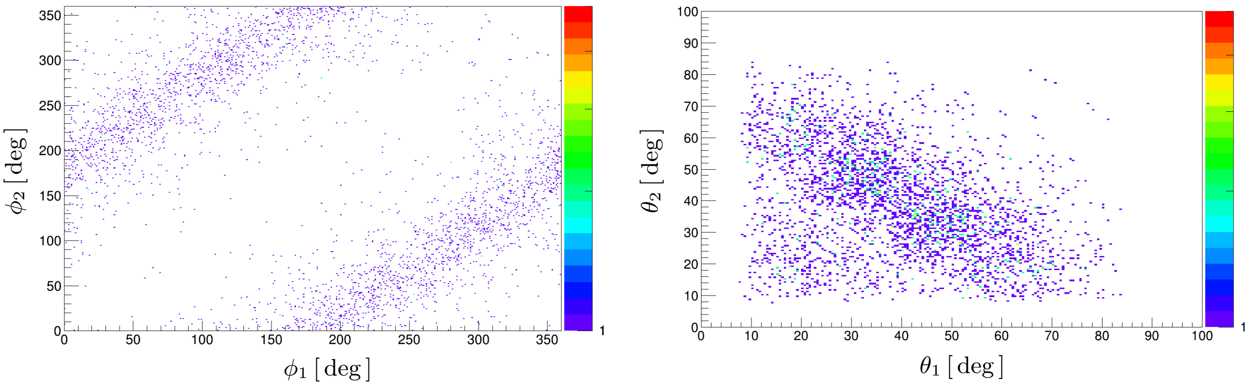

(a) The azimuthal angular correlation, CH_2 target

(b) The polar angular correlation, CH_2 target

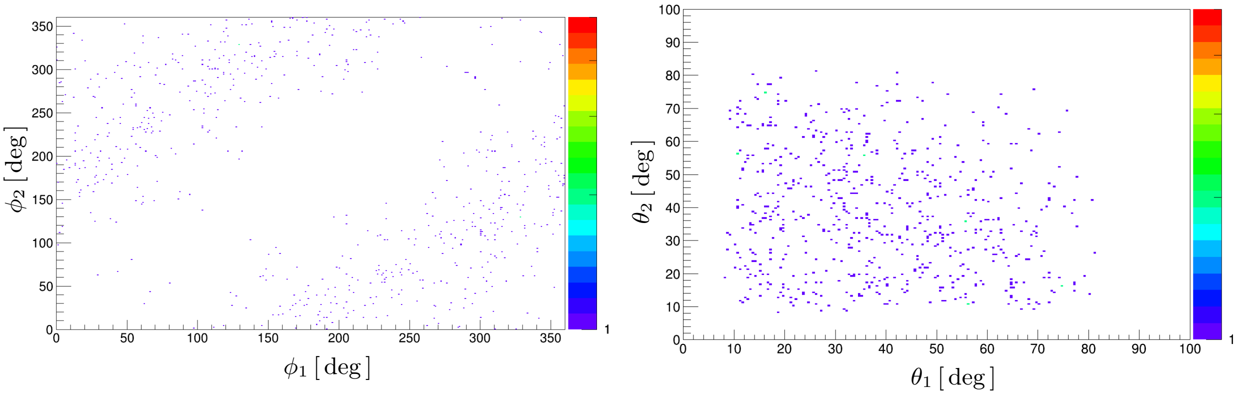

(c) The azimuthal angular correlation, C target

(d) The polar angular correlation, C target

Figure 67: The angular correlation of the scattered protons from the QFS in coincidence with $^{18}\mathrm{N}$ for the CH_2 and C target of setting 3. A cut of Crystal Ball Sum trigger Tpat&8 == 8 and proton multiplicity of 2 was applied.

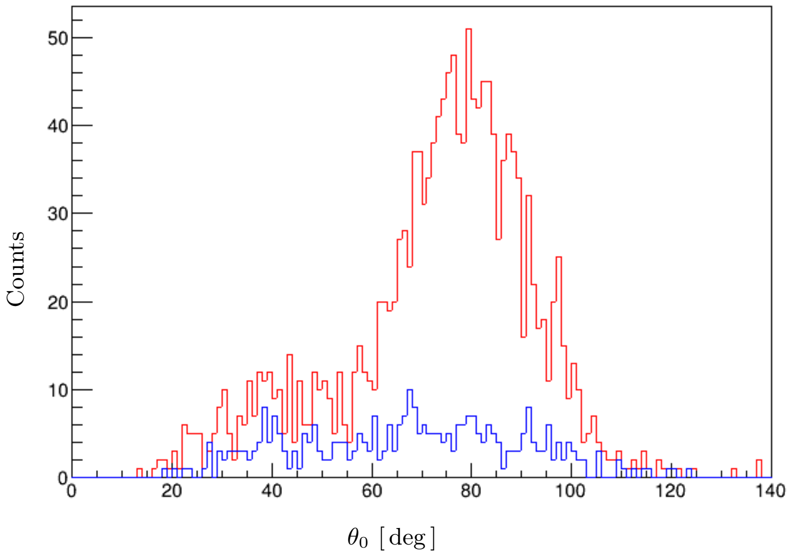

(a) Opening angle distribution.

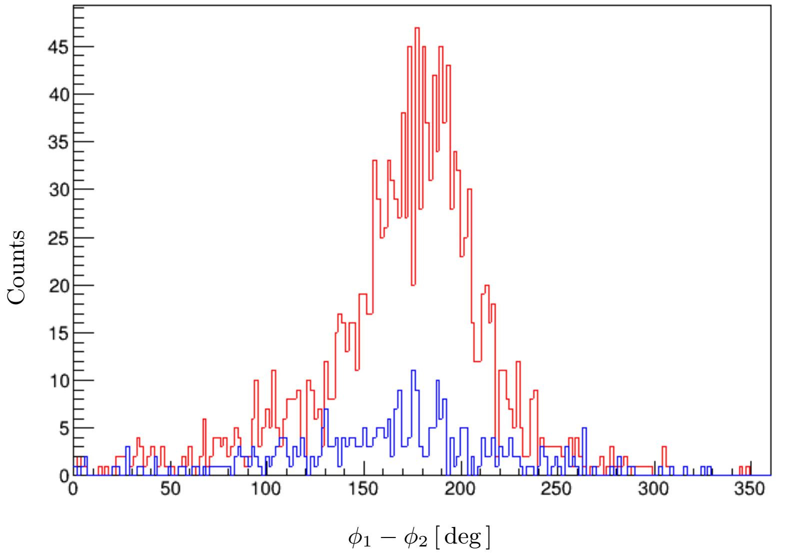

(b) The distribution of $\Delta\phi$.

Figure 68: (a) The distribution of the opening angle (θ_0) between the two protons from QFS in coincidence with ^{18}N for CH_2, the red curve, and C target, the blue curve, of setting 3. A cut of Crystal Ball Sum trigger Tpat&8 == 8 and proton multiplicity of 2 was applied. (b) The distributions of the difference between the azimuthal angles ($\Delta\phi$) of the two scattered protons from quasi-free scattering $^{19}\mathrm{O}(\mathrm{p}, 2\mathrm{p})^{18}\mathrm{N}$ in coincidence with ^{18}N for CH_2 target (red curve) and C target (blue curve) of setting 3. A cut of Crystal Ball Sum trigger Tpat&8 == 8 and proton multiplicity of 2 was applied.

6.2.4 Geometrical Acceptance

The acceptance of the particles involved in the $^{19}\mathrm{O}(\mathrm{p}, 2\mathrm{p})^{18}\mathrm{N}$ reaction channel for the CH_2 target was checked for the SSD02 detector, CH_2 target, and the TFW detector as illustrated in Figure 69. It is apparent from these figures that all the passing particles of interest are covered.

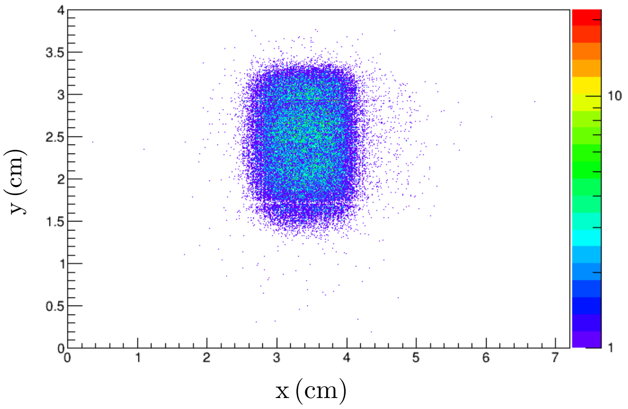

(a) ^{19}O hits at the SSD02 detector.

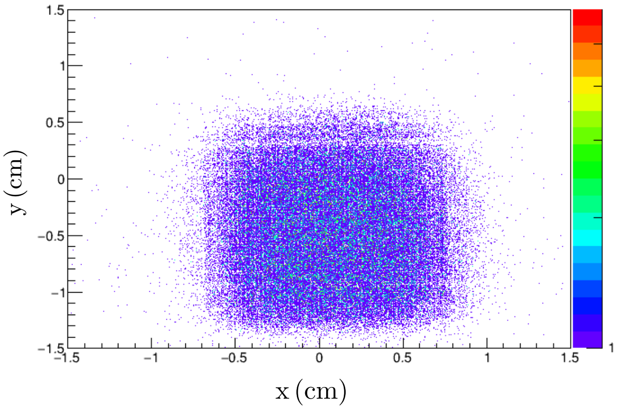

(b) ^{19}O hits at the CH$_2$ target.

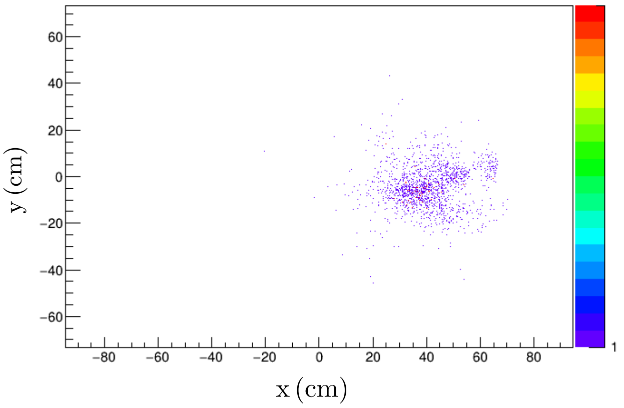

(c) ^{18}N hits at the TFW detector.

Figure 69: The geometrical acceptance of the SSD02 detector with an active area of $7.2 \times 4.0\,\text{cm}^2$, target with an area of 3×3 cm^2, and TFW detector with an active area of 189×147 cm^2 for the $^{19}\text{O(p, 2p)}^{18}\text{N}$ reaction.

6.2.5 Gamma-Rays

The experimental single and sum gamma spectrum of the daughter nucleus ^{18}N are presented with black crosses in Figure 70. Both spectrum show two peaks around 0.627 MeV and 0.473 MeV. They are produced by the decay of the 3^- state at 0.742 MeV to the ground state as indicated in the level scheme of gamma-rays of the bound state of the daughter nucleus ^{18}N in Figure 71. This result can be explained by examining the first three excited states in Figure 71. These states are produced by the coupling between the proton in $\pi 1p_{1/2}$ orbit with the ground state and low-lying states in the isotone ^{17}C ($3/2^+$ g.s., $1/2^+$, $5/2^+$). Thus, the configuration ^{17}C($3/2^+$ g.s.)$\otimes\pi 1p_{1/2}$ produces ($2_2{}^-$, $1_1{}^-$) states in ^{18}N, while the configuration ^{17}C($5/2^+$)$\otimes\pi 1p_{1/2}$ produces ($3_1{}^-$, $2_1{}^-$) states in ^{18}N [61].

Therefore, the decay of the observed state and the background were then added to the simulated QFS to obtain the fitted experimental gamma spectrum as shown in Figure 70. They were fitted simultaneously. The reduced χ^2 of the total fit function is equal to 1.41. The obtained population p_i of the quasi-free scattering reactions for the considered excited state of gamma spectrum of the residual ^{18}N is listed in Table 20.

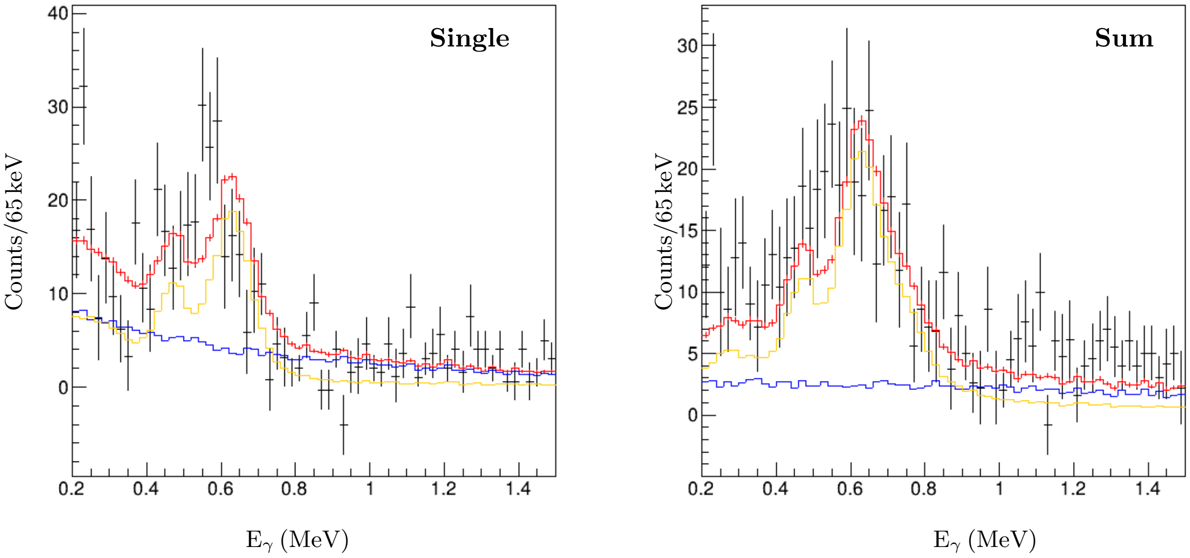

Figure 70: The single and sum of the fitted simulated gamma-ray spectra of the de-excited ^{18}N to the experimental data for the reconstructed H_2 target. The measurement was done in coincidence with the detection of two protons for both data. The reduced χ^2 of the total fit function is equal to 1.41. The experimental data are indicated by black crosses, total fit in red, simulated excited state 3^- in orange, background in blue.

Table 20: The population of the considered excited state of the de-excited ^{18}N residual fragment and the efficiency of detecting the simulated gamma-ray.

J^π	E_{state} (MeV)	Efficiency (%)	p_i (%)
3^-	0.742	53.67	58 ± 4

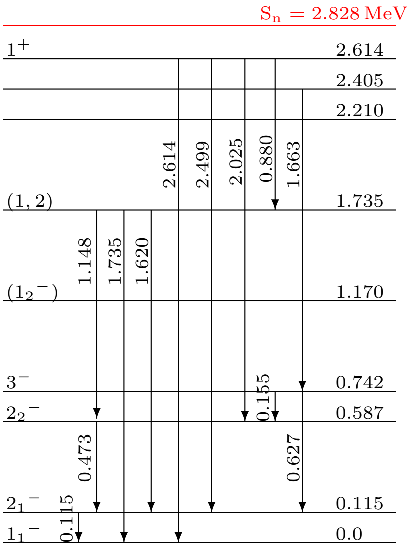

Figure 71: Level scheme of ^{18}N according to [6, 61, 62]. The energy in MeV is given along with each transition arrow.

6.2.6 Cross Sections

The experimental inclusive cross section of the reconstructed H target and its statistical uncertainty were calculated by using equation 37 and 39, respectively. The exclusive experimental cross section for the excited state 3^- was obtained by using equation 43, accordingly, the exclusive experimental cross section of the ground state 1^- and its statistical uncertainty were obtained by using equation 44 and 45, respectively. The cross sections of the quasi-free scattering for all considered states of ^{18}N are shown in Table 21.

Table 21: The experimental inclusive and exclusive cross sections for the quasi-free scattering of the $^{19}\mathrm{O(p,2p)}^{18}\mathrm{N}$ reaction channel for the reconstructed H target.

Inclusive cross section		Exclusive cross section	
σ_H (mb)	J^π	$\mathrm{E_{state}}$ (MeV)	σ_H (mb)
6.5 (3)	3^-	0.742	3.8 (3)
	1^-	0	6.5 (3) − 3.8 (3) = 2.7 (4)

6.2.7 Spectroscopic and Reduction Factor

As previously stated, the $\pi 1\mathrm{p}_{1/2}$ orbit is considered to be fully occupied by $2\mathrm{j}+1=2$ protons and its full cross section is supposed to equal $2\times\sigma_{\mathrm{s.p}}$. In the same way, the $\pi 1\mathrm{p}_{3/2}$ orbit is considered to be fully occupied by $2\mathrm{j} + 1 = 4$ protons and its full cross section is equal to $4 \times \sigma_{\mathrm{s.p}}$ as shown in Table 22. For this reaction channel, it is unlikely that any of the $\pi 1\mathrm{p}_{3/2}$ strength survives in the daughter fragment, as this would lead to unbound state. Therefore, the inclusive reduction factor was obtained by taking the ratio between the inclusive cross section and the full cross section of the $\pi 1\mathrm{p}_{1/2}$ orbit, and it is equal to 0.61(5).

Table 22: The theoretical cross section and SF of the reaction channel $^{19}\mathrm{O(p, 2p)}^{18}\mathrm{N}$.

Level	$\sigma_{\mathrm{s.p}}$ (mb)	$\mathrm{C^2S}$	$\sigma_{\mathrm{full\,state}}$ (mb)
$\pi 1\mathrm{p}_{1/2}$	5.305	2	10.61
$\pi 1\mathrm{p}_{3/2}$	5.471	4	21.88

6.2.8 Momentum Distributions

As indicated previously, measuring the remaining fragment's momentum distribution can deduce the momentum of the removed nucleon and, consequently, its orbit while in the nucleus. Comparison of the width of the momentum distributions of the unreacted beam illustrated in Table 23 with the obtained momentum distributions of the reacted beam in Figure 72 indicates that the nucleon's internal momentum causes broadening of the width of the distribution.

However, the orbit of the removed proton for the $^{19}\mathrm{O(p, 2p)}^{18}\mathrm{N}$ channel was determined by a comparison between the experimental and theoretical momentum distribution of the residual $^{18}\mathrm{N}$. Figure 73 shows a comparative analysis where the experimental momentum distributions for the residual fragment $^{18}\mathrm{N}$ in coincidence with the detection of two protons in the Crystal Ball is compared to theoretical momentum distribution for the $\pi 1\mathrm{p}_{1/2}$ orbit. The theoretical momentum distribution was scaled by the inclusive reduction factor. The comparison shows an agreement between experimental momentum distribution and theoretical one.

Table 23: The momentum resolution of the unreacted $^{19}\mathrm{O}$ beam for $\mathrm{CH_2}$ and C target of setting 3. It is obtained from the Gaussian fit of the momentum distribution.

Target	σ_{p} (MeV/c)	$\sigma_{\mathrm{str,\,p}}$ (MeV/c)
$\mathrm{CH_2}$	$\sigma_{\mathrm{p_x}} = 32.9 \pm 0.1$	$\sigma_{\mathrm{str,\,p_x}} = 15.2 \pm 0.1$
	$\sigma_{\mathrm{p_y}} = 36.4 \pm 0.1$	$\sigma_{\mathrm{str,\,p_y}} = 15.4 \pm 0.2$
C	$\sigma_{\mathrm{p_x}} = 34.0 \pm 0.2$	$\sigma_{\mathrm{str,\,p_x}} = 17.4 \pm 0.2$
	$\sigma_{\mathrm{p_y}} = 37.4 \pm 0.2$	$\sigma_{\mathrm{str,\,p_y}} = 17.6 \pm 0.3$
MT	$\sigma_{\mathrm{p_x}} = 29.2 \pm 0.1$	
	$\sigma_{\mathrm{p_y}} = 33.0 \pm 0.2$	

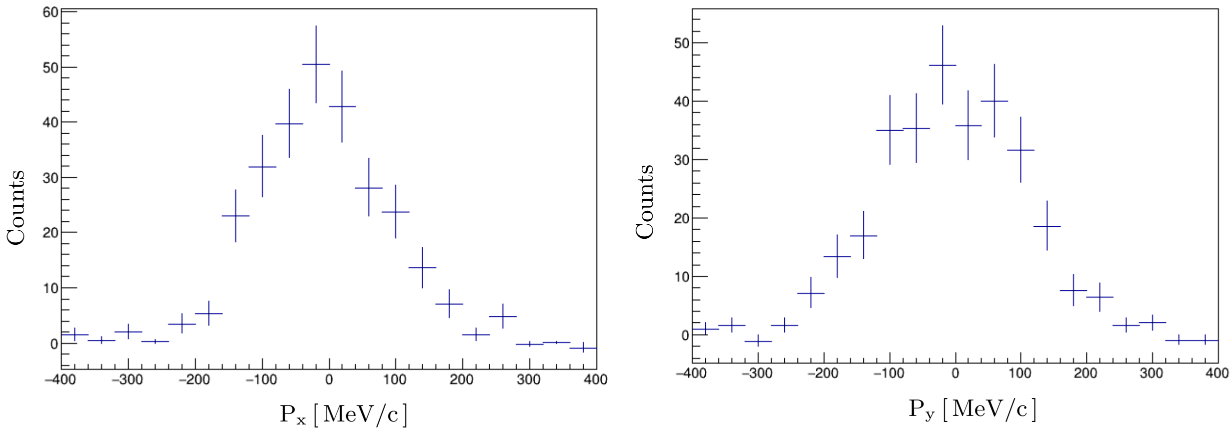

(a) The x-component of the transverse momentum

(b) The y-component of the transverse momentum

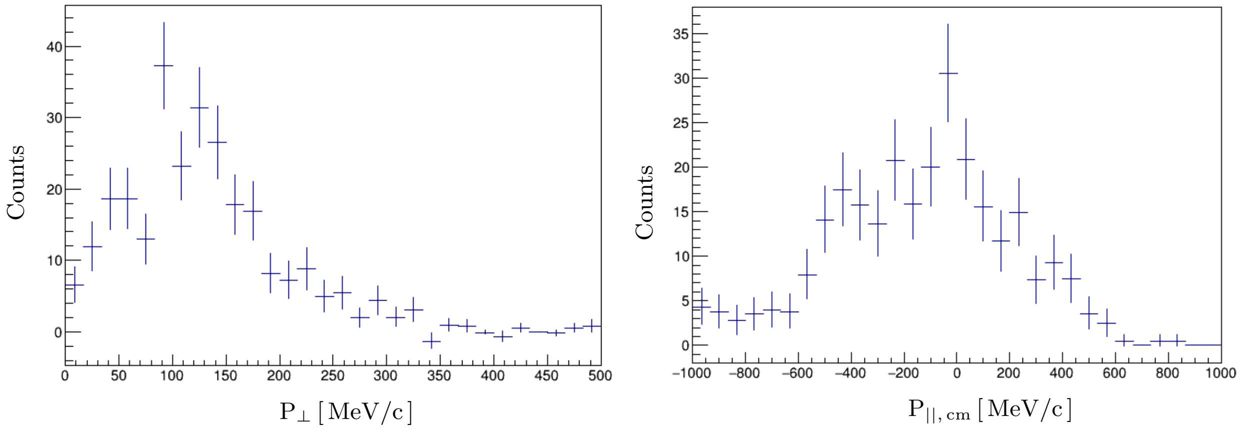

(c) The transverse momentum

(d) The longitudinal momentum

Figure 72: The momentum distributions of the reacted ^{19}O beam for the reconstructed H target. A cut of Crystal Ball trigger Tpat&8 == 8, and a multiplicity of two protons in coincidence with the fragment of interest ^{18}N was applied.

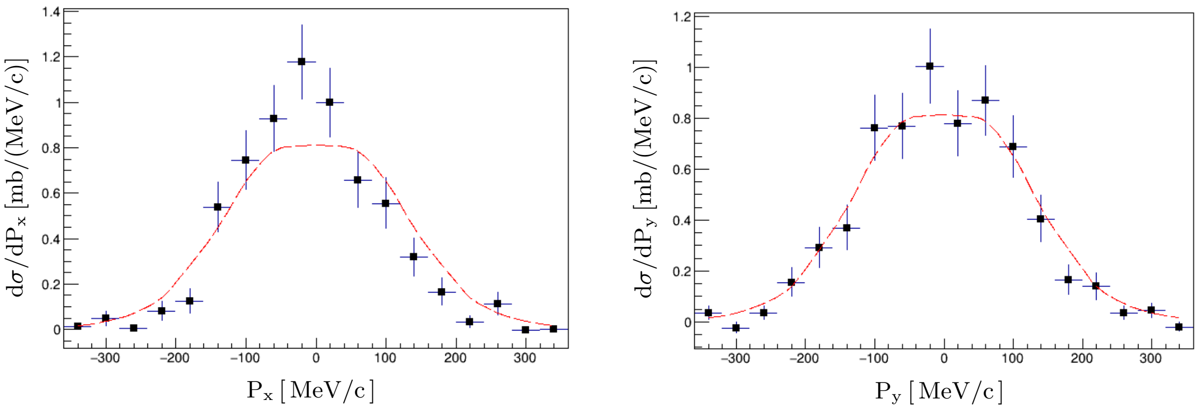

(a) P_x component of the transverse momentum

(b) P_y component of the transverse momentum

Figure 73: The comparison between the experimental and theoretical distributions of the transverse momentum components of the removed proton from the projectile nuclei ^{19}O. The experimental data for the reconstructed H target denoted by the black points and the theoretical one for the $\pi 1p_{1/2}$ orbit is indicated in red.

6.3 The Reaction Channel $^{23}\mathrm{F}(\mathrm{p},2\mathrm{p})^{22}\mathrm{O}$

The odd-even $^{23}_{9}\mathrm{F}_{14}$ beam hits the stationary CH_2, C, and empty targets with an approximate velocity of 0.71 at the center of the target and its equivalent energy is around 395 MeV/nucleon. The filling of the shell model levels is produced as shown in Figure 74. The spin and parity of the ground state of the projectile is determined by the unpaired proton in the $\pi 1\mathrm{d}_{5/2}$ orbit and it equals to $5/2^+$. The binding energy of a proton and neutron of the projectile is $\mathrm{S_p} = 13.290\,\mathrm{MeV}$ and $\mathrm{S_n} = 7.580\,\mathrm{MeV}$, respectively.

The outcome of the QFS is the $^{22}_{8}\mathrm{O}_{14}$ residual fragment. The binding energy of a proton and neutron in the residual is equal to $\mathrm{S_p} = 23.240\,\mathrm{MeV}$ and $\mathrm{S_n} = 6.850\,\mathrm{MeV}$, respectively. The fragment can be in its ground state with spin and parity of O^+ caused by removing a proton from the $\pi 1\mathrm{d}_{5/2}$ orbit as illustrated in the left side of Figure 74. Also, the reaction can occur by removing a proton from the $\pi 1\mathrm{p}_{1/2}$ orbit as illustrated in the right side of Figure 74 leading to a fragment with an excited state. However, the main issue that emerged while analysing this reaction channel is the poor statistics that exclude the analysis of the gamma spectrum and momentum distribution. Consequently, the subsection of the spectroscopic and exclusive reduction factor is not included.

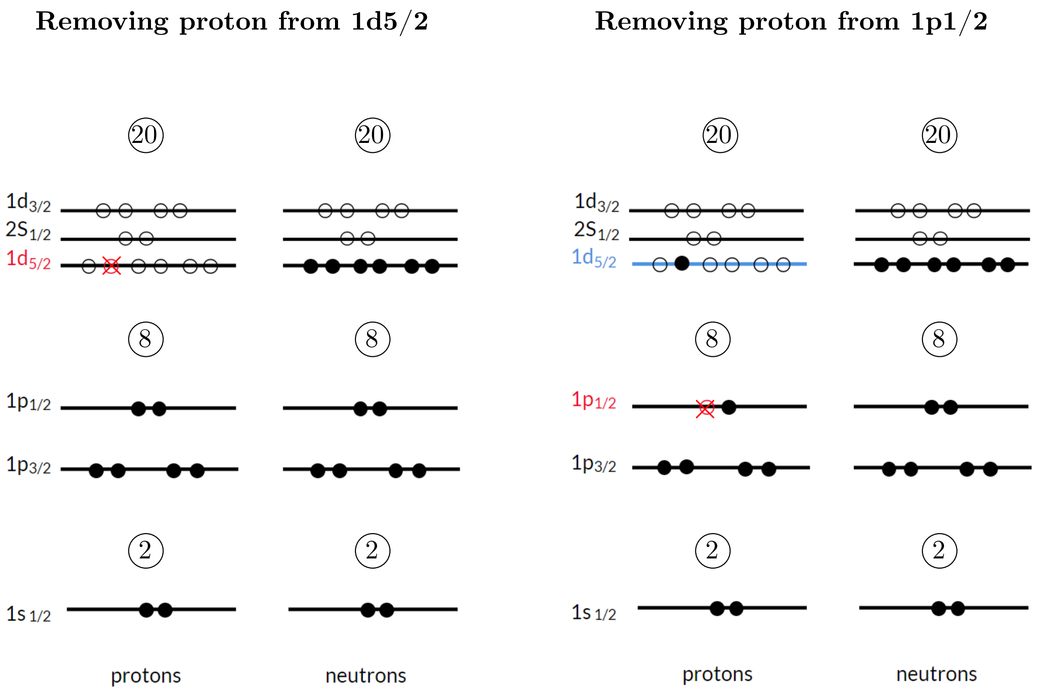

Figure 74: The shell structure of the odd-even $^{23}_{9}\mathrm{F}_{14}$ nucleus in the Independent Particle Model (IPM). The red circle indicates the removed proton in $^{23}_{9}\mathrm{F}_{14}$. The outcome of this reaction is $^{22}_{8}\mathrm{O}_{14}$ in its ground state if the proton was removed from $\pi 1\mathrm{d}_{5/2}$ orbit in the left, or a low-lying excited state if the proton was removed from $\pi 1\mathrm{p}_{1/2}$ orbit in the right.

6.3.1 Mass Identification

The mass distribution for the reacted $^{23}\mathrm{F}$ beam with the CH_2, C, and empty target after gating on the $\mathrm{z}-1=8$ fragments is shown in Figure 75; the Crystal Ball Sum trigger Tpat&8 == 8 was applied in addition to detecting two protons in the Crystal Ball. The oxygen fragment with the mass of interest A=22 is the first peak on the right. The other oxygen isotopes with a mass of 21, 20, etc. are caused by losing additional neutrons during the reaction. The number of tracked events A=22 is obtained by taking the integral under its fitted peak. The low statistics under ^{22}O peak are caused by the neutron separation energy. The highest energy state in the de-excited ^{22}O is equal to 6.936 MeV higher than its neutron separation energy [63].

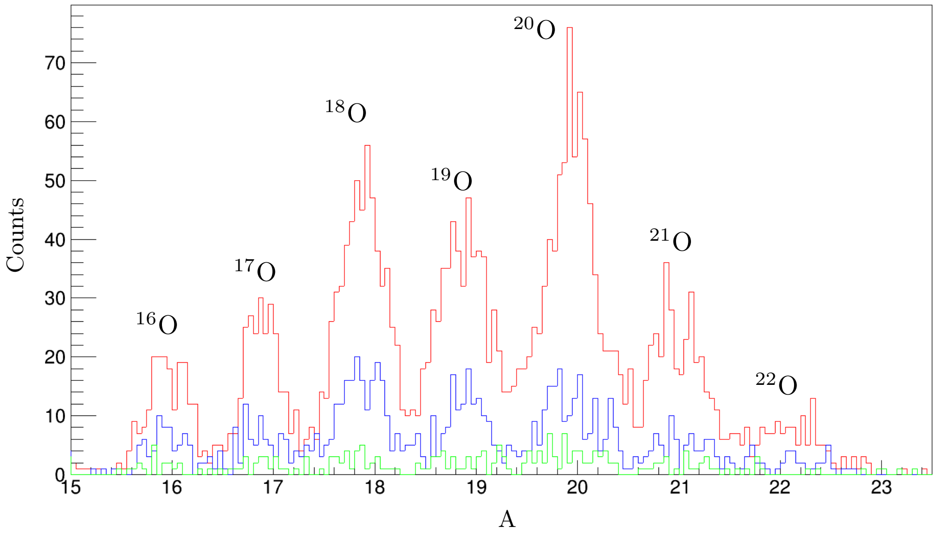

Figure 75: Mass identification of the outgoing nuclei produced by the quasi-free scattering off ^{23}F. ^{22}O is the outgoing particle of interest of the reacted beam. This plot is drawn for setting 3, for all used targets with the trigger of the Crystal Ball Sum Tpat&8 == 8. The reaction with the CH_2 target is indicated in red, C in blue, empty target in green.

6.3.2 Proton multiplicity

The dominated multiplicity of detecting two protons in the Crystal Ball in coincidence with the fragment of interest ^{22}O characterizes the quasi-free scattering off ^{23}F as shown in Figure 76 for the reconstructed H target.

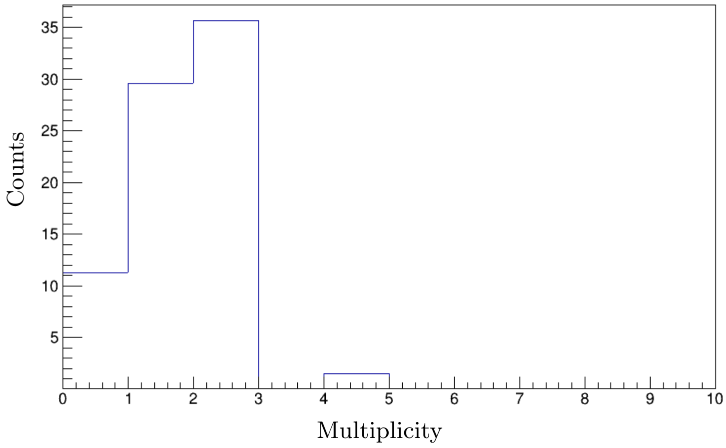

Figure 76: Proton multiplicity (proton clusters) in the Crystal Ball for the reconstructed H target of setting 3. A cut on detecting ^{22}O and the trigger of the Crystal Ball Sum Tpat&8 == 8 were applied.

6.3.3 Angular Correlations

The polar and azimuthal angles of the two scattered protons in QFS reaction $^{23}\mathrm{F}(\mathrm{p}, 2\mathrm{p})^{22}\mathrm{O}$ in Figure 77a and Figure 77b for CH_2 target and Figure 77c and Figure 77d for C target show a correlation as expected. A cut of Crystal Ball Sum trigger Tpat&8 == 8 and proton multiplicity of 2 was applied. Further, the angles are randomized. The distribution of the opening angle θ_0 between the two scattered in coincidence with ^{22}O is approximately 80° as shown in Figure 78a. Moreover, the distributions of the difference between the azimuthal angles ($\Delta\phi$) of the two scattered protons from quasi-free scattering in coincidence with ^{22}O is about 180° as shown in Figure 78b. The red curve indicates the distribution for CH_2 target, and the blue curve indicates the distribution for the C target. Also, a cut of Crystal Ball Sum trigger Tpat&8 == 8 and proton multiplicity of 2 was applied.

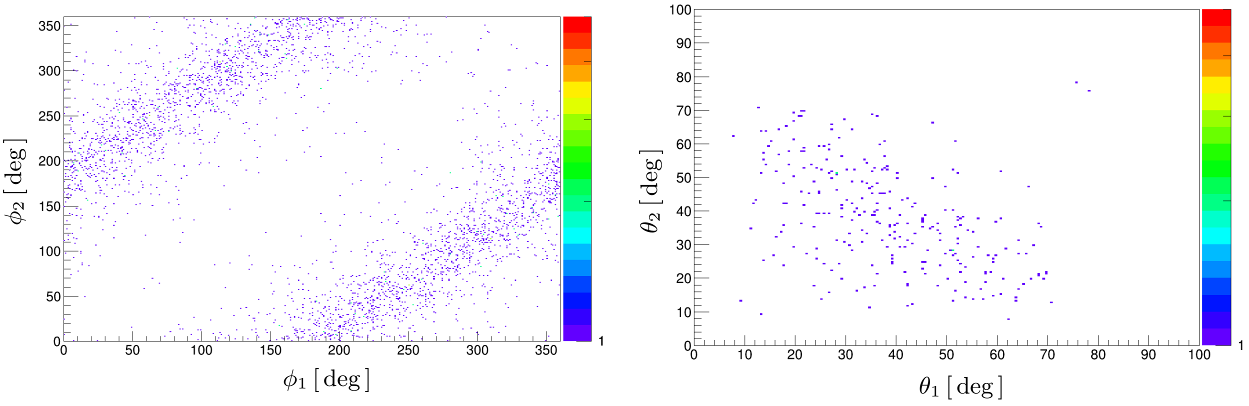

(a) The azimuthal angular correlation, CH_2 target

(b) The polar angular correlation, CH_2 target

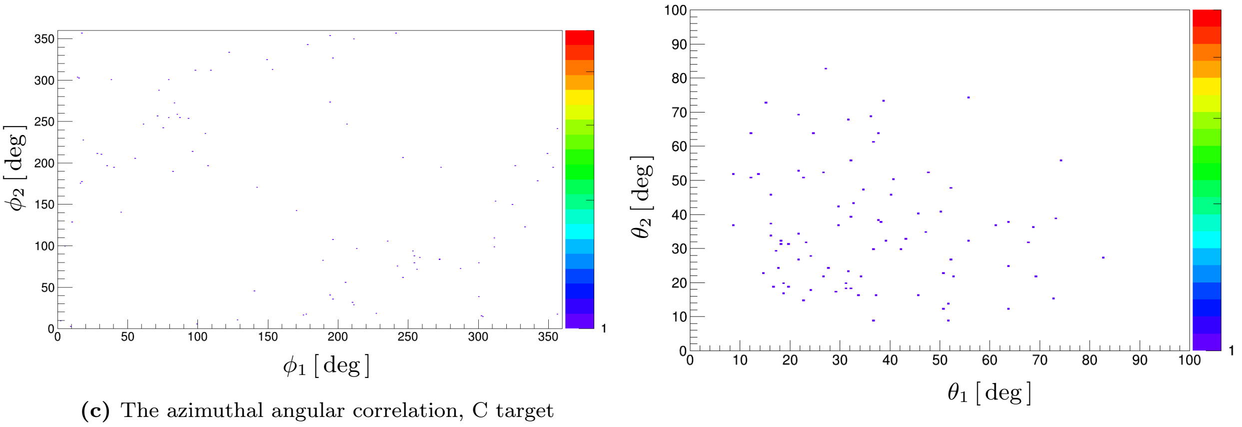

(c) The azimuthal angular correlation, C target

(d) The polar angular correlation, C target

Figure 77: The angular correlation of the scattered protons from the quasi-free scattering reaction in coincidence with ^{22}O for the CH_2 and C target of setting 3. A cut of Crystal Ball Sum trigger Tpat&8 == 8 and proton multiplicity of 2 was applied.

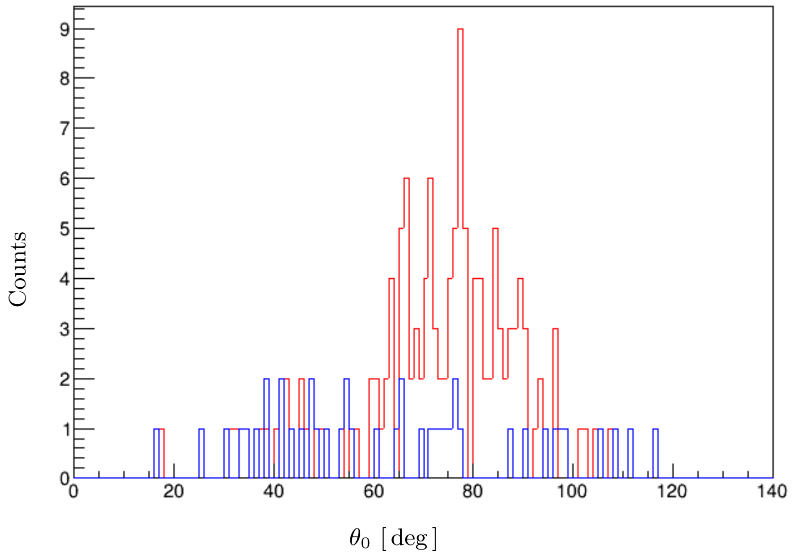

(a) Opening angle distribution.

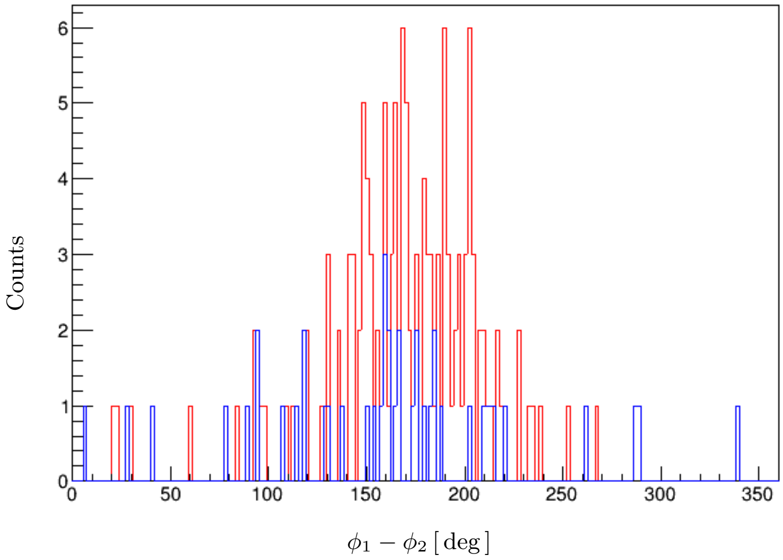

(b) The distribution of $\Delta\phi$.

Figure 78: (a) The distribution of the opening angle (θ_0) between the two protons from quasi-free scattering off ^{23}F in coincidence with ^{22}O for CH$_2$, the red curve, and C target, the blue curve, of setting 3. A cut of Crystal Ball Sum trigger Tpat&8 == 8 and proton multiplicity of 2 was applied. (b) The distributions of the difference between the azimuthal angles ($\Delta\phi$) of the two scattered protons from quasi-free scattering ^{23}F(p, 2p)^{22}O in coincidence with ^{22}O for CH$_2$, the red curve, and C target, the blue curve, of setting 3. A cut of Crystal Ball Sum trigger Tpat&8 == 8 and proton multiplicity of 2 was applied.

6.3.4 Geometrical Acceptance

The acceptance of the particles involved in the ^{23}F(p, 2p)^{22}O reaction channel for the CH$_2$ target was checked for the SSD02 detector, CH$_2$ target, and the TFW detector as illustrated in Figure 79. It is apparent from these figures that all the passing particles of interest are covered though it shows low statistics in the TFW detector.

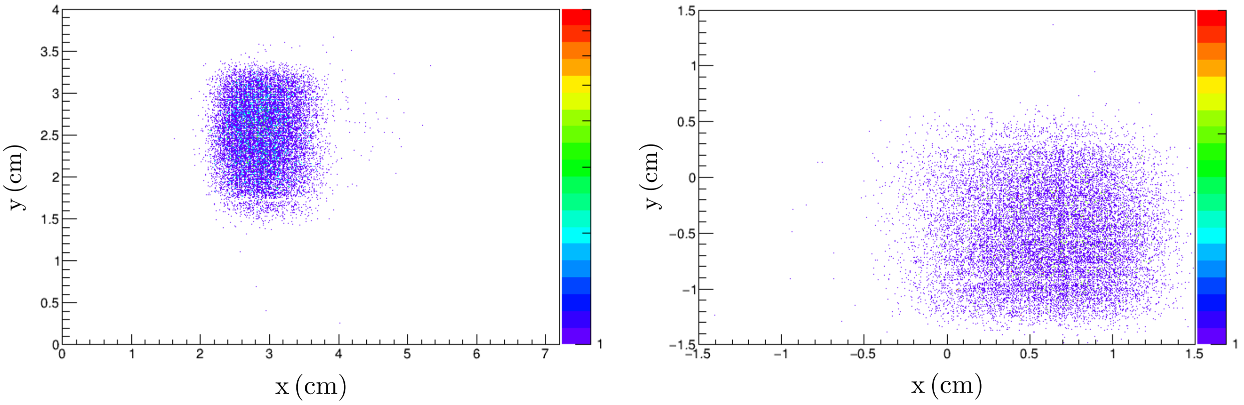

(a) ^{23}F hits at the SSD02 detector.

(b) ^{23}F hits at the CH$_2$ target.

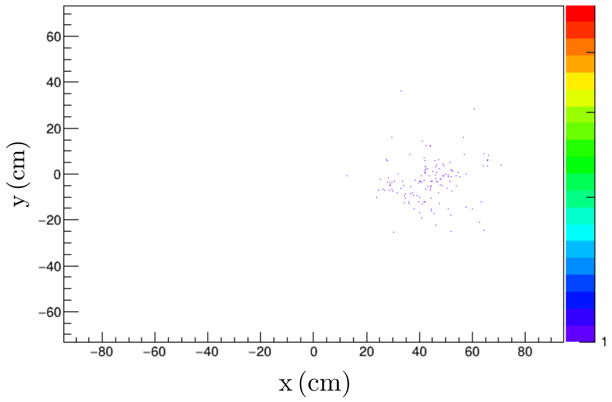

(c) ^{22}O hits at the TFW detector.

Figure 79: The geometrical acceptance of the SSD02 detector with an active area of $7.2 \times 4.0\,\mathrm{cm}^2$, target with an area of 3×3 cm^2, and TFW detector with an active area of $189 \times 147\,\mathrm{cm}^2$ for the $^{23}\mathrm{F(p,2p)}^{22}\mathrm{O}$ reaction.

6.3.5 Cross Sections

The experimental inclusive cross section of the reconstructed H target and its statistical uncertainty 2.4 (4) were calculated by using equation 37 and 39, respectively. However, the experimental exclusive cross sections for the ^{22}O excited states i are not included because of the poor statistics.

6.3.6 Spectroscopic and Reduction Factor

As previously stated, the $\pi 1p_{1/2}$ orbit is considered to be fully occupied by $2j + 1 = 2$ protons and its full cross section is equal to $2 \times \sigma_{s.p}$. In contrast, the $\pi 1d_{5/2}$ orbit is considered to be occupied by one proton and its full cross section is equal to $1 \times \sigma_{s.p}$ as shown in Table 24. However, this reaction channel $^{23}F(p, 2p)^{22}O$ is probably a complicated case, because there is some $\pi 1p_{1/2}$ strength surviving in the bound daughter nucleus but not all of it. Therefore, the inclusive cross section can not divide by the sum of the theoretical full cross sections of the related orbits $\pi 1d_{5/2}$ and $\pi 1p_{1/2}$. As a result, the inclusive reduction factor is not presented for this reaction channel.

Table 24: The theoretical cross section and SF of the reaction channel $^{23}F(p, 2p)^{22}O$.

Level	$\sigma_{\text{single particle}}$ (mb)	C^2S	$\sigma_{\text{full state}}$ (mb)
$\pi 1d_{5/2}$	4.856	1	4.856
$\pi 1p_{1/2}$	4.193	2	8.386

6.4 The Reaction Channel $^{22}F(p, 2p)^{21}O$

The odd-odd $^{22}_{9}F_{13}$ projectile hits the stationary CH_2, C, and empty targets with a velocity approximately 0.73 at the center of the target and its equivalent energy is around 427 MeV/nucleon. The filling of the shell model levels is produced as shown in Figure 80. The spin and parity of the ground state of the ^{22}F is determined by its unpaired nucleons in the $1d_{5/2}$ orbit and assigned as 4^+. The binding energy of a proton and neutron is $S_p = 12.558$ MeV and $S_n = 5.230$ MeV, respectively.

The outcome of the QFS reaction is an even-odd $^{21}_{8}O_{13}$ residual fragment, where the binding energy of a proton and neutron is $S_p = 20.990$ MeV and $S_n = 3.805$ MeV, respectively. Removing a proton from the $\pi 1d_{5/2}$ orbit as illustrated in the left side of Figure 80 lead to the ground state $5/2^+$ while removing a proton from the $\pi 1p_{1/2}$ orbit as shown in the right side of Figure 80 lead to an excited residual with a negative parity state. Unfortunately, the analysis of the gamma spectrum for this reaction channel is not included because of the poor statistics.

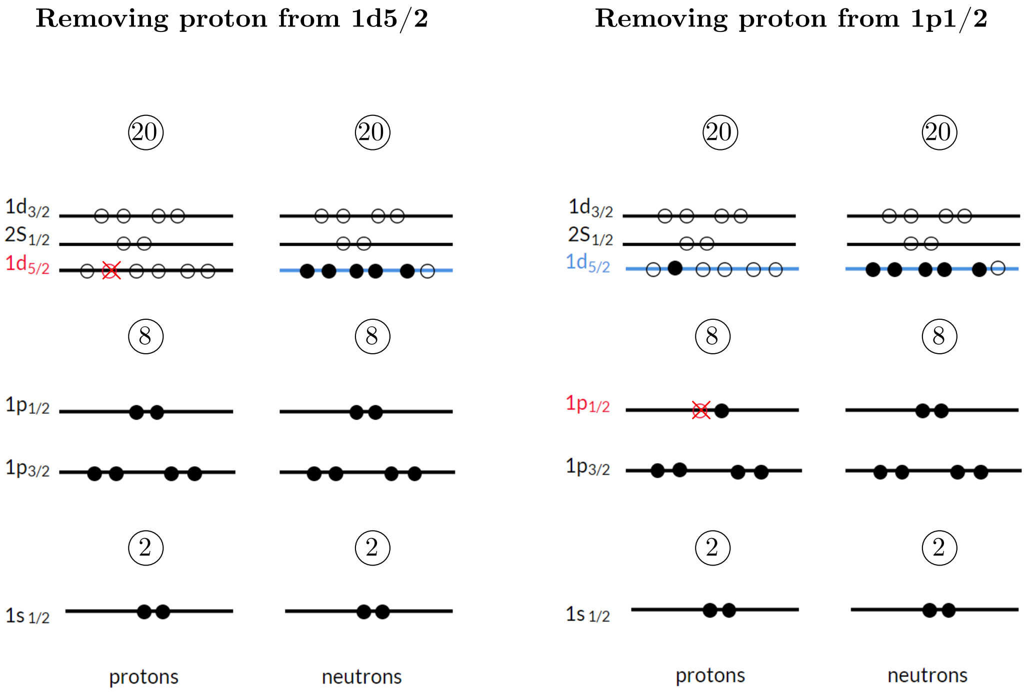

Figure 80: The shell structure of the odd-odd $^{22}_{9}F_{13}$ nucleus in the Independent Particle Model (IPM). The red circle indicates the removed proton in $^{22}_{9}F_{13}$. The outcome of this reaction is $^{21}_{8}O_{13}$ in its ground state if the proton was removed from $\pi 1d_{5/2}$ orbit in the left, or a low-lying excited state if the proton was removed from $\pi 1p_{1/2}$ orbit in the right.

6.4.1 Mass Identification

The mass distribution of the reacted ^{22}F beam with the CH_2, C, and empty target after gating on the $z - 1 = 8$ is shown in figure 81; the Crystal Ball Sum trigger Tpat&8 == 8 was applied in addition to detecting two protons in the Crystal Ball. The oxygen fragment with the mass of interest A=21 is the first peak on the right. The other oxygen isotopes with a mass of 20, 19, etc. are caused by losing additional neutrons during the reaction. The number of tracked events A=21 is obtained by taking the integral under its fitted peak. The statistics under ^{21}O peak are affected by the neutron separation energy. The highest energy state in the de-excited ^{21}O is equal to 4.927 MeV higher than its neutron separation energy [63].

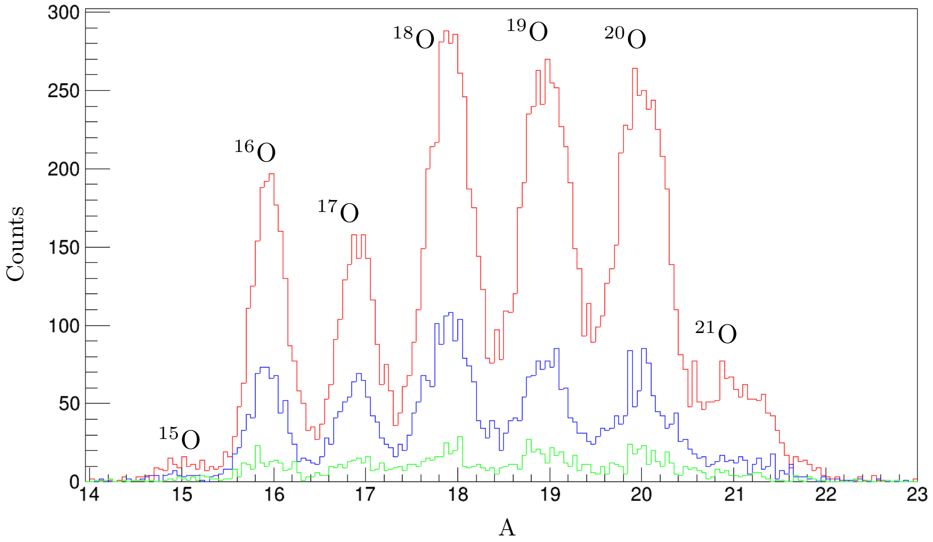

Figure 81: Mass identification of the outgoing nuclei produced by the reacted $^{22}_{9}F_{13}$. ^{21}O is the outgoing particle of interest since it is caused by the quasi-free scattering off $^{22}_{9}F_{13}$. This plot is drawn for setting 3, for all targets with the trigger of the Crystal Ball Sum Tpat&8 == 8. The reaction with the CH_2 target is indicated in red, C in blue, empty target in green.

6.4.2 Proton multiplicity

The dominated multiplicity of detecting two protons in the Crystal Ball in coincidence with the fragment of interest ^{21}O characterizes the quasi-free scattering off $^{22}_{9}F_{13}$, as shown in Figure 82.

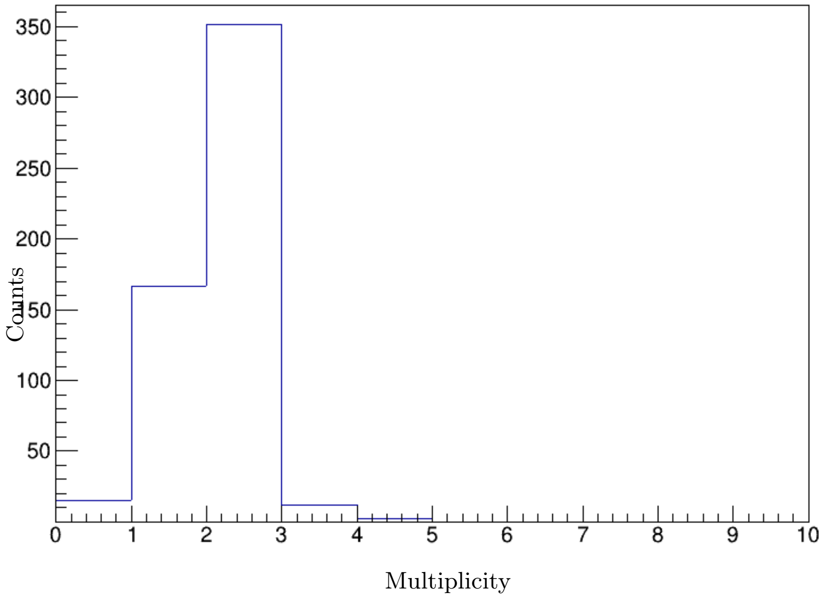

Figure 82: Proton multiplicity (proton clusters) in the Crystal Ball for the reconstructed H target of setting 3. A cut of detecting ^{21}O and the trigger of the Crystal Ball Sum Tpat&8 == 8 was applied.

6.4.3 Angular Correlations

The polar and azimuthal angular correlation of the two scattered protons from the QFS in coincidence with ^{21}O are illustrated in Figure 83a and Figure 83b for CH_2 target and Figure 83c and Figure 83d for C target. A cut of Crystal Ball Sum trigger Tpat&8 == 8 and proton multiplicity of 2 was applied. The distribution of the opening angle θ_0 between the two scattered protons from QFS in coincidence with ^{21}O is around 80°, as displayed in Figure 84a. Furthermore, the distributions of the difference between the azimuthal angles ($\Delta\phi$) of the two scattered protons in coincidence with ^{21}O is approximately 180°, as exhibited in Figure 84b. The red curve shows the distribution for CH_2 target, and the blue curve shows the distribution for the C target. Additionally, a cut of Crystal Ball Sum trigger Tpat&8 == 8 and proton multiplicity of 2 was applied.

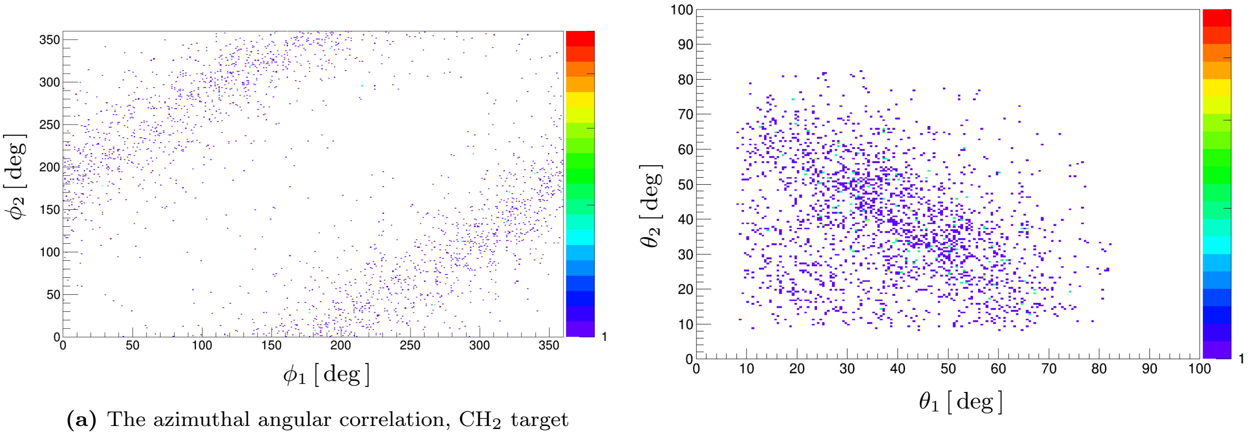

(a) The azimuthal angular correlation, CH_2 target

(b) The polar angular correlation, CH_2 target

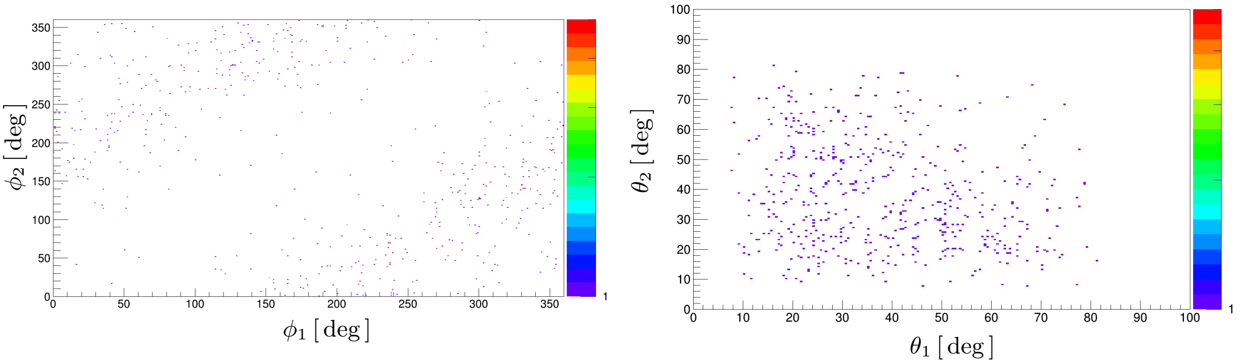

(c) The azimuthal angular correlation, C target

(d) The polar angular correlation, C target

Figure 83: The angular correlation of the scattered protons from the QFS reaction in coincidence with ^{21}O for the CH_2 and C target of setting 3. A cut of Crystal Ball Sum trigger Tpat&8 == 8 and proton multiplicity of 2 was applied.

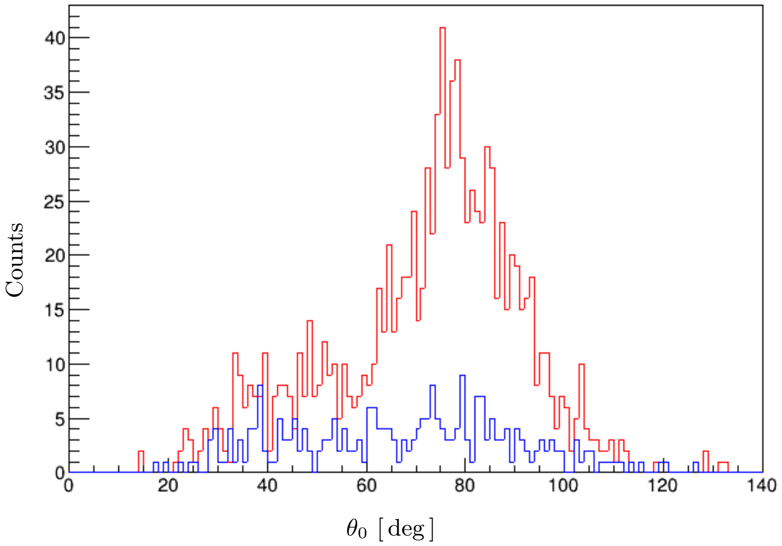

(a) Opening angle distribution.

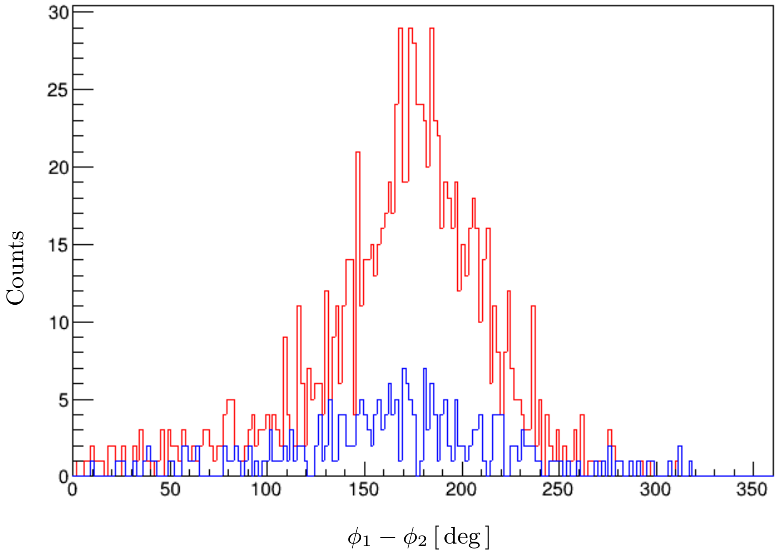

(b) The distribution of $\Delta\phi$.

Figure 84: (a) The distribution of the opening angle (θ_0) between the two protons from quasi-free scattering in coincidence with ^{21}O for CH$_2$, the red curve, and C target, the blue curve, of setting 3. A cut of Crystal Ball Sum trigger Tpat&8 == 8 and proton multiplicity of 2 was applied. (b) The distributions of the difference between the azimuthal angles ($\Delta\phi$) of the two scattered protons from quasi-free scattering $^{22}\mathrm{F}(\mathrm{p}, 2\mathrm{p})^{21}\mathrm{O}$ in coincidence with ^{21}O for CH$_2$, the red curve, and C target, the blue curve, of setting 3. A cut of Crystal Ball Sum trigger Tpat&8 == 8 and proton multiplicity of 2 was applied.

6.4.4 Geometrical Acceptance

The acceptance of the particles involved in the $^{22}\mathrm{F}(\mathrm{p}, 2\mathrm{p})^{21}\mathrm{O}$ reaction channel for the CH$_2$ target was checked for the SSD02 detector, CH$_2$ target, and the TFW detector as illustrated in Figure 85. It is apparent from these figures that all the passing particles of interest are covered.

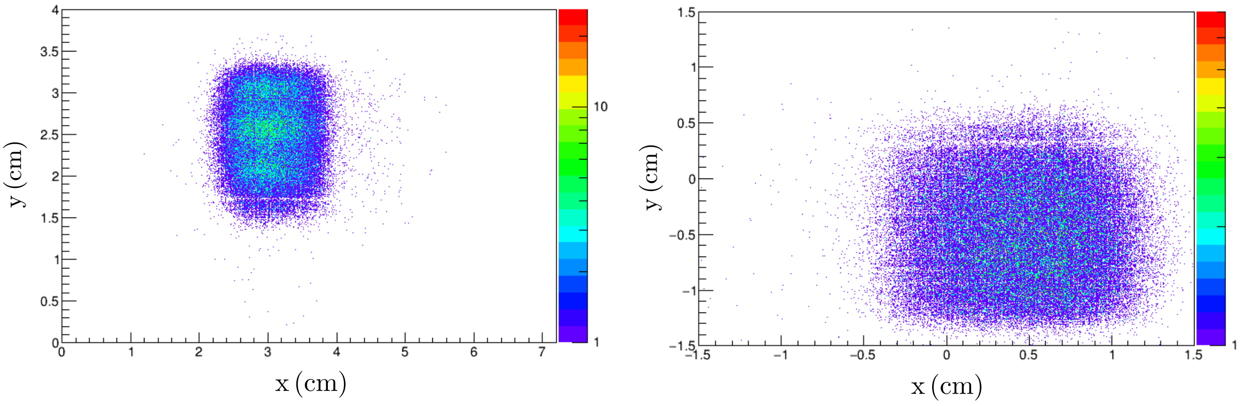

(a) ^{22}F hits at the SSD02 detector.

(b) ^{22}F hits at the CH_2 target.

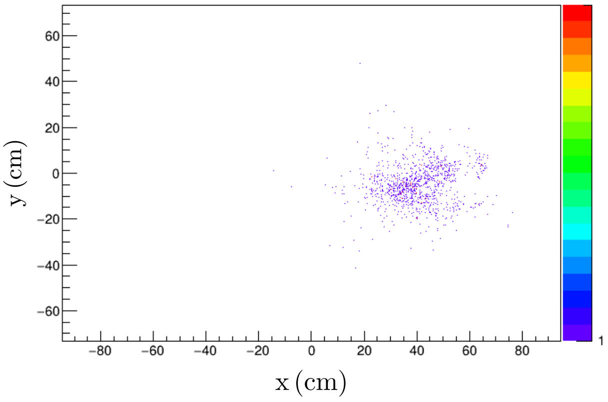

(c) ^{21}O hits at the TFW detector.

Figure 85: The geometrical acceptance of the SSD02 detector with an active area of $7.2 \times 4.0\,\mathrm{cm}^2$, target with an area of 3×3 cm^2, and TFW detector with an active area of 189×147 cm^2 for the $^{22}\mathrm{F(p, 2p)}^{21}\mathrm{O}$ reaction.

6.4.5 Cross Sections

The experimental inclusive cross section of the reconstructed H target and its statistical uncertainty 3.7 (2) were calculated by using equation 37 and 39, respectively. However, the experimental exclusive cross sections for the excited states of the daughter nucleus ^{21}O are not included because of the poor statistics.

6.4.6 Spectroscopic and Reduction Factor

As indicated previously, the $\pi 1_{p1/2}$ orbit is considered to be fully occupied by $2j + 1 = 2$ protons and its full cross section is equal to $2 \times \sigma_{s.p}$. In contrast, the $\pi 1d_{5/2}$ orbit is considered to be occupied by one protons and its full cross section is supposed to equal $1 \times \sigma_{s.p}$, as shown in Table 25. The inclusive reduction factor was obtained by taking the ratio between the inclusive cross section and the full cross section of the $\pi 1d_{5/2}$ orbit, and it is equal to 0.68(6).

Table 25: The theoretical cross section and SF of the reaction channel $^{22}\mathrm{F}(\mathrm{p},2\mathrm{p})^{21}\mathrm{O}$.

Orbit	$\sigma_{\mathrm{single\,particle}}$ (mb)	C^2S	$\sigma_{\mathrm{full\,state}}$ (mb)
$\pi 1d_{5/2}$	5.376	1	5.376
$\pi 1p_{1/2}$	4.664	2	9.328

6.4.7 Momentum Distributions

The momentum distribution of the removed nucleon before the reaction equals the momentum distribution of the recoil nucleus. The comparison between the width of the momentum distributions of the unreacted beam shown in Table 26 and the width of the momentum distributions of the reacted beam in Figure 86 indicates that the nucleon's internal momentum causes the broadening of the width of the momentum distribution of the reacted beam. The width and the shape of the momentum distribution indicates the orbit of the removed nucleon. Thus, the orbit of the removed proton for the $^{22}\mathrm{F}(\mathrm{p},2\mathrm{p})^{21}\mathrm{O}$ channel was determined by comparing the experimental momentum distribution of the residual $^{21}\mathrm{O}$ to a theoretical one. The results of the comparative analysis are illustrated in Figure 87, where the experimental momentum distributions for the residual fragment $^{21}\mathrm{O}$ in coincidence with the detection of two protons in the Crystal Ball are compared to theoretical momentum distributions for the $\pi 1d_{5/2}$ orbit.

Table 26: The momentum resolution of the unreacted $^{22}\mathrm{F}$ beam for CH_2 and C target of setting 3. It was obtained from the Gaussian fit of the momentum distribution .

Target	σ_{p} (MeV/c)	$\sigma_{\mathrm{str,\,p}}$ (MeV/c)
CH_2	$\sigma_{\mathrm{p_x}} = 34.7 \pm 0.3$	$\sigma_{\mathrm{str,\,p_x}} = 16.5 \pm 0.4$
	$\sigma_{\mathrm{p_y}} = 49.2 \pm 0.2$	$\sigma_{str,\,p_y} = 16.6 \pm 0.3$
C	$\sigma_{\mathrm{p_x}} = 36.4 \pm 0.3$	$\sigma_{\mathrm{str,\,p_x}} = 19.7 \pm 0.4$
	$\sigma_{\mathrm{p_y}} = 50.1 \pm 0.3$	$\sigma_{str,\,p_y} = 19.1 \pm 0.4$
MT	$\sigma_{\mathrm{p_x}} = 30.5 \pm 0.3$	
	$\sigma_{\mathrm{p_y}} = 46.3 \pm 0.2$	

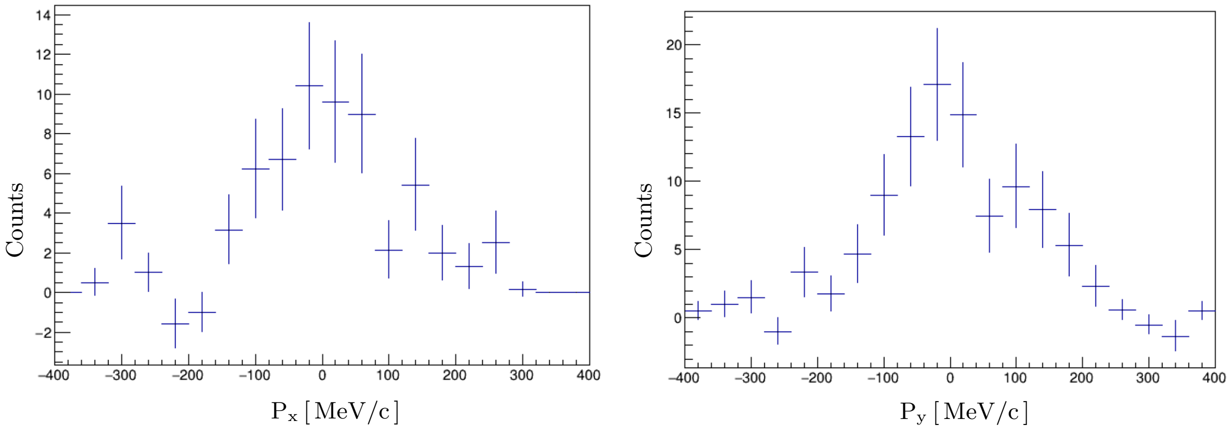

(a) The x-component of the transverse momentum **(b)** The y-component of the transverse momentum

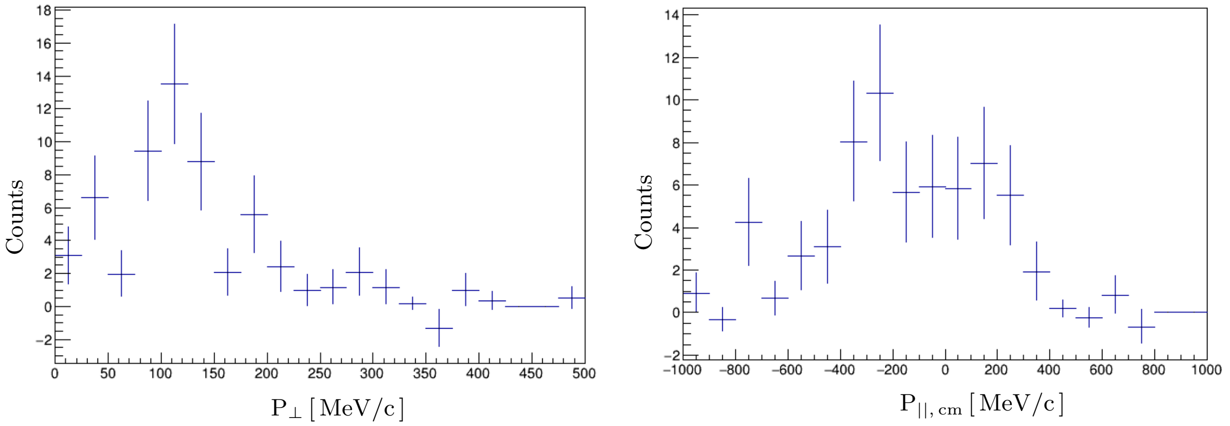

(c) The transverse momentum **(d)** The longitudinal momentum

Figure 86: The momentum distributions of the reacted ^{22}F beam for the reconstructed H target. A cut of XB trigger Tpat&8 == 8, and a multiplicity of two protons in coincidence with the fragment of interest ^{21}O was applied.

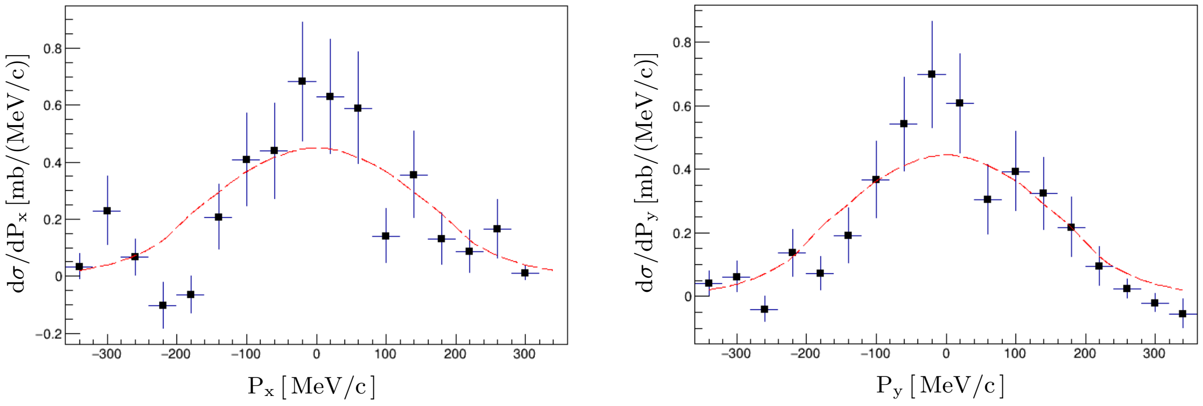

(a) P_x component of the transverse momentum **(b)** P_y component of the transverse momentum

Figure 87: The comparison between the experimental and theoretical distributions of the transverse momentum components of the removed proton from the projectile nuclei ^{22}F. The black points indicate the experimental data for the reconstructed H target and red curve indicates the theoretical one for the $\pi 1d_{5/2}$ orbit.

6.5 The Reaction Channel $^{21}\mathrm{F(p,2p)}^{20}\mathrm{O}$

The odd-even $^{21}_{9}\mathrm{F}_{12}$ nuclei hits the stationary $\mathrm{CH_2}$, C, and empty targets with a velocity approximately 0.74 at the center of the target and its equivalent energy is around 462 MeV/nucleon. The filling of the shell model levels is produced as shown in Figure 88. The ground state of the odd-even projectile is determined by the unpaired proton in $\pi 1\mathrm{d}_{5/2}$ orbit, thus its spin and parity assigned as $5/2^{+}$. The binding energy of a proton and neutron of the projectile is $\mathrm{S_p} = 11.1327\,\mathrm{MeV}$ and $\mathrm{S_n} = 8.1015\,\mathrm{MeV}$, respectively.

The outcome of QFS reaction is $^{20}_{8}\mathrm{O}_{12}$, where the binding energy of a proton and neutron is $\mathrm{S_p} = 19.349\,\mathrm{MeV}$ and $\mathrm{S_n} = 7.6080\,\mathrm{MeV}$, respectively. The residual fragment is characterized by the orbit of the removed proton. If the proton is removed from the $\pi 1\mathrm{d}_{5/2}$ orbit as illustrated in the left side of Figure 88, the fragment is considered in its ground state with a spin and parity of 0^{+}. Another possible reaction is removing a proton from the $\pi 1\mathrm{p}_{1/2}$ orbit as illustrated in the right side of Figure 88 leading to an excited residual with an assigned spin and parity of 2^{-} and 3^{-}.

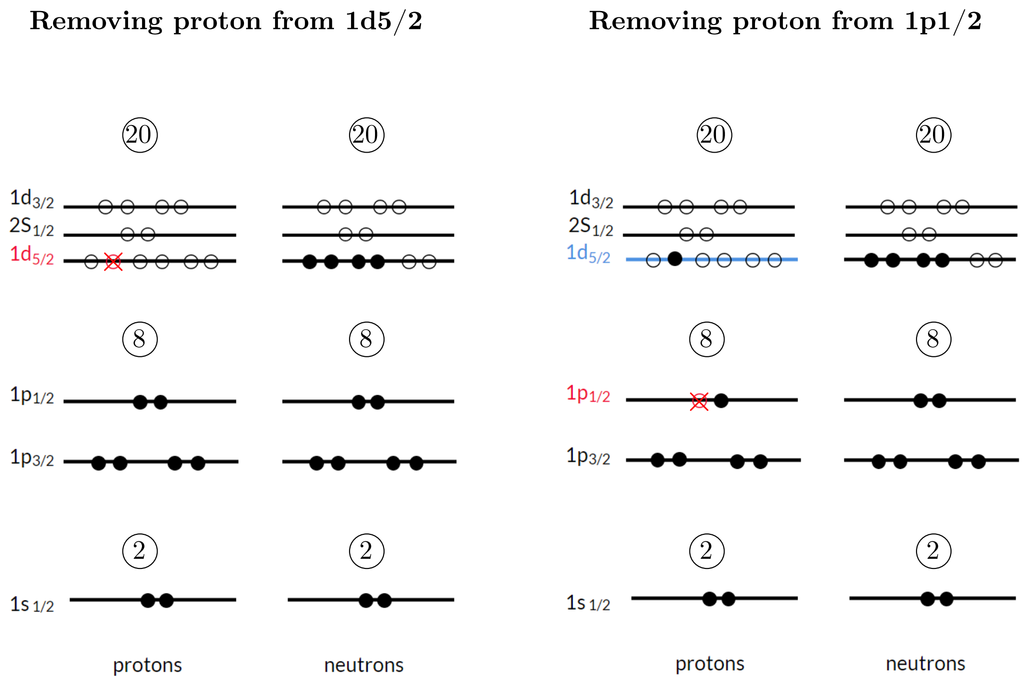
Removing proton from 1d5/2 **Removing proton from 1p1/2**

Figure 88: The shell structure of the odd-even $^{21}_{9}\mathrm{F}_{12}$ nucleus in the Independent Particle Model (IPM). The red circle indicates the removed proton in $^{21}_{9}\mathrm{F}_{12}$. The outcome of this reaction is $^{20}_{8}\mathrm{O}_{12}$ in its ground state if the proton was removed from $\pi 1\mathrm{d}_{5/2}$ orbit in the left, or a low-lying excited state if the proton was removed from $\pi 1\mathrm{p}_{1/2}$ orbit in the right.

6.5.1 Mass Identification

The mass distribution of the reacted $^{21}\mathrm{F}$ beam with the $\mathrm{CH_2}$, C, and empty target after gating on the $z - 1 = 8$ fragments is shown in Figure 89; the Crystal Ball Sum trigger Tpat&8 == 8 was applied in addition to detecting two protons in the Crystal Ball. The oxygen fragment with the mass of interest A=20 is the first peak on the right. The other oxygen isotopes with a mass of 19, 18, etc. are caused by losing additional neutrons during the reaction. The number of tracked events at A=20 is obtained by taking the integral under its fitted peak. The statistics under ^{20}O peak are affected by the neutron separation energy, which is higher than the energies of the excited states of ^{20}O as shown in Figure 95.

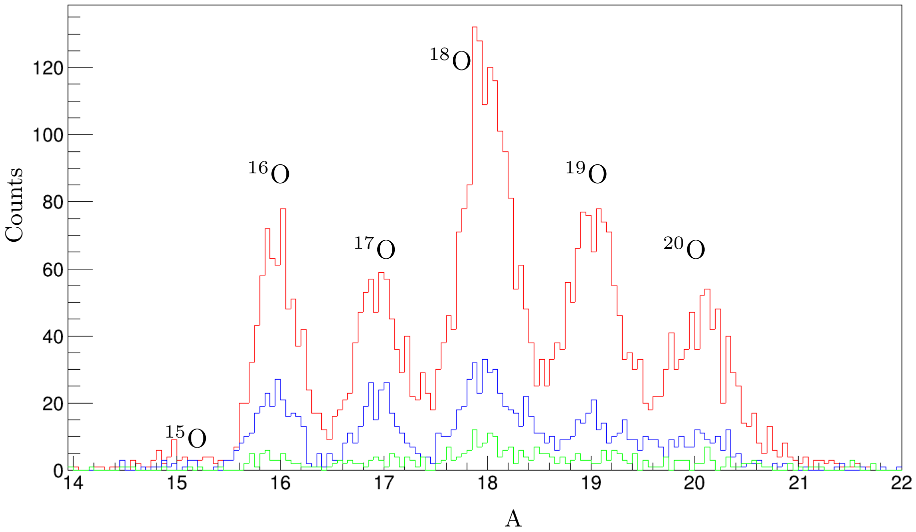

Figure 89: Mass identification of the outgoing nuclei produced by the reacted beam ^{21}F. ^{20}O is the outgoing particle of interest since it is caused by the QFS off ^{21}F. This plot is drawn for setting 3, for all targets with the trigger of the Crystal Ball Sum Tpat&8 == 8. The reaction with the CH_2 target is indicated in red, C in blue, empty target in green.

6.5.2 Proton multiplicity

The dominated multiplicity of detecting two protons in the Crystal Ball in coincidence with the fragment of interest ^{20}O characterizes the QFS off ^{21}F, as shown in Figure 90.

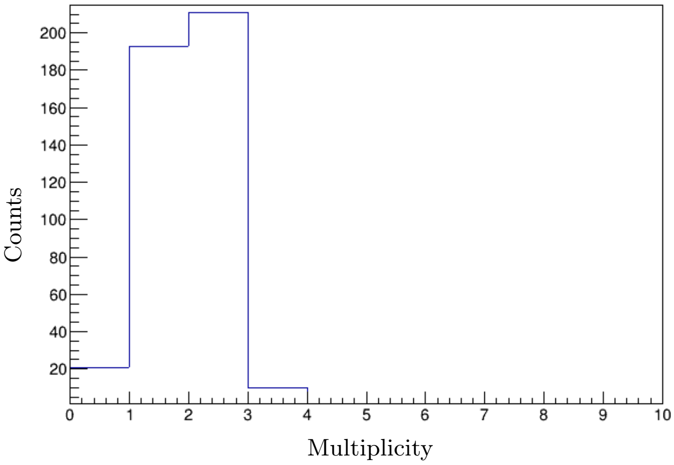

Figure 90: Proton multiplicity (proton clusters) in the Crystal Ball for the reconstructed H target of setting 3. A cut of detecting ^{20}O and the trigger of the Crystal Ball Sum Tpat&8 == 8 was applied.

6.5.3 Angular Correlations

The polar and azimuthal angular correlation of the two scattered protons from the QFS in coincidence with ^{20}O are shown in Figure 91a and Figure 91b for CH_2 target and Figure 91c and Figure 91d for C target, where a cut of Crystal Ball Sum trigger Tpat&8 == 8 and proton multiplicity of 2 was applied.
The distribution of the opening angle θ_0 between the two scattered protons from ^{21}F(p, 2p)^{20}O reaction in coincidence with ^{20}O is close to 80°, as shown in Figure 92a. Moreover, the distributions of the difference between the azimuthal angles ($\Delta\phi$) of the two scattered protons in coincidence with ^{19}N is approximately 180° as shown in Figure 92b. For both distributions, the red curve indicates the distribution for CH_2 target, and the blue curve indicates the distribution for the C target. Additionally, a cut of Crystal Ball Sum trigger Tpat&8 == 8 and proton multiplicity of 2 was applied.

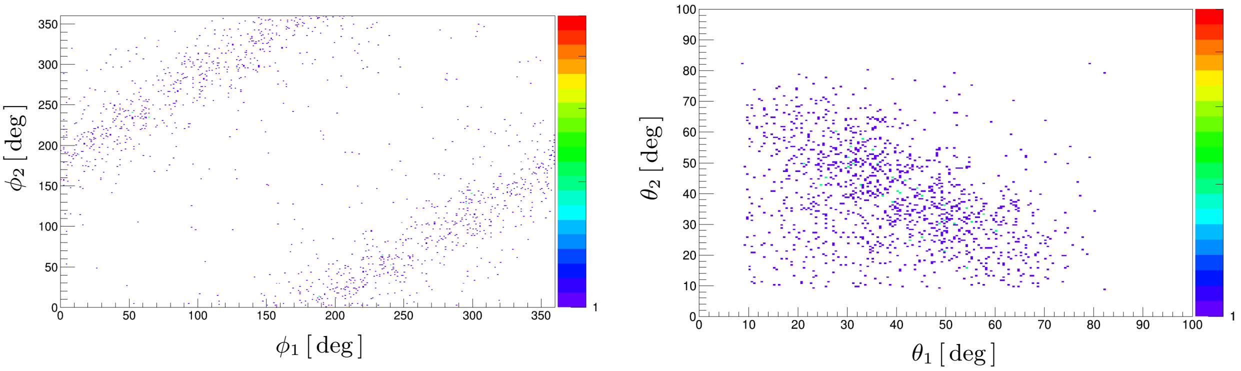

(a) The azimuthal angular correlation, CH_2 target

(b) The polar angles correlation, CH_2 target

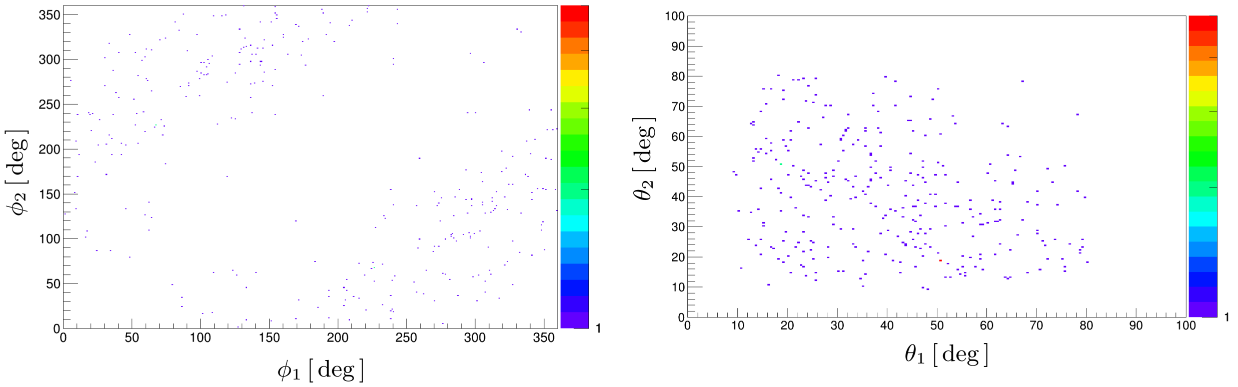

(c) The azimuthal angular correlation, C target

(d) The polar angular correlation, C target

Figure 91: The angular correlation of the scattered protons from the QFS reaction in coincidence with ^{20}O for the CH_2 and C target of setting 3. A cut of Crystal Ball Sum trigger Tpat&8 == 8 and proton multiplicity of 2 was applied.

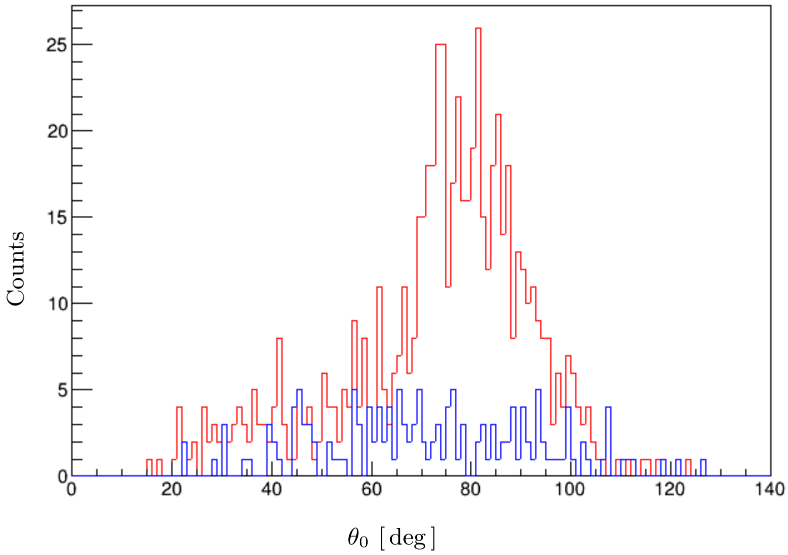

(a) Opening angle distribution.

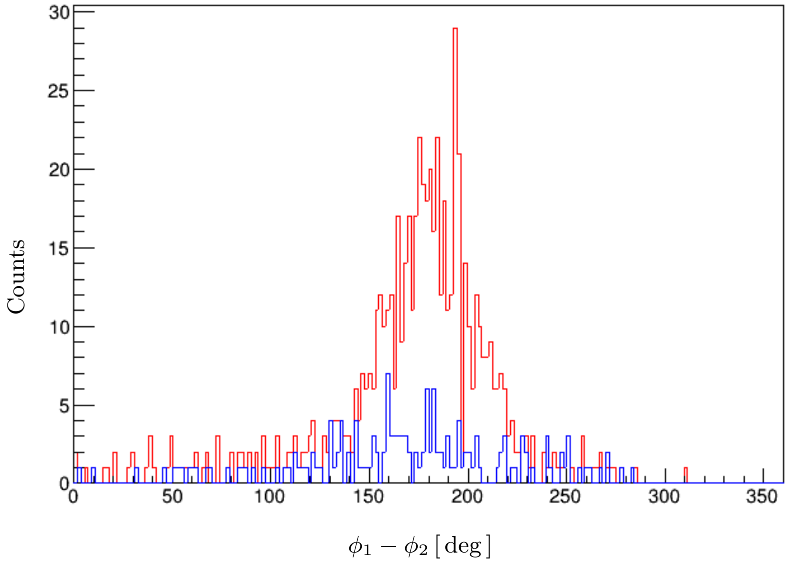

(b) The distribution of $\Delta\phi$.

Figure 92: (a) The distribution of the opening angle (θ_0) between the two protons from quasi-free scattering in coincidence with ^{20}O for CH_2, the red curve, and C target, the blue curve, of setting 3. A cut of Crystal Ball Sum trigger Tpat&8 == 8 and proton multiplicity of 2 was applied. (b) The distributions of the difference between the azimuthal angles ($\Delta\phi$) of the two scattered protons from quasi-free scattering $^{21}\mathrm{F(p,2p)}^{20}\mathrm{O}$ in coincidence with ^{20}O for CH_2, the red curve, and C target, the blue curve, of setting 3. A cut of Crystal Ball Sum trigger Tpat&8 == 8 and proton multiplicity of 2 was applied.

6.5.4 Geometrical Acceptance

The acceptance of the particles involved in the $^{21}\mathrm{F(p,2p)}^{20}\mathrm{O}$ reaction channel for the CH_2 target was checked for the SSD02 detector, CH_2 target, and the TFW detector as illustrated in Figure 93. It is apparent from these figures that all the passing particles of interest are covered.

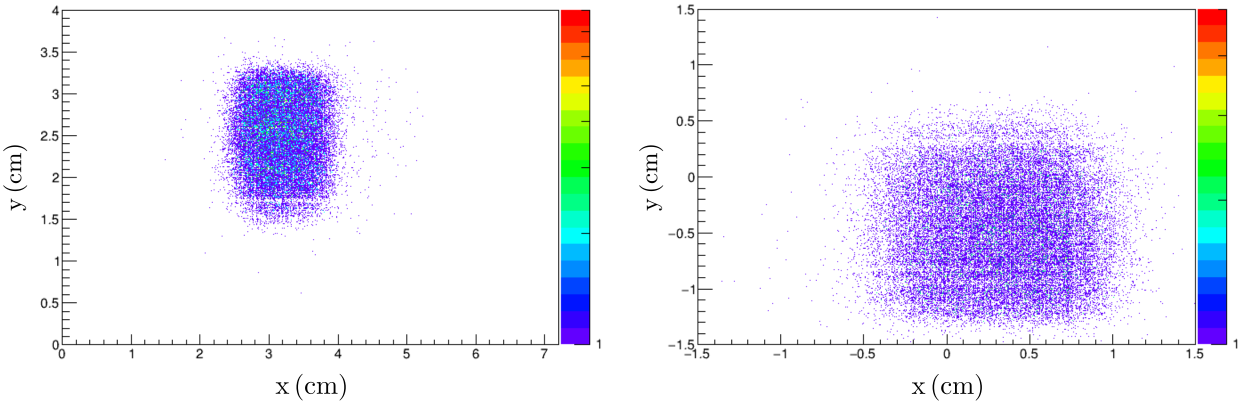

(a) ^{21}F hits at the SSD02 detector.

(b) ^{21}F hits at the CH$_2$ target.

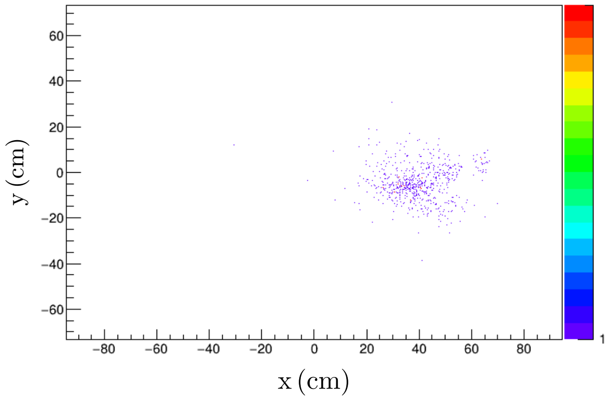

(c) ^{20}O hits at the TFW detector.

Figure 93: The geometrical acceptance of the SSD02 detector with an active area of $7.2 \times 4.0\,\mathrm{cm}^2$, target with an area of 3×3 cm^2, and TFW detector with an active area of 189×147 cm^2 for the $^{21}\mathrm{F(p,2p)}^{20}\mathrm{O}$ reaction.

6.5.5 Gamma-Rays

The experimental single and sum gamma spectrum of the residual fragment ^{20}O are presented with black crosses in Figure 94. The experimental single spectrum on the left side shows two peaks at 1.674 MeV and 3.940 MeV. From the level scheme of the bound state of the daughter nucleus ^{20}O in Figure 95, we can see that the 3.940 MeV transition feeds the first excited state at 1.674 MeV. Thus, this cascade is assigned to the decay of the (3^-) state through the 2^+ state to the ground state 0^+. The sum energy of the cascade can be seen at 5.614 MeV in the experimental sum spectrum on the right side of Figure 94. The spin and parity of this state were predicted in section 6.5. Therefore, the observed (3^-) state and the background were then added to the simulated QFS to obtain the fitted experimental gamma spectrum as shown in Figure 94. Both spectra were fitted simultaneously. The value of the reduced χ^2 of the total fit function is equal to 1.18. The obtained population $\mathrm{p_i}$ for the (3^-) state of the residual ^{20}O is shown in Table 27.

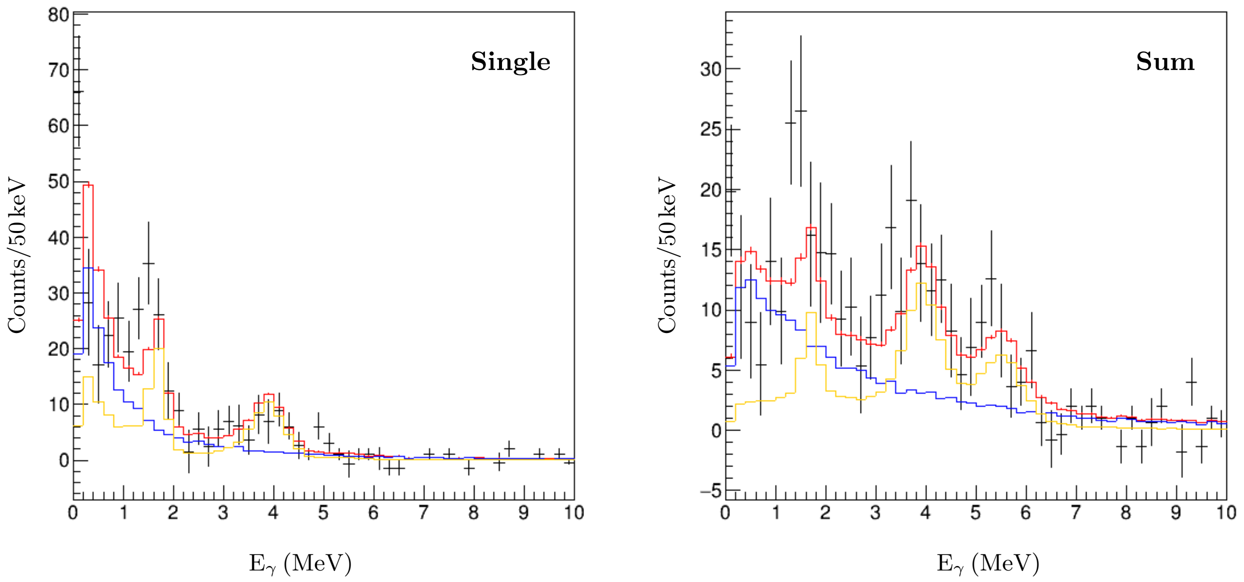

Figure 94: The single and sum of the fitted simulated gamma-ray spectra of the de-excited ^{20}O to the experimental data for the H_2 target. The measurement was done in coincidence with the detection of two protons for both data. The reduced χ^2 of the total fit function is equal to 1.18. The experimental data are indicated by black crosses, total fit in red, simulated excited state (3^-) in orange, background in blue.

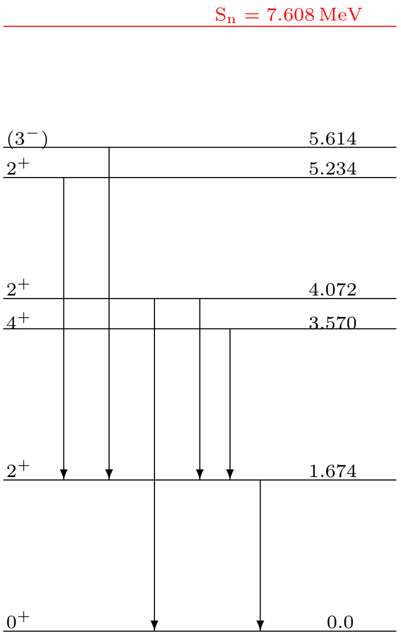

Figure 95: Level scheme of the residual fragment ^{20}O in MeV according to [6, 64]. The red line indicates the neutron separation energy.

Table 27: Population of the observed excited state of the de-excited ^{20}O residual fragment and the efficiency of detecting the simulated gamma-ray.

J^{π}	E_{state} (MeV)	Efficiency (%)	p_i (%)
(3^-)	5.614	42	75 ± 8

6.5.6 Cross Sections

The experimental inclusive cross section of the reconstructed H target and its statistical uncertainty were calculated by using equation 37 and 39, respectively. The exclusive experimental cross section for the excited state (3^-) was obtained by using equation 43. The exclusive experimental cross section of the ground state 0^+ and its statistical uncertainty were then obtained by using equation 44 and 45, respectively. The cross sections of the quasi-free scattering for all considered states of ^{20}O with the statistical uncertainty are shown in Table 28.

Table 28: The experimental inclusive and exclusive cross sections for QFS of the $^{21}\mathrm{F(p,2p)}^{20}\mathrm{O}$ reaction channel for the reconstructed H target.

Inclusive cross section	Exclusive cross section		
σ_{H} (mb)	J^{π}	E_{state} (MeV)	σ_{H} (mb)
8.4 (5)	(3^-)	5.614	6.3 (8)
	0^+	0	8.4 (5) - 6.3 (8) = 2.1 (9)

6.5.7 Spectroscopic and Reduction Factor

The $\pi 1p_{1/2}$ orbit is considered to be fully occupied by $2j + 1 = 2$ protons and its full cross section is equal to $2 \times \sigma_{\mathrm{s.p}}$. In contrast, the $\pi 1d_{5/2}$ orbit is occupied by one proton and its full cross section is supposed to equal $1 \times \sigma_{\mathrm{s.p}}$, as shown in Table 29. However this reaction channel seems to be a complicated case. Its inclusive cross section 8.4(5) mb is higher than the inclusive cross section 3.7(2) mb of the reaction channel $^{22}\mathrm{F(p,2p)}^{21}\mathrm{O}$ and 2.4(4) mb of the reaction channel $^{23}\mathrm{F(p,2p)}^{22}\mathrm{O}$. It means that large part of the $\pi 1p_{1/2}$ strength survives as bound state in the residual fragment ^{20}O but not all. Some structure calculation is needed to obtained the contribution of the states. Therefore, the inclusive cross section can not divide by the sum of the theoretical full cross sections of the related orbits. As a result, the inclusive reduction factor is not presented for this reaction channel.

Table 29: The theoretical cross section and SF of the reaction channel $^{21}\mathrm{F(p,2p)}^{20}\mathrm{O}$.

Level	$\sigma_{\mathrm{single\,particle}}$ (mb)	C^2S	$\sigma_{\mathrm{full\,state}}$ (mb)
$\pi 1d_{5/2}$	6.051	1	6.051
$\pi 1p_{1/2}$	5.281	2	10.56

6.5.8 Momentum Distributions

As indicated previously, measuring the remaining fragment's momentum distribution can deduce the momentum of the removed nucleon and, consequently, its orbit while in the nucleus. The width of the momentum distributions of the unreacted beam illustrated in Table 30 is deffer from the width of the momentum distributions of the reacted beam in Figure 96 which indicates that the nucleon's internal momentum causes the broadening of the width of the momentum distribution of the reacted beam.

Table 30: The momentum resolution of the unreacted ^{21}F beam for CH_2 and C target of setting 3. It was obtained from the Gaussian fit of the momentum distribution .

Target	σ_{p} (MeV/c)	$\sigma_{\mathrm{str,\,p}}$ (MeV/c)
CH_2	$\sigma_{\mathrm{p_x}} = 35.3 \pm 0.3$	$\sigma_{\mathrm{str,\,p_x}} = 16.5 \pm 0.4$
	$\sigma_{\mathrm{p_y}} = 44.3 \pm 0.4$	$\sigma_{\mathrm{str,\,p_y}} = 16.8 \pm 0.6$
C	$\sigma_{\mathrm{p_x}} = 36.4 \pm 0.4$	$\sigma_{\mathrm{str,\,p_x}} = 18.7 \pm 0.5$
	$\sigma_{\mathrm{p_y}} = 45.1 \pm 0.4$	$\sigma_{\mathrm{str,\,p_y}} = 18.8 \pm 0.6$
MT	$\sigma_{\mathrm{p_x}} = 31.2 \pm 0.3$	
	$\sigma_{\mathrm{p_y}} = 41.0 \pm 0.5$	

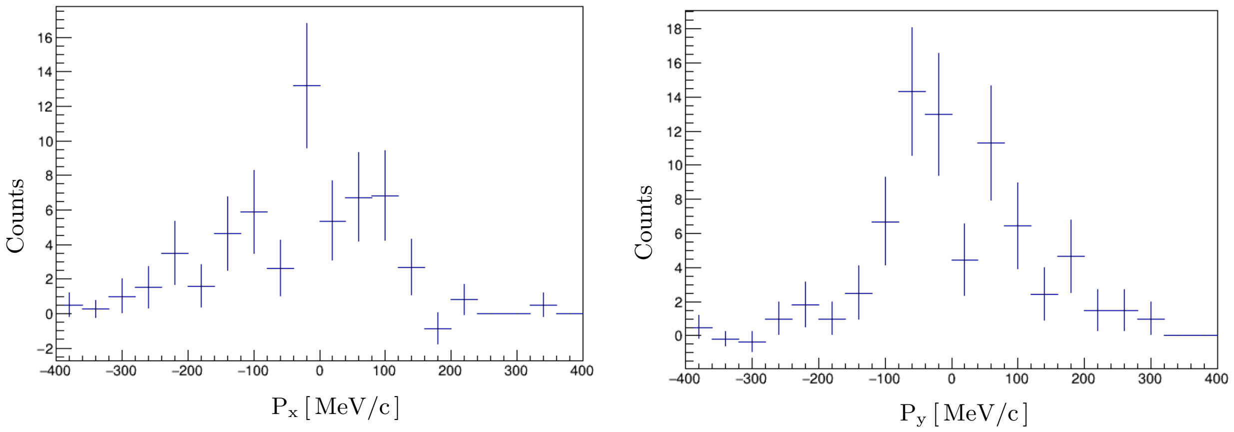

(a) The x-component of the transverse momentum

(b) The y-component of the transverse momentum

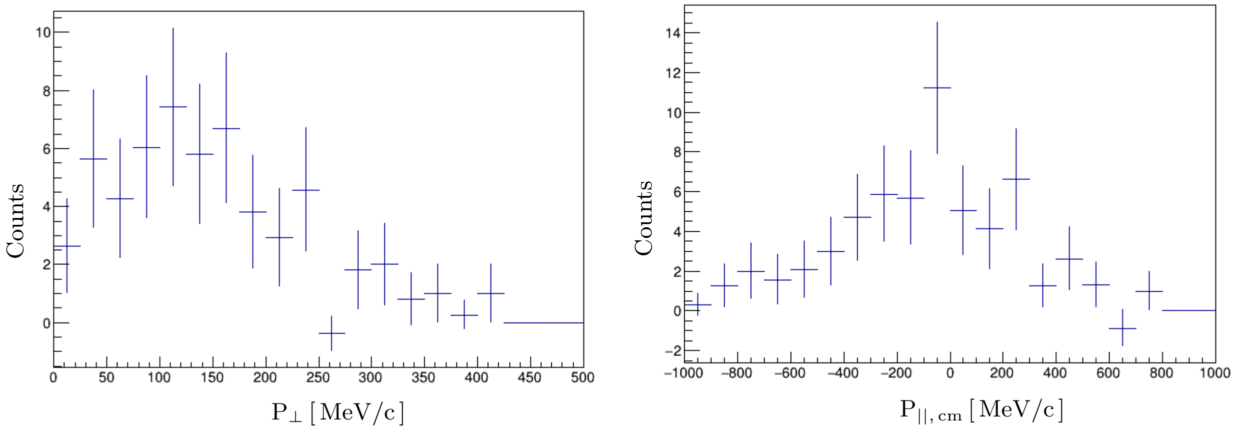

(c) The transverse momentum

(d) The longitudinal momentum

Figure 96: The momentum distributions of the reacted ^{21}F beam for the reconstructed H target. A cut of XB trigger Tpat&8 == 8, and a multiplicity of two protons in coincidence with the fragment of interest ^{20}O was applied.

Chapter 7: Discussion

This chapter provides a brief overview of recent results for reaction channels $^{19-20}$O and $^{21-23}$F; it compares the results of this study with previous literature.

In this study, the quasi-free scattering reaction (p,2p) in inverse kinematics was utilized to provide essential insights into the single-particle strength's dependence on the isospin asymmetry of the nuclei of interest. Thus, the separation energy of the parent and daughter nuclei is shown in Table 31. The QFS reaction is characterized by the angular correlations of the emerged proton pairs; the opening angle between them is around 80 °. The internal momenta of the removed nucleon while in the projectile nuclei affect the momentum distribution's width and shape of the remaining fragment. Thus, a comparison between the experimental and theoretical momentum distribution $\mathrm{P_y}$ of the residual nuclei for the $^{19}\mathrm{O(p,2p)}^{18}\mathrm{N}$ and $^{22}\mathrm{F(p,2p)}^{21}\mathrm{O}$ reaction channel is presented in Figure 97. It is apparent from this figure that the theoretical inclusive distributions show good agreement with the experimental distributions. Furthermore, the experimental momentum distributions $\mathrm{P_y}$ of the residual nuclei for the $^{20}\mathrm{O(p,2p)}^{19}\mathrm{N}$ and $^{21}\mathrm{F(p,2p)}^{20}\mathrm{O}$ reaction channel are shown in Figure 98.

Table 31: Separation energies of the parent and daughter nuclei of the reaction of interest [16].

Reaction channel	Parent			Daughter		
	$\mathrm{S_p}$ (MeV)	$\mathrm{S_n}$ (MeV)	ΔS (MeV)	$\mathrm{S_p}$ (MeV)	$\mathrm{S_n}$ (MeV)	ΔS (MeV)
$^{20}\mathrm{O(p,2p)}^{19}\mathrm{N}$	19.349	7.608	11.741	16.350	5.328	11.022
$^{19}\mathrm{O(p,2p)}^{18}\mathrm{N}$	17.069	3.956	13.113	15.208	2.828	12.380
$^{23}\mathrm{F(p,2p)}^{22}\mathrm{O}$	13.290	7.580	5.710	23.240	6.850	16.390
$^{22}\mathrm{F(p,2p)}^{21}\mathrm{O}$	12.558	5.230	7.328	20.990	3.805	17.185
$^{21}\mathrm{F(p,2p)}^{20}\mathrm{O}$	11.133	8.102	3.031	19.349	7.608	11.741

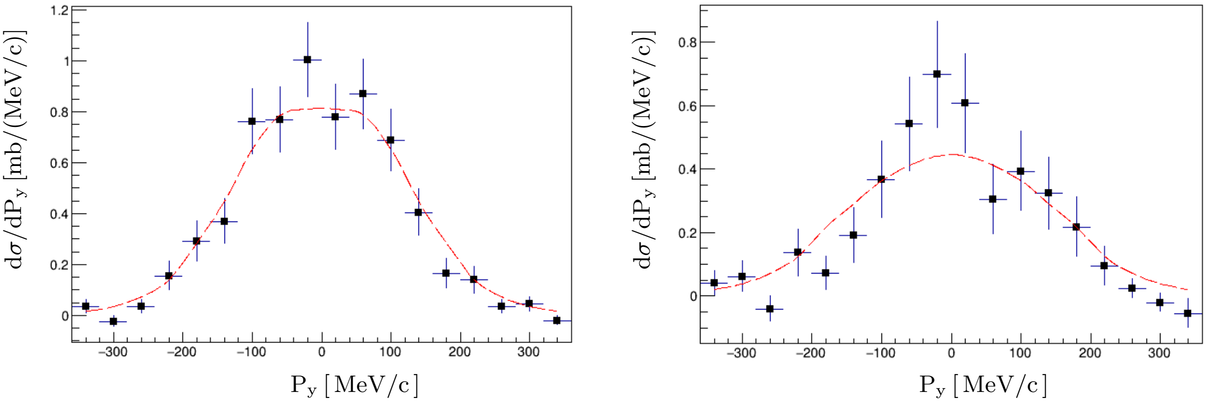

(a) The P_y distribution of $^{19}O(p,2p)^{18}N$.

(b) The P_y distribution of $^{22}F(p,2p)^{21}O$.

Figure 97: The y-component of the transverse momentum distribution of the residual nuclei caused by the QFS off the reacted nuclei of interest ^{19}O and ^{22}F for the reconstructed H target in comparison to the theoretical calculations. The red curve represents the theoretical distributions while the black points indicate the experimental distribution.

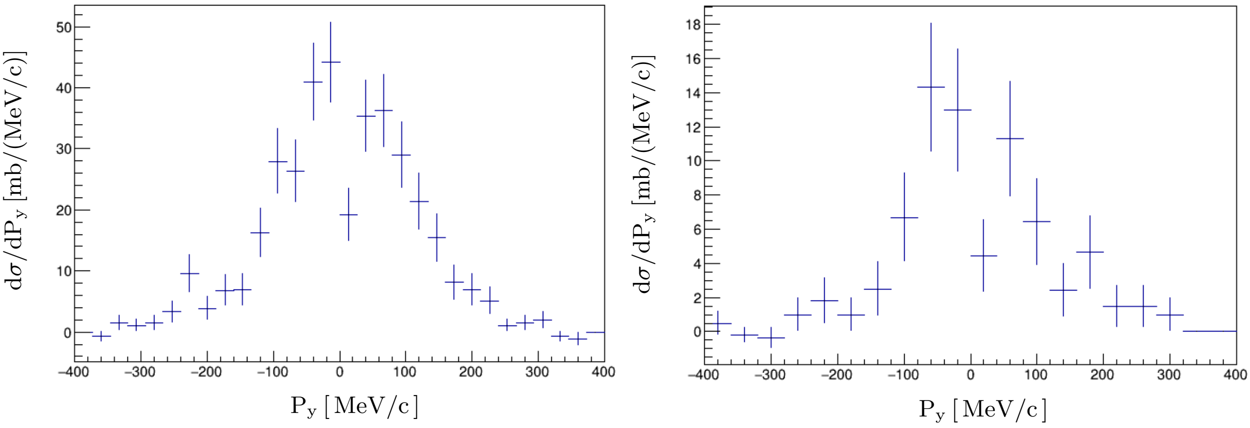

(a) The P_y distribution of $^{20}O(p,2p)^{19}N$.

(b) The P_y distribution of $^{21}F(p,2p)^{20}O$.

Figure 98: The experimental y-component of the transverse momentum distribution of the residual nuclei caused by the QFS off the reacted nuclei of interest ^{20}O and ^{21}F for the reconstructed H target. A cut of XB trigger Tpat&8 == 8, and a multiplicity of two proton in coincidence with the fragment of interest ^{19}N was applied.

The other main finding in this research is extracting the single particle spectroscopic strength obtained by comparing the measured cross section of the single nucleon removal and the theoretical calculations of the related orbits. The results of the inclusive reduction analysis are found in Table 32, where the uncertainty includes both statistical and systematic errors. The results of the inclusive reduction factors of quasi-free scattering of the oxygen isotopic chain $^{14-17}O$ and $^{21,23}O$ in [13] are listed in Table 33, which links these research findings to the previous literature.

Table 32: The obtained inclusive reduction factor of the QFS off the oxygen and fluorine isotopes.

Reaction channel	ΔS (MeV)	R_s
$^{20}O(p,2p)^{19}N$	11.7	...
$^{19}O(p,2p)^{18}N$	13.1	0.61 (5)
$^{23}F(p,2p)^{22}O$	5.7	...
$^{22}F(p,2p)^{21}O$	7.3	0.68(6)
$^{21}F(p,2p)^{20}O$	3.0	...

Table 33: The inclusive reduction factor of the QFS off the oxygen isotopes from previous literature. The reaction channel is given in the first column. The difference in the nucleon binding energy is given in the second column. The neutron and proton separation energy of the daughter nucleus in MeV are given in the third and fourth column, respectively. The inclusive reduction factor is given in the fifth column.

Reaction channel	ΔS (MeV)	$S_n[^{A-1}N]$	$S_n[^{A-1}N]$	R_s	Reference
$^{14}O(p,2p)^{13}N$	-18.6	20.1	1.9	0.68 (7)	[13]
$^{16}O(p,2p)^{15}N$	-3.5	10.9	10.2	0.70 (5)	[13]
$^{17}O(p,2p)^{16}N$	9.6	2.5	11.5	0.65 (5)	[13]
$^{21}O(p,2p)^{20}N$	17.2	2.2	17.9	0.58 (4)	[13]
$^{23}O(p,2p)^{22}N$	22.3	1.3	21.2	0.62 (13)	[13]

What stands out in Tables 31, 32, and 33 is that the neutron or proton separation energy of the daughter nucleus affects the related orbits that contribute to the inclusive cross section as illustrated in Figure 99. Case 1 in Figure 99a is considered for a daughter nucleus with a small S_n or S_p (range 2 to 3 MeV). For this case, only the theory cross section of the valence is used. This consideration seems to be very much in line with previous results presented in Ref. [13], where the reduction factors are only given for the cases where the separation energies of the daughter nucleus of the reaction channels $^{14}O(p,2p)^{13}N$, $^{17}O(p,2p)^{16}N$, $^{21}O(p,2p)^{20}N$, and $^{23}O(p,2p)^{22}N$ is $2-3$ MeV. This gives us confidence that as soon as a proton from a deeper bound orbit is removed, i.e. from $\pi 1p_{3/2}$, the daughter nucleus is left in an unbound state and so it does not contribute to the inclusive cross section. Thus, we can then safely divide the inclusive experimental cross section by the theoretical $\pi 1p_{1/2}$ cross section. Similarly, the $^{22}F(p,2p)^{21}O$ reaction channel has separation energies of the daughter nucleus 3.8 MeV, which may be low enough to consider the same. In other words, only the $\pi 1d_{5/2}$ proton contributes and as soon as the $\pi 1p_{1/2}$ is knocked out, we end up with an unbound daughter nucleus which is not measured in the cross section. Hence, we can divide the inclusive experimental cross section by the $\pi 1d_{5/2}$ theoretical cross section for removing one proton from there.

On the other end, we do not have a case where the daughter nucleus has such a high separation energy that we can safely assume that we remove both valence and protons from deeper orbits and still stay in a bound daughter nucleus as illustrated in Figure 99c. This medium difficulty case is the case for the $^{16}O(p,2p)^{15}N$ reaction channel in Ref. [13], where the daughter nucleus has separation energies higher than 10 MeV; hence, in none of our reaction channels we can "safely" divide the inclusive experimental cross section by all the theoretical cross section of the related orbits. The $^{23}F(p,2p)^{22}O$, $^{21}F(p,2p)^{20}O$, and $^{20}O(p,2p)^{19}N$ reaction channels are considered complicated cases as illustrated in Figure 99b.

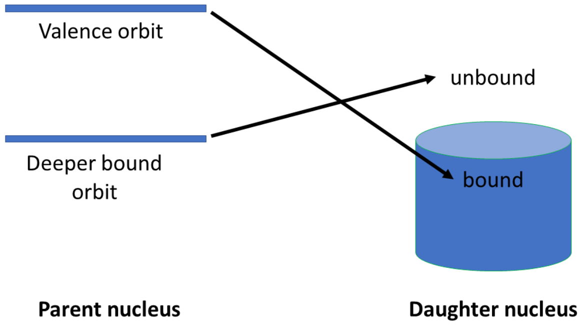

(a) Case 1: simple

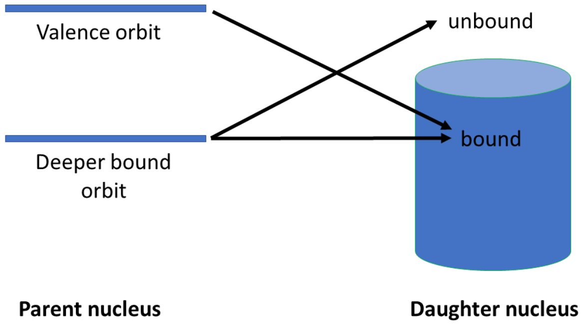

(b) Case 2: complicated

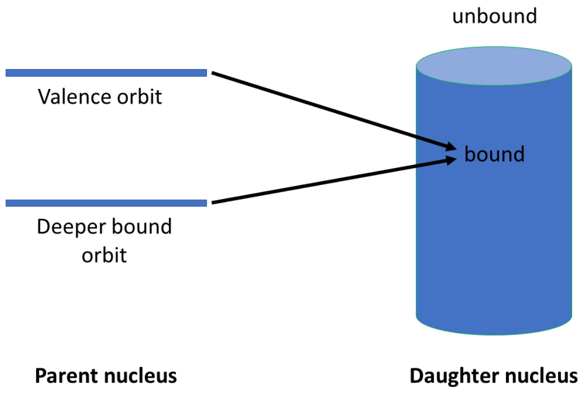

(c) Case 3: medium difficulty

Figure 99: Three main cases of the orbits contribution to the total cross section. (a) simple case, where the daughter nucleus has small S_n or S_p, 2-3 MeV. Only the valence orbit contributes to the cross section. (b) complicated case, where the daughter nucleus has medium S_n or S_p. The valence and part of the deeper bound orbit strength contribute to the cross section. Thus, a structure calculation is needed. (c) medium difficulty case, where the daughter nucleus has large S_n or S_p. The valence and deeper bound orbit strength contribute to the cross section.

Together, these data of the inclusive reduction factors are presented in Figure 100. The ^{19}O is consistent with the claim of the absence of dependence on the isospin asymmetry within the oxygen isotopic chain as shown in Figure 100. Furthermore, the obtained inclusive reduction factor of ^{22}F is within the range of the reduction factors of the oxygen isotopic chain.

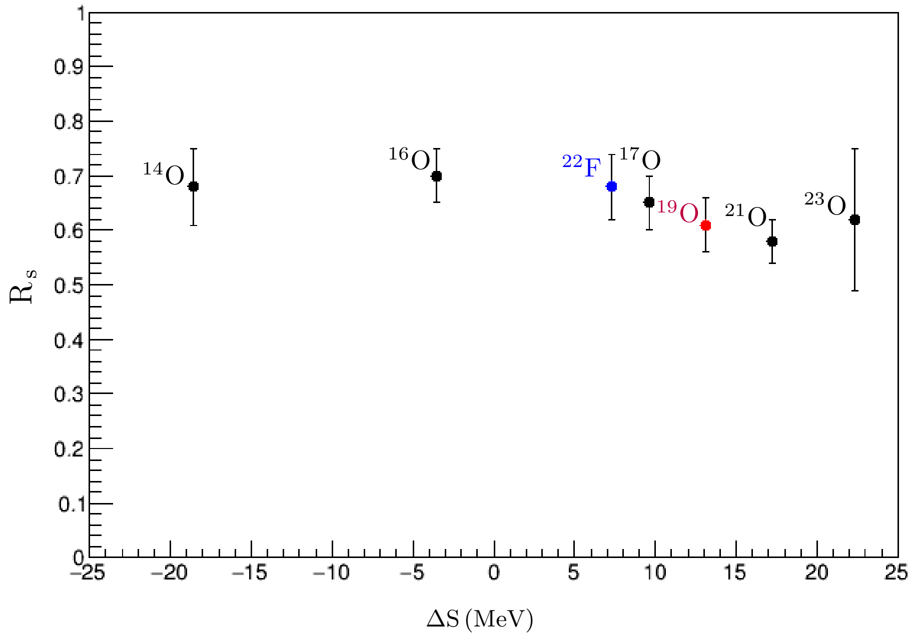

Figure 100: The inclusive reduction factor as a function of the difference in the nucleon binding energy $\Delta S = S_p - S_n$ for proton removal. The black closed markers indicate proton removal via the QFS from previous research [13]. The colored markers indicate the result of this work; oxygen isotope in red and fluorine isotope in blue.

Chapter 8: Development and Testing of the R^{3}B Si-tracker

This chapter introduces the basic information about the potential future R^{3}B Si-tracker and summarizes the test results. It is organized in the following way; the first section of this chapter briefly introduces the potential future R3B Si-tracker. The second chapter illustrates the detector design, starts with its sensors, and ends with the completed detector. The third section summarizes the utilized simulation. Finally, the last section presents the results of alpha source measurements.

8.1 Introduction

The potential future R^3B silicon tracker is a novel UK-built instrument that aims to increase the sensitivity of hadron-induced quasi-free scattering at R^3B setup in the near future. A team of UK universities and Laboratories designed and constructed the silicon tracker. And STFC Daresbury and Rutherford Appleton Laboratories provided front-end electronics [65, 66]. The R^3B silicon-tracker is set inside a vacuum vessel and surrounding the target in the R3B setup to obtain particle interaction information and vertex measurements [65, 66] .

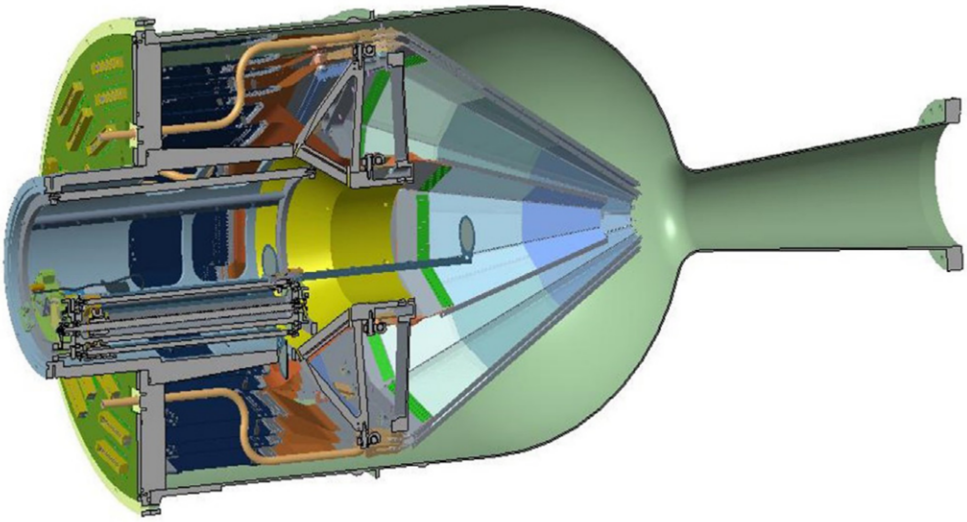

Figure 101: The R^{3}B Si-tracker is fixed in a vacuum chamber that made of aluminum and has a thickness of $2\,mm$ and a volume of approximately $0.148\,m^3$ [66]. Despite the picture, the target is surrounded by two layers of the existing R^{3}B silicon tracker; one inner layer and one outer layer.

8.2 Detector Design

The R^3B Si-tracker is made of two individualistic layers of double-sided silicon. One inner layer is located closest to the target, and one outer layer is placed farther away from the inner layer as shown in Figure 101. Its total active area is around $0.31\,\mathrm{m}^2$ made of a total of 18 silicon detectors connected to 528 ASICs (Application Specific Integrated Circuit) and each ASIC has 128 channels, that gives a total of 67584 channels as illustrated in Table 34. The inner layer comprises six detectors, while the outer layer consists of twelve detectors. Its arrangement provides an angular coverage that goes from 6 to 103°. Its unique design provides high-resolution position (x,y,z), time and energy loss measurement for the passing charged particle, mostly protons [65, 66].

Table 34: The characteristics of the layers in the R^3B Si-tracker layers [65].

Layer	No. of Detectors	Active Area (cm^2)	No. of ASICs	No. of Channels
Inner	6	722	144	18432
1st Outer	12	2426	384	49152
Total	18	3148	528	67584

8.2.1 Sensors

The detectors in the inner and outer layer are made of different types of double-sided strip sensors wire (A, B, C, D) as shown in Figure 102, and they are alike from the technology view. Sensors bulk is an n-type with high resistivity, approximately $103\,\Omega\,\mathrm{cm}$, and a thickness of $300\,\mu\mathrm{m}$. However, their active area and number of strips vary, as illustrated in Table 35. Figure 103 shows that each detector within the inner layers comprises two sensors (B and D) connected to a total of 24 ASICs; 12 ASICs for each face. In contrast, individual detector within the outer layer is more significant than the detector in the inner layer. It comprises three sensors (A, B, and C) bonded to a total of 32 ASICs; each face has 16 ASICs. Furthermore, the n-type strips are covered with a p-spray implant to decrease the damage on the silicon oxide caused by the Total Ionizing Dose (TID) [66].

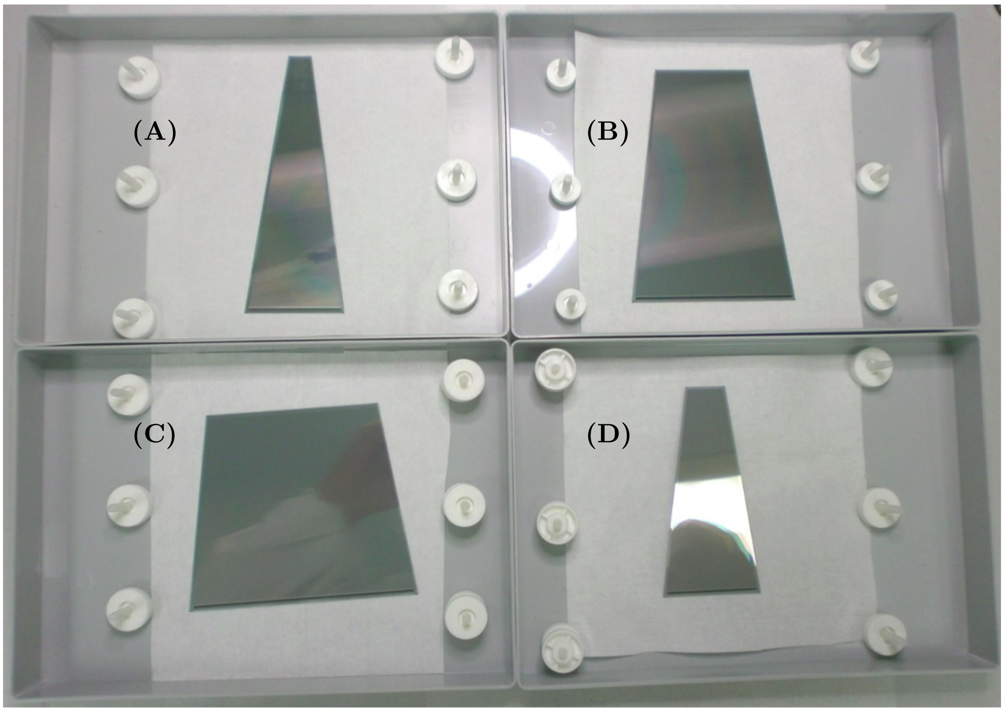

Figure 102: Photograph of the different types of the double-sided Si sensors (A, B, C, D) for the construction of the Si detectors of the inner and outer layer of the R^3B Si-tracker [65].

Table 35: The characteristics of different types of Si-tracker sensors (A, B, C, D) that are utilized for the formation of the Si detectors for the R^{3}B Si-tracker layers [65, 66].

Sensor Type	No. of Strips	Thickness (μm)	Active Area (cm^2)
A	889	300	31
B	1536	300	48
C	2048	300	49
D	876	300	24

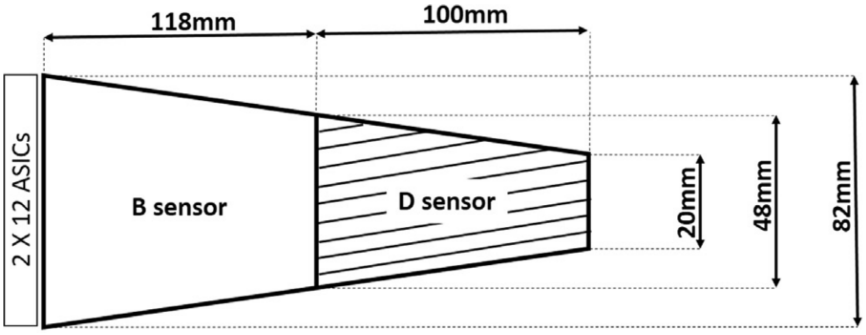

(a) The inner detector of the R^3B Si-tracker.

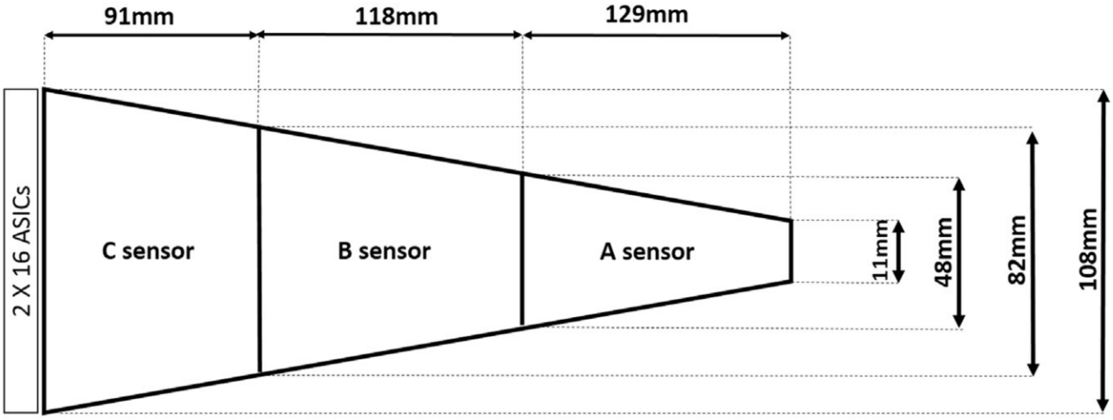

(b) The outer detector of the R^3B Si-tracker

Figure 103: A schematic drawing for the R^3B Si-tracker layers; (a) The inner detector comprises two sensors (B and D) connected to a total of 24 ASICs. (b) The outer detector comprises three Si-sensors (A, B, and C) connected to a total of 32 ASICs [66].

Every strip pitch in the sensor has a fixed width equal to $50\,\mu$m; $38\,\mu$m for the strip width and $12\,\mu$m for the gap width. In contrast, the strip length variety when running from one tilted side to the other since the strips are inclined with an angle of $16.2\,^\circ$ and set parallel to one of the two tilted sides, as shown in sensor D in Figure 103a [66]. The same adjustment was applied to the strips on the opposite face, as shown in Figure 104. This arrangement is essential to reduce the chance of having ghost combination hits besides the original hits. Ghost combination is manifest in the orthogonal arrangement, where a single strip on one face crosses the whole strips on the opposite face of the sensor, as shown in Figure 105a. Thus, a hit of a charged particle on the vertical strips only gives a position in the x-axis. Consequently, position in the y-axis is obtained by examining all recorded hits in the opposite strips. In the case illustrated in Figure 105a, there are two real hits and two ghost hits, which is not seen in the tilted strips, Figure 105b. [65].

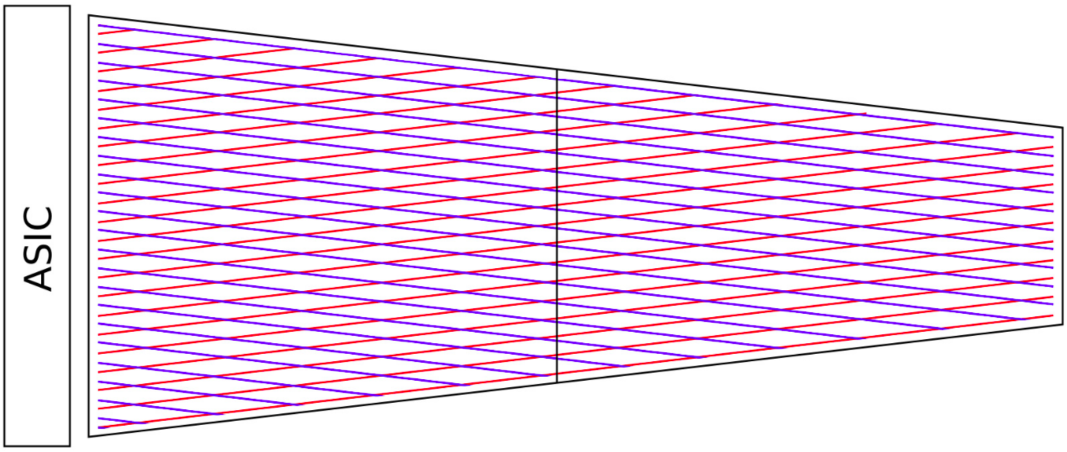

Figure 104: The tilted arrangement for the strips on the inner detector of the R^{3}B Si-tracker. The red lines indicate the strips on one face, while the blue lines show strips on the other [65].

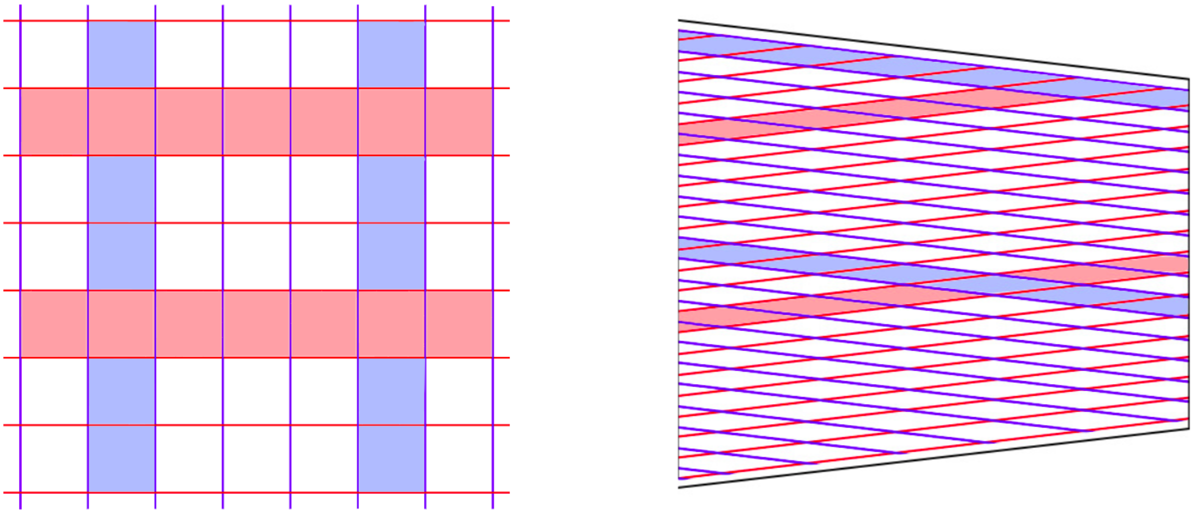

(a) The orthogonal strips arrangement.

(b) The tilted strips arrangement.

Figure 105: (a) The schematic of the orthogonal strip arrangement, where each strip crosses whole strips on the other face, shows two real hits and two combination ghost hits. (b) The schematic of the tilted strip arrangement, where the strips on each face are tilted with 16 deg, exhibits two real hits. Thus, the ghost combination hits are reduced in this arrangement [65].

8.2.2 Si Assembly

Appropriate silicon sensors for the layer type are fixed on a suitable Carbon Fibre Frame (CFF), as shown in Figure 106a for an outer detector, and glued by using the Araldite 2011. The CFF is made by combining several various carbon fibre bars in the shape of trapezoidal. The bars are produced by putting carbon fibres into a container and filling the container with epoxy resin. Then they are covered with an insulating lacquer. The sensors are wire-bonded unitedly strip by strip on both faces as illustrated in Figure 106b for the Si-assembly of the outer detector [66].

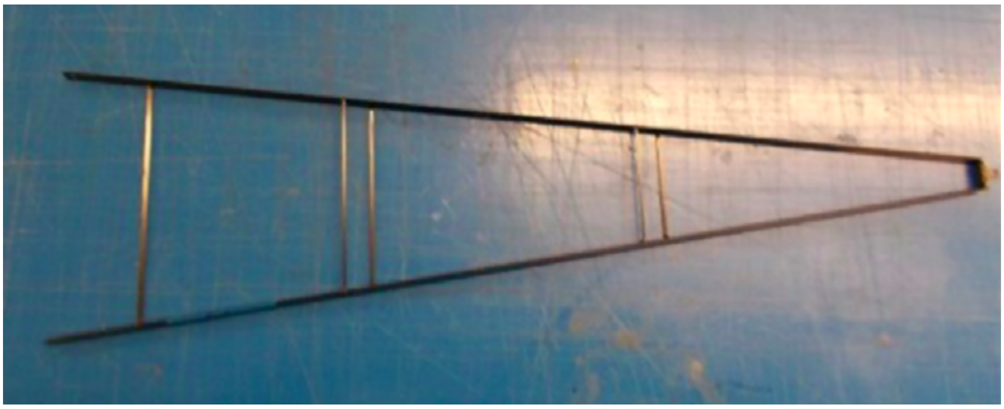

(a) The Carbon Fibre Frame (CFF) for an outer detector.

(b) The Si-assembly of the outer detector.

Figure 106: (a) The used carbon fibre bars to mount the sensors of the Si-assembly for an outer detector. (b) The Proper sensors are mounted on the CFF, and the strips are bonded together [66].

8.2.3 ASIC Assembly

The signals of the charged particles in the inner and outer layers are read out from the sensor's strips by the ASIC chips. Then the digitized signals are transferred to a Flexible Printed Circuit board (FPC) connected to the buffer card. However, heat is generated by the ASICs, and to arise it, the ASIC assembly carries a copper cooling block, as illustrated in Figure 107a. Hence, a mixture of water and glycol is used to maintain the temperature of the detectors around $20\,^{\circ}$C. A similar Flexible Printed Circuit (FPC) is used in an ASIC assembly on the other side of the cooling block and connected to ASIC chips, as shown in Figure 107b. Both FPCs are attached to cooling blocks by utilizing bi-adhesive copper tape. The ASICs are set up on the FPC by using thermally conductive glue [65, 66].

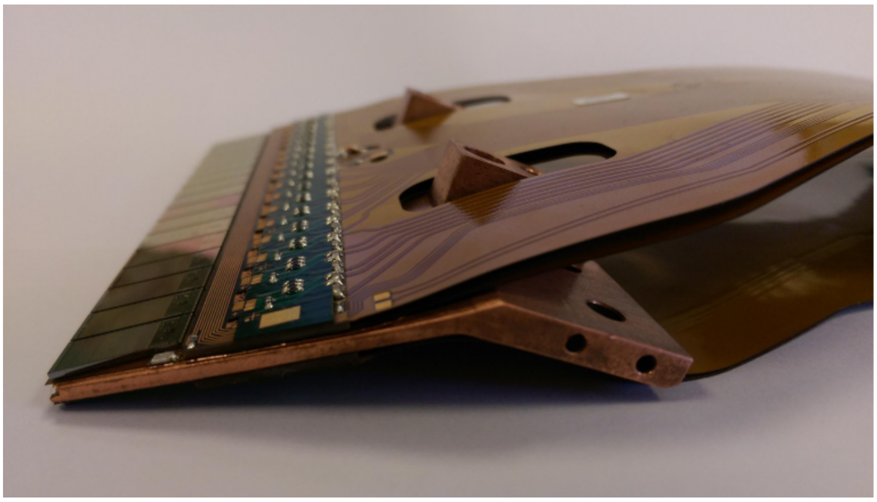

(a) Side photo of the ASCI assembly.

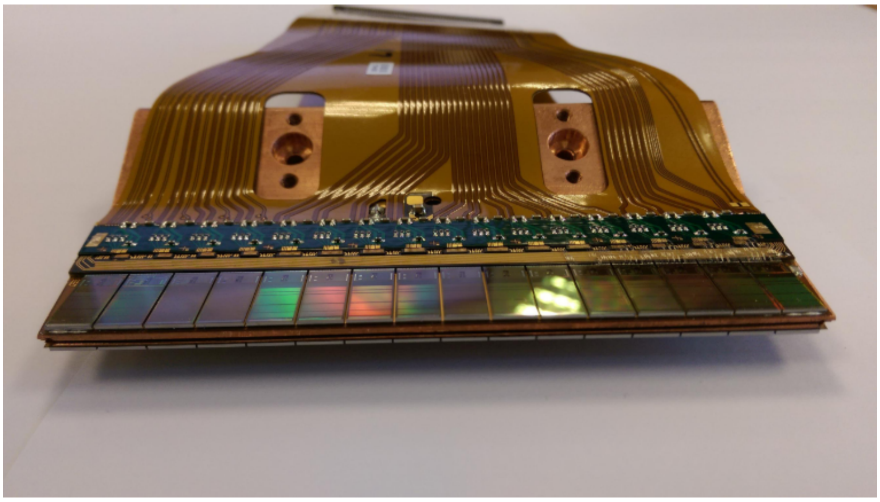

(b) Front photo of the ASCI assembly.

Figure 107: Pictures of the ASIC assembly of the outer detector. (a) A side view of an assembly of the FPC, ASIC chips, and cooling block. (b) A front view of the ASIC assembly shows 16 ASICs on each side, two identical FPCs, and a cooling block [65]

8.2.4 Completed Detector

Both Si and ASIC assembly are connected to build the complete detector represented in Figure 108 for an outer detector. Each silicon strip in the Si assembly is connected to a channel in ASIC assembly, where the individual ASIC has 128 channels [65], as shown in Figure 109.

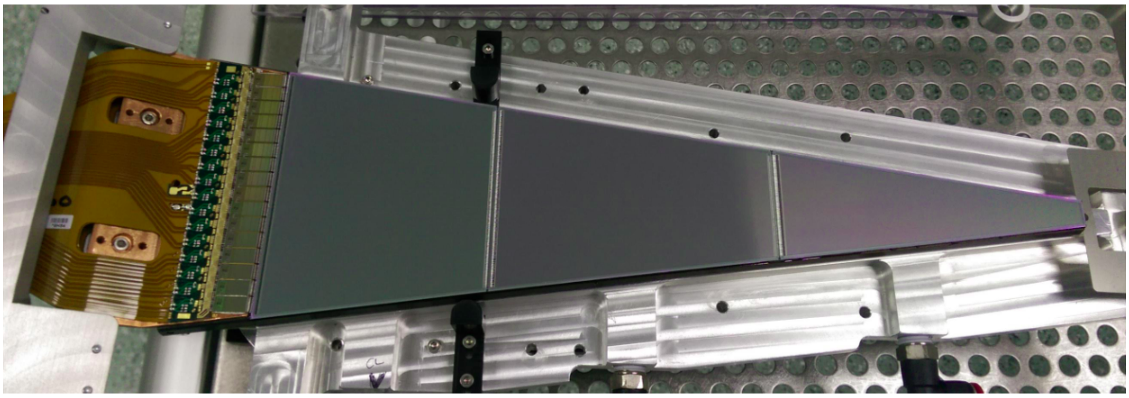

Figure 108: The production of the outer detector [65].

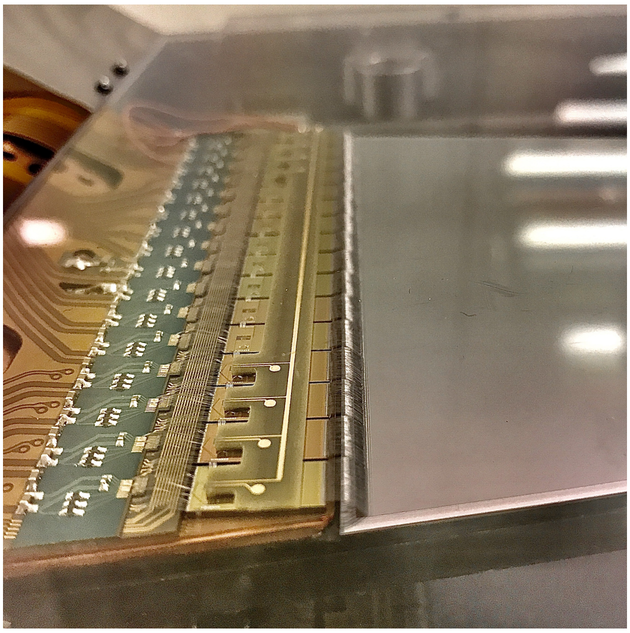

Figure 109: The connection of the Si-strips in the Si-assembly to the channels in the ASIC-assembly.

8.3 Simulation

The simulation of the R^3B Si-tracker in the R3BRoot has been developed by Marc Labiche at STFC Daresbury Laboratory. The R3BRoot [57] software package was used to simulate and analyse the response of the R^{3}B Si-tracker to the scattered protons from the quasi-free scattering reaction ^{48}Ca$(p, 2p)^{47}$K in inverse kinematics at different relativistic energy. The energy threshold of the R^{3}B Si-tracker for the QFS scattering reaction was then evaluated.

The QFS event generator, as illustrated previously in section 5.2.1, was utilized to produce the scattered protons for the reaction at an energy of 500 and 1000 MeV with Liquid Hydrogen target (LiH_2). The ASCII output file of the generator was then used as an input for the R3BRoot simulation. The LiH_2 target and the R^{3}B Si-tracker were included as shown in the simulated geometry in Figure 110.

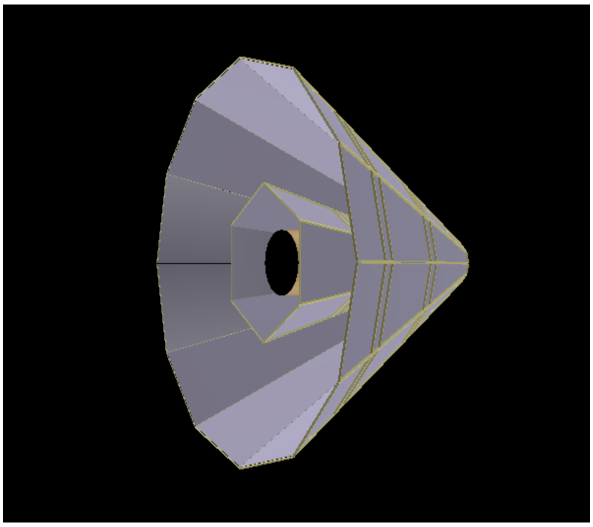

Figure 110: The simulated geometry of the R^3B Si-tracker included the LiH_2 target implemented in the R3BRoot.

Subsequently, the angular distribution and energy loss of the scattered proton were analysed. Figure 111 shows the angular correlations of the polar (θ) and azimuthal (ϕ) angles of the detected scattered protons, and Figure 112 shows the opening angle between them nearly 80° as expected for the QFS scattering.

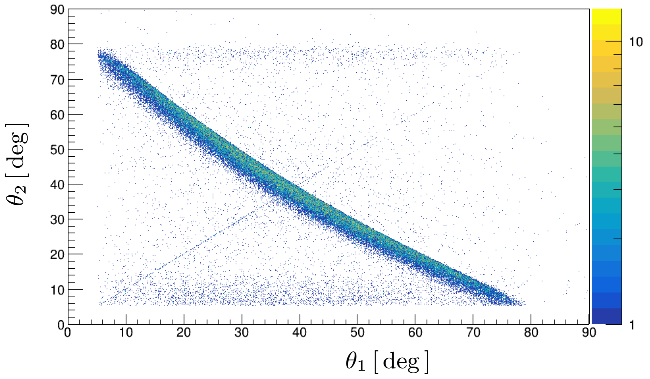

(a) Polar (θ) angles.

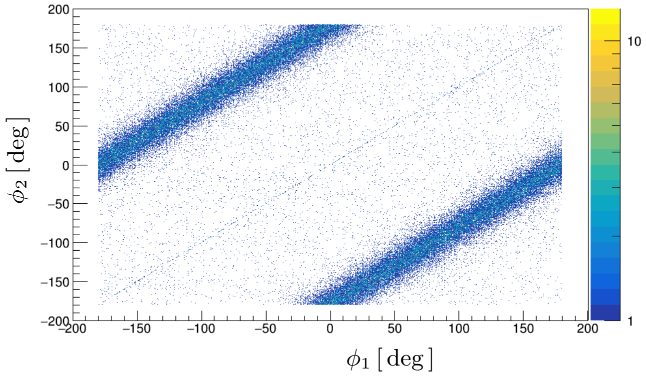

(b) Azimuthal (ϕ) angle.

Figure 111: The simulated correlations of the polar and azimuthal angles of the two detected protons from the quasi-free scattering in inverse kinematics.

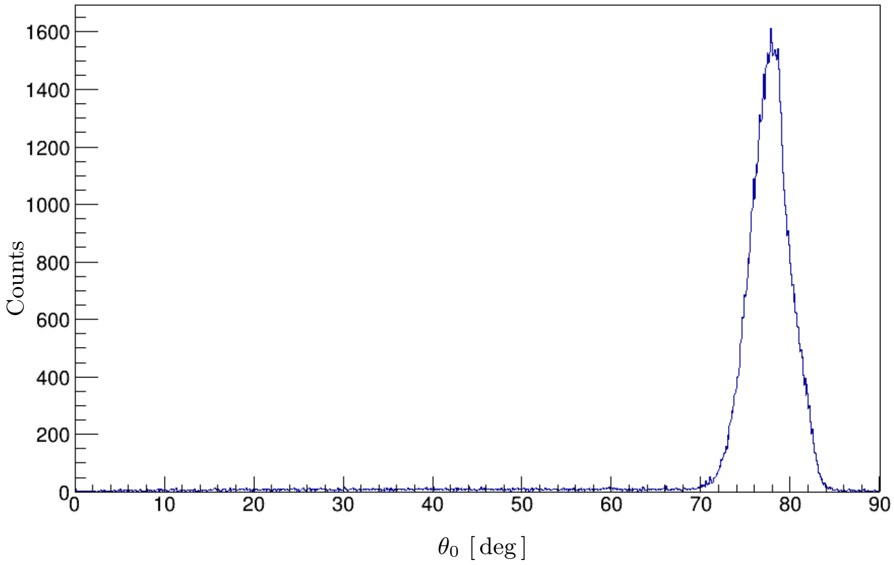

Figure 112: The simulated opening angles of the two detected protons from quasi-free scattering in inverse kinematics.

For the energy loss of the detected protons by the R^{3}B tracker, the simulation was used at two relativistic beam energies, 500 MeV and 1000 MeV, as shown in Figure 113. Most of the events are going to be around 0.1 MeV, which indicates the required minimum threshold energy of the future R^{3}B silicon detectors.

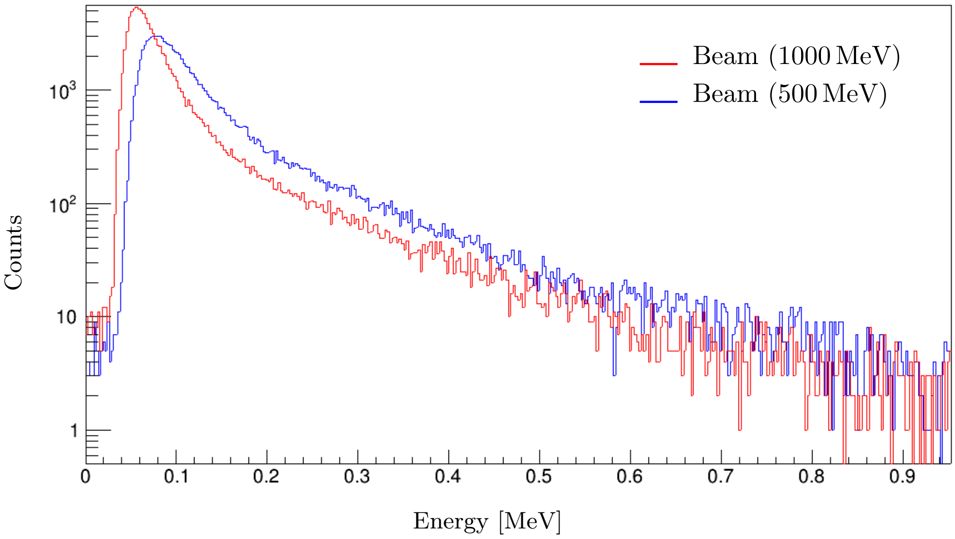

Figure 113: The simulated energy loss of the detected proton from quasi-free scattering at 500 MeV, and 1000 MeV in the R^3B silicon tracker.

8.4 Alpha Source Measurements

The R^3B Si-tracker detector is placed at STFC Daresbury Laboratory, Daresbury in the UK, to be tested under clean-room conditions to evaluate and characterise the tracker. Figure 114 shows a vacuum chamber where the Si-tracker is mounted inside. As illustrated in Table 36, a mixed alpha source Pu-239, Am-241, and Cm-244 with well-defined energies were used in 2018 to calibrate the inner silicon detectors and obtain energy resolution for the inner detectors.

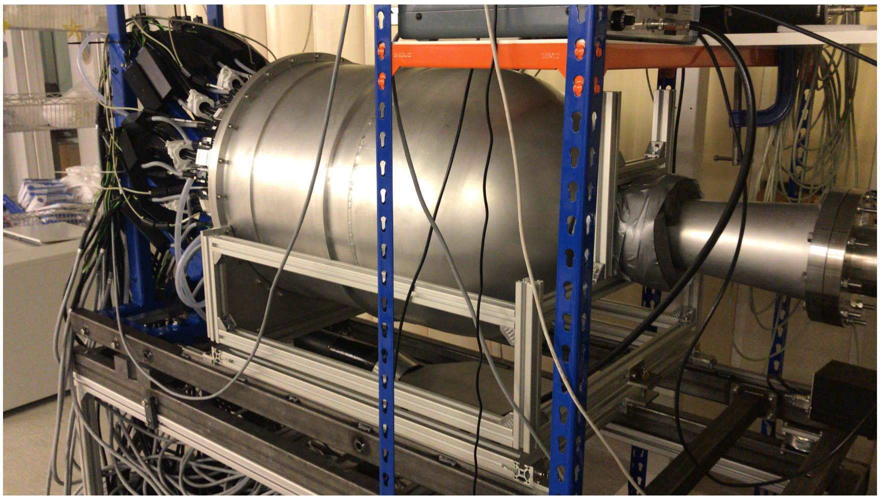

(a) Photo of the closed-chamber

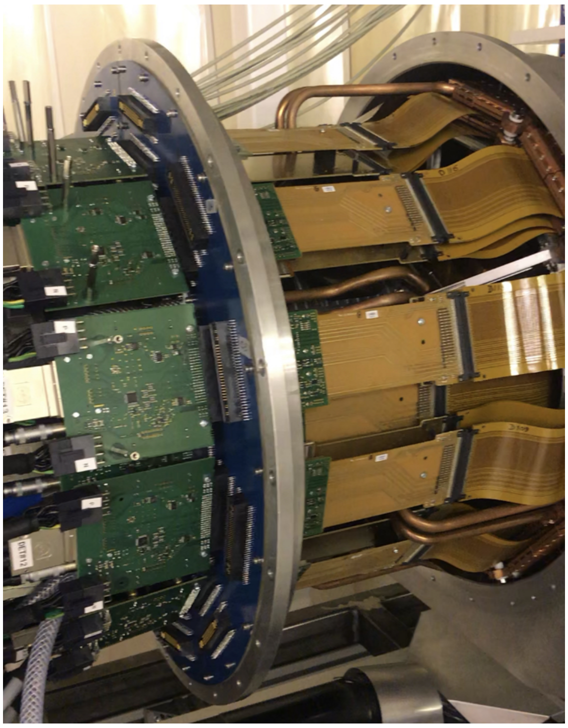

(b) A Photo of the partially opened-chamber.

Figure 114: A photograph of a vacuum chamber at STFC Daresbury Laboratory. The R^3B Si-tracker is mounted inside the chamber.

Table 36: The characteristics of the mixed alpha source that was used for testing the performance of the R^{3}B Si-tracker.

Radioactive Nuclei	Energy of the strongest alpha peak (MeV)
Pu-239	5.155
Am-241	5.486
Cm-244	5.805

The calibrated spectrum of the detected alpha source is shown in Figure 115. The calibration was carried out automatically for thousands of strips of the R^{3}B Si-tracker by a written script.

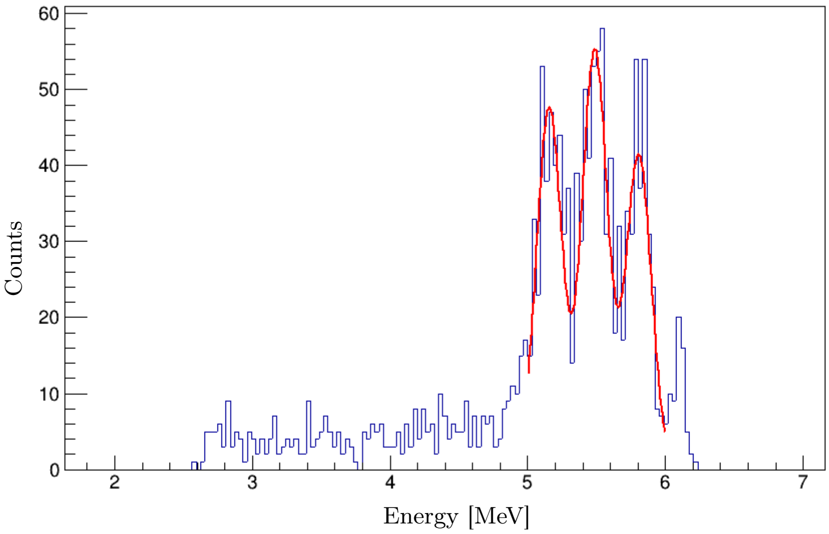

Figure 115: The energy for module 55, ASIC 5, channel 125.

Then, the strip number in the same detector was calculated by the following formula for the final result:

$$\text{Strip} = (\text{ASIC} \times 128) + \text{Channel} \tag{63}$$

Overall, the result of this chapter is illustrated in Figure 116, it shows the energy resolution following the length of the strip. At a more recent investigation carried out by Aaron Stott and Luke Rose this has been attributed to incident angle of the alphas due to the geometry of the measurement rather than due to the strip capacitance. Thus, when this geometric effect is corrected, the average energy resolution is approximately 0.13 MeV.

The work is still ongoing by Aaron Stott, Luke Rose, Stefanos Paschalis (university of York), and Marc Labiche (STFC Daresbury Laboratory).

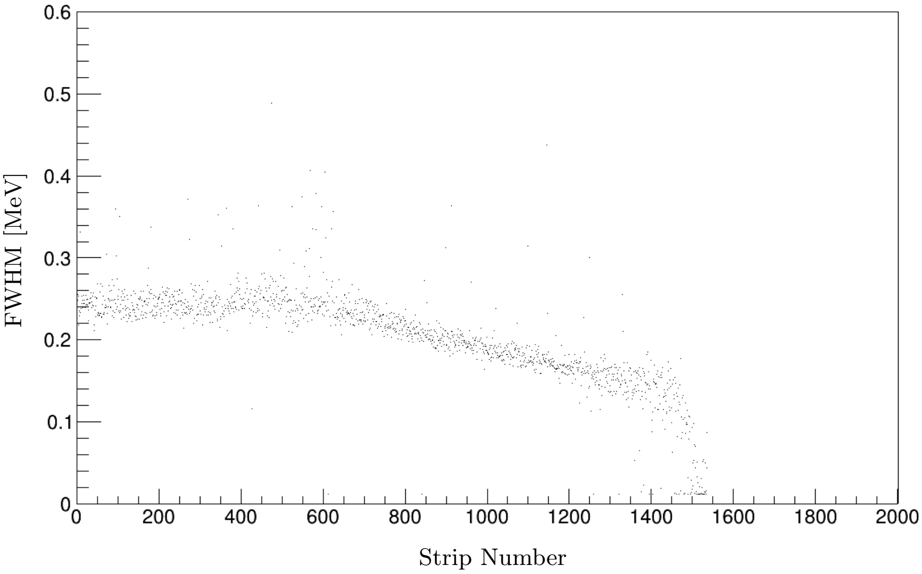

Figure 116: The energy resolution (FWHM in MeV) of Module 55 of the future R^3B silicon detector.

Chapter 9: Conclusion and Outlook

The research aimed to investigate the dependence of the neutron-rich side of oxygen and fluorine isotopic chain on the neutron-proton asymmetry by removing a proton from nuclei of interest $^{19-20}$O and $^{21-23}$F, utilizing the QFS reaction (p,2p) in the inverse kinematics. The S393 experiment was performed at the R^{3}B setup in GSI (Germany). Two main types of targets were used for this research, CH$_2$ and C, to reconstruct the hydrogen target.

To obtain the reduction factor, two values were extracted from the experiment: the inclusive cross section by identifying the incoming and outgoing particles of interest for the reaction channel and the population of each observed excited state by measuring the gamma-ray of the de-excited residual nuclei in coincidence with detecting the residual nuclei and two scattered protons. The inclusive reduction factor was calculated by taking the ratio between the inclusive experimental cross section and the total theoretical cross section of the related orbits predicted from DWIA calculations done by Carlos Bertulani [27]. Moreover, a comparison of the experimental and theoretical momentum distributions of the residual nuclei for the $^{19}\mathrm{O(p,2p)}^{18}\mathrm{N}$ and $^{22}\mathrm{F(p,2p)}^{21}\mathrm{O}$ reaction channels is presented in Figure 97. The shown comparisons for the analysed channels indicate good agreement between the experimental and theoretical distributions. Furthermore, the experimental momentum distribution $\mathrm{P_y}$ of the residual nuclei for the $^{20}\mathrm{O(p,2p)}^{19}\mathrm{N}$ and $^{21}\mathrm{F(p,2p)}^{20}\mathrm{O}$ reaction channels is shown in Figure 98.

The resulting inclusive reduction factors of this investigation are plotted with the individual difference of the proton and neutron separation energy ΔS and compared with other isotopes from the literature, as illustrated in Figure 100. Overall, the obtained results presented in Figure 100 indicate the absence of any strong dependence of the reduction factor on the neutron-proton asymmetry. Furthermore, the obtained inclusive reduction factor of ^{22}F is within the range of the reduction factors of the oxygen isotopic chain. However, further studies need to be carried out to obtain the inclusive reduction factors of the complicated cases and to develop a full picture of the fluorine isotopic chain.

Furthermore, this thesis presents part of the development and testing of the R^{3}B Si-tracker at the STFC Daresbury Laboratory in the UK.

References

[1] H. Kragh, "Rutherford, Radioactivity, and the Atomic Nucleus," pp. 1–30, 2012.

[2] J. Chadwick, "The Existence of a Neutron." *Proceedings of the Royal Society of London. Series A, Containing Papers of a Mathematical and Physical Character*, vol. 136, no. 1930, pp. 692–708, 1932.

[3] M. G. Mayer, "On closed shells in nuclei. II," *Physical Review*, vol. 75, no. 12, pp. 1969–1970, 1949.

[4] O. Haxel, J. H. D. Jensen, and H. E. Suess, "On the "magic numbers" in nuclear structure," *Physical Review*, vol. 75, no. 11, p. 1766, 1949.

[5] A. Obertelli and H. Sagawa, *Modern Nuclear Physics: From Fundamentals to Frontiers.* Springer, 2021.

[6] "The National Nuclear Data Center." [Online]. Available: https://www.nndc.bnl.gov/

[7] J. A. Tostevin and A. Gade, "Updated systematics of intermediate-energy single-nucleon removal cross sections," *Physical Review C*, vol. 103, no. 5, p. 054610, 2021.

[8] D. A. Divaratne, C. R. Brune, H. N. Attanayake *et al.*, "One- and two-neutron removal cross sections of 24O," *Physical Review C*, vol. 98, no. 2, p. 024306, 2018.

[9] J. A. Tostevin and A. Gade, "Systematics of intermediate-energy single-nucleon removal cross sections," *Physical Review C*, vol. 90, no. 5, p. 057602, 2014.

[10] Z. Y. Sun, D. Yan, S. T. Wang *et al.*, "Knockout reactions from 14O at 305 MeV/nucleon," *Physical Review C*, vol. 90, no. 3, p. 037601, 2014.

[11] B. A. Brown, P. G. Hansen, B. M. Sherrill *et al.*, "Absolute spectroscopic factors from nuclear knockout reactions," *Physical Review C*, vol. 65, no. 6, p. 061601, 2002.

[12] J. Lee, M. B. Tsang, D. Bazin *et al.*, "Neutron-Proton Asymmetry Dependence of Spectroscopic Factors in Ar Isotopes," *Physical review letters*, vol. 104, no. 11, p. 112701, 2010.

[13] L. Atar, S. Paschalis, C. Barbieri *et al.*, "Quasifree (p,2p) Reactions on Oxygen Isotopes : Observation of Isospin Independence of the Reduced Single-Particle Strength," *Physical review letters*, vol. 120, no. 5, p. 052501, 2018.

[14] S. Kawase, T. Uesaka, T. L. Tang *et al.*, "Exclusive quasi-free proton knockout from oxygen isotopes at intermediate energies," *Progress of Theoretical and Experimental Physics*, vol. 2018, no. 2, p. 021D01, 2018.

[15] T. L. Tang, T. Uesaka, S. Kawase *et al.*, "How Different is the Core of 25F from 24Og.s. ?" *Physical Review Letters*, vol. 124, no. 21, p. 212502, 2020.

[16] M. Wang, W. J. Huang, F. G. Kondev *et al.*, "The AME 2020 atomic mass evaluation (II). Tables, graphs and references," *Chinese Physics C*, vol. 45, no. 3, p. 030003, 2021.

[17] K. S. Krane, *Introductory Nuclear Physics.* Hoboken NJ:Wiley, 1987.

[18] A. Kamal, *Nuclear physics.* Springer, 2014.

[19] J. Al Khalili and E. Roeckl, *Lecture Notes in Physics.* Springer.

[20] P. G. Hansen and J. A. Tostevin, "Direct Reactions with Exotic Nuclei," *Annual review of nuclear and particle science*, vol. 53, pp. 219–261, 2003.

[21] L. Atar, "Investigation of the Single-Particle Structure of Oxygen Isotopes in Quasi-free Knockout Reactions at the R3 B/LAND Setup," Ph.D. dissertation, Technische Universität, 2015.

[22] V. Panin, M. Holl, J. T. Taylor *et al.*, "Quasi-free proton knockout from 12C on carbon target at 398 MeV/u," *Physics Letters B*, vol. 797, p. 134802, 2019.

[23] M. Holl, "Quasi-Free Scattering from Relativistic Neutron-Deficient Carbon Isotopes," Ph.D. dissertation, Technische Universität, 2014.

[24] P. Díaz Fernández, "An investigation into quasi-free scattering of light neutron-rich nuclei around N=14," Ph.D. dissertation, Universidade de Santiago de Compostela, 2013.

[25] I. J. Syndikus, "Proton-Knockout Reactions from Neutron-Rich N Isotopes at R3B," Ph.D. dissertation, Technische Universität, 2019.

[26] C. A. Bertulani and A. Gade, "MOMDIS: a Glauber model computer code for knockout reactions," *Computer Physics Communications*, vol. 175, no. 5, pp. 372–380, 2006.

[27] T. Aumann, C. A. Bertulani, and J. Ryckebusch, "Quasifree (p,2p) and (p,pn) reactions with unstable nuclei," *Physical Review C*, vol. 88, no. 6, p. 064610, 2013.

[28] "UNILAC Overview." [Online]. Available: https://www.gsi.de/en/work/beschleunigerbetrieb/beschleuniger/unilac

[29] "Heavy-Ion-Synchrotron SIS18." [Online]. Available: https://www.gsi.de/en/work/accelerator_operations/accelerators/heavy_ion_synchrotron_sis18

[30] "Fragment Separator FRS." [Online]. Available: https://www.gsi.de/en/researchaccelerators/accelerator_facility/fragment_separator

[31] H. Geissel, P. Armbruster, K. H. Behr *et al.*, "The GSI projectile fragment separator (FRS): a versatile magnetic system for relativistic heavy ions," *Nuclear Instruments and Methods in Physics Research Section B: Beam Interactions with Materials and Atoms*, vol. 70, no. 1, pp. 286–297, 1992.

[32] S. N. Ahmed, "Physics and engineering of radiation detection," p. 784, 2007.

[33] D. M. Rossi, "Investigation of the Dipole Response of Nickel Isotopes in the Presence of a High-Frequency Electromagnetic Field," Ph.D. dissertation, Johannes Gutenberg-Universität Mainz, 2009.

[34] "R3B Setup." [Online]. Available: https://www.gsi.de/work/forschung/nustarenna/nustarenna_divisions/kernreaktionen/activities/r3b

[35] M. F. L'Annunziata, *The atomic nucleus, nuclear radiation, and the interaction of radiation with matter*, 2020, vol. 1.

[36] W. R. Leo, *Techniques for Nuclear and Particle Physics Experiments: A How-to Approach*, 1994.

[37] H. T. Johansson, “The DAQ always runs Performing large scale nuclear physics experiments,” Ph.D. dissertation, Chalmers University of Technology, 2006.

[38] S. Paschalis, “Relativistic One-Nucleon Removal Reactions,” Ph.D. dissertation, University of Liverpool, 2008.

[39] R. Thies, “Prototype tests and pilot experiments for the R 3 B scintillator-based detection systems,” 2011.

[40] V. Metag, R. Fischer, W. Kühn *et al.*, “Physics with 4 π γ-detectors,” *Nuclear physics. A*, vol. 409, pp. 331–342, 1983.

[41] F. Wamers, “Quasi-Free-Scattering and One-Proton-Removal Reactions with the Proton-Dripline Nucleus 17Ne at Relativistic Beam Energies,” *Ph.D. Thesis*, 2011.

[42] S. Beceiro Novo, “Coulomb Dissociation of 27P at 498 A MeV: an indirect measurement of the astrophysical 26Si (p ,γ) reaction,” Ph.D. dissertation, 2011.

[43] R. THIES, “Across the drip-line and back: examining 16B,” Ph.D. dissertation, Chalmers University of Technology, 2014.

[44] T. Blaich, T. Elze, H. Emling *et al.*, “A large area detector for high-energy neutrons,” *Nuclear Instruments and Methods in Physics Research Section A: Accelerators, Spectrometers, Detectors and Associated Equipment*, vol. 314, no. 1, pp. 136–154, 1992.

[45] K. Mahata, H. T. Johansson, S. Paschalis *et al.*, “Position reconstruction in large-area scintillating fibre detectors,” *Nuclear Instruments and Methods in Physics Research Section A: Accelerators, Spectrometers, Detectors and Associated Equipment*, vol. 608, no. 2, pp. 331–335, 2009.

[46] G. R. Jimenez, “Studies beyond the neutron dripline using Quasifree (p,2p) reactions The: case of 13Be,” 2015.

[47] L. Jones, S. Bell, Q. Morrissey *et al.*, “A readout ASIC for the R3B silicon tracker,” pp. 1–6, 2015.

[48] M. Heine, “Measurement of (n, γ)-Rates of Light Neutron-Rich Nuclei for the r-Process Nucleosynthesis,” 2015.

[49] C. Caesar, “Beyond the Neutron Drip-Line: Superheavy Oxygen Isotopes,” 2012.

[50] H. Johansson, “ucesb - unpack check every single bit.” [Online]. Available: http://fy.chalmers.se/~f96hajo/ucesb/

[51] A. Movsesyan, “Quasi-free one-proton and one-neutron knockout reactions on 57Ni,” 2013.

[52] R. Plag, “Ralf’s tracker.” [Online]. Available: http://ralfplag.de/tracker/

[53] “Atima.” [Online]. Available: https://www.isotopea.com/webatima/

[54] D. Sohler, M. Stanoiu, Z. Dombrádi *et al.*, “In-beam γ-ray spectroscopy of the neutron-rich nitrogen isotopes 19–22N,” *Physical Review C*, vol. 77, no. 4, p. 044303, 2008.

[55] M. Holl, V. Panin, H. Alvarez-Pol *et al.*, “Quasi-free neutron and proton knockout reactions from light nuclei in a wide neutron-to-proton asymmetry range,” *Physics Letters B*, vol. 795, pp. 682–688, 2019.

[56] “Fairroot.” [Online]. Available: https://fairroot.gsi.de/

[57] “R3BRoot.” [Online]. Available: https://www.r3broot.gsi.de/

[58] V. Panin, “Fully Exclusive Measurements of Quasi-Free Single-Nucleon Knockout Reactions in Inverse Kinematics,” 2012.

[59] L. Chulkov, F. Aksouh, A. Bleile *et al.*, “Quasi-free scattering with 6,8He beams,” vol. 759, no. 1, pp. 43–63, 2005.

[60] A. S. Goldhaber, “STATISTICAL MODELS OF FRAGMENTATION PROCESSES,” *Physics Letters B*, vol. 53, no. 4, pp. 306–308, 1974.

[61] S. Ziliani, S. Leoni, B. Fornal *et al.*, “Complete set of bound negative-parity states in the neutron-rich 18N nucleus,” *Physical Review C*, vol. 104, no. 4, p. L041301, 2021.

[62] D. R. Tilley, H. R. Weller, C. M. Cheves *et al.*, “Energy Levels of Light Nuclei A = 18-19,” *Nuclear Physics A*, vol. 595, no. 1, pp. 1–170, 1995.

[63] M. Stanoiu, F. Azaiez, Z. Dombrádi *et al.*, “N=14 and 16 shell gaps in neutron-rich oxygen isotopes,” *Physical Review C*, vol. 69, no. 3, p. 034312, 2004.

[64] D. R. Tilley, C. M. Cheves, J. H. Kelley *et al.*, “Energy levels of light nuclei, A=20,” *Nuclear Physics A*, vol. 636, no. 3, pp. 249–364, 1998.

[65] W. Powell, “Development of a Silicon Tracker and Front-End Electronics for R3B,” p. 224, 2016.

[66] M. Borri, R. Lemmon, J. Thornhill *et al.*, “Detector production for the R3B Si-tracker,” *Nuclear Instruments and Methods in Physics Research, Section A: Accelerators, Spectrometers, Detectors and Associated Equipment*, vol. 836, pp. 105–112, 2016.